Experimental and Numerical Studies on the Performance and Emission Characteristics of Waste Cooking Oil Biodiesel fuel and its Blends in a Direct Injection Diesel Engine

S BAHMANISANGESARI

PhD 2022

Experimental and Numerical Studies on the Performance and Emission Characteristics of Waste Cooking Oil Biodiesel fuel and its Blends in a Direct Injection Diesel Engine

SAJJAD BAHMANISANGESARI

A THESIS SUBMITTED IN PARTIAL FULFILMENT OF THE REQUIREMENTS OF MANCHESTER METROPOLITAN UNIVERSITY FOR

THE DEGREE OF DOCTOR OF PHILOSOPHY

Faculty of Science and Engineering, Department of Engineering

Manchester Metropolitan University

2022

Acknowledgement

The journey that culminated in this thesis has been one of immense personal and academic growth. Navigating the complexities and challenges of this endeavour was made possible through the unwavering support, guidance, and encouragement of many individuals who surrounded me.

Foremost, I owe a profound debt of gratitude to my supervisor, Dr. Olawole Kuti. His wisdom, patience, and belief in my capabilities were instrumental at every stage.

My heart swells with gratitude when I think of my family. To my parents, Dr. Rahman Bahmanisangesari and Prof. Nahid Ashrafi: even though distances separated us, your love, trust, and unwavering faith in my abilities never diminished. Your sacrifices and resilience have been my guiding light. To my brother, Saeid: your consistent support and encouragement have been my steadfast anchor during the most challenging times.

I am deeply appreciative of Paul Aldred's expertise and assistance in the initial phases of my research, and I extend a special note of gratitude to Argent Energy Biodiesel for supplying the essential fuel for my tests, making this research possible.

My colleagues and dear friends, Aytac Gokce, Faisal Almutairi, and Hakan Merdan, have enriched this journey with their fellowship and shared wisdom. Your presence has made this voyage both enjoyable and meaningful.

Finally, I'm forever grateful to the Almighty ALLAH for giving me strength and purpose. Alhamdulillah for the endless blessings on this journey.

Abstract

Internal combustion engines, especially diesel engines, have sustained the transportation industry for over a century. As the global emphasis shifts towards renewable energy sources and improved air quality, biodiesel especially from waste cooking oil (WCO) emerges as a potential solution to the inherent challenges of emissions from diesel engines. This research endeavours to address the prevailing gaps in the understanding of combustion characteristics and emissions of Waste Cooking Oil Biodiesel (WCO B100) and its blends. While previous studies have primarily focused on vessel models and overlooked real-world dynamics like piston movement and the splash model, this research illuminates these vital elements by incorporating them into the ANSYS Fluent IC Engine model. To further deepen our understanding, a detailed chemical reaction sensitivity analysis was executed using the 0-D ANSYS Chemkin-Pro DI Engine diesel reactor simulation. Methodologically, the research combined experimental platforms, a 0-D Direct Injection engine model on ANSYS Chemkin-Pro, and Computational Fluid Dynamics (CFD) simulations via ANSYS Fluent. Core findings reveal that waste cooking oil biodiesel has a shortened ignition delay, attributed to its reduced heat capacity and enhanced evaporative characteristics. Additionally, this fuel exhibits accelerated evaporation rates and superior thermal conductivity, especially noticeable at heightened temperatures during the piston bowl's ascent. Notably, there's an initial extension in its liquid penetration length, quickly followed by a significant decrease. This pattern suggests a potential for a more localized and richer combustion zone. Compounding these observations, waste cooking oil biodiesel displays shorter liquid and vapour penetration lengths, a characteristic likely influenced by its lower heating value. This suggests less energy availability for propelling the vapour cloud further into the chamber, further affecting the vapour penetration length adversely. In terms of emissions, waste cooking oil biodiesel significantly reduced HC particulate and NOx emissions. Sensitivity analyses revealed key reactions influencing emissions, such as formaldehyde production through reactions involving OH and O radicals and the intricate nature of combustion chemistry, highlighted by interactions of acetylene and other hydrocarbons. In conclusion, this study provides vital insights into waste cooking oil biodiesel's combustion, spray, and emission dynamics, underscoring the importance of diesel engine optimization for a cleaner and sustainable future.

Declaration

This is to certify that the material contained in this thesis has been produced by author and has not been accepted in substance for any other degree and is not currently submitted in candidature for any other academic award.

Table of Contents

List of Figures

List of Tables

ABBREVIATION

NAMES	ABBREVIATIONS
1-Hexene	nC_6H_{12}
Air-To Fuel Ratio	AFR
Before Top Dead Centre	BTDC
Cetane Number	CN
Cresol radical (fenoxy like)	RCRESOLO
Coherent Flamelet Model	CFM
Compressed Natural Gas	CNG
Compression Ignition	CI
Computational Fluid Dynamic	CFD
Damköhler	Da
Degree Of Unsaturation	DU
Discrete Phase Model	DPM
Fatty Acid Methyl Ester	FAME
Favre joint PDF of composition	**P**
Formaldehyde	CH_2O
Heat Release Rate	HRR
Hydroxyl Radical	OH
Hydroperoxyl	HO_2
Intergovernmental Panel on Climate Change	IPCC
Internal Combustion	IC
Kelvin-Helmholtz/Rayleigh-Taylor	KH-RT
K-Epsilon	K-ε
Lagrangian Wall Film	LWF

Lewis Number	Le
Liquefied Natural Gas	LNG
Liquefied Petroleum Gas	LPG
Low Temperature Combustion	LTC
Methyl- 5-Decenoate	MD5D
Methyl Decanoate	MD
Methyl Linoleate	MLINO ($C_{19}H_{34}O_2$)
Methyl Linolenate	MLIN1 ($C_{19}H_{32}O_2$)
Methyl Oleate	MEOLE ($C_{19}H_{36}O_2$)
Methyl Palmitate	MPA ($C_{17}H_{34}O_2$)
Methyl Stearate	MSTEA ($C_{19}H_{38}O_2$)
Methyl-9-Decenoate	MD9D
Methyl formate radical	CH_3OCO
Methyl palmiate radicals	RPMAX
Methyl stearate radicals	RSTEAX
Normal	N
N-Heptane	$n\mathrm{C_7H_{16}}$
Nitrogen Oxide	NOX
Nondispersive Infrared	NDIR
Nusselt Number	Nu
Palm Methyl ester	PME
Particulate Matter	PM
Polycyclic Aromatic Hydrocarbon	PAH
Pressure	p
Pressure-Implicit with Splitting of Operators	PISO
Probability Density Function	PDF

Producer Gas	PG
Pure Biodiesel	B100
Rad methyl linoleate all	RMLINA
Rad melinolenate	RMLIN1X
Representative Interactive Flamelet	RIF
Reynolds Number	Re
Reynolds-Averaged Navier–Stokes	RANS
Sauter Mean Diameter	SMD
Secondary Radical methyl oleate	RMEOLES
Soybean Methyl Ester	SME
Spalding Mass Number	B_m
Spark Ignition	SI
Start Of Injection	SOI
Stefan-Boltzmann Constant	σ
Sulphur Dioxide	SO_2
Toluene	C_7H_8
Top Dead Centre	TDC
Turbulent Kinetic Energy	TKE
Unburned Hydrocarbon	HC
Variable Compression Ratio	VCR
Waste Cooking Oil	WCO
Weber Number	We

Chapter 1 - Introduction

Over the last century and a half, reliance on internal combustion engines, particularly for transportation, has grown significantly. However, it's crucial to consider air quality. To meet increasingly stringent emissions regulations and utilise renewable energy sources, there's been a significant push for the adoption of biodiesel. A promising solution is the use of waste cooking oil (WCO) biodiesel from domestic sources and restaurants. While diesel engines offer high thermal efficiency compared to SI engines, they face challenges in emissions. Therefore, the development of alternative biofuels is essential to address this issue.

1.1 What is Combustion ?

Combustion is a chemical phenomenon denoting the intricate interplay between a fuel substance and an oxidizing agent, commonly oxygen, resulting in the emission of energy in the form of radiant heat and luminous radiation. This intricate process transpires when a substance, often exemplified by a hydrocarbon-centric fuel such as diesel, engages in a complex chemical reaction with oxygen, leading to the emergence of carbon dioxide, water vapour, and a multifaceted array of combustion-related by-products. The culmination of this interaction precipitates rapid oxidation, instigating the fervent generation of thermal energy, which can be judiciously harnessed for multifarious applications, ranging from the propulsive power of engines to the provision of thermal comfort through diverse heating systems. In its quintessence, combustion constitutes a meticulously orchestrated and regulated phenomenon, orchestrated to effectuate the methodical discharge of energy.

1.2 IC Engine Fundamental Procedure

The internal combustion engine (IC engine) stands as a hallmark of modern transportation and energy conversion, propelling vehicles and powering a diverse range of machinery (Heywood, 2018; Taylor, 1985; Stone, 1999). Its fundamental procedure involves a sequence of intricate thermodynamic and mechanical processes that culminate in the conversion of chemical energy in fuel into mechanical work (Heywood, 2018).This exposition delves into the key stages of an IC engine's operation, elucidating its underlying principles and mechanics while citing relevant references and employing illustrative figures.

1- Intake Stroke: The engine's cycle initiates with the intake stroke. As the piston descends within the cylinder, a mixture of fuel and air is drawn into the combustion chamber from the intake manifold. This phase sets the stage for the subsequent combustion process.
2- Compression Stroke**:** The intake valve closes, and the piston ascends, compressing the fuel-air mixture. The compression stroke raises the temperature and pressure within the chamber, optimizing conditions for efficient combustion.
3- Combustion Stroke: When the fuel-air mixture reaches its optimal compressed state, an ignition source initiates combustion. This rapid reaction releases a surge of energy, resulting in a sharp increase in pressure and temperature within the chamber. This pressure forces the piston to move downward, generating mechanical work.
4- Power Stroke: The combustion-driven expansion continues into the power stroke, where the piston's downward movement is harnessed to turn the crankshaft. This rotational motion transfers power to the engine's output shaft, enabling the conversion of chemical energy into mechanical work.
5- Exhaust Stroke: As the power stroke concludes, the exhaust valve opens, and the piston ascends once more. The expanding gases from combustion are expelled from the combustion chamber into the exhaust manifold, paving the way for the next cycle.

This fundamental operational sequence, known as the four-stroke cycle (Heywood, 2018; Stone, 1999), is intrinsic to the operation of most internal combustion engines. Variants, such as the two-stroke cycle, exist, but the four-stroke configuration remains prevalent due to its efficiency and reduced emissions.

Various factors impact an engine's performance, such as compression ratio, air-fuel mixture, ignition timing, and valve timings (Taylor, 1985). Advancements in combustion technology, fuel injection, and engine management systems have refined engine efficiency and emissions control. Modern engines often incorporate technologies like turbocharging, direct injection, and variable valve timing to optimize power output, fuel efficiency, and emissions.

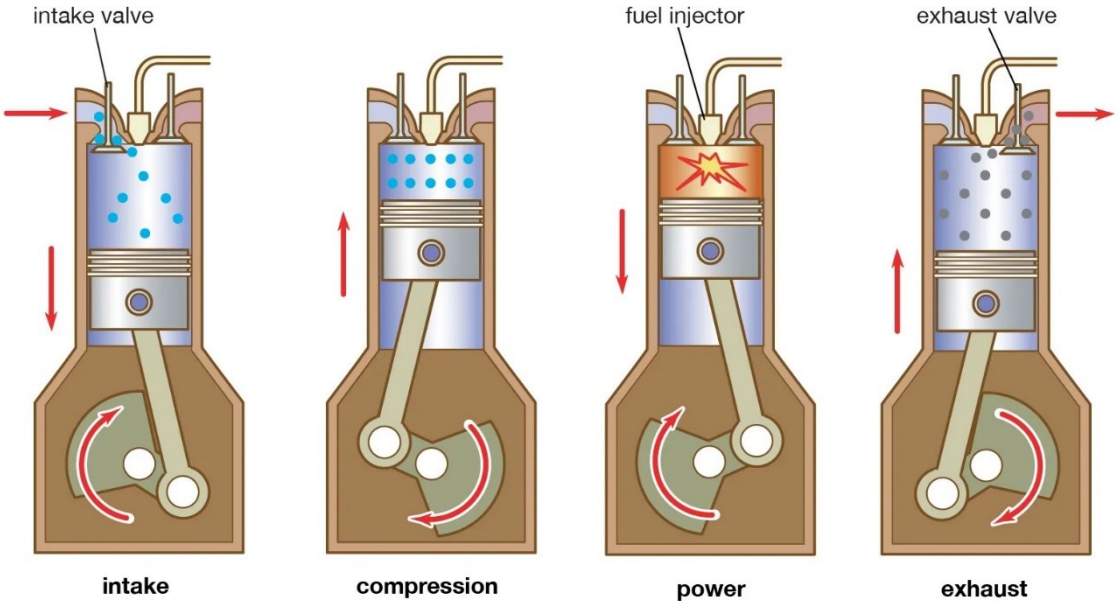

Figure 1 - A schematic diagram illustrating the four-stroke cycle of an internal combustion engine. The diagram depicts the stages of intake, compression, power, and exhaust, along with the movement of the piston within the cylinder during each stage (Proctor and Armstrong, 2023).

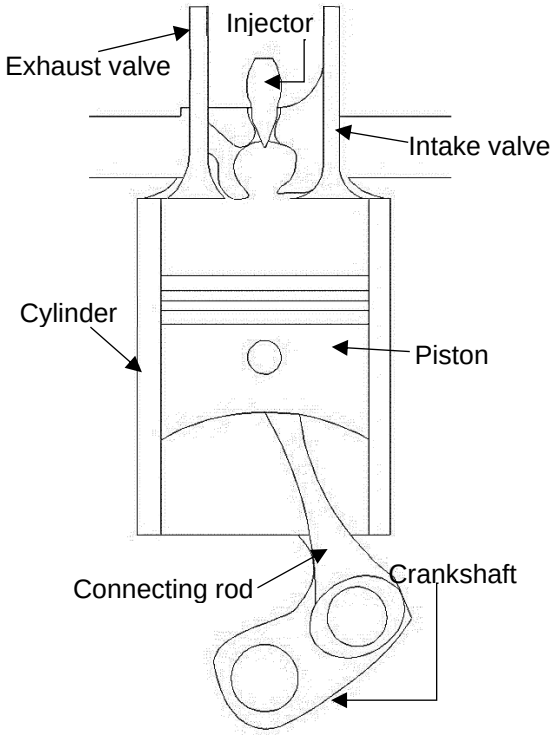

Figure 2 - A cross-sectional diagram showcasing the internal components of a reciprocating diesel engine. The diagram displays key elements, including the piston, cylinder, valves, connecting rod, injector, and crankshaft.

To visually elucidate these stages, Figure 1 illustrates the sequence of a four-stroke cycle, while Figure 2 showcases the internal components of a reciprocating internal combustion engine.

In conclusion, the internal combustion engine's fundamental procedure involves a cyclic series of intake, compression, combustion, and exhaust strokes, converting chemical energy into mechanical work.

1.3 Emission and Need of Better Fuels (Clean Energy)

As the global challenges arising from environmental transformations and air quality deterioration have heightened, there has been an increased impetus to advance ignition technologies with the objectives of augmenting operational efficiency and curbing the propagation of noxious substances. Over the span of the last three decades, a diverse array of research inquiries and consequential findings have been undertaken in response to the phenomenon of global warming, thereby shedding significant light on the compelling necessity to adopt strategies of minimal carbon emissions. Notably, the Intergovernmental Panel on Climate Change (IPCC), inaugurated during the 1980s by the collaboration of the World Meteorological Organization and the United Nations Environment Programme, has strategically elevated the priority of integrating low-carbon methodologies. Emblematic of this stance is the Kyoto Protocol, wherein a pivotal international assembly convened on February 16, 2005, emphasizing the commitment of industrialized nations to effectuate substantial reductions in carbon discharges.

The exigency for low-carbon energy solutions has attained prominence in contemporary discourse, precipitated by mounting apprehensions regarding pollutants, prompting a discerning turn towards cleaner fuel options capable of ameliorating the ramifications of combustion-based emissions. Researchers, driven by ecological concerns and an impending depletion of fossil fuel resources, have embarked on an exploratory quest for viable and sustainable alternative energy sources. Within this ambit, a gamut of fuel categories emerges as prospective hydrocarbon-based alternatives for employment in internal combustion engines, encompassing Compressed Natural Gas (CNG), Liquefied Natural Gas (LNG), Liquefied Petroleum Gas (LPG), alcohols, vegetable oils, biogas, Producer Gas (PG), and hydrogen.

Notwithstanding the prevalence of compression ignition engines in the transportation domain, diesel-fuelled vehicles are implicated in the emission of pollutants surpassing acceptable thresholds. This dilemma assumes pronounced significance within the purview of the public transportation sector, necessitating a

concerted endeavour to abate emissions. A plausible avenue to address this concern manifests through the adoption of fuel sources characterized by diminished hydrocarbon emissions, thereby aligning diesel engines with rigorous emission standards.

1.4 Waste Cooking Oil Biodiesel

The potential implementation of biodiesel as an alternative fuel for diesel engines presents an avenue to mitigate emissions of particulate matter and other pollutants (Smith *et al.*, 2015). Nonetheless, concerns have emerged due to the competition between biodiesel feedstock and food resources, raising critical debates over its viability (Kulkarni and Dalai, 2006). A pragmatic approach to address this concern is the recycling of post-consumer cooking oil from commercial kitchens and dining establishments. Employing esterification methods, the repurposed cooking oil, devoid of threats to the food chain, can be converted into Waste Cooking Oil (WCO) biodiesel (Demirbas, 2009a).

The distinctive advantage of WCO biodiesel lies in its heightened oxygen concentration, positioning it as an optimal choice for curbing emissions in diesel engines (Atabani *et al.*, 2012). Cooking oil, subjected to frying and heating, undergoes complex chemical transformations including polymerization, oxidation, and hydrolysis, ultimately diminishing its nutritional value and giving rise to by-products like polymeric triglycerides and polar molecules (Nayak *et al.*, 2016).

Improper disposal of used cooking oil into water bodies, common in developing regions, leads to harmful consequences like transmission of compounds through aquatic systems and health risks (Pagotto *et al.*, 2007; Maceiras, Míguez and González, 2019). This practice also triggers eutrophication, disrupting ecosystems and limiting sunlight penetration (Rosenberg, McCully and Allen, 2019). Converting waste cooking oil into biodiesel emerges as a comprehensive solution. It addresses pollution, protects food resources (Barnwal and Sharma, 2005), and enhances energy security through repurposing resources for sustainable biodiesel production (Karmee and Chadha, 2005).

1.5 About ANSYS Fluent

ANSYS Fluent constitutes a pivotal fluid simulation software widely employed across industries. It is adept at analysing fluid dynamics, heat and mass transfer, chemical reactions, and interconnected fluidic phenomena. The software

facilitates advanced fluid modelling, regardless of the complexity of hypotheses, thus providing precise industry-relevant insights. Its remarkable versatility in addressing intricate challenges has positioned it as a preeminent fluid simulation solution. Applications range from electric vehicle airflow modelling to internal combustion engine combustion simulations. Profound capabilities encompass heat transfer, electromagnetic radiation, multiphase flow, comprehensive chemical and combustion simulations, and acoustic modelling. In essence, ANSYS Fluent offers a comprehensive and potent platform for multifaceted fluid-related simulations.

1.6 Contribution of Study

Previous studies on combustion characteristics including ignition delay, evaporation processes, spray formation, and spray penetration length in CFD vessel models, often omit crucial real-world diesel engine dynamics, such as the effects of piston movement. Additionally, there is a lack of attention to the splash model, which is not considered in typical vessel reactors. This study addresses these oversights and contributes by bridging this knowledge gap.

Existing literature does not provide detailed chemical reaction explanations that contribute significantly to the emission species of waste cooking oil biodiesel, such as NOx, hydrocarbon (HC), CO, and CO_2. As a response, this study has established an extensive chemical reaction sensitivity analysis model, shedding light on the major species impacting emissions from waste cooking oil biodiesel variants.

A key contribution of this study is the implementation of a 0-D ANSYS Chemkin-Pro DI Engine diesel reactor simulation. This integrates the advantages of CFD numerical models with detailed chemical reaction mechanisms. The study assesses the chemical reactions that have the most substantial impact on emissions from both diesel and waste cooking oil biodiesel, providing a more realistic approach to Waste Cooking Oil Biodiesel (WCO B100) emission studies.

1.6.1 Aim

The primary aim of this PhD research is to delineate the combustion behaviour, spray formation, and emission properties of Waste Cooking Oil Biodiesel (WCO B100) and its blends in diesel engines. This is achieved through experimental setups and numerical modelling, incorporating the splash model and piston

movements in ANSYS Fluent, and an extensive chemical reaction sensitivity analysis in 0-D ANSYS Chemkin-Pro DI Engine.

1.6.2 Objective

The main objectives of this study are:

- To establish an experimental setup for a diesel engine test bench equipped with the necessary acquisition tools.
- To conduct engine tests for waste cooking oil biodiesel, diesel, and their blends under various load conditions, obtaining experimental in-cylinder pressure vs. crank angle and emission data.
- To develop a 3D computational fluid dynamic model using ANSYS Fluent commercial software, based on the Robin DY23-2D small-duty diesel engine configuration.
- To validate CFD results against experimental data, including pressure vs. crank angle, empirical heat release rates, and emission outputs.
- To analyse combustion characteristics like heat release rate, ignition delay, combustion efficiency, and thermal efficiency using both CFD and experimental results for waste cooking oil biodiesel, diesel, and their blends.
- To conduct parametric studies on spray formation, considering factors like liquid penetration length, vapour penetration length, ignition delay, and evaporation process. This should account for the rising movement of the engine piston and the splash model.
- To undertake emission behaviour parametric studies for carbon monoxide (CO), carbon dioxide (CO_2), nitrogen oxides (NOx), and unburned hydrocarbons (HC) using both CFD and experimental results for waste cooking oil biodiesel, diesel, and their blends.
- To design a 0-D ANSYS Chemkin-Pro DI Engine simulator for sensitivity analysis and validate it against experimental pressure data.

- To execute sensitivity analysis studies, aiming to identify major reactions that notably impact the consumption and production of key emission species.

1.7 Outline of thesis

Chapter 2 delves into established literature that has explored both experimental and numerical characteristics of bio-fuel variants in diesel engines. These characteristics span across combustion, spray formation, and emissions.

Chapter 3 presents the prevailing numerical models utilised in diesel engine combustion. This chapter also outlines the boundary conditions formulated to simulate a realistic numerical model of engine operations. Chapter 4 describes the experimental setup, enumerating the requisite acquisition tools and components necessary for conducting successful experiments. Following this, the chapter details the numerical modelling setup for the 0-D ANSYS Chemkin-Pro DI Engine, intended for sensitivity analyses. It also covers the ANSYS Fluent CFD setup for waste cooking oil biodiesel and diesel fuel, specifically for the Robin DY23-2D small-duty diesel engine configuration.

Chapter 5 offers an analysis and discussion on the CFD and experimental data gathered. This includes insights on parameters such as pressure versus crank angle, heat release rate, ignition delay, combustion efficiency, and thermal efficiency. The results pertain to waste cooking oil biodiesel, diesel, and their blends under varied load conditions. Chapter 6 provides an in-depth examination of the spray evaporation process. It analyses the liquid and vapour penetration lengths for waste cooking oil biodiesel, diesel, and their blends across different load conditions.

Chapter 7 centres on the emission data derived from the Horiba MEXA-584L emission kit during experiments. This chapter juxtaposes this data with CFD results on key emission species. Subsequently, an extensive chemical reaction sensitivity analysis using the 0-D ANSYS Chemkin-Pro DI Engine reactor is conducted, elucidating the primary species that influence emissions from waste cooking oil biodiesel variants. Chapter 8, the concluding chapter, provides a summation of the entire thesis. It outlines the conclusions drawn from the research and recommends directions for future work.

Chapter 2 - Literature Survey

2.1 Introduction

The pursuit of sustainable and environmentally benign energy sources has led researchers to extensively explore biofuels as potential alternatives to conventional fossil fuels. Among these, Waste Cooking Oil (WCO) biodiesel has emerged as a promising candidate, showing notable combustion characteristics that could reshape the landscape of fuel technology. This chapter delves deep into the expansive body of literature surrounding the experimental and computational numerical modelling, specifically Computational Fluid Dynamics (CFD), of bio-fuel variants with an emphasis on WCO biodiesel in diesel engines.

Initially, the literature review underscores the fundamental structure and chemical makeup of conventional fossil diesel fuels, laying a foundational understanding for the subsequent discussions. As the exploration delves further into the bio-fuel domain, the chapter delineates the chemistry and properties of methyl esters. A special focus is accorded to esters as biodiesels, highlighting their unique chemical structures and potential advantages over traditional diesel.

Building upon the foundational chemistry, the review then delves into the heart of combustion characteristics. Here, specific attention is granted to biodiesels, like WCO and other Fatty Acid Methyl Ester (FAME) fuels. Key among these characteristics is the ignition delay - a pivotal metric in understanding combustion behaviour. The very essence and definition of ignition delay, and its implications in engine performance, are dissected in detail.

Beyond combustion, the intricacies of spray formation of these biofuels, as documented in existing literature, are presented. This section elucidates the atomisation, penetration, and vaporisation processes, providing critical insights into the fuel-air mixing dynamics, essential for optimal engine operation.

The subsequent chapter pivots towards emissions, addressing both the environmental and performance implications of using biodiesels. Delving deeper into the intricacies of emission formation, the review elucidates the mechanisms responsible for the generation of various pollutants and underscores their potential impact on the environment.

The literature review's culmination emphasizes the methodologies employed in this research, highlighting the chemistry mechanisms pivotal for both CFD and 0-D simulations. Gleaning insights from a multitude of studies and experiments, the objective is to provide a comprehensive understanding of biodiesel's behaviour, particularly within the context of diesel engines. This foundation paves the way for the subsequent chapters, where the intricacies of biodiesel dynamics, as inferred from experimental and simulation data, will be further elaborated and discussed.

2.2 Fossil Diesel Fuel

Fossil diesel fuel is a complex mixture comprised of hundreds of distinct chemical species. It represents a fractional distillate of crude oil. The main constituents of fossil diesel fuel are approximately 66% paraffins (C_nH_{2n+2}) and cycloparaffins (C_nH_{2n}), which have chain lengths varying from C_{12} to C_{22}. Aromatics, hydrocarbons that contain at least one benzene ring, make up about 30% of the composition, while olefins (C_nH_{2n}) contribute around 4%. The specific composition of fossil diesel fuel can be influenced by refining methods and the unique proportions of the crude oil source (Isidro, 1992).

For compression ignition engines, a suitable cetane number typically hovers around 49, with an estimated boiling point range of 450K to 630K. As a point of reference, hexane (C_6) has been assigned a cetane number of 53 when measured using the ASTM method D6890. Furthermore, a cetane number of 105 has been proposed for heptadecane (C_{17}) (Yanowitz *et al.*, 2017).

Among the properties of diesel fuel, viscosity and cold flow characteristics stand out due to their pronounced impact on engine operation. Fuels with elevated viscosity often necessitate specialized components like heated fuel lines or glow-plugs. This suggests that diesel fuels with higher molecular masses tend to form waxy deposits at reduced temperatures. Nonetheless, an array of fuel additives has been developed, offering enhancements to cetane number (CN), viscosity, and cold flow properties of various diesel formulations (Stone, 1999).

While crude oil refining remains a primary source for hydrocarbon fuels, there are alternative methodologies. Notably, hydrocarbon fuels can be derived from renewable sources through advanced bio-processing techniques. Economic considerations, however, currently drive the predominance of crude oil refining in diesel fuel production. Bio-process-derived hydrocarbons, typically a result of

metabolic engineering, serve more as a testament to innovative approaches in alternative fuel production rather than competing with the commercial scale of traditional hydrocarbons (Lee, Kim and Cheon, 2015; Schirmer *et al.*, 2010; Steen *et al.*, 2010).

2.3 Methyl esters

Biodiesel represents a renewable energy source primarily composed of mono-alkyl esters derived from long-chain fatty acids present in vegetable oils and animal fats. This transformation of fatty acids into esters is facilitated through transesterification reactions, typically employing alcohols like methanol and ethanol. In regions like Europe and the USA, excess edible oils such as soybean, sunflower, and rapeseed oils are favoured as feedstocks for biodiesel production.

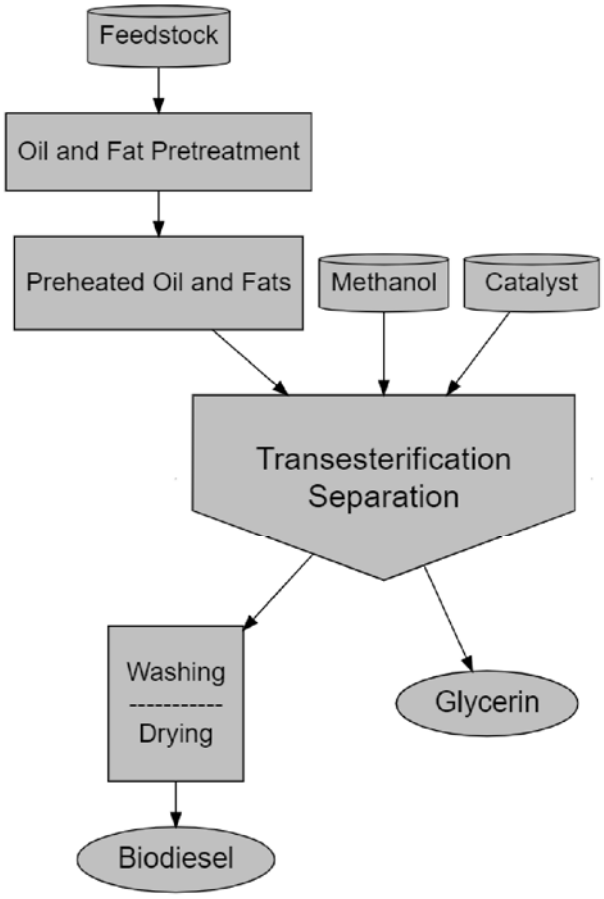

Figure 3 - Biodiesel production process

Figure 3 illustrates the complex yet methodical process of biodiesel production. Initially, the raw feedstock undergoes a purification process, ensuring the removal of any contaminants. Once refined, this feedstock is then subject to a thermal conditioning process, elevating its temperature to approximately 327.6 K (Gerveni, Hubbs and Irwin, 2023). During this thermal phase, rigorous tests are conducted

to ascertain the free fatty acid composition of the feedstock, ensuring its suitability for the subsequent stages. With the temperature meticulously maintained, the conditioned feedstock is introduced into the primary reactor vessel. Here, it's combined with methanol and basic catalysts. In specific scenarios, and less frequently in the U.S., enzymes might also be added. This concoction is agitated to facilitate the transesterification reaction, which typically concludes within an hour (Gerveni, Hubbs and Irwin, 2023).

Post-reaction, the blend is left undisturbed for an extended duration, allowing for the natural separation of biodiesel and glycerine based on their density disparities (Gerveni, Hubbs and Irwin, 2023). This gravitational differentiation ensures the heavier glycerine settles at the reactor's base, while the biodiesel floats atop.

Subsequent to this segregation phase, glycerine is methodically siphoned off and subjected to a purification protocol, wherein surplus methanol is extracted. Following its refinement, it is systematically stored in dedicated containment units. In parallel, the methyl esters are transitioned to a separate reservoir. Here, they undergo rigorous aqueous wash cycles to meticulously cleanse them of residual catalysts, soaps, salinity, methanol, and any traces of glycerine (Gerveni, Hubbs and Irwin, 2023). Upon achieving the desired purity, the esters are subjected to an exhaustive drying regimen, ensuring the complete eradication of any residual moisture. This culminates in the production of premium-quality biodiesel, which is then safely stored, awaiting distribution and utilisation (Gerveni, Hubbs and Irwin, 2023).

An intrinsic characteristic of biodiesel is its oxygen content, typically ranging between 11-15 wt. percent. This inherent oxygenation can enhance combustion efficiency in diesel engines, leading to potential reductions in emissions such as CO, CO_2, HC, particulate matter, SOx, and Polycyclic Aromatic Hydrocarbons (PAH) (Kuti *et al.*, 2013b).

For example, it has been reported that by using palm biodiesel and implementing two important strategies such as, smaller nozzle injector and higher injection pressure particulates can be reduced in diesel engine (Kuti *et al.*, 2010). As a result of its higher cetane number and oxygen content, biodiesel tends to have a shorter ignition delay (faster reactivity) and produce less particulates. The WCO biofuel consists a mixture of methyl decanoate ($C_{11}H_{22}O_2$), methyl 9-decenoate

($C_{11}H_{20}O_2$) and n-heptane (C_7H_{16}), while methyl decanoates are the unsaturated compounds found in Fatty Acid Methyl Ester (FAME) fuels, (Wang, Gowdagiri and Oehlschlaeger, 2013).

The composition of the unsaturated surrogate fuel, particularly the proportions of its constituent mixtures, markedly influences emission profiles. An increased level of unsaturation in the biodiesel enhances fuel-air mixing and elevates local temperatures. This, in turn, leads to a rise in the production of NO emissions. Concurrently, there's a pronounced reduction in CO emissions (Li *et al.*, 2018).

2.3.1 Esters as Biodiesel

Biodiesel, as a renewable alternative to fossil fuels, presents a unique set of properties that differ from traditional fossil diesel. One of the primary distinctions between the two is biodiesel's high oxygen content. This attribute reduces its fuel energy density. However, with its inherently higher density, biodiesel's volumetric energy percentage remains only about 5-6% less than that of fossil diesel. This distinction extends to other attributes as well, with biodiesel exhibiting increased viscosity, higher surface tension, and poorer cold flow properties than its fossil counterpart (Ejim, Fleck and Amirfazli, 2007; Hoekman *et al.*, 2012).

Animal fats and vegetable oils are foundational materials for biodiesel production. However, they can pose challenges when combusted in compression ignition engines, primarily due to the large molecular sizes of the triglycerides they contain. For reference, standard commercial biodiesel typically has a Cetane Number (CN) of around 57 and a boiling point ranging between 622-632K (Knothe, 2014; Yuan, Hansen and Zhang, 2005).

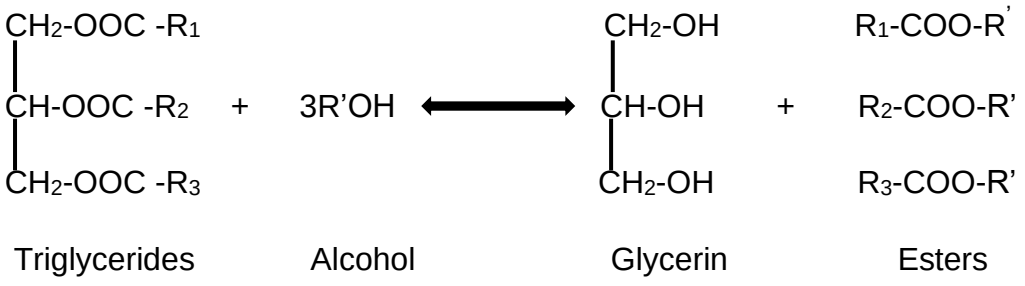

Figure 4 - Transesterification process of biodiesel production from triglycerides (Abbaszaadeh *et al.*, 2012).

The production of biodiesel centres around the transesterification process. In this method, triglycerides are combined with alcohols, usually methanol or ethanol, in the presence of catalysts such as potassium hydroxide or sodium. This results in

the formation of Fatty Acid Methyl Ester (FAME) and glycerol, a process illustrated in Figure 4.

Interestingly, incorporating higher alcohols like ethanol, isopropanol, or butanol into this process can produce biodiesel variants with longer carbon chains. Due to its economic advantage, methanol remains the most popular choice amongst these alcohols (Hoekman *et al.*, 2012). Numerous review articles offer deeper insights into the prevailing methods of biodiesel production (Borugadda and Goud, 2012; Bharathiraja *et al.*, 2014; Abbaszaadeh *et al.*, 2012; Daud *et al.*, 2015; Adewale, Dumont and Ngadi, 2015; Aransiola *et al.*, 2014).

Waste cooking oil (WCO) has garnered significant attention as a viable feedstock for biodiesel production. The attraction to WCO stems not only from its cost-effectiveness and sustainability but also from its distinctive fatty acid profile (Fangfang, Alagumalai and Mahian, 2021). Specifically, the composition of WCO biodiesel is enriched with both saturated and unsaturated fatty acids. The ratio of these fatty acids plays a pivotal role in determining the overall properties and performance of the resulting biodiesel (Fangfang, Alagumalai and Mahian, 2021).

Saturated fatty acids in WCO biodiesel impart better oxidative stability, ensuring a longer shelf-life of the fuel. They also contribute to a higher cetane number, which is desirable for improved ignition quality (Knothe, 2005). On the downside, an elevated concentration of saturated fatty acids tends to raise the biodiesel's cloud point, which might lead to solidification issues under colder temperatures (Schumacher, Wetherell and Fischer, 1999). On the other hand, unsaturated fatty acids, commonly abundant in WCO biodiesel, enhance fuel fluidity and reduce viscosity. However, a higher content of unsaturated fatty acids can make the biodiesel more susceptible to oxidative degradation, necessitating the use of stabilizers or antioxidants for longer storage (Vidigal *et al.*, 2021).

In essence, the balance between saturated and unsaturated fatty acids in WCO biodiesel dictates its operational suitability and storage stability. As such, understanding the fatty acid composition of the WCO source becomes crucial in tailoring biodiesel properties for specific applications (Kulkarni and Dalai, 2006).

Finally, it's worth noting that the composition of biodiesel is intricately linked to its feedstock. As an illustration, vegetable oils tend to be richer in unsaturated

triglycerides than animal fats. This highlights the need for careful feedstock selection in biodiesel production to achieve desired fuel properties (Knothe, 2014).

2.4 Combustion Characteristics

Combustion characteristics of Waste cooking oil (WCO) biodiesel blended with diesel have been explored extensively. As the blend's percentage increases, there's a notable reduction in ignition delay, a decrease in the heat release rate, and an elongation in combustion time (Kannan *et al.*, 2011).

Biodiesel displayed a higher peak cylinder pressure than diesel in certain engine tests. This earlier start of the heat release rate for biodiesel was attributed to combustion starting near the Top Dead Centre (TDC) (Gharehghani, Mirsalim and Hosseini, 2017).

Various methods are used to identify the ignition time delay in combustion studies. The most accepted method for determining ignition delay is the time from the start of injection (SOI) to a sharp rise in the pressure gradient, specifically $(\frac{dP}{d\theta})_{max}$, which corresponds to an inflection on a pressure-crank angle graph, as shown in Figure 5 (ASTM, 2010; Bogin Jr *et al.*, 2011; Elhalwagy and Zhang, 2019; Garzón, Oliveira and Bazzo, 2019; Naik *et al.*, 2012; Yang, 2012).

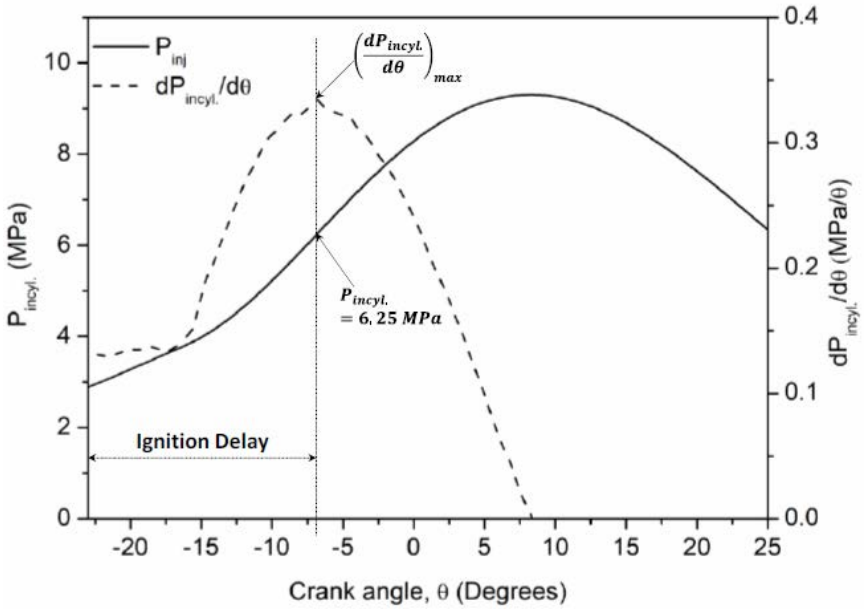

Figure 5 - Pressure vs. Crank angle graph Illustrating ignition delay from Start of Injection (SOI) to the inflection point (Kuti et al., 2022).

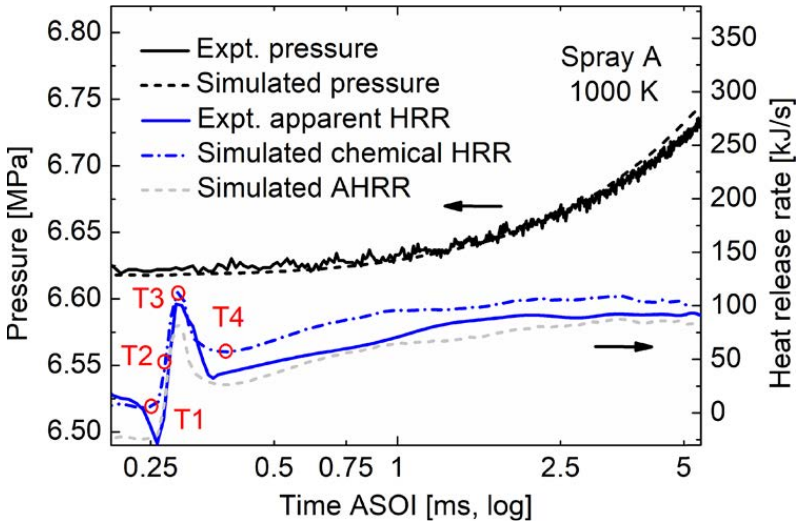

Figure 6 - Combustion period timing and a comparison of pressure and heat release rate of experiment with simulation, (Liu *et al.*, 2019).

Subsequent research determined the ignition delay time as the duration from the start of injection (SOI) to the point of ignition observation (T2) (Liu *et al.*, 2019).

The timing of combustion analysis proposed by Liu et al. (2019) in Figure 6 are as follows:

1) T1, only timing before ignition.
2) T2, when the ignition is taken place.
3) T3, when peak of premixed heat release has occurred.
4) T4, indicating the start of established diffusion combustion.

In terms of chemical dynamics, there's an interest in the consumption of formaldehyde (CH_2O) primarily in the T3 region, where exothermic reactions are prevalent. This established the reaction between O_2 and H as the main source of the OH radical (Liu *et al.*, 2019).

Conducted studies on cotton seed methyl esters mixed with diesel found that diesel had a higher heat release rate and in-cylinder gas pressure than the methyl ester blends. Conversely, methyl ester blends had shorter ignition delays and combustion periods (Vijayaraj and Sathiyagnanam, 2016).

Experimental investigations into the Variable Compression Ratio (VCR) engine's combustion and emission characteristics revealed certain peculiarities when using a blend of Simarouba-Jatropha oil biodiesel fuel under diesel engine conditions.

When the compression ratio of the engine was increased, a notable decrease in both peak pressure and net heat release rate was observed for the B100 biodiesel derived from a blend of Simarouba-Jatropha oil. Notably, the start of the heat release rate shifted before TDC, suggesting that B100 biodiesel derived from a blend of Simarouba and Jatropha oil with a higher compression ratio experiences reduced ignition delay. In fact, this specific B100 displayed a shorter ignition delay than diesel. Interestingly, the rate of pressure rise for the Simarouba-Jatropha oil-based B100 was slower than that of diesel, indicating a direct relationship between the reduction in delay period and an increase in diffusion combustion period for this biodiesel (Hosamani and Katti, 2018).

A correlation was identified between the molecular structural properties of biodiesel feedstock and elevated CO levels for WCO and refinery streams at high loads (Erman, Hellier and Ladommatos, 2020). Increased ignition delays were found to contribute to higher CO emissions due to the production of over-diluted mixtures and quenching at cylinder walls (Erman, Hellier and Ladommatos, 2020).

A crucial property for biodiesel composition is its degree of unsaturation (DU), which is characterized by the amount of double bonds in its structure (Li *et al.*, 2018). Higher unsaturation levels lead to shorter ignition delays and increased soot formation. An increase in biodiesel unsaturation seems to reduce the duration of its premixed combustion phase, which then results in more soot precursor formation and a lengthier reaction residence time (Li *et al.*, 2018).

As the cetane number of the fuel increases, there is a notable shortening in ignition delay, particularly when subject to higher injection pressures. This can be attributed to faster fuel breakup and vaporisation associated with higher pressures and the greater ignitability of fuels with higher cetane numbers. However, a higher cetane number also extends the combustion duration, leading to a longer diffusion-governed combustion phase and consequently, a shorter premixed combustion phase (Cowart, Luning Prak and Hamilton, 2015).

Conversely, biodiesel fuels, despite having higher viscosities than their petroleum counterparts, have a higher cetane number. This explains the shorter ignition delay observed in waste cooking oil (WCO) biodiesel compared to diesel (Yu, Bari and Ameen, 2002).

Notably, biofuels, despite having higher boiling points than diesel, undergo chemical reactions during injection at elevated temperatures, breaking down unsaturated fatty acids into compounds of lower molecular weight (Yu, Bari and Ameen, 2002). These lighter compounds accelerate gasification on the spray's periphery, which expands the jet, leading to earlier ignition and a shorter delay period (Yu, Bari and Ameen, 2002). Further, the higher boiling components in biodiesel that don't evaporate during the main combustion period continue to burn in the later stages, resulting in higher exhaust temperatures and reduced thermal efficiency in WCO biodiesel compared to diesel (Yu, Bari and Ameen, 2002).

Biodiesel's lower heat capacity compared to diesel implies that it heats up faster. Consequently, biodiesel droplets have a higher temperature rise rate than diesel for the same heat input, enhancing biodiesel's vaporisation rate (Ismail *et al.*, 2012). Biodiesel's higher thermal conductivity means that heat transfer between its droplets is faster, resulting in quicker droplet breakup. Latent heat of vaporisation is defined as the sum of energy which must be included in a liquid to convert an amount of substance into a gas (Sazhin, 2006). WCO biodiesel derived from soybean methyl ester feedstock exhibits a lower latent heat of vaporisation during its boiling point. As a result, less energy is needed to change its phase from liquid to gas (Ismail *et al.*, 2012). Reduced surface tension in biodiesel compared to diesel accelerates droplet breakup, leading to the production of smaller droplets and consequently, increased evaporation (Ismail *et al.*, 2012).

Factors such as in-cylinder peak pressures and the average in-cylinder temperature during the delay phase are generally lower for biodiesel than diesel, excluding fuel composition considerations (Labecki *et al.*, 2012; Labecki and Ganippa, 2012; Rodríguez, Sierens and Verhelst, 2011).

Insights into the combustion behaviour of saturated and unsaturated biodiesels reveal that biodiesels with higher saturated constituents are primarily influenced by spray and breakup processes. In contrast, increased unsaturation levels result in more prominent effects of chemical delay and low-temperature reactions on combustion and ignition delay (Elhalwagy and Zhang, 2019).

In understanding biodiesel combustion, certain compounds are frequently used as representative models for their respective categories. For saturated components, characterized by single bonds, compounds like methyl stearate (MSTEA)

$C_{19}H_{38}O_2$ and methyl palmitate (MPA) $C_{17}H_{34}O_2$ are commonly employed (An *et al.*, 2013; Brakora and Reitz, 2013; Brakora, 2012; Elhalwagy and Zhang, 2019; Ismail *et al.*, 2012; Kuti *et al.*, 2013a; Kuti, Sarathy and Nishida, 2020; Mohan *et al.*, 2015; Tootoonchi and Micklow, 2016).

Similarly, for unsaturated components, methyl oleate (MEOLE) $C_{19}H_{36}O_2$ with one double bond, methyl linoleate (MLINO) $C_{19}H_{34}O_2$ with two double bonds, and methyl linolenate (MLIN1) $C_{19}H_{32}O_2$ with three double bonds are standard references (An *et al.*, 2013; Brakora and Reitz, 2013; Brakora, 2012; Elhalwagy and Zhang, 2019; Ismail *et al.*, 2012; Kuti *et al.*, 2013a; Kuti, Sarathy and Nishida, 2020; Mohan *et al.*, 2015; Tootoonchi and Micklow, 2016). A positive correlation was observed between biodiesel unsaturation and liquid density, while a negative correlation was noted with vapour pressure and viscosity (Elhalwagy and Zhang, 2019).

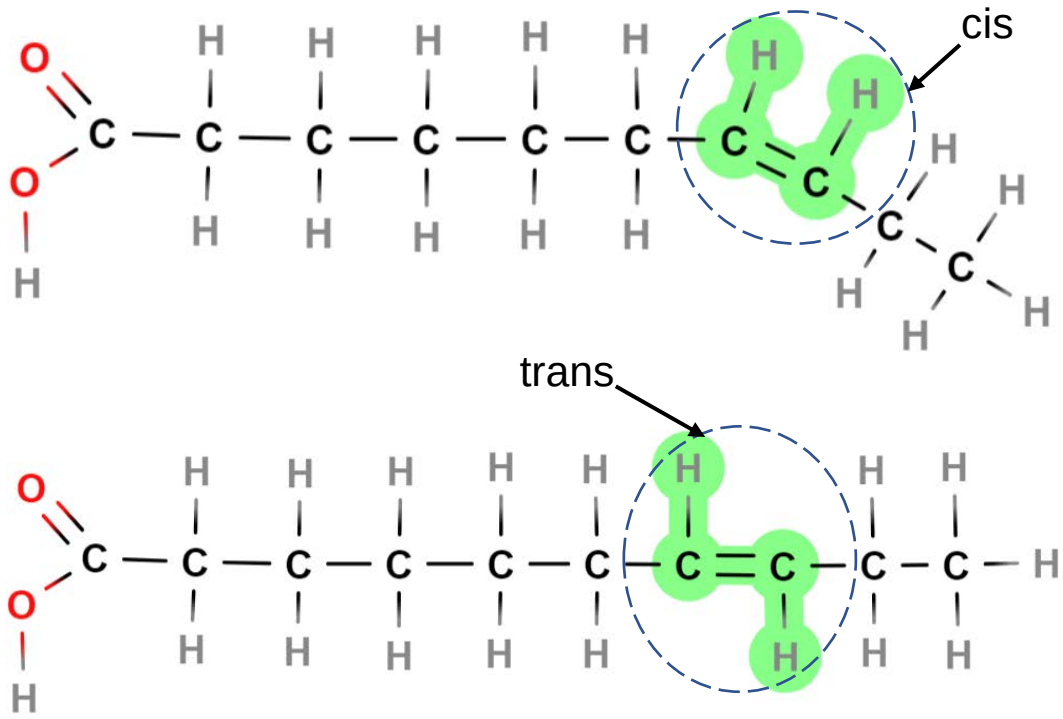

Figure 7 - Comparison of cis and trans configurations in fatty acids. The cis configuration showcases a distinct bend due to hydrogen atoms being on the same side of the double bond.

Unsaturated fatty acid methyl esters (FAME) are characterized by smaller molecular weights and a higher oxygen content, making them more volatile than their saturated counterparts. This results in faster evaporation and, subsequently, more rapid combustion (Ibadurrohman, Hamidi and Yuliati, 2022). The term "cis" refers to a specific spatial arrangement of atoms or functional groups in a

molecule. In unsaturated fatty acids or fatty acid methyl esters (FAMEs), the cis configuration describes the arrangement where hydrogen atoms attached to the carbon-carbon double bonds are on the same side (Singh *et al.*, 2019). This is in contrast to the "trans" configuration, where hydrogen atoms are on opposite sides of the double bond as shown in Figure 7 (Gopinath *et al.*, 2015).

The spatial arrangement in the cis configuration results in a bend in the molecular structure, which impacts its physical and chemical properties (Ibadurrohman, Hamidi and Yuliati, 2022).

The significance of the cis configuration in unsaturated FAME is multifaceted. The curved molecular shape arising from the cis configuration disrupts the ability of molecules to pack closely together, leading to a decrease in the melting point, hence making oils more liquid at room temperature compared to their trans or saturated counterparts (Gopinath *et al.*, 2015). From a combustion standpoint, this configuration has implications on the reactivity of the molecule (Ibadurrohman, Hamidi and Yuliati, 2022).

The cis configuration introduces an allyl group within the molecular structure of FAME. An allyl group is a structural unit that comprises a carbon atom bonded to another carbon atom with a double bond, accompanied by a single bond to another carbon atom (Singh *et al.*, 2019). This structural feature makes molecules more chemically reactive (Ibadurrohman, Hamidi and Yuliati, 2022). Specifically, the allyl group enables the rapid abstraction of a hydrogen atom from the carbon atom adjacent to the double-bonded carbon (Singh *et al.*, 2019). As a result, the energy barrier for certain chemical reactions, such as those involved in combustion, is lowered (Gopinath *et al.*, 2015). This means that unsaturated FAME with a cis configuration requires less activation energy to undergo combustion, which subsequently affects the ignition temperature (Ibadurrohman, Hamidi and Yuliati, 2022). In essence, the cis configuration ensures that unsaturated FAME burns more readily, which can be beneficial in certain combustion applications like in diesel engines (Gopinath *et al.*, 2015; Singh *et al.*, 2019).

Lastly, poor atomisation causes WCO biodiesel to have extended ignition delays, producing fewer emissions such as CO, unburned hydrocarbons, and particulate matter than diesel (Zhong *et al.*, 2018).

2.5 Spray Formation

The density effect on penetration length is paramount when considering spray formation. As literature indicates, as density diminishes, droplets travel less due to reduced momentum across the combustion chamber, producing a shorter spray penetration length. This leads to diminished air utilisation, which can potentially limit combustion efficiency (Ismail *et al.*, 2012). The way droplets form and penetrate has direct implications on combustion efficiency.

Understanding the vaporisation and evaporation characteristics of biodiesel is essential for grasping its spray behaviour. Biodiesel components predominantly exhibit a lower vapour pressure at temperatures below 550 ℃. This is mainly because of the reduced presence of volatile compounds. Vapour pressure, in turn, balances between droplet sizes, heat transfer, and distribution, making it a key player in the spray and evaporation process. At lower temperature ranges, the initial breakup of the flow inside the injector takes precedence. This is closely followed by the coalescence and collision of fuel droplets, factors that influence the physical delay before ignition (Elhalwagy and Zhang, 2019).

Notably, in the combustion chamber, unsaturated biodiesel components tend to complete spray vaporisation in the core. However, ignition mainly occurs near the wall where temperatures are typically higher. This divergence in behaviour between unsaturated and saturated biodiesel components can be linked to 'low temperature combustion chemistry effects' (Elhalwagy and Zhang, 2019).

An observed phenomenon that impacts both combustion and spray formation is the occurrence of a first stage, or cold flame, ignition prior to the primary ignition. This is characterized by the formation of formaldehyde (CH_2O) species during the low-temperature heat release. Interestingly, this cool flame plays a role in stabilizing the downstream lifted flame of both fuels. When considering WCO against diesel, the former has a shorter lift-off length. This is due to its cool flame being closer to the injector, highlighting the significant role the initial spray formation plays in subsequent combustion stages (Kuti, Sarathy and Nishida, 2020).

In computational simulations related to spray characteristics, the liquid length is defined by the axial position covering 95% of the fuel's mass at a specific post-injection time (Senecal *et al.*, 2003).

Observations indicate that as injection pressure rises, the liquid phase length reduces while the vapour phase length increases. Particularly, WCO and its surrogate demonstrate extended liquid phase lengths compared to diesel across various injection pressures (Kuti, Sarathy and Nishida, 2020). This behaviour may be attributed to WCO's imperfect atomisation, which in turn slows its evaporation rate due to less air mixing in the spray. Factors like WCO's high boiling point and reduced volatility could also be contributing factors to its prolonged liquid phase length, tying back to the importance of understanding spray formation (Kuti, Sarathy and Nishida, 2020).

Biodiesel's inherent structure introduces oxygen into its spray molecules during combustion, possibly enhancing soot oxidation (McCormick *et al.*, 2001).

Such molecular interactions in the spray phase directly influence combustion behaviours. For instance, CH_2O species, which are indicative of flames at lower temperatures, emerge predominantly in the early fuel-rich premixed reaction zone (Alfazazi *et al.*, 2016).

The hydroxyl radical (OH) serves as a reliable indicator of high temperatures and heat release (Kathrotia, 2011).

In non-premixed flames, the primary exothermic reaction producing OH is given by:

$$CH + O_2 \rightarrow CO + OH \qquad (2.1)$$

The appearance of CH_2O before OH species indicates an early start to the ignition phase, characterized by a low-temperature heat release and a cool flame (Vasudevan *et al.*, 2007). The timing of their emergence, as well as these species themselves, are influenced by the quality of the initial spray formation. As oxidation progresses, the quantity and size of CH_2O species reach a maximum. After this peak, oxidation processes that produce OH species cause the CH_2O concentration to decline. The emergence of OH species signifies auto-ignition accompanied by high-temperature heat release (Kuti, Sarathy and Nishida, 2020). Reduced peak values of CH_2O and OH can be attributed to WCO's weaker atomisation properties, resulting in reduced air entrainment (Kuti, Sarathy and Nishida, 2020).

Spray formation is a foundational aspect of combustion processes, dictating various subsequent behaviours and outcomes. One such outcome is the behaviours of OH in the combustion environment. The OH species, upon formation, promptly return to their ground state, governed by chemiluminescence and collisional quenching mechanisms (Kuti, Sarathy and Nishida, 2020). This dynamic behaviour sheds light on the spatial characteristics of flames and underscores the intricate interactions between the sprays that feed them. Particularly in combustion environments, the way WCO and diesel sprays form and behave can lead to stark differences. WCO flames, for instance, often propagate more towards the injector area, unlike diesel flames. This distinction arises from WCO's propensity to draw a greater volume of hot air upstream during its fuel injection phase (Kuti, Sarathy and Nishida, 2020). The ensuing interaction between this hot air and cooler flame regions culminates in pronounced high-temperature ignition events. Such observations elucidate the profound influence of initial spray formation, behaviour, and characteristics on the overarching combustion process (Kathrotia, 2011).

2.5.1 Leidenfrost Effect on Fuel Droplet

The Leidenfrost effect's influence on evaporation time is pivotal when considering various liquids. Spanning from one to two orders of magnitude, this variation presents a significant hurdle in the efficient conversion and utilisation of energy during hydrocarbon combustion. This challenge becomes salient in contexts such as scramjet engines or internal combustion engines. With combustors' static temperatures typically ranging between 450 and 600 K, this interval converges with the Leidenfrost region for liquid hydrocarbons (Zhao *et al.*, 2022). An insulating vapour layer, originating from the Leidenfrost phenomenon during evaporation and combustion, substantially undermines heat transfer efficiency.

The combined influence of the Leidenfrost effect and the fuel's chemical reactivity underscores the role of physicochemical characteristics in total ignition. Both elements serve as determinants that can diminish droplet heat transfer efficiency (Zhao *et al.*, 2022).

Delving deeper, when a droplet descends onto a heated surface from a fixed elevation, the surface's heat navigates through the vapour barrier before infiltrating the liquid droplet. This interaction, termed "droplet impingement," has a critical

relationship with heat conductivity, impacting evaporation rate. Thus, the omnipresence of the Leidenfrost effect in combustion becomes evident, influencing both evaporation and ignition sequences.

A specific challenge arises from spray penetration. When it becomes too pronounced, the spray might contact the piston bowl, leading to spray wall impingement. This scenario is accentuated with palm acid oil biodiesel, which shows greater susceptibility compared to conventional diesel (Tripathi and Subramanian, 2018). The dynamics at play involve a high-pressure fuel spray meeting the wall of the piston bowl, while concurrently, air pursues an inward radial motion into the bowl to ensure optimal mixing. Sub-optimal spray penetration can compromise this mixing efficiency. However, when penetration is too extensive, wall impingement becomes a tangible risk. Evidence suggests that palm acid oil biodiesel's spray penetration surpasses that of diesel (Tripathi and Subramanian, 2018). Factors like increased speed can amplify penetration distance, escalating impingement risks, a phenomenon further documented with other biodiesels, such as Karanja (Lahane and Subramanian, 2014).

The intricacies of the oxidation process dictate the trajectory of combustion. Initial stages are marked by a gentle oxidation, where the emergent heat mainly boosts the temperature of combustibles and augments the ratio of activated molecules (Zhao *et al.*, 2022).

In their meticulous research, Islamova *et al.* (2023) discerned that fuel oil droplets attain peak atomisation at wall temperatures around 300 °C. Deviations from this temperature could curtail the emergence of secondary droplet fragments. Specifically, when temperatures eclipse 300 °C, the ensuing rapid evaporation rates of fuel oil pre-empt droplet fragmentation. This culminates in a rapid vapour release that, upon mingling with an oxidizer, catalyses ignition, birthing a stream of flue gases. This behaviour mirrors the Leidenfrost effect's intricacies. A droplet, upon making contact with a superheated surface, produces a vapour barrier. This vaporised shield repels the droplet, preventing adherence to the surface and underscoring the profound ramifications of the Leidenfrost effect on droplet-surface interplay and heat exchange (Islamova *et al.*, 2023).

In encapsulation, shorter evaporation times are indicative of enhanced heat transfer between the droplet and the heated surface. When the Leidenfrost effect

is in action, a vapour cushion emerges, isolating the droplet from the heated surface, and consequently stymieing boiling and direct heat conveyance.

2.6 Emission Formation

Biodiesel fuel usage in diesel engines has evolved, leading to discernible combustion and emission characteristics different from traditional diesel. This is primarily because while diesel mainly contains hydrocarbons, biodiesel is rich in alkyl esters. An overall reduction in exhaust emissions, especially Particulate Matter (PM), has been observed with biodiesel compared to diesel. Reduction levels varied between 75% and 83% across different feedstocks (Demirbas, 2009b).

Soybean Methyl Ester (SME) biodiesel in diesel engine conditions produced about half the total soot mass as diesel (Liu *et al.*, 2014). The reduced soot formation of biodiesel, when compared to similar length n-alkanes, is attributed to the presence of methyl functional groups containing extra oxygen atoms (Feng *et al.*, 2012). However, as the unsaturation level of biodiesel increases, its soot formation does too. This increase is likely due to the presence of double bonds in FAME elements, which promote the formation of unsaturated species (Gaïl *et al.*, 2008; Schönborn *et al.*, 2009).

Regarding NOx formation, literature suggests that pure biodiesel consumption can elevate NOx levels by up to 44.8% depending on the biodiesel's feedstock (Xue, Grift and Hansen, 2011). In contrast, some studies report biodiesel's NOx production to be either comparable to or less than that of diesel (Lapuerta *et al.*, 2008; Fontaras *et al.*, 2010).

The discrepancies in these results might stem from biodiesel's intricate unsaturated composition and the complexities of combustion and pollutant chemistry in turbulent non-premixed flames. The behaviour of vaporised and pre-mixed fuel in the turbulent flow within the engine chamber further intensifies these discrepancies (Bergthorson and Thomson, 2015).

When examining varying compression ratios, B100 biodiesel derived from a blend of Simarouba-Jatropha oil was found to produce lower NOx, HC, and CO levels than diesel. As compression ratios increased, a rise in fuel combustion was noted (Hosamani and Katti, 2018).

The presence of SO_2 in WCO biodiesel exhaust has been linked to the sulphur content in fried food oil. Emissions of CO, NO, and SO_2 were reported to be higher for WCO biodiesel compared to diesel (Yu, Bari and Ameen, 2002). It's also been noted that saturated FAMEs produces less soot than its unsaturated counterpart (Garner, Sivaramakrishnan and Brezinsky, 2009).

High HC emissions are often a result of prolonged ignition delays, which occur when fuel accumulates in the combustion chamber. WCO biodiesel blends, due to their elevated oxygen content and higher cetane number, lead to a decrease in HC emissions. A well-atomized fuel during combustion is indicated by reduced HC emissions. Tests on a diesel engine using WCO biodiesel reported fewer hydrocarbon emissions. However, the increased viscosity of WCO biodiesel often results in heightened CO emissions due to inadequate atomisation in unmodified engines (Yaqoob *et al.*, 2021). At lower loads, CO emissions were found to be lesser than those from diesel fuel. As the load percentage increased, however, the rise in CO emissions surpassed that of diesel fuel. CO_2 emissions are influenced by the engine's compression ratio and the properties of WCO biodiesel components. As the proportion of biodiesel in diesel increases, CO_2 emissions have been observed to rise. As engine loads increase, both WCO biodiesel and diesel display a similar trend in CO_2 emissions. NOx emissions are influenced by the peak in-cylinder temperature, which is directly associated with the adiabatic flame temperature, thus determining the NOx production rate (Yaqoob *et al.*, 2021). Interestingly, WCO biodiesel elevates the cylinder temperature in comparison to diesel, leading to increased NOx emissions. This has been attributed to the higher oxygen content in biodiesel molecules (Yaqoob *et al.*, 2021). Additionally, incomplete fuel combustion in engines results in smoke emissions at the exhaust. This emission amplifies with an increase in output power, particularly for diesel, due to its branched and ring structure. In contrast, WCO biodiesel tends to reduce smoke emission levels because of its high oxygen content (Yaqoob *et al.*, 2021).

2.7 Chemistry Mechanism

Various surrogate fuel representatives have been used to establish biodiesel chemistry mechanisms in the literature. One such approach involved a two-component biodiesel mechanism utilising Methyl Butanoate and n-Heptane as surrogate fuels to model soybean biodiesel with a fuel ratio of 1/3 to 2/3 (Brakora *et al.*, 2009).

Another distinct mechanism employed a triple component surrogate system, which consisted of 115 species and 460 reactions. This system used Methyl Decanoate (MD), Methyl-9-Decenoate (MD9D), and n-Heptane to elucidate the biodiesel combustion process (Luo *et al.*, 2012).

Similarly, a tri-component biodiesel reaction mechanism, coupled with a hydrogen oxidation sub-mechanism, was proposed. This incorporated 107 species and 443 reactions using components like MD, MD9D, and n-Heptane (An *et al.*, 2014).

Recent research introduced a biodiesel surrogate mechanism that combined MD, Methyl-5-Decenoate (MD5D), and n-Decane. This mechanism was notably concise, featuring only 60 species and 172 reactions (Chang *et al.*, 2015).

A tri-component biodiesel mechanism was developed, consisting of MD, MD9D, and n-Heptane. Employing a decoupling methodology, a skeletal sub-mechanism of these tri-components was incorporated. Additionally, this mechanism integrated iso-Octane, a reduced C_2-C_3 mechanism, detailed H_2,CO,C_1 mechanisms, and a reduced NOx mechanism (Mohan *et al.*, 2015). The resulting mechanism encompassed 68 species and 183 reactions. When this mechanism was assessed, benchmarks such as ignition delay, laminar flame speed, and 3D CFD CI simulations were considered (Mohan *et al.*, 2015).. Furthermore, the results were specifically applied to understand the laminar flame speed for pure components like Palm Methyl Ester (PME) biodiesel. It was observed that the skeletal mechanism aligned well with 3D CFD simulation results, demonstrating a notable agreement in in-cylinder pressure and heat release rates when juxtaposed with experimental data for both diesel and biodiesel (Mohan *et al.*, 2015).

2.7.1 ERC-MultiChem plus Bio mechanism

A chemistry mechanism integrating realistic physical properties was developed, which served both in the vaporisation model for multi-component fuel sprays and in biodiesel combustion chemistry. Additionally, a two-species biodiesel surrogate fuel representative, which originally consisted of Methyl Decanoate (MD) and Methyl-9-Decenoate (MD9D) with 3299 species created by the Lawrence Livermore National Laboratory, was reduced to 85 species. This reduction process adopted a combination of isomer lumping, limited reaction rate adjustments, and the Directed Relation Graph method. A further reduction introduced n-Heptane (nC_7H_{16}) as a novel strategy to enhance the low-temperature combustion behaviour of the mechanism (Brakora, 2012).

This resulted in a concise triple-component biodiesel fuel reaction mechanism, comprising MD, MD9D, and n-Heptane, encompassing 69 species and 204 reactions (Brakora and Reitz, 2013).

The presented results indicated that the developed mechanism accurately predicted the MD/MD9D components' ignition delay across diverse CI engine operating conditions. To conclude, the final mechanism of 69 species and 204 reactions was integrated with the thermo-physical properties of the five primary methyl ester components of biodiesel. This integration aimed to validate the mechanism under real diesel engine operating conditions, both in conventional and low-temperature combustion (LTC). Notably, the model exhibited a significant capability in capturing both ignition and emission results in line with experimental data (Brakora, 2012).

2.7.2 CRECK Modeling Group (Politecnico di Milano)

The proposed chemistry mechanism from Politecnico di Milano emphasizes the intricate interaction between hydrocarbons and NOx during reburning and thermal oxidation. This mechanism provides insight into the precise impact of NO across a broad temperature range and for various stoichiometry conditions and fuels (Frassoldati, Faravelli and Ranzi, 2003).

A study of an unsteady counterflow diffusion flame demonstrated that the formation of emission species, such as soot precursors and NOx, is significantly influenced by turbulence-chemistry interactions (Cuoci *et al.*, 2009).

Rate constants were determined using analogy and similarity rules for established reactions, while theoretical calculations were employed for preliminary estimates of reaction channels that lacked a reference reaction. This approach facilitates the inclusion of new reaction classes to describe the production of oxygenated species, notably organic acids and dicarbonyl species (Ranzi *et al.*, 2015).

The lumped approach, a foundational expansion of the kinetic scheme of methyl butanoate and methyl decanoate proposed by Westbrook et al. (2011), was applied to the chemistry mechanism of the pyrolysis and oxidation of biodiesel fuels (Westbrook *et al.*, 2011; Saggese *et al.*, 2013). his methodology introduced 60 lumped species and 2000 reactions, aiming to offer a straightforward application and a more adaptable model without the need for kinetic reductions (Saggese *et al.*, 2013). Ultimately, a comprehensive mechanism was proposed, consisting of 482 species and 19,072 reactions. This mechanism encompasses the pyrolysis, partial oxidation, and combustion of hydrocarbon and oxygenated fuels, integrating turbulence/chemistry interactions of NOx, and both high and low-temperature kinetics (Cuoci *et al.*, 2009; Frassoldati, Faravelli and Ranzi, 2003; Ranzi *et al.*, 2015; Saggese *et al.*, 2013).

Chapter 3 - Theory Background

3.1 Introduction

The complexity of simulating the internal dynamics of a diesel engine is underpinned by a multitude of physical and chemical phenomena. Given the multifaceted nature of such simulations, it's imperative to have a comprehensive understanding of the foundational theories and models that govern them. This chapter delves into the intricate theoretical underpinnings and methodologies harnessed in the 3D Computational Fluid Dynamics (CFD) simulation of a diesel engine.

Firstly, the details of sector-based internal combustion engine simulations will be explored. These simulations, typically utilised for their efficiency and accuracy, require a thorough understanding of how engines function in a cyclic manner. Key to these simulations is the pressure-based model, a cornerstone for modelling the rapid pressure variations inherent in engine combustion processes.

Mesh generation, an essential precursor to any CFD analysis, will be discussed with an emphasis on dynamic mesh techniques. Dynamic meshing, crucial for capturing the moving boundaries within an engine, presents challenges. Ways to mitigate issues like skewness and ensure the accuracy and reliability of the simulation will be highlighted.

The suite of conservation equations is fundamental to CFD simulations. These equations, encompassing mass, momentum, and energy conservation, form the backbone of the simulation and offer a window into the fluid dynamics and thermodynamics at play within the engine.

Turbulence, with its chaotic and unpredictable nature, poses its own set of challenges. This exploration will delve into the turbulent viscous $k-\varepsilon$ model, elucidating its relevance and application in capturing the turbulent flows characteristic of engine environments.

Furthermore, the energy equation, essential in quantifying the thermal dynamics, will be addressed in conjunction with the Probability Density Function (PDF) model. The PDF model, offering a statistical approach to turbulent reactive flows, provides an essential tool in predicting species concentration and temperature in turbulent flames.

Combustion, the heart of any engine operation, will be dissected through the lens of the non-premixed diesel unsteady laminar flamelet model. This model, known for its capability in capturing the layered combustion sequences in diesel engines, will be elaborated upon, helping readers grasp its significance and application.

Lastly, the spray model, crucial in understanding fuel injection and atomisation processes, will be outlined. A pivotal component of this is the Discrete Phase Model (DPM), which simulates the trajectory and behaviour of discrete particles or droplets in a continuous phase. DPM effectively takes into account various forces like drag and thermophoresis, offering an in-depth perspective into fuel spray dynamics. Integral to this understanding is the evaporation theory, which delves into the phase transition of fuel droplets to vapour. This transformation, governed by heat and mass transfer between the droplet and its surrounding gaseous environment, is fundamental to determining the initial conditions for the ensuing combustion process, thereby playing a crucial role in setting the stage for subsequent chemical reactions.

This chapter integrates various theories and models essential for 3D CFD diesel engine simulations. The foundation laid here sets the stage for detailed analysis in subsequent sections.

3.2 Computational Fluid Dynamics

Internal Combustion (IC) engines have been central to the evolution of automobiles and industrial machines. With the constant push for efficiency, reduced emissions, and performance improvements, the simulation of IC engines has become essential. ANSYS Fluent, as a leading computational fluid dynamics (CFD) tool, provides robust solutions for modelling IC engine processes. One of the unique simulation approaches ANSYS Fluent offers is the "sector simulation''.

3.2.1 Sector IC Engine Simulation

In the real world, the combustion chamber of an IC engine exhibits radial symmetry, especially in engines with a centrally located injector or spark plug. The idea behind sector simulations is to utilise this symmetry and simulate only a sector (or a fraction) of the entire combustion chamber.

Using sector simulations in IC engine modelling offers several advantages. Simulating the entire geometry of an engine demands extensive computational

resources and time due to its complexity. In contrast, a sector model significantly reduces the number of computational cells, streamlining the simulation process to be faster and more efficient. Additionally, sector simulations allow engineers to concentrate on specific areas of interest, such as regions around the injector. This concentration enables a higher mesh resolution, which is crucial for investigating detailed phenomena like fuel spray atomisation or ignition processes.

3.2.2 Pressure Base Model

The pressure-based solver, as employed by ANSYS Fluent, addresses the fundamental challenges in Computational Fluid Dynamics (CFD) by effectively dealing with the Navier-Stokes equations. The crux of this solver hinges upon the projection method, where a pressure correction equation plays a pivotal role in ensuring the mass continuity of the velocity field.

Mathematically, the momentum equation is given by:

$$\frac{\partial(\rho u)}{\partial t} + \nabla . (\rho \mathrm{u} \otimes \mathrm{u}) = -\nabla \mathrm{p} + \nabla . (\mu \nabla \mathrm{u}) + \mathbf{F} \quad , \quad \mathrm{u} = (\mathrm{u}, \upsilon, \mathrm{w}) \tag{3.1}$$

Where ρ is the fluid density, u is the velocity vector in a three-dimensional space , t represents time, p is the pressure field, μ denotes the fluid's dynamic viscosity, and **F** signifies the body forces. For u , each component represents the velocity in the respective x, y, and z directions.

The continuity equation, which encapsulates the conservation of mass, is expressed as:

$$\nabla . u = 0 \tag{3.2}$$

From these, the pressure equation can be derived, emphasizing the interconnected relationship between velocity and pressure. The purpose of this derived equation is to iteratively adjust the velocity field, ensuring it satisfies mass continuity.

The non-linearity and coupling of these equations necessitate iterative solutions. In this iterative framework, the entire set of governing equations is repeatedly solved until the solution converges. This means that the velocity and pressure fields are iteratively adjusted, ensuring they satisfy both momentum balance and mass conservation.

The pressure-based solver's efficacy is attributed to its ability to decouple the pressure and velocity fields, making it computationally efficient. This is crucial in scenarios with complex geometries or intricate flow patterns where computational resources could be extensively taxed.

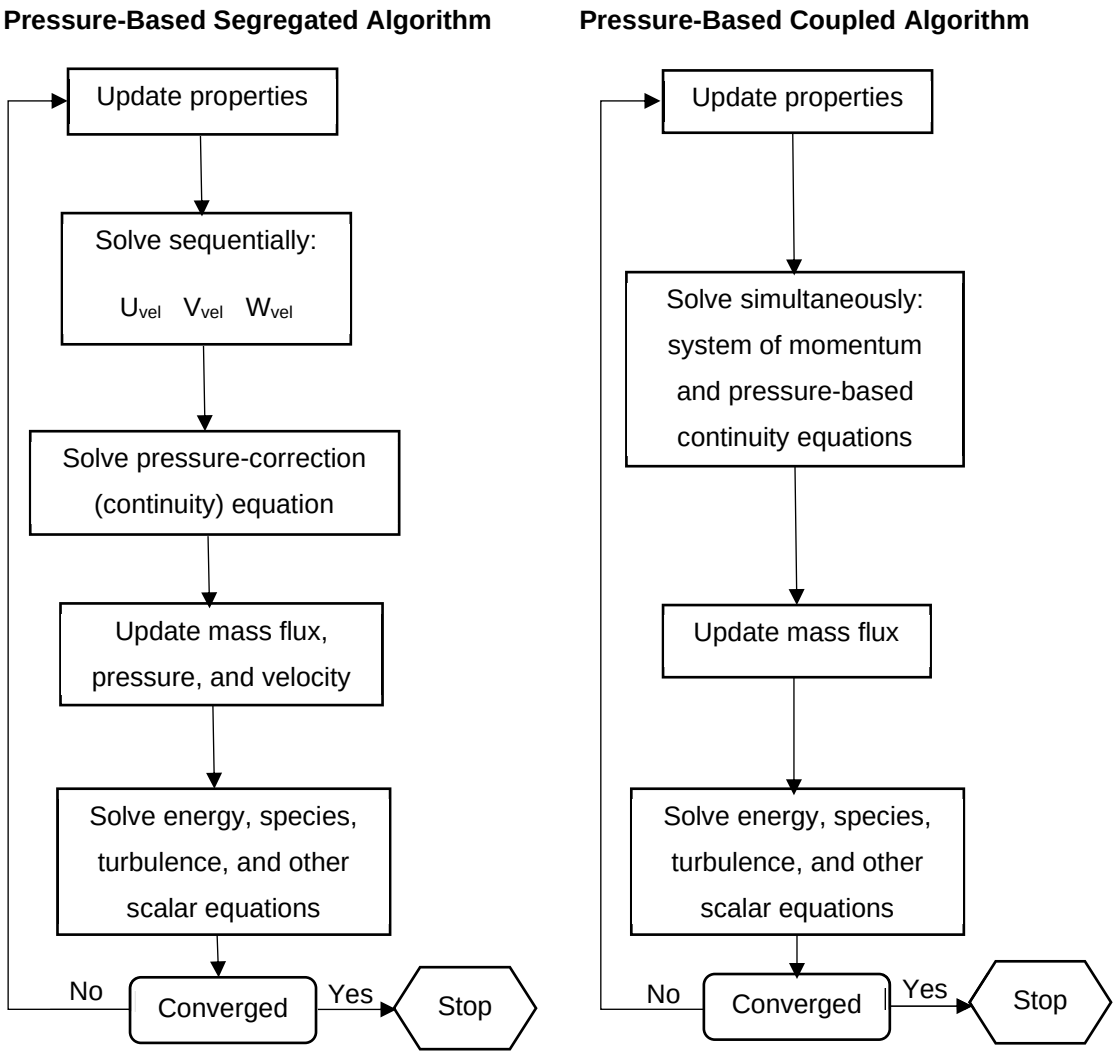

Figure 8 - Pressure based solver implementation in ANSYS Fluent as flow chart.

Figure 8 clearly differentiates the two pressure-based solver approach. Coupled pressure-based solver requires a simultaneous combination of momentum and pressure continuity equation. Afterwards, to be able to solve turbulence, energy, species, and related equations an update for the mass flux is needed. Hence, the major sign to express the solution convergence is the equation of continuity response to the flow field.

Five major coupling methods are presented as below.

- Phase Coupled Simple
- PISO
- Simple
- SIMPLEC
- Coupled

The significant difference of these methods above are linked to transient and steady state condition. SIMPLE, SIMPLEC, and PISO are mainly used is steady state environment. However, PISO (Pressure-Implicit with Splitting of Operators) can solve transient condition which provides users to use quasi-state method approach. In ANSYS Fluent, for flow calculations that require transient computations and larger time steps, the use of the PISO algorithm is recommended (ANSYS, 2020c). One distinct advantage of the PISO solver algorithm is its ability to manage skewness through neighbour coupling and a correction model. Owing to its pressure-correction equation, the algorithm efficiently addresses any discrepancies between the new velocities and the associated fluxes in maintaining the momentum balance.

3.2.2.1 Skewness Correction

The skewness correction in ANSYS Fluent, as with many computational fluid dynamics (CFD) tools, is vital for ensuring the accuracy of simulations, especially when the mesh isn't uniform or isn't aligned with the flow direction. As part of its solver algorithms, Fluent detects high skewness and applies a correction factor to the face fluxes. This action counters the errors from skewed faces, stabilizing the solution. In essence, when navigating non-uniform meshes or intricate geometries, skewness correction is essential for reliable simulation outcomes.

3.2.2.2 Skewness-Neighbour Coupling

Skewness-neighbour coupling is a term often discussed in the context of computational fluid dynamics (CFD) and grid quality. High grid skewness can affect the accuracy of the flow solution. This term refers to the correction methodology implemented in certain solver algorithms (like PISO) to mitigate the inaccuracies introduced by high skewness. In skewed cells, the face centre (where the flux is computed) may not lie along the line connecting the two adjacent cell centres (ANSYS, 2020c). This misalignment can introduce inaccuracies in the

interpolation of variables, leading to errors in the computed face fluxes. The skewness-neighbour correction compensates for this by introducing an adjustment or correction factor in the face flux computation (ANSYS, 2020c).

3.2.3 Dynamic Mesh

The dynamic mesh capability in ANSYS Fluent allows for the simulation of problems where the mesh changes over time, adapting to the motion of boundaries, or other influencing factors (ANSYS, 2020d). Essentially, it offers the flexibility to modify the boundaries of a cell zone in relation to other zone limits and subsequently updates the mesh to accommodate these changes. As per ANSYS Fluent guidelines on mesh configuration, the motion should be defined based on face or cell zones (ANSYS, 2020d). It's imperative to partition the regions undergoing deformation into distinct zones right from the start within the initial volume mesh. This ensures accurate and efficient computational analysis as the mesh evolves with time.

3.2.4 Conservation Equations

For a generic scaler φ (e.g., temperature, concentration, etc.) with arbitrary control volume V, the following integral form of the conservation equation can be incorporated:

$$\frac{d}{dt}\int_V \rho\varphi dV + \int_{\partial V} \mathrm{p}\varphi(\vec{u} - \overrightarrow{u_g}).\overrightarrow{dA} = \int_{\partial V} \Gamma\nabla\varphi.\overrightarrow{dA} + \int_V S_\varphi dV \tag{3.3}$$

S_φ is the source term of φ . The vector $\vec{u}$ represents the flow velocity, while $\overrightarrow{u_g}$ denotes the velocity of mesh motion. The symbol $\overrightarrow{dA}$ signifies a differential area vector, and $\nabla\varphi$ is the gradient of the scalar φ. The terms ρ and p stand for the fluid density and static pressure, respectively, and Γ represents the diffusion coefficient.

The period derivative may be represented as below by utilising first-order backward differentiation formula.

$$\frac{d}{dt}\int_V \rho\varphi dV = \frac{(\rho\varphi V)^{n+1} - (\rho\varphi V)^n}{\Delta t} \tag{3.4}$$

The values at the present and subsequent time levels are defined by the variables n and $n+1$, respectively. The time step size is represented as Δt and V^{n+1} is described below as:

$$V^{n+1} = V^n + \frac{dV}{dt}\Delta t \tag{3.5}$$

The volume-time gradient of the control volume is calculated as follows:

$$\frac{dV}{dt} = \int_{\partial V} \vec{u}_g . \overrightarrow{dA} = \sum_{j}^{n_f} \vec{u}_{g.j} . \overrightarrow{A_j} \tag{3.6}$$

$\overrightarrow{A_j}$ is the area vector of face j and n_f is equal to number of faces within volume control. The product of the following variables is as below:

$$\overrightarrow{u_{g.j}} . \overrightarrow{A_j} = \frac{\delta V_j}{\Delta t} \tag{3.7}$$

The swept volume of the volume control face j is δV_j, which Δt illustrates δV_j time step. The time derivative is calculated by performing a second order backward for volume differences.

$$\frac{d}{dt}\int_V \rho\varphi dV = \frac{3(\rho\varphi V)^{n+1} - 4(\rho\varphi V)^n + (\rho\varphi V)^{n-1}}{2\Delta t} \tag{3.8}$$

Finally, the product of $\vec{u}_{g.j} . \vec{A}_j$ is presented below is followed by a second-order upwind scheme.

$$(\vec{u}_{g.j} . \vec{A}_j)^{n+1} = \frac{3}{2}(\vec{u}_{g.j} . \vec{A}_j)^n - \frac{1}{2}\left(\vec{u}_{g.j} . \vec{A}_j\right)^{n-1} = \frac{3}{2}\left(\frac{\delta V_j}{\delta t}\right)^n - \frac{1}{2}\left(\frac{\delta V_j}{\delta t}\right)^{n-1} \tag{3.9}$$

The terms $\left(\delta V_j\right)^n$ and $\left(\delta V_j\right)^{n-1}$ represent the volumes swept out of the control volume during the time intervals n and n−1, respectively.

3.2.5 Turbulent Model

Computational fluid dynamics (CFD) offers an advanced methodology for examining systems that involve fluid movement, heat transition, and related phenomena such as chemical reactions. Its applicability spans diverse sectors, ranging from industrial use cases like examining combustion in gas turbines and internal combustion engines to predicting weather patterns . One of its significant merits is its ability to showcase intricate fluid flow details that might elude experimental observation (Versteeg and Malalasekera, 2007).

Turbulence is commonly observed in most combustion processes, stemming from inherent disruptions that cause a shift from laminar flows to turbulent ones. Over the years, the scientific community has put significant effort into refining turbulent modelling strategies, aiming to better understand and optimize these systems. Presently, there are three primary turbulence modelling techniques: Direct Numerical Simulations (DNS), Large Eddy Simulation (LES), and Reynolds Averaged Navier–Stokes (RANS). Each varies in terms of precision, computational requirements, and associated costs (Rutland, 2011).

In essence, equations serve as representations of physical processes, implying that flows can be scrutinised either analytically or computationally. Viewing flow as a volumetric occurrence, it's possible to break down the volume into minute grids. These grids, by virtue of their size, can capture even the most minuscule physical actions. Given that the Navier–Stokes equations characterize Newtonian fluids, it stands to reason that solving these equations numerically using CFD will provide a detailed depiction of such fluids. To attain this, it's essential to discretize the flow area with fine grids and adopt short time intervals, ensuring the Kolmogorov scale is addressed (Abraham, Bracco and Reitz, 1985; Banerjee *et al.*, 2010; Rutland, 2011; Versteeg and Malalasekera, 2007). DNS stands out in this context since it eschews modelling, focusing instead on detailing turbulent scales in their entirety.

When assessing eddies based on size, distinct behaviours emerge. Large eddies, endowed with more energy compared to their smaller counterparts, exhibit anisotropic tendencies, influenced by the specific geometry and boundary conditions of the system (Rutland, 2011; Versteeg and Malalasekera, 2007). In contrast, smaller eddies tend to be approximately isotropic, displaying consistent

behaviour. Such variations paved the way for the LES method, which zeroes in on computing large eddies while modelling the smaller ones.

The study in question leveraged the RANS turbulence modelling approach, spotlighted in the succeeding sub-section. Chosen for its computational efficiency and respectable accuracy relative to DNS and LES, RANS has found considerable application in simulating internal combustion engines, delivering commendable precision.

3.2.5.1 Reynolds averaged Navier–Stokes

Reynolds averaging breaks down the variables present in the instantaneous Navier-Stokes equations into two parts: the average (either ensemble-averaged or time-averaged) and the fluctuating parts.

For velocity components, the following applies:

$$u_i = \bar{u}_i + \acute{u}_\iota \qquad i \in \{1,2,3\} \tag{3.10}$$

In which $\bar{u}_i$ and $\acute{u}_\iota$ signify the averaged and fluctuating parts of the velocity, respectively.

Similarly, for pressure and other scalar measures:

$$\varphi = \bar{\varphi} + \acute{\varphi} \tag{3.11}$$

Here, φ the symbol represents a generic scalar quantity, which could be pressure, energy, or species concentration.

By integrating Equation 3.1 and Equation 3.2 into the conservation Equation 3.3, and subsequently replacing the flow variables with the expressions from Equations 3.10 and 3.11, followed by time (or ensemble) averaging, the ensemble-averaged momentum equations are obtained. These are represented in Cartesian tensor notation as:

$$\frac{\partial \rho}{\partial t} + \frac{\partial}{\partial x_i}(\rho u_i) = 0 \tag{3.12}$$

$$\frac{\partial}{\partial t}(\rho u_i) + \frac{\partial}{\partial x_j}(\rho u_i u_j) = -\frac{\partial \mathrm{p}}{\partial x_i} + \frac{\partial}{\partial x_j}\left[\mu\left(\frac{\partial u_i}{\partial x_j} + \frac{\partial u_j}{\partial x_i} - \frac{2}{3}\,\delta_{ij}\frac{\partial u_l}{\partial x_l}\right)\right] + \frac{\partial}{\partial x_j}\left(-\rho\overline{\acute{u}_\iota \acute{u}_j}\right) \tag{3.13}$$

Where δ_{ij} is the Kronecker delta function, x_i and x_j are the spatial coordinates for *i*-th and *j*-th directions, respectively. Dynamic viscosity is represented as μ in Equation 3.13 .

Equations 3.12 and 3.13 are commonly known as the Reynolds-averaged Navier-Stokes (RANS) equations.

In the context of the momentum equation, several terms have distinct physical interpretations. The term $\frac{\partial}{\partial t}(\rho u_i)$ embodies the rate of change of momentum in the *i*-th direction concerning time, acting as the unsteady term capturing temporal momentum fluctuations. The convective effects, which denote the transport of momentum in the *i*-th direction due to the fluid's velocity in the *j*-th direction, are represented by $\frac{\partial}{\partial x_j}(\rho u_i u_j)$. The influence of the pressure gradient on the fluid, either accelerating or decelerating its particles, is encapsulated by $-{}^{\partial \mathrm{p}}/_{\partial x_i}$. The viscous diffusion term is given by $\frac{\partial}{\partial x_j}\left[\mu\left(\frac{\partial u_i}{\partial x_j}+\frac{\partial u_j}{\partial x_i}-\frac{2}{3}\,\delta_{ij}\frac{\partial u_l}{\partial x_l}\right)\right]$, representing momentum diffusion due to the fluid's inherent viscosity. Lastly, the term $\frac{\partial}{\partial x_j}\left(-\rho\overline{\acute{u}_i\acute{u}_j}\right)$ captures the effects of turbulence on momentum transport, known as the Reynolds stress, and is often modelled since capturing all its nuances directly in most practical scenarios is challenging.

These turbulence-induced stresses, $-\rho\overline{\acute{u}_i\acute{u}_j}$, often referred to as Reynolds stresses, need to be formulated to adequately solve Equation 3.13. A prevalent technique uses the Boussinesq hypothesis to associate the Reynolds stresses with the average velocity gradients.

$$-\rho\overline{\acute{u}_i\acute{u}_j} = \mu_t\left(\frac{\partial u_i}{\partial x_j}+\frac{\partial u_j}{\partial x_i}\right)-\frac{2}{3}\left(\rho k+\mu_t\frac{\partial u_k}{\partial x_k}\right)\delta_{ij} \tag{3.14}$$

The $k-\varepsilon$ model utilises the Boussinesq hypothesis. One of the primary advantages of this approach is the minimized computational load required to compute the turbulent dynamic viscosity, μ_t. In the $k-\varepsilon$ model, two supplementary transport equations are introduced: one for the turbulence kinetic energy, k, and another for the turbulence dissipation rate, ε. μ_t is then determined based on k and ε.

3.2.5.2 Turbulent Viscous Model $k-\varepsilon$ Standard

The standard $k-\varepsilon$ model in ANSYS Fluent relies on two independent transport equations for its accurate functionality. These equations facilitate the determination of the turbulent length and time scales. The model's resilience and precision have been supported by various academic and industrial studies (Abraham, Bracco and Reitz, 1985; ANSYS, 2020c; Banerjee *et al.*, 2010; Rutland, 2011; Versteeg and Malalasekera, 2007). This model's foundation centres on the definition of the turbulence kinetic energy (k) and its dissipation rate (ε) as transport equations (Launder and Spalding, 1972). The transport equation for ε while derived from physical reasoning, has only a loose resemblance to its mathematically rigorous counterpart. One of the foundational assumptions behind the $k-\varepsilon$ standard model is that the flow environment is entirely turbulent. This assumption, critical for driving the model, isn't contested when dealing with unstable non-premixed combustion since the flow is deemed fully turbulent. The transport equations capture the turbulence's kinetic energy, k, and its dissipation rate, ε, as follows:

$$\frac{\partial}{\partial t}(\rho k)+\frac{\partial}{\partial x_i}(\rho k u_i)=\frac{\partial}{\partial x_j}\left[\left(\mu+\frac{\mu_t}{\sigma_k}\right)\frac{\partial k}{\partial x_j}\right]+G_k+G_b-\rho\varepsilon-Y_M+S_k \tag{3.15}$$

$$\frac{\partial}{\partial t}(\rho \varepsilon)+\frac{\partial}{\partial x_i}(\rho \varepsilon u_i)=\frac{\partial}{\partial x_j}\left[\left(\mu+\frac{\mu_t}{\sigma_\varepsilon}\right)\frac{\partial \varepsilon}{\partial x_j}\right]+C_{1\varepsilon}\frac{\varepsilon}{k}(G_k+C_{3\varepsilon}G_b)-C_{2\varepsilon}\rho\frac{\varepsilon^2}{k}+S_\varepsilon \tag{3.16}$$

In this context, G_k and G_b represent the generation of turbulence kinetic energy from mean velocity gradients and the effects of buoyancy, respectively. Y_M accounts for the contributions of fluctuating dilatation in turbulence when it's compressible, influencing the total dissipation rate. The Prandtl numbers for k and ε denoted as σ_k and σ_ε, indicate the relationship between momentum and thermal diffusivities, connecting diffusivity with the turbulent dynamic viscosity, μ_t. Including ε/k ensures dimensional accuracy in the ε transport equation, while $C_{1\varepsilon}$ and $C_{2\varepsilon}$ maintain proportionality in the ε transport equation terms. Lastly, S_k and S_ε serve as source terms.

The turbulent dynamic viscosity, μ_t, is defined as follows, within which C_μ is a constant.

$$\mu_t = \rho C_\mu \frac{k^2}{\varepsilon} \tag{3.17}$$

The remaining variables are constant and have the following values assigned to them:

$$C_{1\varepsilon} = 1.44, C_{2\varepsilon} = 1.92, C_\mu = 0.09, \sigma_k = 1.0, \sigma_\varepsilon = 1.3$$

While users can modify the default values of the model constants, the standard values remain widely accepted and used across various fields.

3.2.6 Probability Density Function Theory (PDF)

While the Navier-Stokes equations are highly accurate, their application in modelling real flows can be prohibitively expensive. In scenarios involving species transport and finite-rate chemistry, it becomes essential to use Reynolds-averaged species. This involves utilising turbulent scalar flux and the mean reaction rate. The model, denoted by **P**, provides insight into the fluid's interaction with each species, based on the fraction of time spent at specific temperature and pressure states. With this PDF approach, one can analyse any mean or Root Mean Square (RMS) temperature and any mean reaction rate from a single-point chemical perspective.

From the Navier-Stokes equation, the composing PDF transport formula is obtained as follows:

$$\frac{\partial}{\partial t}(\rho \mathbf{P}) + \frac{\partial}{\partial x_i}(\rho u_i \mathbf{P}) + \frac{\partial}{\partial \psi_k}(\rho S_k \mathbf{P}) = -\frac{\partial}{\partial x_i}[\rho \langle u_i'' | \psi \rangle \mathbf{P}] + \frac{\partial}{\partial \psi_k}\left[\rho \left\langle \frac{1}{\rho}\frac{\partial J_{i,k}}{\partial x_i} \middle| \psi \right\rangle \mathbf{P}\right] \tag{3.18}$$

The $\langle A|B \rangle$ notation indicates that if there is a particular condition probability for the occurrence of event A, then the occurrence of event B is predicted. In Equation 3.18, the initial term on the left represents the transient variation. The subsequent term depicts the alteration in the PDF resulting from convection associated with the mean velocity field. Meanwhile, the third term highlights the modifications in the PDF attributed to chemical reactions.

Table 1 exhibits definition of Equation 3.18 variables.

Table 1 - Equation 3.18 variables

Name	Variable
Favre joint PDF of composition	$\mathbf{P}$
mean fluid density	ρ
Favre mean fluid velocity	u_i
reaction rate for species k	S_k
composition space vector	ψ
fluid velocity fluctuation vector	u_i''
molecular diffusion flux	$J_{i,k}$

The turbulent tensor flux is an open term derived from the gradient-diffusion hypothesis, as follows:

$$-\frac{\partial}{\partial x_i}[\rho\langle u_i''|\psi\rangle\mathbf{P}] = \frac{\partial}{\partial x_i}\left(\frac{\rho\mu_t}{Sc_t}\frac{\partial\mathbf{P}}{\partial x_i}\right) \tag{3.19}$$

The turbulent dynamic viscosity is represented by μ_t, whereas the turbulent Schmidt number is represented by Sc_t.

3.2.7 Energy

Given the inherent complexities of simulating combustion, techniques for heat transfer become essential. By equipping ANSYS Fluent with the necessary physical models, thermal boundary conditions, and material properties, users can conduct simulations rooted in energy principles.

The solution utilises the following version for the energy equation:

$$\frac{\partial}{\partial t}(\rho E) + \nabla.\left(\vec{v}(\rho E + \rho)\right) = \nabla.\left(k_{eff}\nabla T - \sum_j h_j\overrightarrow{J_j} + \left(\bar{\bar{\tau}}_{eff}.\vec{v}\right)\right) + S_h \tag{3.20}$$

Which $\overrightarrow{J_j}$ is the diffusion flux of species j, k_{eff} is the effective conductivity. The first term on the right-hand side of the Equation 3.20, $k_{eff}\nabla T$, reflects energy transfer owing to conduction. The second term, $\sum_j h_j\overrightarrow{J_j}$, is species diffusion, whereas the last term, $\bar{\bar{\tau}}_{eff}.\vec{v}$, is viscous dissipation. S_h represents a

comprehensive parameter that accounts for the heat from chemical processes as well as any user-specified volumetric heat sources.

Total energy per unit mass E is defined as below:

$$E = h - \frac{\mathrm{p}}{\rho} + \frac{v^2}{2} \tag{3.21}$$

h as sensible enthalpy is presented in equation below:

$$h = \sum_j Y_j h_j + \frac{\mathrm{p}}{\rho} \quad , h_j = \int_{T_{ref}}^{T} c_{p,j} dT \tag{3.22}$$

Y_j is the mass ratio of species j. The default setting for T_{ref} in the pressure-based solution is 298.15 K; however, users have the flexibility to modify this value.

3.2.7.1 Energy equation in non-premixed combustion model

The ANSYS Fluent solver uses the following equation to compute the total enthalpy when the non-premixed combustion model is activated:

$$\frac{\partial}{\partial t}(\rho H) + \nabla.(\rho \vec{v} H) = \nabla.\left(\frac{k_{eff}}{C_p}\nabla H\right) + S_h \tag{3.23}$$

Assuming the Lewis number (Le) is equal to one, the right-hand side of Equation 3.23 consists of two terms. The first represents a type of non-conservative viscous dissipation, while the second combines a conduction and species diffusion term.

The definition of the total enthalpy H is as follows:

$$H = \sum_j Y_j H_j \ , \quad H_j = \int_{T_{ref,j}}^{T} c_{p,j} dT + h^0{}_j\left(T_{ref,j}\right) \tag{3.24}$$

The symbol $h^0{}_j\left(T_{ref,j}\right)$ denotes the formation enthalpy of species j at the temperature used as the reference, $T_{ref,j}$.

3.2.8 Combustion Model

Combustion modelling involves representing chemical reaction rate terms in terms of energy and linking them to species conservation equations. As previously mentioned, these models often require the aid of additional transport equations for mixture fractions or flame surface expressions (Pitsch, 2005; Menon, 2000). Combustion modelling is a complex and continually evolving field. A detailed

explanation exceeds the scope of this report. For more in-depth information, the author recommends investigating the studies by Menon (2000) and Pitsch (2005). In this subsection, the Representative Interactive Flamelet (RIF) and diesel unsteady laminar flamelet models are investigated.

3.2.8.1 Blended Model

3.2.8.1.1 RIF

The Representative Interactive Flamelet (RIF) model employs an approach that links a CFD flow model with a heat release model at a system level. This approach allows for the integration of more detailed chemistry kinetics without the burden of increased computational time (Hergart, Barths and Peters, 1999). Individual flamelet provided are tracked by using a Lagrangian method trough the domain (combustion process).

Within the framework, individual flamelets are tracked using a Lagrangian method throughout the combustion process domain. In ANSYS Fluent, the RIF is based on a coordinate transformation that utilises the mixture fraction as an independent coordinate. This independent transformation facilitates the model in converting the enthalpy and species into the mixture fraction space. Consequently, this results in a one-dimensional calculation that captures the intricate structure of the reaction zone.

The mixture fraction (Z) formulae is:

$$Z = \sum_{i=1}^{n_s} \frac{N_{C-1} W_C Y_i}{W_i} + \sum_{i=1}^{n_s} \frac{N_{H-1} W_H Y_i}{W_i} \tag{3.25}$$

Where i is the species, n_s is the number of species, N_{C-1}, N_{H-1} are the number of Carbon and Hydrogen atoms respectively in species $i. W_C, W_H$ are the molecular weights of Carbon and Hydrogen respectively, Y_i is the species mass fraction, and W_i is the molecular weight of species i.

The first-order flamelet equations utilise local coordinate transformation and boundary layer methods to determine the species mass fraction.

$$\rho \frac{\partial Y_i}{\partial t} - \rho \frac{\chi}{2\widehat{Le_i}} \frac{\partial^2 Y_i}{\partial Z^2} = \dot{\omega}_i \quad , \quad \widehat{Le_i} = \begin{cases} Le_i & (\text{Laminar}) \\ \widehat{D}/\left(\widehat{D} + D_i\right) & (\text{Turbulent}) \approx 1.0 \end{cases} \tag{3.26}$$

And the temperature:

$$\rho\frac{\partial T}{\partial t} - \rho\frac{\chi}{2}\frac{\partial^2 T}{\partial Z^2} - \rho\frac{\chi}{2c_p}\left[\sum_{i=1}^{n_s}\frac{c_{p_i}}{\widehat{Le_i}}\frac{\partial Y_i}{\partial Z} + \frac{\partial c_p}{\partial Z}\right]\frac{\partial T}{\partial Z} = \frac{1}{c_p}\left(\frac{\partial \mathbf{P}}{\partial t} - \sum_{i=1}^{n_s}\dot{\omega}_i h_i\right) \tag{3.27}$$

In Equations 3.26 and 3.27 n_s denotes the number of chemical species and c_p is the heat capacity at constant pressure. Y_i is the mass fraction of the chemical species i, h_i is the enthalpy of the chemical species i, $\dot{\omega}_i$ is the net chemical production rate, D_i is the diffusivity, $\widehat{D}$ is the turbulent diffusivity, and $\widehat{Le_i}$ is the Lewis number of species i.

For this model, in the context of laminar flamelet models, assuming a unity Lewis number can reduce the complexity of the manifold by making it only a function of mixture fraction. This significantly reduces computational effort.

In the RIF model, the scalars are convected at the same velocity, owing to the absence of any relative convective velocity between the mixture fraction, temperature, and species mass fraction. To couple these equations in phase space with the flow field, integration is done through the pressure and scalar dissipation rate. Consequently, this leads to a representation in the mixture fraction (Z) space as follows:

$$\tilde{Y}_i(x_i, t) = \int_0^1 \widetilde{\mathbf{P}}(Z; x_i, t)\, Y_i(Z, t)\, dZ \tag{3.28}$$

The RIF model benefits from the presumed probability function (PDF) model, which requires information about the Favre mean mixture fraction and its variance in both space and time. The equations below provide this information:

$$\frac{\partial(\tilde{\rho}\tilde{Z})}{\partial t} + \frac{\partial}{\partial x_i}\left(\tilde{\rho}\tilde{u}_i\tilde{Z}\right) = -\frac{\partial}{\partial x_i}\left(\tilde{\rho}\widetilde{u_i''Z''}\right) + S_{RIF} \tag{3.29}$$

$$\widetilde{u_i''Z''} = -D_t\frac{\partial \tilde{Z}}{\partial x_i} \tag{3.30}$$

$$\frac{\partial(\tilde{\rho}\widetilde{Z''^2})}{\partial t} + \frac{\partial}{\partial x_i}\left(\tilde{\rho}\tilde{u}_i\widetilde{Z''^2}\right) = -\frac{\partial}{\partial x_i}\left(\tilde{\rho}\widetilde{u_i''Z''^2}\right) - 2\left(\tilde{\rho}\widetilde{u_i''Z''}\right)\frac{\partial \tilde{Z}}{\partial x_i} - \tilde{\rho}\tilde{\chi} \tag{3.31}$$

For Equations 3.29 to 3.31, $\tilde{\rho}$ is the density, x_i is the spatial coordinate in the i-th direction, t is time, S_{RIF} is the source term, D_t is the turbulent diffusivity. $\tilde{\chi}$ is the scalar dissipation rate and it can be represented as:

$$\tilde{\chi} \cong c_{\chi} \frac{\varepsilon}{k} \widetilde{Z''^2} \tag{3.32}$$

Here, ε represents the turbulent dissipation, k stands for the turbulent kinetic energy and c_{χ} is a time scale ratio. It's assumed that c_{χ} remains constant. In ANSYS Fluent the default value assigned to c_{χ} is 2.0. The scalar dissipation rate, denoted as $\tilde{\chi}$, is integrated across the flamelet surface, and this calculation is derived from the flow solver in ANSYS Fluent.

The following expression represents the relationship between stochiometric mixture fraction and scalar dissipation rate.

$$\widetilde{\chi_{st}}(x,t) = \frac{\tilde{\chi} f(Z_{st})}{\int_0^1 f(Z')\widetilde{\mathbf{P}}(Z';x,t)dZ'} \tag{3.33}$$

Where $\widetilde{\mathbf{P}}(Z';x,t)$ is the probability density function, and the surface-averaged scalar dissipation rate at the stoichiometric mixture fraction is given by:

$$f(Z') = \exp\left(-2[erfc^{-1}(2Z')]^2\right) \tag{3.34}$$

$$\hat{\chi}_{st} = \frac{\int_V \overline{\rho}(\tilde{x})\widetilde{\chi_{st}}^{3/2}(\tilde{x})\widetilde{\mathbf{P}}(Z_{st})dV'}{\int_V \overline{\rho}(\tilde{x})\widetilde{\chi_{st}}^{1/2}(\tilde{x})\widetilde{\mathbf{P}}(Z_{st})dV'} \tag{3.35}$$

Here, Z_{st} represents the fuel mass fraction when the equivalence ratio is 1.0. V denotes the volume of the entire computational domain. Additionally, the function $erfc$ is known as the complementary error function.

3.2.8.1.2 RIF Multiple Flamelet Theory

In unsteady flamelet modelling, if the parameters such as scalar dissipation rate and boundary conditions vary significantly in the physical domain, then different flamelet history must be used. A flamelet history represents the history of the scalar dissipation rate and boundary conditions which illustrates the solution of a flamelet. Hence, for the spatial inhomogeneity of χ, a multiple flamelets are needed.

$$\hat{\chi}_{st}(l) = \frac{\int_V \widetilde{I}_l(\tilde{x})\overline{\rho}\,(\tilde{x})\widetilde{\chi_{st}}^{3/2}(\tilde{x})\widetilde{\mathbf{P}}(Z_{st})dV'}{\int_V \widetilde{I}_l(\tilde{x})\overline{\rho}\,(\tilde{x})\widetilde{\chi_{st}}^{1/2}(\tilde{x})\widetilde{\mathbf{P}}(Z_{st})dV'} \quad (3.36)$$

$$\widetilde{I}_l(x,t) = \frac{Z_l}{\sum Z_l} \quad (3.37)$$

In ANSYS Fluent, Z_l represents the mixture fraction for each flamelet, where l can range from zero up to the total number of flamelets. The first flamelet is initialised at the beginning of the spray, while subsequent flamelets are initialised at specified crank angle degrees.

3.2.8.1.3 RIF model and CFD solver interaction

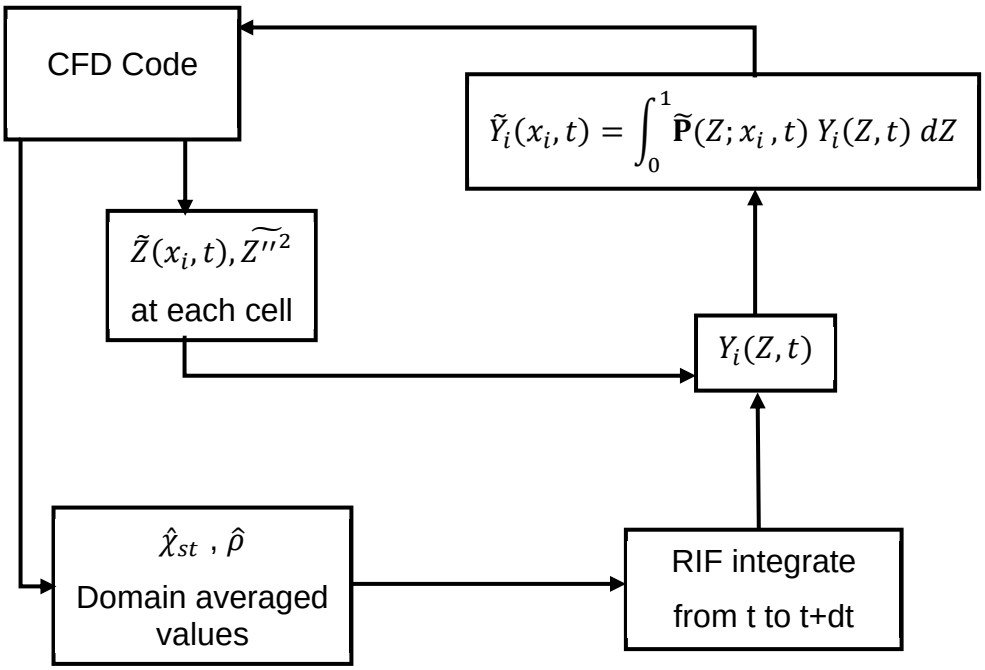

Figure 9 - An illustration of Representative interactive flamelet model concept by (Chen, Herrmann and Peters, 2000).

Figure 9 provides a clear illustration of how ANSYS Fluent implements the RIF model in CFD simulations. To determine the temperature, the energy conservation equation is solved. The scalar dissipation rate, conditioned on the stoichiometric mixture, and pressure are derived from the turbulent flow and mixing field domain averaged flamelet parameters. Subsequent calculations yield the species mass fraction and temperature, as depicted in Equations 3.30 and 3.31, for the upcoming time-step (n+1). This process also entails refining the chemical

timescales by subdividing the time-step determined by the CFD code's turbulent model. Leveraging the PDF function, defined by the mixture fraction and its variance, turbulent mean values for species mass fractions within the physical space can be deduced. As a result, updated values for each species' mass fraction and corresponding cell temperatures are sourced from the species transport and energy equations.

Furthermore, the transport equations for terms $\widetilde{Z}\ and\ \widetilde{Z^{"2}}$ (representing mean mixture fraction and variance, respectively) are addressed as passive entities. Both the scalar dissipation rate and pressure, which serve as feedback for the RIF model, are determined based on the mean and variance mixture fraction.

3.2.8.2 Non-premixed Combustion for Diesel Unsteady Laminar Flamelet Model

As a result of significant research contributions, the approach has evolved into an industrial application of CFD modelling for diesel engines (Pitsch, Barths and Peters, 1996). The foundational assumption, which posits a finite number of one-dimensional laminar flamelets, was adopted to confine the chemical kinetic computation to a singular dimension, thus reducing computational costs. This method offers a notable decrease in the required processing time when juxtaposed with laminar-finite rate, Eddy Dissipation Concept (EDC), or PDF transport models.

$$\rho \frac{\partial Y_i}{\partial t} = \frac{1}{2}\rho\partial\chi \frac{\partial^2 Y_i}{\partial f^2} + S_i \tag{3.38}$$

$$\rho \frac{\partial T}{\partial t} = \frac{1}{2}\rho\partial\chi \frac{\partial^2 T}{\partial f^2} - \frac{1}{c_p}\sum_i H_i S_i + \frac{1}{2C_p}\rho\chi\left[\frac{\partial c_p}{\partial f} + \sum_i c_{p,i}\frac{\partial Y_i}{\partial f}\right]\frac{\partial T}{\partial f} \tag{3.39}$$

Equations 3.38 and 3.39 are solved simultaneously within the flow context.

The Equation 3.38 represents the species of the flamelet, while Equation 3.39, that follows illustrates the energy. Y_i, T, ρ, and f are the i^{th} species mass fraction, temperature, density, and mixture fraction, respectively. $c_{p,i}$ and c_p are the i^{th} species specific heat and mixture-averaged specific heat, respectively. S_i is the i^{th} species reaction rate, and H_i is the specific enthalpy of the i^{th} species.

The conditions of the flamelet and the environment of the flow field are intrinsically interconnected. When one converges to a solution, it informs the other, allowing it to advance within the same fractional time step. This progression sets the stage

for subsequent evaluations. Notably, the computational domain underscores that every flamelet introduced into this domain presents as a mixed distribution yet remains unburned.

To account for the temperature increase due to compression, an additional term is incorporated into the right-hand side of the flamelet energy Equation 3.39. This term is defined as follows:

$$q^{\cdot} = \frac{1}{c_p}\frac{\partial \mathrm{p}}{\partial t} \tag{3.40}$$

In Equation 3.40 , c_p stands for the specific heat, and p represents the in-cylinder volume averaged pressure.

As the flamelet undergoes further compression, its temperature rises, moving it closer to ignition. Once the flamelet equations have advanced sufficiently to address the fractional time step, the PDF table is constructed. Leveraging the Non-Adiabatic Steady Flamelet table, as detailed in section 3.2.6, enables the computation of the subsequent fractional time step, culminating in the production of the diffusion flamelet. To shape the assumed PDFs appropriately, flamelet profiles are derived using the equation that follows:

$$\bar{\varphi} = \iint \varphi(f, \chi_{st})\, p(f, \chi_{st}) df d\chi_{st} \tag{3.41}$$

Furthermore, once tabulated, these tables serve as references for subsequent generations. The dimensions of the non-adiabatic PDF tables are analogous to those that follow:

$$\bar{T}\left(\bar{f}, \overline{f''^2}, \bar{H}, \bar{\chi}\right) \tag{3.42}$$

$$\bar{Y}_i\left(\bar{f}, \overline{f''^2}, \bar{H}\right) \; for\; \chi = 0 \qquad \text{(Equilibrium solution)} \tag{3.43}$$

$$\bar{Y}_i\left(\bar{f}, \overline{f''^2}, \bar{\chi}\right) for\; \chi \neq 0 \tag{3.44}$$

$$\bar{\rho}\left(\bar{f}, \overline{f''^2}, \bar{H}, \bar{\chi}\right) \tag{3.45}$$

The scalar dissipation field is determined by concurrently solving both the turbulence field and the mixture fraction variance during the simulation. As a result,

the continuity and momentum equations can be computed for both mass and time. This stems from the foundational link between the scalar dissipation field and the turbulence field. The ensuing equations respectively represent the scalar dissipation rate in relation to mass, and the momentum equations for both mass and time:

$$\overline{\chi_{st}} = \frac{C_\chi \varepsilon \overline{\acute{f}^2}}{k} \tag{3.46}$$

$$\frac{\partial \mathrm{p}}{\partial t} + \nabla \cdot (\rho U) = 0 \tag{3.47}$$

$$\frac{\partial (\rho U)}{\partial t} + \nabla \cdot (\rho U \otimes U) = -\nabla \mathrm{p} + \nabla \cdot \tau + S_M \tag{3.48}$$

τ, the stress tensor, is linked to strain rate by:

$$\tau = \mu \left(\nabla U + (\nabla \mathrm{U})^T - \frac{2}{3} \delta \nabla \cdot U \right) \tag{3.49}$$

3.2.9 Spray Model

In a two-fluid mixed condition, the liquid and vapour phases are treated independently, necessitating two separate conservation equations. The predominant models used to describe these conditions are the Eulerian-Eulerian and Eulerian-Lagrangian models. For the Eulerian-Eulerian model, the governing equation originates from the differences between local pressure and vapour pressure. This results in a phase transition source term and a volume fraction. Cavitation can often be attributed to microbubbles present within the liquid, which may either expand or collapse. This expansion and collapse process is illustrated by Rayleigh's simple bubble dynamics (Som *et al.*, 2010).

The Eulerian-Lagrangian model has two primary components. In the Eulerian frame of reference, the liquid is depicted as the carrier phase. Conversely, in the Lagrangian frame of reference, vapour is portrayed as the dispersed phase. To simulate the entire population of real bubbles, 'bubble parcels' are created. Each of these parcels is presumed to contain a collection of identical, non-interacting bubbles.

An artificial nucleus is introduced to initiate cavitation. These nuclei are sourced from a probability density function model. Factors such as turbulent dispersion, pressure gradients, lift forces, and drag forces are taken into account, highlighting the detailed nature of this model. The non-linear Rayleigh-Plesset equation further aids in calculating bubble dynamics.

The Kelvin-Helmholtz/Rayleigh-Taylor (KH-RT) approach represents the Eulerian-Lagrangian concept and serves as a wave breakup model. It is utilised to predict the primary and secondary atomisation, as well as the breakup process, in diesel spray simulations. The droplet sizes derived from the KH-RT model depend on several parameters, including:

- Fuel's physical properties, such as viscosity, surface tension, and density.
- The KH-RT time constant.
- The KH-RT size constant.
- The breakup length constant.

3.2.9.1 Kelvin-Helmholtz/Rayleigh-Taylor (KH-RT)

In this section, the essential equations associated with the KH-RT coupled model are outlined. For more detailed information, readers are advised to refer to the ANSYS Fluent 2020 R2 theory manual (2020) and the work of Tsang and Rutland (2015).

KH-RT breakup length can be specified as:

$$L_b = C_{bl}\sqrt{\frac{\rho_l}{\rho_g}}d_0 \tag{3.50}$$

Where as C_{bl} is break up length constant, $\rho_l \; and \; \rho_g$ are the density of the gas and liquid respectively and d_0 is the orifice or nozzle hole diameter.

KH-RT breakup time equation is as follows:

$$\tau_{\mathrm{KH}} = \frac{\mathrm{B}_1}{U}\sqrt{\frac{\rho_l}{\rho_g}}r_0 \tag{3.51}$$

U is the liquid jet velocity out of the nozzle, B_1 is the KH breakup time constant.

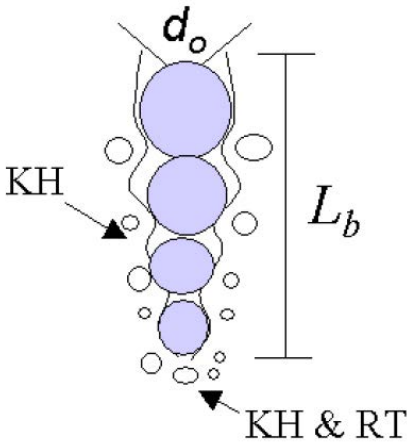

Figure 10 - Schematic of the KH-RT spray breakup model. Note that liquid blobs are injected with a diameter equal to the injector nozzle (Richards, Senecal and Pomraning, 2017).

As observed in Figure 10, the breakup length L_b has a significant influence on the characteristic area of the KH-RT model. Initially, the KH (Kelvin-Helmholtz) mechanism is responsible for the breakup. Following this, the RT (Rayleigh-Taylor) mechanism examines its potential to cause a secondary breakup. If this secondary breakup does not occur, the KH mechanism resumes its role.

It's worth noting that the breakup time constant B_1 varies across injectors. Consequently, its typical value can range between 5 and 100. The smaller the value, the quicker the breakup occurs. Given a very high gas Weber number We_g (which is typical for diesel sprays) and when $\mu_l = 0$, the breakup time for the KH model can be reformulated as follows:

$$L_{\mathrm{KH}} = U\tau_{\mathrm{KH}} \tag{3.52}$$

$$L_{\mathrm{KH}} = \mathrm{B}_1\sqrt{\frac{\rho_l}{\rho_g}}r_0 \tag{3.53}$$

A comparison between Equations 3.50 and 3.53 reveals that C_{bl} should be equal to $\mathrm{B}_1/2$. This ensures consistency between L_b and L_{KH}. Adjusting the two spray constants in tandem has proven to yield accurate predictions of spray penetration when compared to experimental results (Tsang and Rutland, 2015).

The KH-ACT model addresses cavitation by considering the combined effects of aerodynamics, cavitation, and turbulence on the primary breakup. A brief overview of this model is provided below.

3.2.9.1.1 Aerodynamic-induced breakup

It employs the same configuration as the KH model. The formula provided below encapsulates the breakup length and time associated with this concept.

$$L_{\mathrm{KH}} = r - r_{\mathrm{KH}} \tag{3.54}$$

$$\tau_{\mathrm{KH}} = \frac{3.276\mathrm{B}_1 r}{\Omega_{\mathrm{KH}}\Lambda_{\mathrm{KH}}} \tag{3.55}$$

Maximum growth rate and corresponding wavelength are shown by $\Omega_{\mathrm{KH}}\ and\ \Lambda_{\mathrm{KH}}$, respectively.

3.2.9.1.2 Cavitation-Induced Breakup

This model postulates that cavitation manifests in patterns which are conveyed to the jet periphery via two distinct mechanisms. These mechanisms are:

- Transportation to the jet periphery by turbulence viscosity within the liquid domain.
- Bursting at the periphery (collapsing before reaching it).

For both scenarios, a timescale is determined. The characteristic timescale can be computed as:

$$\tau_{CAV} = \min(\,\tau_{\mathrm{collapse}} : \tau_{\mathrm{burst}}\,) \tag{3.56}$$

In this model the length scale L_{CAV} is equal to the effective radius R_{CAV} of an identical bubble from the nozzle.

$$L_{CAV} = R_{CAV} = r_{\mathrm{hole}}\sqrt{(1 - C_a\,)} \tag{3.57}$$

The coefficient C_a represents the area reduction, and it is obtained from flow simulations within the nozzle.

Meanwhile, r_{hole} denotes the exit radius of the nozzle (orifice). The time for bubble collapse is informed by the Rayleigh-Plesset equation, which is derived as follows:

$$\tau_{\mathrm{collapse}} = 0.9145 R_{CAV}\sqrt{\frac{\rho_l}{\mathrm{p}_v}} \tag{3.58}$$

The p_v is the fuel vapour pressure and ρ_l is the fuel density.

An effective bubble is situated at the centre of the liquid spray upon injection. The average time required for this cavitation bubble to migrate to the jet's periphery is estimated as:

$$\tau_{\mathrm{burst}} = \frac{r_{\mathrm{hole}} - R_{CAV}}{u'_{\mathrm{turb}}} \tag{3.59}$$

$$u'_{\mathrm{turb}} = \sqrt{\frac{2\mathrm{K}(t)}{3}} \tag{3.60}$$

3.2.9.1.3 Turbulence-Induced Breakup

Initial perturbations on the jet surface arise from turbulent fluctuations within the liquid jet's frame of reference, manifesting as waves. Influenced by KH instabilities, these waves intensify. When these disturbances grow large enough to disrupt the jet's coherence, a breakup on the jet surface occurs due to the Kelvin-Helmholtz (KH) instabilities. The associated length and time scales are presented below:

$$L_T(t) = \frac{C_\mu \mathrm{K}(t)^{1.5}}{\varepsilon(t)} \tag{3.61}$$

$$\tau_T(t) = \frac{C_\mu \mathrm{K}(t)}{\varepsilon(t)} \tag{3.62}$$

$C_\mu and\ C_\varepsilon$ are turbulence model constants. The instantaneous turbulent kinetic energy and dissipation rate are represented by $\mathrm{K}(t)$ and $\varepsilon(t)$, respectively.

To simplify these terms, one can consider isentropic turbulence for the liquid phase and neglect the diffusion, convection, and production terms in the $k - \varepsilon$ equation. This simplification yields an equation that relates the instantaneous turbulent kinetic energy and dissipation rate to their initial values at the nozzle exit, which corresponds to the start of injection (SOI).

$$\mathrm{K}(t) = \left\{\frac{(\mathrm{K}_0)^{C_\varepsilon}}{\mathrm{K}_0 + \varepsilon_0 t(C_\varepsilon - 1)}\right\}^{1/(C_\varepsilon - 1)} \tag{3.63}$$

$$\varepsilon(t) = \varepsilon_0 \left\{\frac{\mathrm{K}(t)}{\mathrm{K}_0}\right\}^{C_\varepsilon} \tag{3.64}$$

To determine the outcomes of Equations 3.63 and 3.64, one must compute the initial turbulent kinetic energy and turbulent dissipation rate. The following formulas can be employed for this purpose:

$$\mathrm{K}_0 = \frac{U_{\mathrm{inj}}^2}{8\left(\frac{L}{D}\right)}\left\{\frac{1}{C_d^2} - \mathrm{K}_c - (1 - s^2)\right\} \tag{3.65}$$

$$\varepsilon_0 = \mathrm{K}_\varepsilon \frac{U_{\mathrm{inj}}^3}{2L}\left\{\frac{1}{C_d^2} - \mathrm{K}_c - (1 - s^2)\right\} \tag{3.66}$$

The model constants can be altered; however, the recommendations are $\mathrm{K}_c = 0.45, \mathrm{K}_\varepsilon = 0.27, s = 0.01$ (Som *et al.*, 2010). Once the initial K_0 and ε_0 values at the nozzle exit are determined, the length and timescales for the turbulence-induced breakup can be calculated.

Finally, ANSYS Fluent calculates the ratios of length and time scale for each model, as presented below:

$$\frac{L_A}{\tau_A} = \max\left\{\frac{L_{\mathrm{KH}}(t)}{\tau_{\mathrm{KH}}(t)}; \frac{L_{CAV}}{\tau_{CAV}}; \frac{L_T(t)}{\tau_T(t)}\right\} \tag{3.67}$$

It is evident that the rate of decrease in droplet radius (dr/dt) is proportional to the length-to-time scale ratio (L_A/τ_A). Consequently, the largest ratio dictates the dominant breakup concept.

3.2.9.2 Discrete Phase Model (DPM)

ANSYS Fluent employs the Euler-Lagrange method to treat the fluid phase as a continuum. This is achieved by solving the Navier-Stokes equations while tracking a multitude of species, particles, droplets, or bubbles throughout the flow field. Alterations in the dispersed phase not only ripple through the fluid phase but also significantly affect its momentum, mass, and energy. ANSYS Fluent defaults to the theory of collision and droplet coalescence for simulations of this nature. In this model, two droplets can potentially collide if they occupy the same discrete phase cell (O'Rourke, 1981). Such an assumption might prevent droplets that are merely in close proximity but not within the same cell from colliding. However, the impact of this potential oversight is mitigated, as it also permits some droplets farther apart

to collide. As a result, the model's precision can be considered second-order in space (O'Rourke, 1981).

By integrating the breakup model (KH-RT) with the standard approach of the DPM model in Fluent's default settings, the collision model's potential inaccuracies are minimized due to its inherent design. The subsequent equations, which track particle motion, are solved using coupled ordinary differential equations and are outlined as follows:

$$\frac{dx}{dt} = u_p \quad , \quad \frac{du_p}{dt} = \frac{1}{\tau_p}(u - u_p) + a \tag{3.68}$$

In Equation 3.68 , x represents the position of the particle, t denotes the passage of time, and the velocities u_p and u indicate the motion of the particle and the flow field, respectively. The symbol a represents acceleration. However, when this formula is multiplied by the particle's mass, it results in the particle's inertia force within the Lagrangian reference frame. The symbol τ_r denotes the time required for a particle to relax, and it is computed as follows:

$$\tau_r = \frac{\rho_p {d_p}^2}{18\mu} \frac{24}{C_d Re} \tag{3.69}$$

Where ρ_p is the density of the particles, d_p is the diameter of the particles, μ is the dynamic viscosity, C_d and Re are the drag coefficient and the Reynolds number, correspondingly.

To determine the new position of the particles at the next time step, Equations 3.68 and 3.69 must first be solved using an analytical discretization model.

3.2.9.3 Evaporation Theory

In order to predict the vaporisation that will occur from a discrete phase droplet, the Convection/Diffusion Controlled model is employed. The process begins when the temperature of the droplet reaches the vaporisation temperature, known as T_{vap}, and continues either until the droplet temperature reaches the boiling point, denoted as T_{bp}, or until the droplet's volatile fraction is completely consumed.

When the rate of vaporisation is high, the impact of the Stefan Flow becomes critical. This flow describes the convective movement of material evaporating from the droplet surface to the bulk gas phase. ANSYS Fluent has incorporated this

concept under the name 'Convection/Diffusion Controlled model' as a result of seminal works in the field (Sazhin, 2006; Miller, Harstad and Bellan, 1998).

$$\frac{d_{m_p}}{dt} = \mathrm{K}_c A_p \rho \ln\left(1 + \mathrm{B}_m\right) \tag{3.70}$$

Table 2 - Definitions and Units of Variables Used in Equations 3.70

Name	Variable
Gas density $^{\mathrm{kg}}/_{\mathrm{m}^3}$	ρ
Droplet surface area m^2	A_p
Mass transfer coefficient $\mathrm{m/s}$	K_c
Droplet mass kg	m_p

Symbol $\mathrm{B_m}$ is the Spalding mass number resulting from:

$$\mathrm{B_m} = \frac{Y_{i,s} - Y_{i,\infty}}{1 - Y_{i,s}} \tag{3.71}$$

$Y_{i,s}$ is the surface vapour mass fraction and $Y_{i,\infty}$ is the bulk vapour mass fraction.

The Sherwood number Sh_{AB} correlation equation is employed to calculate the mass transfer coefficient, as illustrated below:

$$Sh_{\mathrm{AB}} = \frac{\mathrm{K}_c d_p}{D_{i,m}} = 2.0 + 0.6 Re_d^{1/2} {S_c}^{1/3} \tag{3.72}$$

The symbols $D_{i,m}, S_c, and\ d_p$ represent the diffusion coefficient of vapour in the bulk $(\mathrm{m}^2/\mathrm{s})$, the Schmidt number $(\mu/\rho D_{i,m})$, and particle (droplet) diameter (m), respectively.

Both the boiling point, represented by T_{bp}, and the latent heat, denoted by h_{fg}, are set as constant attribute inputs for the droplet particle materials. The default values in the ANSYS Fluent property database for these properties correspond to a pressure of one atmosphere, the standard boiling point. It's noteworthy that as the particle temperature varies during evaporation, the latent heat adjusts in line with Equation 3.73.

$$h_{fg} = -\int_{T_p}^{T_{bp}} c_{p,g}dT + h_{fg,bp} + \int_{T_p}^{T_{lp}} c_{p,p}dT \tag{3.73}$$

The boiling point is denoted by T_{bp} (K). The Symbol $h_{fg,bp}$ represents the latent heat at the boiling point, measured in joules per kilogram. The specific heats of the gaseous and liquid phases are given by $c_{p,g}$ and $c_{p,p}$, respectively, both measured in joules per kilogram per Kelvin.

In the end, the temperature of the droplet is updated in accordance with a heat balance that establishes a relationship between the change in sensible heat in the droplet and the convective and latent heat transfer between the droplet and the continuous phase, as follows:

$$m_p c_p \frac{dT_p}{dt} = hA_p(T_\infty - T_p) - \frac{dm_p}{dt}h_{fg} + A_p\varepsilon_p\sigma\left(\theta_R^4 - T_p^4\right) \tag{3.74}$$

Table 3 - Definitions and Units of Variables Used in Equation 3.74

Name	Variable
Droplet heat capacity (J/kg-K)	c_p
Droplet temperature (K)	T_p
Convective heat transfer coefficient $\mathrm{W/m^2 - K}$	h
Temperature of continuous phase (K)	T_∞
Rate of evaporation (kg/s)	dm_p/dt
Latent heat (J/kg)	h_{fg}
Particle emissivity (dimensionless)	ε_p
Stefan-Boltzmann constant ($5.67 \times 10^{-8}\,\mathrm{W/m^2 - K^4}$)	σ
Radiation temperature (K)	θ_R

Note that $\theta_R = (\mathrm{G}/4\sigma)^{1/4}$.

Whereas incident radiation G (W/m^2) is calculated by equation 3.75 :

$$G = \int_{\Omega=4\pi} I d\Omega \tag{3.75}$$

Symbols I and Ω are the radiation intensity and the solid angle, respectively.

During successive computations of the continuous phase energy equation, the heat that is transmitted to or from the gas phase becomes a source or sink of energy.

Equation 3.70 of the Convection/Diffusion Controlled model calculates the vaporisation rate, and Equation 3.74 of same model generates the convective heat transfer coefficient h using a modified Nu value, as follows:

$$Nu = \frac{hd_p}{k} = \frac{ln(1+\mathrm{B}_T)}{\mathrm{B}_T}\left(2 + 0.6Re_d^{1/2}Pr^{1/3}\right) \tag{3.76}$$

Particle diameter (m), thermal conductivity of the phase that is continuous (W/m.K), Reynolds number, and the continuous phase Prandtl number are presented as, d_p, k, Re_d, and Pr, receptively.

The Spalding heat transfer number is denoted by the letter B_T and is defined as follows:

$$\mathrm{B}_T = \frac{C_{pv}(T_\infty - T_p)}{h_{fg} - \dot{q}_p / \dot{m}_p} \tag{3.77}$$

Symbols define equation 3.77 are explained as below:

- $\dot{q}_p$ is heat transferred to the droplet (w).
- $\dot{m}_p$ presented as particle evaporation rate (kg/s).
- The droplet vapour specific heat (J/kg-K) is indicated as symbol C_{pv} .

The symbol B_T is derived from the Spalding mass number using the following formula:

$$\mathrm{B}_T = (1+\mathrm{B}_m)^{\frac{1}{Le}\cdot\frac{Sh}{Nu}\cdot\frac{C_{pv}}{c_{pg}}} - 1 \tag{3.78}$$

The symbol Le is determined as the Lewis number which is equal to $k/c_{pg}\rho D_{i,m}$ and mixtures of gas specific heat is written as symbol c_{pg} with unit of (J/kg-K).

Assuming that $c_{pv} = c_{pg}$ and use the Lewis number as 1, Equation 3.78 can be simplified as follows:

$$\mathrm{B}_T = \mathrm{B}_m \tag{3.79}$$

When there is a substantial temperature difference between the droplet and the bulk gas, transient effects become more prominent. In such cases, the assumptions of uniform droplet temperature and vapour temperature being in equilibrium with the bulk gas are subject to scrutiny. A more realistic outcome might be achieved by averaging the Spalding heat transfer term. Specifically, in Equation 3.76, ANSYS Fluent offers an option to average the term $ln(1+\mathrm{B}_T)/\mathrm{B}_T$ with the surface mass fraction of the evaporating species, as shown below:

$$F_T = 1 - Y_{is}(1 - F_{T_0}) \tag{3.80}$$

The term F_{T_0} is defined as $ln(1+\mathrm{B}_T)/\mathrm{B}_T$, and the mass fraction of the evaporating species at the surface is denoted by the symbol Y_{is}.

3.2.9.4 Leidenfrost

Within the Convection/Diffusion Controlled model, Equation 3.81 assumes that the liquid film maintains complete contact with the wall while determining the wall film vaporisation rate. This presumption is mirrored in the Lagrangian Wall Film (LWF) model. Even as the wall film's temperature nears the boiling point, initiating a boiling rate calculation, it's taken for granted that the liquid film uniformly covers the wall.

$$\dot{N}_\iota = k_{film}\rho_\infty ln(1+B_m) \tag{3.81}$$

$$\mathrm{B_m} = \frac{Y_{i,surf} - Y_{i,\infty}}{1 - Y_{i,surf}}$$

$\dot{N}_\iota$is defined as vapour mass flux of species (kg/m^2/s), $Y_{i,surf}\ and\ Y_{i,\infty}$symbols represent the mass fraction of species i on the film surface and the bulk, correspondingly. Symbol k_{film} is indicated as transfer coefficient of film mass (m/s), and bulk gas density (kg/m^3) is ρ_∞.

$$\dot{m}_p = \frac{A_p}{h_{fg}}\left[-k_p\left(1+\frac{h_{\mathrm{film}}}{k_p+h_{\mathrm{film}}}\right)T_p + k_p T_w + h_{\mathrm{film}}\left(1-\frac{h_{\mathrm{film}}}{k_p+h_{\mathrm{film}}}\right)T_\infty\right] \tag{3.82}$$

$$k_p = k_l/(h/2) \tag{3.83}$$

$$h_{\text{film}} = \frac{k_\infty}{len} Nu \tag{3.84}$$

Table 4 – Definitions and Units of Variables Used in Equations 3.82 to 3.84

Name	Variable
Film Parcel boiling rate (kg/s)	$\dot{m}_p$
The film parcel area (m^2)	A_p
Latent heat (J/kg)	h_{fg}
Film parcel temperature (K)	T_p
Wall temperature (K)	T_w
Temperature in the bulk phase (K)	T_∞
The film height (m)	h_{film}
Thermal conductivity of the liquid film (W/m/K)	k_l
Thermal conductivity of the continuous phase (W/m/K)	k_∞
The characteristic length (m)	len

The LWF boiling rate equation, presented as Equation 3.82, suggests a linear relationship between the boiling rate and the wall temperature when the temperature is constant. However, the reality of boiling events in liquid films is more intricate. The heat transfer rate from a hot wall to a liquid film does not maintain a linear pattern, especially when there's a substantial temperature difference between the wall and the liquid film. This non-linearity is attributed to the formation of vapour pockets between the hot wall surface and the boiling film.

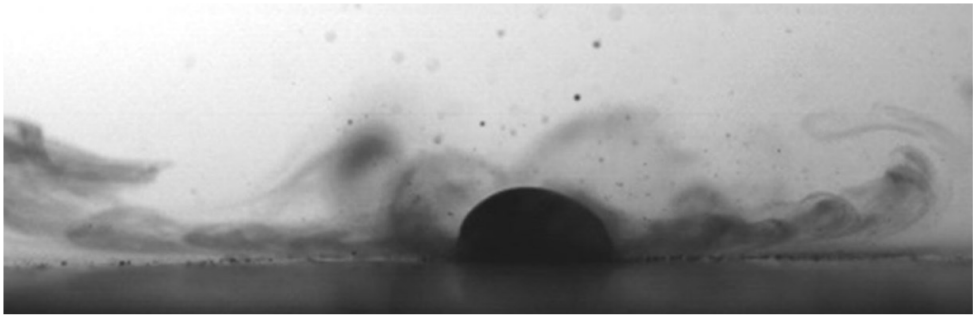

Figure 11 - Fuel oil droplet deposition on a hot solid wall (Islamova *et al.*, 2023).

An illustrative depiction of this phenomenon can be seen in Figure 11, where a fuel oil droplet impinges on a hot wall, highlighting the layers of vapour beneath and indicating the occurrence of the Leidenfrost effect based on investigative

findings (Islamova *et al.*, 2023).These vapour pockets significantly influence both the heat transfer and the hydrodynamic characteristics of the film boiling process. An extreme scenario is the Leidenfrost point, where an insulating vapour layer entirely covers the heated wall.

In the LWF model, accurately predicting the Leidenfrost point is crucial to determine the appropriateness of the LWF boiling rate and to avoid results that deviate from physical reality. ANSYS Fluent calculates the Leidenfrost temperature and compares it to the wall temperature during its LWF computations. If the wall temperature exceeds the Leidenfrost temperature, Fluent will issue a warning to the user. It's important to note, however, that this Leidenfrost point calculation is purely informational and doesn't act to limit the wall temperature in any subsequent calculations.

The Leidenfrost temperature $T_{Leid,iso}$ for an isothermal surface can be effectively approximated as a function of the liquid's critical temperature T_{crit} and surface tension (σ) .

$$T_{Leid,iso} = \frac{27}{32} T_{crit} \left(1 - exp\left(-0.52 \left[\frac{10^4 (\rho/A)^{4/3}}{\sigma} \right]^{1/3} \right) \right) \tag{3.85}$$

Where ρ is the density of the solid and A is the atomic number of the solid. The final term in Equation 3.85 accounts for the effects of solid-liquid surface tension.

By referencing $T_{Leid,iso}$ and the heat transmission properties of the solid surface, the Leidenfrost temperature T_{Leid} can be determined as follows:

$$\frac{T_{Leid,iso} - T_f}{T_{Leid} - T_f} = exp(0.00175\beta) erfc\left(0.042\sqrt{\beta}\right) \tag{3.86}$$

Where T_f is the temperature of the liquid film in Kelvin, $erfc$ is the complementary error function, and β is defined as below:

$$\beta = \frac{1}{k\rho c_p} \tag{3.87}$$

Thermal conductivity of solid (W/m-K), solid density (kg/m3), and heat capacity of solid (J/kg-K) are presented in Equation 3.87 as, k, ρ, c_p , respectively.

3.2.10 Compressibility Effect

Compressibility effects become pronounced in gas flows with high velocities or significant pressure changes. These effects are especially noticeable when the flow velocity approaches or exceeds the speed of sound of the gas or when there's a substantial relative pressure change in the system ($\Delta p/p$). In these conditions, variations in gas density due to pressure play a crucial role in determining the flow's velocity, pressure, and temperature. It's imperative to activate the 'Compressibility Effects' option within the Species Model dialogue box for the real-gas models to be available, especially when working with the non-premixed and partially-premixed models (ANSYS, 2020c; ANSYS, 2020d).

The system's Operating Pressure is integrated into the density calculation based on the ideal gas law. For non-adiabatic simulations, the 'Compressibility Effects' under PDF Options should be employed to accommodate significant pressure variations over time or space (ANSYS, 2020c; ANSYS, 2020d).

Literary sources and the ANSYS Fluent theory guideline emphasize that during the droplets' injection and breakup phase (Eulerian-Eulerian), the flow is presumed incompressible (Anderson and Wendt, 1995; ANSYS, 2020c; Banerjee *et al.*, 2010; Crowe *et al.*, 2011; Rutland, 2011; Versteeg and Malalasekera, 2007). This assumption holds until gases are produced in the Eulerian-Lagrangian framework. From this point, the compressible flow effects become integral to the in-cylinder non-premixed combustion flow. The CFD literature highlights that the fuel's liquid properties exhibit marked temperature-driven changes. Moreover, when the combustion mach number exceeds 0.3, it signifies a compressible flow within the Eulerian-Lagrangian context (Anderson and Wendt, 1995; ANSYS, 2020c; Crowe *et al.*, 2011; Versteeg and Malalasekera, 2007).

Chapter 4 – Methodology

4.1 Introduction

To scrutinise the combustion and emission characteristics of Diesel (B7), Waste Cooking Oil (WCO) biodiesel (B100), and their blends in diesel engine conditions, the methodology was profoundly rooted in the precision of diverse analytical setups. Initially, an experimental platform was developed to monitor pressure against crank angle and methodically capture emission data. Complementing this, a 0-D Direct Injection engine model was configured on ANSYS Chemkin-Pro, tailored to delve deep into emission dynamics and sensitivity analyses of the varied fuels. Lastly, an Internal Combustion (IC) engine was primed for Computational Fluid Dynamics (CFD) simulations using ANSYS Fluent. Through this setup-centric approach, the aim was to obtain thorough insights into the intricacies of combustion and emission behaviours from various perspectives.

4.2 Experiment Setup

To accurately observe the combustion behaviour of Diesel (B7), Waste Cooking Oil (WCO) biodiesel (known as B100), and their respective blends under diesel engine conditions, it's imperative to capture detailed pressure versus crank angle data, along with pertinent emission metrics. Thus, a dedicated engine setup, equipped with precise acquisition tools, has been established. Within this section, the specifics of the acquisition instruments are elucidated, detailing the engine's configuration and the conditions under which it operates.

Prior to data collection for the different fuel variants, the engine was operated for ten minutes to circumvent cold start effects and to establish a stable engine condition with a steady speed of 1300 RPM (revolutions per minute). To gather pressure versus crank angle data and emission metrics for each fuel type at various loads, ten separate runs were conducted for each condition. Subsequently, the results from these runs were averaged to ensure accuracy and consistency in the findings.

The specific settings and conditions applied to the engine for the experiment, encompassing both operational and environmental parameters, are detailed in Table 5.

Table 5 – Experimental engine conditions

Condition	Value
Atmospheric pressure	1 bar
Atmospheric temperature	28-30 Celsius
Engine Rpm	1300
Fuel quantity at no load consumed	10 ml in 210 s
Fuel quantity at half load consumed	10 ml in 93 s
Fuel quantity at full load consumed	10 ml in 61 s
Inlet air velocity at no load	3.8 $\mathrm{m/s}$
Inlet air velocity at half load	3.6 $\mathrm{m/s}$
Inlet air velocity at full load	3.4 $\mathrm{m/s}$

4.2.1 Engine

A rig (see Appendix F) was set up using a purchased Robin DY23-2D small-duty diesel engine. The engine's specifications are detailed in Table 6, while Figure 12 displays the stock horsepower graph for the engine.

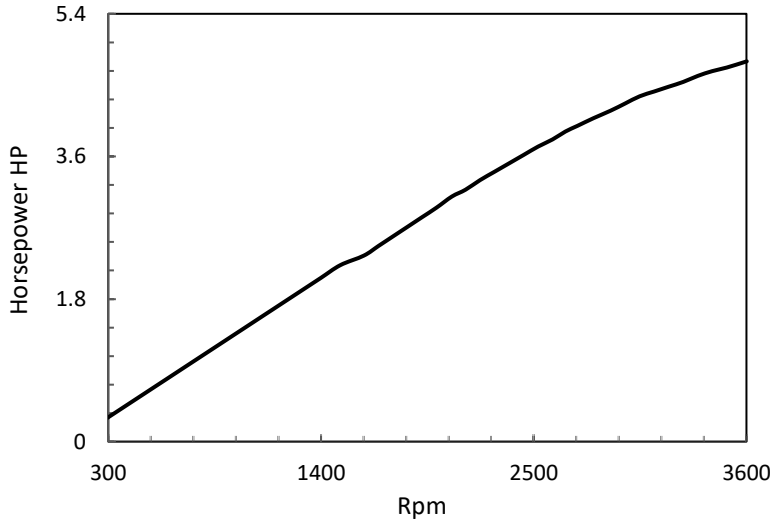

Figure 12 - Engine stock horsepower curve versus rpm for Robin DY23-2D (Engines, 2000).

Table 6 - Robin DY23-2D diesel engine specifications

Specifications	
Engine model	Robin DY23-2D Diesel
Type	Air-cooled, 4cycle, overhead valve, single cylinder, direct injection
Bore*Stroke	70 mm * 60 mm
Piston displacement	230 cc
Compression ratio	21
Output	4.8 Hp @3600 rpm
Crank rod	90 mm
Crankshaft radius	30 mm
Injection start (fixed)	23 BTDC
Injection pressure (fixed)	191.23 bar
Injector model	DLLA150PN52
Injector position	2.3 mm height, 3.1 mm radius, 45-degree angle
Number of injector holes	4
Injector hole diameter	0.22 mm
Fuel pump model	ZEXEL PFRIMD55/2NP1

Fuel is pumped from the plunger pump and directed through the high-pressure pipe (1), then passed to the fuel line passage (2). Upon reaching the nozzle body (3), the fuel is pressurized to a consistent 191.23 bar, causing the needle valve (4) to lift by 0.18mm. Following this, the fuel is injected into the combustion chamber via the jet-hole (5). Any excess fuel then returns through the nozzle spring (6) and is redirected via the overflow pipe (7) back to the fuel tank (refer to Figure 13).

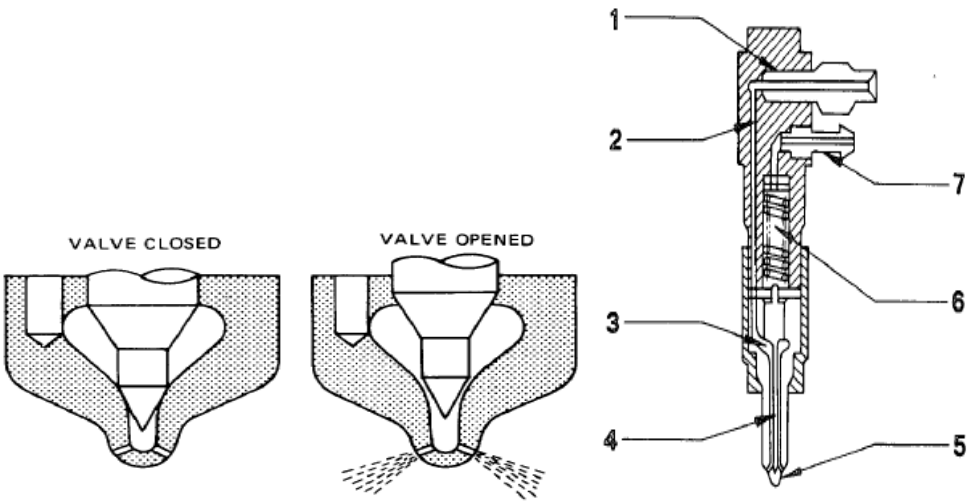

Figure 13 - Robin DY23-2D injector model (Engines, 2000).

From Figure 14, the positioning of the nozzle holes is evident. This visualization supports the assertion that a 45-degree sector is sufficient for CFD analysis.

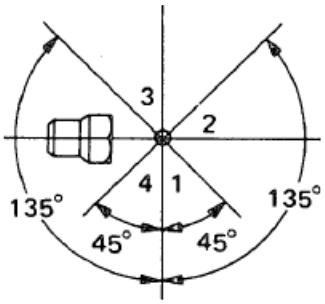

Figure 14 - Injector nozzle holes location (Engines, 2000).

The duration from the closing of the intake valve to the opening of the exhaust valve for the Robin DY23-2D spans a total of 252 crank angles, as illustrated in Figure 15.

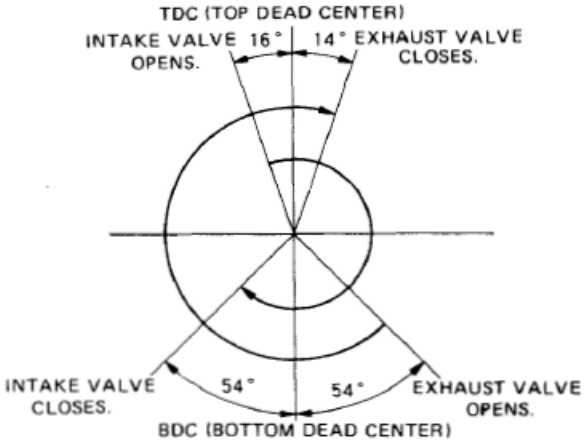

Figure 15 - Robin DY23-2D default valve timing (Engines, 2000).

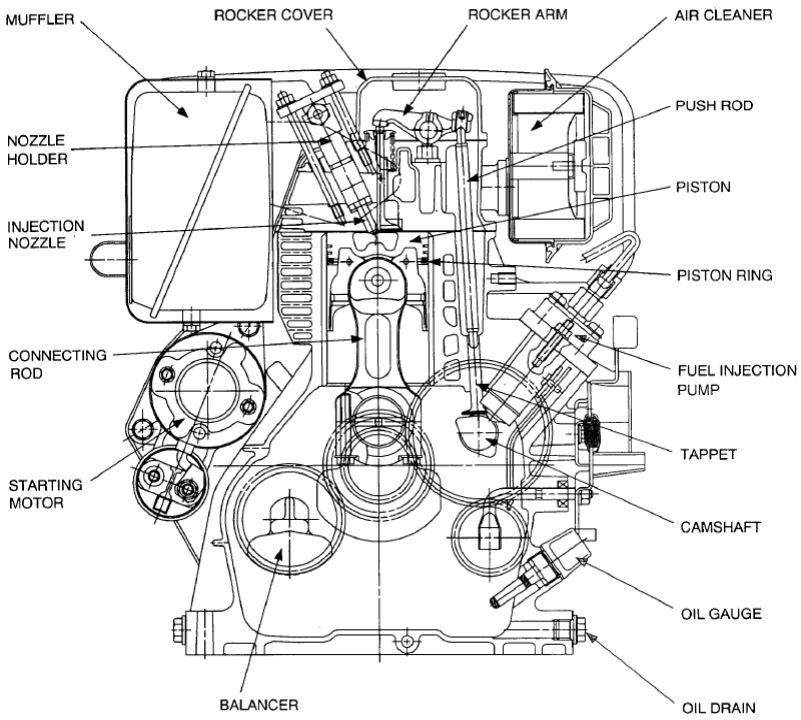

Figure 16 - Robin DY23-2D engine side view section (Engines, 2000).

A detailed side-sectional view of the Robin DY23-2D engine, illustrating all its internal components, can be seen in Figure 16.

4.2.2 Sensor and Data Acquisition Tools

4.2.2.1 Pressure Piezoelectric Sensor

A KISTLER 6125B pressure piezoelectric sensor was acquired and subsequently calibrated by the KISTLER company. The uncertainties and sensitivity associated with this sensor are detailed in Table 7.

Table 7 - Calibration Data for KISTLER 6125B Piezoelectric Sensor

Calibrated Range	Sensitivity	Uncertainty
0…..250bar	-15.64 pC/bar	±1%

4.2.2.2 Crankshaft Sensor and Rotary Disk

A four-digit digital signal encoder, which employs two sensors, was used. This encoder outputs four distinct signals, as depicted in black in Figure 17. The uncertainty value for this sensor is ± 0.25 counts.

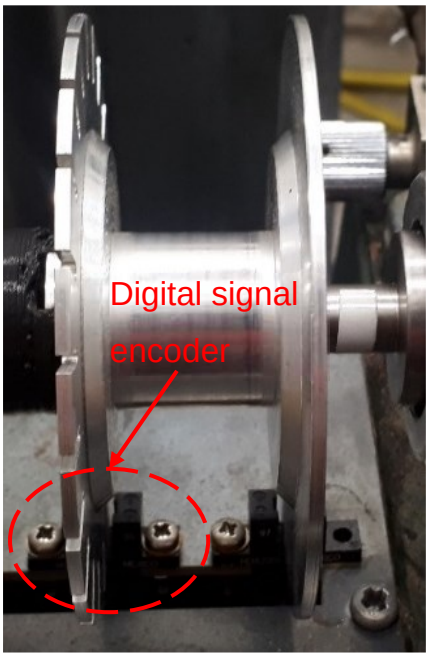

Figure 17 – Digital encoder and disk for crank angle display.

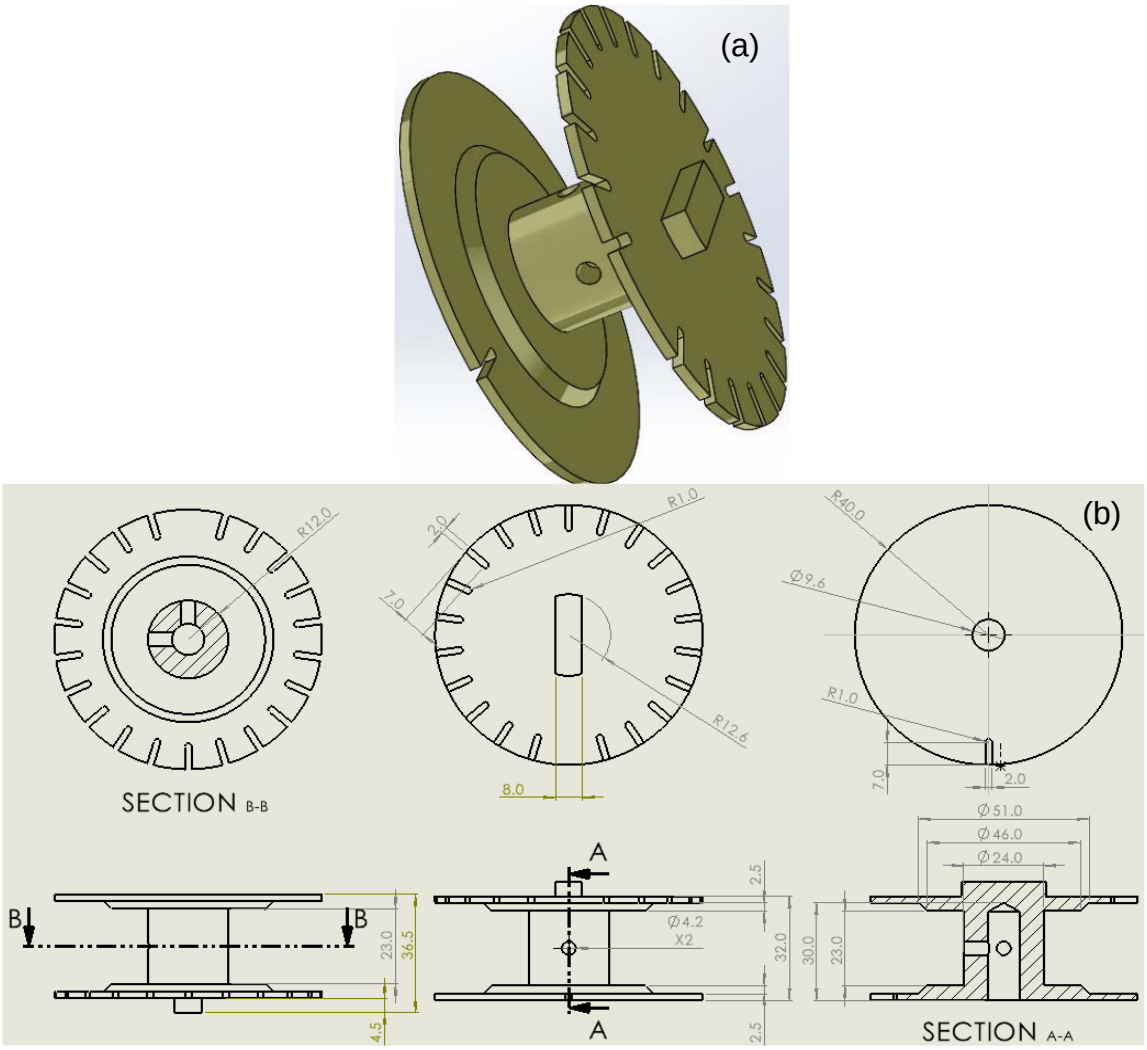

Figure 18 - a) Rotary disk design view. b) Design sketch of crankshaft rotary disk with dimensions (in mm).

A rotary disk has been fabricated to integrate a design that can simultaneously couple to the engine shaft and represent the crank angle degrees. This is achieved by sending on and off signals to the digital encoder (see Figure 18).

Furthermore, 22 holes were incorporated to represent increments of 16.36 CA over a 360-degree crank angle. As observed in Figure 18b, there are two disks: one has 21 holes, and the remaining hole is on the other disk to indicate the top dead centre of the engine. Utilising a dual-sensor system for the crank helps mitigate noise and false readings. Given the engine speed of 1300 rpm, the data collection frequency of 16000Hz, the need to prevent false or duplicate readings, and constraints on the disk diameter, the maximum number of holes that can be incorporated into the rotary disk is limited to 22.

4.2.3 Amplifier

A Bruel & Kjaer Amplifier, model 2635, is utilised in the setup. This amplifier is calibrated based on a pressure sensor sensitivity of 15.64 pC/Bar. To avoid amplifier overload and to ensure a precise output corresponding to the known pressure input to the sensor, the transducer sensitivity nodes are adjusted accordingly. The amplifier's sensitivity range spans from 0.01 mV to 10 V/pC, equivalent to −40 to +80 dB.

Equation 4.1 and 4.2 are related to the mV output and the transducer sensitivity of 15.64 pC/Bar.

$$S_P = \frac{\left({}^{\mathrm{mV}}/_{\text{Unit Out switch setting}}\right)}{\text{output unit selected on Acc.} - \text{Vel.} - \text{Displ. switch}} \tag{4.1}$$

S_P is for determining the output sensitivity for charge amplifier.

$$L_{FSD} = \frac{V_{FSD}}{S_P} \tag{4.2}$$

L_{FSD} is the signal level correspondent to full scale deflection on the indicating instrument. V_{FSD} is the voltage range set or output.

$$\text{Final pressure} = \frac{10 \times (\text{pressure converted from amplifier to KISTLER calibration} + \text{lower limit})}{(\text{higher limit} + \text{lower limit})} \tag{4.3}$$

Equation 4.3 is the final conversion from amplifier and pressure transducer conversion. Appendix A explains the calculation method.

4.2.4 Fuel Tank

A 300 ml transparent fuel tank equipped with a gauge measurement tool, marked in 10 ml increments, was used to observe the fuel quantity consumed by the engine for each individual experiment.

Based on engine configuration the injection pressure of fuel injected in combustion chamber is constant, which results in a uniform injection profile. The mass flow rate for different fuel blends under various load conditions, corresponding to a single injection cycle, is represented in Figure 19.

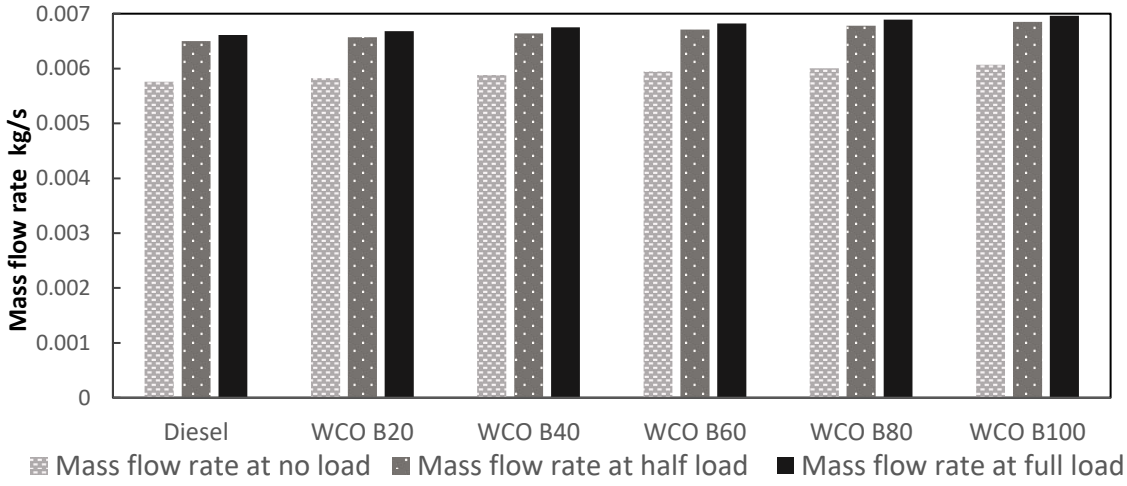

Figure 19 - Mass flow rate of different fuel blends under varying load conditions for each engine cycle.

For calculation of fuel mass flow rate, refer to Appendix B.

4.2.5 Anemometer

To measure the air velocity entering the engine's intake port, the Xplorer edition 2 anemometer was employed, which has an accuracy of ± 3% in its measurements. Notably, the diameter of the engine's intake port is 25 mm.

The air velocity is provided in Table 5, and the corresponding air mass flow rate to the engine cylinder during intake is derived using Equation 4.4.

$$v\ (^{m}/_{s}) \times A\ (m^{2}) \times \rho\ (^{kg}/_{m^{3}}) = {}^{kg}/_{s} \tag{4.4}$$

Appendix C provides more information regarding air mass flow rate calculation.

Table 8 - Engine air mass flow rate at intake port for different load conditions.

Load	Air mass flow rate
No load	$2.24\ {}^{g}/_{s}$
Half load	$2.12\ {}^{g}/_{s}$
Full load	$2\ {}^{g}/_{s}$

4.2.6 Turbomachinery Load System and Load Cell

In the engine rig configuration (refer to Appendix F), a hydraulic variable fill dynamometer is mechanically integrated with the Robin DY23-2D. The operation of this dynamometer is based on the principle that as water circulates around its vanes, it forms a toroidal vortex, resulting in a torque reaction within the dynamometer casing. This torque is countered and quantified by the dynamometer through a load cell, as depicted in Figure 22. Structurally, hydraulic dynamometers share similarities with fluid flywheels; they gauge the frictional forces between impeller vanes and the circulating liquid (refer to Figure 20). A sectional view of the rotor and stator of the employed hydraulic dynamometer is presented in Figure 21.

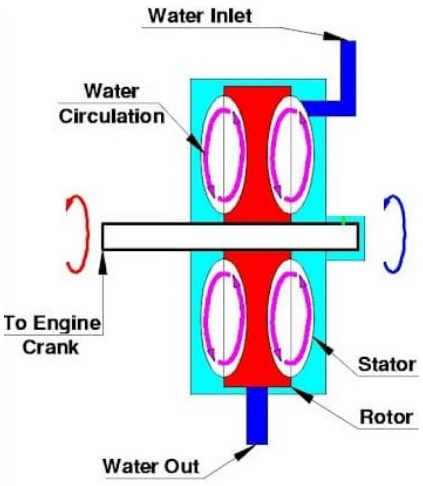

Figure 20 - Hydraulic dynamo-meter variable fill graphic demonstration.

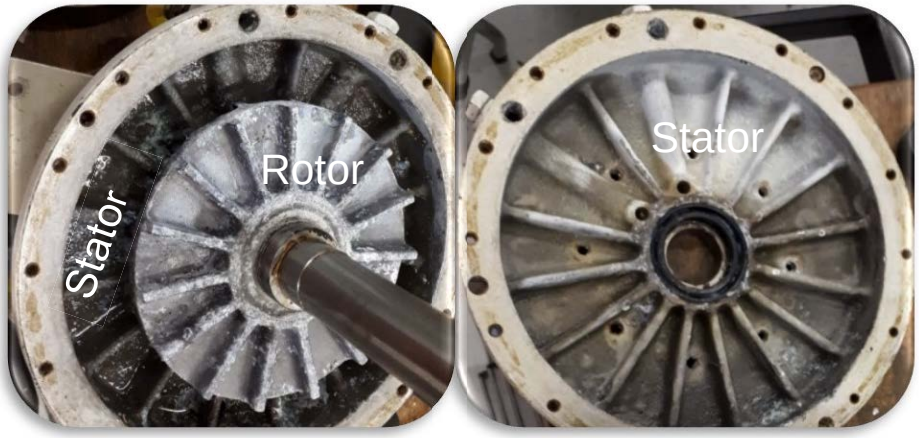

Figure 21 - Cut view of stator and rotor of hydraulic dynamo-meter variable fill, used as input load on Robin DY23-2D engine.

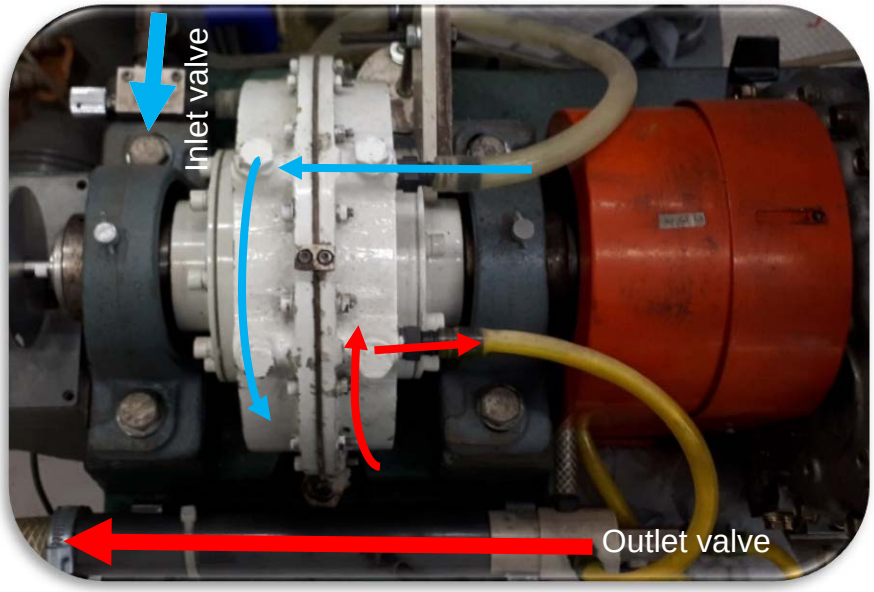

Figure 22 - Test bench water inlet and outlet of hydraulic dynamometer demonstrated.

The load cell model employed with the hydraulic dynamometer is designed with traditional springs and weight units. Figure 23 illustrates a rod affixed to the dynamometer's stator, facilitating the attachment of weight units. The primary spring and weight unit, displayed in Figure 24, allow the dynamometer's stator a reciprocal motion.

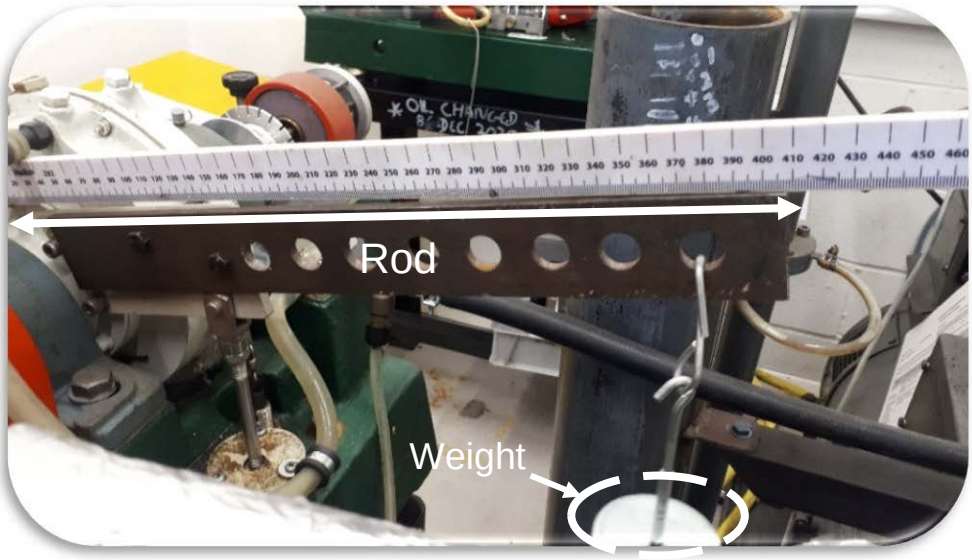

Figure 23 - Hydraulic dynamo-meter rod, weight, and distance from weight to mid of shaft.

Figure 24 - Hydraulic dynamo-meter rod, and spring load cell.

This subsequent movement characterizes the dynamometer's resistance to engine torque. As weight is added, a point is reached where the stator of the dynamometer is on the verge of lifting the weights. This point signifies the equilibrium of negative torque, which is the force acting upon the engine. Critically, this force maintains a perpendicular relationship with **r**, where **r** signifies the distance from the pivot point, a concept further elaborated in Figure 25.

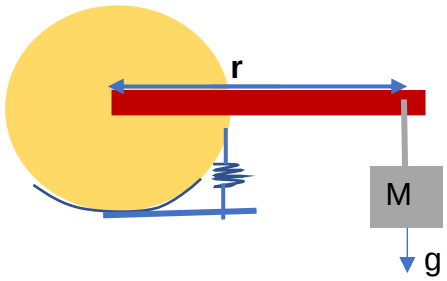

Figure 25 - Graphic representation of dynamo-meter load cell

Hence, the Equation 4.5 is used to calculate the torque.

$$\mathrm{T\ (N.m)} = \mathrm{F} \times \mathbf{r} = \mathrm{M\ (kg)} \times \mathrm{g\ (^{m}/_{s^2})} \times \mathbf{r}\ \mathrm{(m)} \qquad (4.5)$$

Further calculation is provided in Appendix D.

Experiments were conducted at a consistent engine speed of 1300 rpm across all fuel blends and load conditions. Based on the engine rig capabilities, three distinct loads were chosen: no load, half load, and full load.

The values of negative torque applied to the engine are presented in Table 9.

Table 9 - Negative load quantity on Robin DY23-2D engine

Load	Torque
No load	None applied
Half load	1.86 N m
Full load	3.73 N m

As a load is applied to the engine, its speed tends to decrease. Through fuel control adjustments, more fuel is introduced to maintain a stable 1300 rpm, especially at half and full load conditions. Nevertheless, in all experiments constant 1300 rpm, similar environment condition, and equal loads are achieved for each individual fuel.

4.2.7 Digital Tachometer

To maintain a consistent speed throughout all experiments, a digital tachometer is utilised. For accurate readings with the Lutron DT-2234B digital laser rpm tachometer, a white sticker is affixed to the rotary crank sensor shaft, as depicted in Figure 26. The accuracy of this device is ± (0.05% + 1 digit). Its display resolution

is 0.1 RPM for speeds less than 1,000 RPM and 1 RPM for speeds greater than 1,000 RPM.

Figure 26 - The tachometer is positioned close to the rotary disk to detect the white sticker, which indicates the instantaneous rpm speed of the engine.

4.2.8 NI DAQ Setup

A National Instrument NI cDAQ-9178 chassis acquisition hardware is employed for this study. This versatile hardware allows for the integration of various sensors like thermocouples, pressure sensors, and optical sensors within a singular platform. To facilitate this comprehensive setup, three distinct modules are incorporated:

- NI 9214 module: Tailored for thermocouple sensors, it has the capacity to simultaneously capture outputs from 22 different thermocouple sensors.
- NI 9215 module: Designed for pressure sensors that operate based on voltage fluctuation analog signals. This module can interpret four distinct analog signals concurrently, premised on voltage disparities. It is important to note that the pressure sensor is initially connected to the 2635 Bruel & Kjaer Amplifier for noise filtration, after which the amplified signal is relayed to this module.
- NI 9401 module: This module is crafted specifically for digital sensors, such as optical ones. It facilitates four input and four output signals. To ensure its functionality, a circuit incorporated with resistors is essential, generating an adequate current for optical sensor data acquisition.

4.2.8.1 LabVIEW Model

This software serves as a data acquisition tool, enabling researchers to collect pertinent data from various environments using specialized hardware tailored to distinct experimental settings. A model code has been introduced that facilitates the collection of data from piezoelectric pressure sensors, thermocouples, and optical crank sensors. Notably, this code employs two distinct synchronisation methods, ensuring consistent time readings across different sensors, as presented in Appendix E.

In the channel settings, three sensors are configured: pressure, thermocouple, and crankshaft optical sensor. Both the pressure and thermocouple provide analog signals, allowing them to be coupled from the start. Conversely, the optical sensor, being digital, necessitates separate reading. To facilitate this, a DAQ system provides a 5V difference to power the optical sensor. Synchronised time sampling is crucial. This is achieved by sharing a single sample clock, ensuring uniform start times. The block diagrams for these configurations can be found in Appendix E. The sampling frequency is then adjusted according to Equation 4.6, enabling data storage on the user's hard drive.

$$\text{Sample frequency } = 2 * \frac{\text{RPM}}{60} * (\text{number of holes on crankshaft} = 22) \tag{4.6}$$

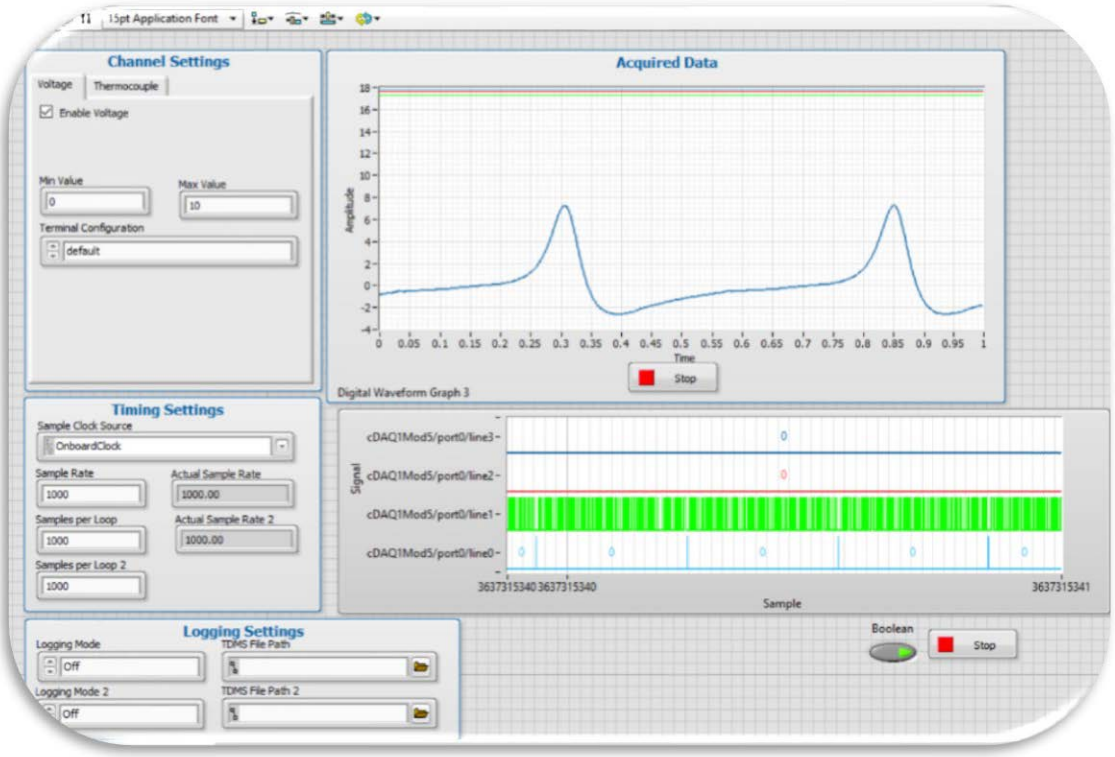

Figure 27 - Real-time data display from LabVIEW on user's monitor

While data is being written, it can simultaneously be displayed on the user's monitor by synchronising with the trigger (activated by the start button). To retrieve the data, a read function operates within a while loop, displaying both analog and digital signals on a waveform chart. This process continues until the user selects 'stop', terminating the while loop and halting the program as shown in Figure 27.

4.2.9 Bio-fuel Mixtures

Argent Energy Biodiesel company supplied a waste cooking oil biofuel derived from Soybean Methyl Ester and Methyl Tallowate. In addition, Diesel (B7), which is the most commonly used diesel in the UK, was sourced from a Shell gas station in Manchester. Blends of WCO B20, WCO B40, WCO B60, and WCO B80 were prepared by mixing volume percentages of the primary fuels (diesel and WCO B100). Using a 200 ml beaker, different mixtures of the biofuel and diesel were prepared in-house. For instance, to produce 200 ml of B20 fuel, 160ml of Diesel (B7) was combined with 40 ml of WCO B100, as illustrated in Figure 28.

Figure 28 - 200 ml of A)Diesel, B)WCO B20, C)WCO B40, D)WCO B60, E)WCO B80, and F)WCO B100

4.2.10 Horiba Emission Kit

The Horiba MEXA-584L, when operating in idle mode, is capable of measuring a range of parameters and gases. Specifically, it can determine the concentrations of CO, HC, and CO_2 using the non-dispersive infrared (NDIR) method. Additionally, it provides readings for the air-to-fuel ratio (AFR), excess air ratio (lambda), engine speed (RPM), and oil temperature (TEMP). While the device also has the capacity to measure O_2 and NOx, its primary approach for calculating AFR and lambda relies on the carbon balance method in its standard configuration, which encompasses the Brettschneider method and includes O_2 measurements. The uncertainty associated with the measurements of NOx, HC, CO, and CO_2 are ± 1.3%, ± 1.3%, ± 0.1%, and ± 3%, respectively. Correspondingly, the accuracy

for these measurements is as follows: NOx at 1 ppm, HC at 1 ppm, CO at 0.01% vol, and CO_2 at 0.02% vol.

4.3 Numerical Setup 0-D ANSYS Chemkin-Pro DI Engine

The limitations of the present version that are known are listed as below, (ANSYS, 2020a).

- The temperature of the droplets remains constant throughout the simulation.
- Constant liquid injection rate.
- There is no diffusion flame combustion mode in the example project. This results in a remarkably low fuel consumption rate of 0.25, attributed to the complete utilisation of fuel during the auto-ignition process. For the diffusion flame mode to be validated, a fuel-rich condition must be present.
- The air is contained in a single zone.
- No wall impingement model.
- There must be no mixing of the spray packets.
- The heat lost through the walls is solely associated with the air zone.

In this project, a model is utilised to represent and engage with complex chemical reaction mechanisms involving numerous species. Specifically, the model employs the detailed mechanism from the CRECK Modeling Group at Politecnico di Milano, which encompasses 482 species and 19,072 reactions (Cuoci *et al.*, 2009; Frassoldati, Faravelli and Ranzi, 2003; Ranzi *et al.*, 2015; Saggese *et al.*, 2013). This model provides an in-depth analysis of species sensitivities, making it possible to pinpoint the most critical reaction pathways for surrogate fuels.

4.3.1 Injector Model Setup

This section outlines the essential data required for configuring the injector system, ensuring optimal performance and accuracy in simulation. Key specifications include:

- The total number of holes is equal to four, and there are one total number of injections.
- The author has measured and modelled the injector using the Robin DY23-2D injector model. The placements of the holes were established using illustrations from the engine manual (Engines, 2000), with specific reference to Figure 13.

- To determine the commencement and duration of injection based on varying loads, the data presented in Figure 19 is utilised.
- The nozzle hole diameter can be found in Table 6. Other important injector attributes include the nozzle hole length-to-diameter ratio and the nozzle rounded corner radius-to-diameter ratio. The ratio for the nozzle hole length to its diameter and the ratio for the nozzle rounded corner radius to its diameter are 0.22 and 2.72, respectively, as depicted in Figure 29.
- Due to the consistent injection pressure, a uniform injection rate profile as outlined in the engine handbook is utilised (Engines, 2000).

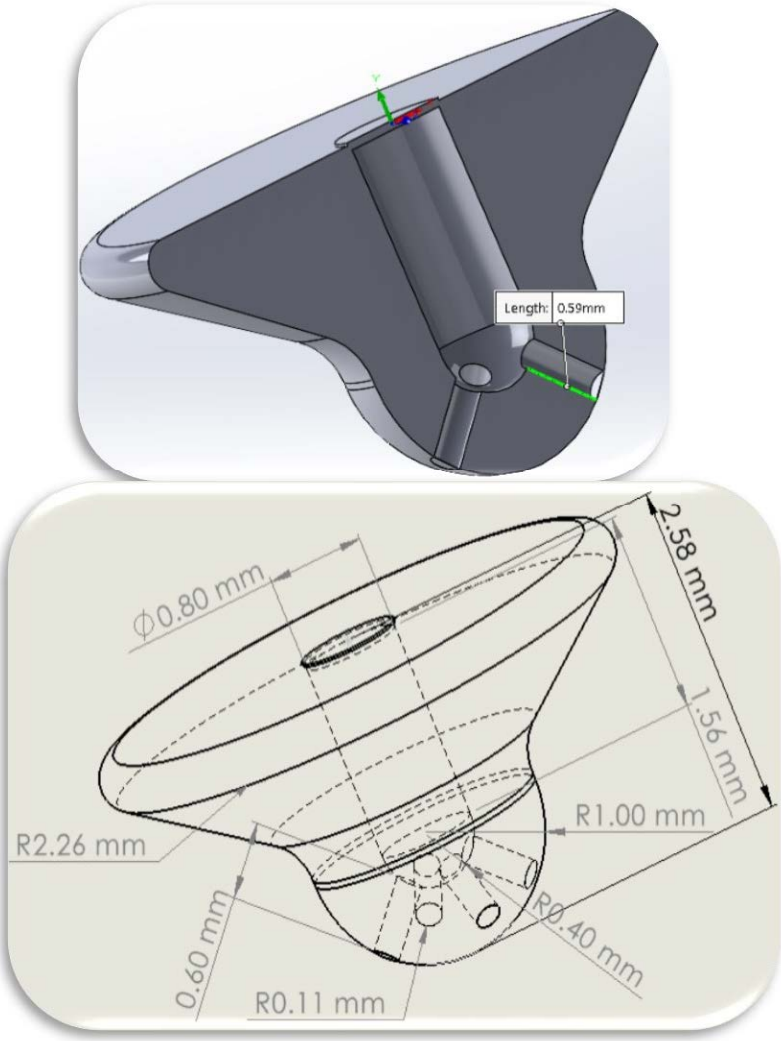

Figure 29 - The CAD design of the Robin DY23-2D injector was created based on real-size measurements.

According to the ANSYS Chemkin-Pro documentation, the number of parcels in the radial direction is set to three, while the temporal direction is set to ten (ANSYS, 2020a). This configuration arises from the specific capacity of the DY23-2D

engine's combustion chamber, which stands at 11.5 cc. The initial gas volume of the spray parcel parameter should be minimized as much as possible to optimize computational efficiency. However, it should still remain sufficiently large to avert simulation failure due to negative volumes that can occur during the compression phase. This establishes a criterion such that $3 \times 10 \times \text{parcel volume} > 11.5\,\text{cc}$, Consequently, the spray cone is segmented into three rings in the radial direction and divided into ten portions temporally. Although a finer grid can be used, the author noted a 2.56% overprediction in maximum pressure when comparing simulations with 30 zones to those with 180 zones, as shown in Figure 30. The only significant disparity was the heightened computational cost associated with the denser grid.

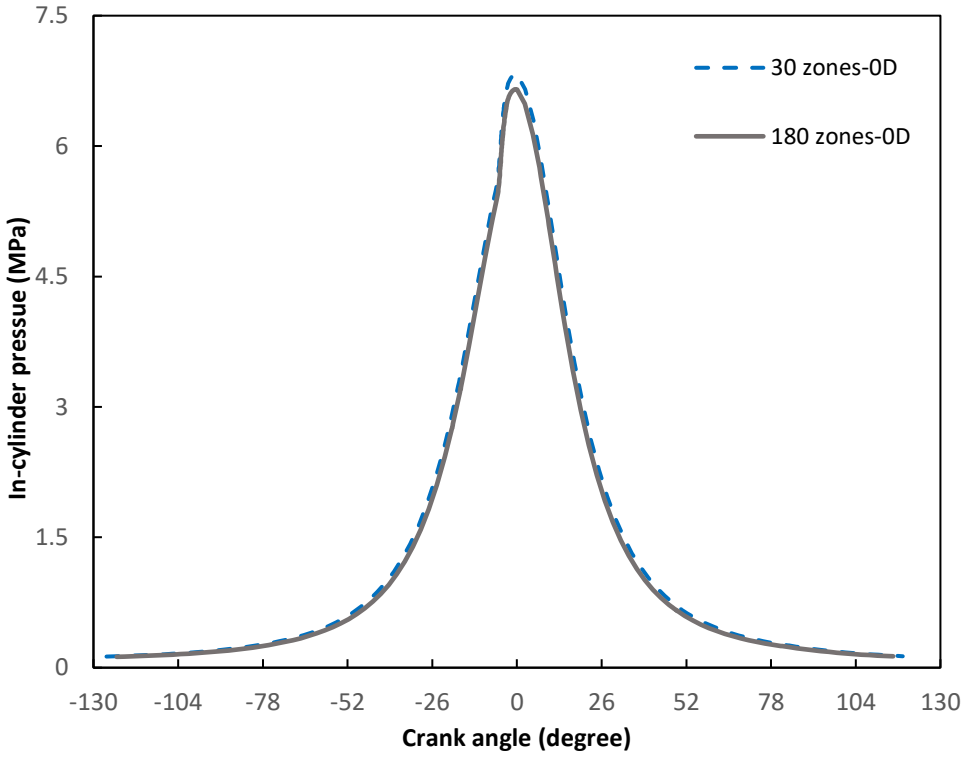

Figure 30 - Pressure vs. Crank Angle for Two Zone Configurations

For a more detailed focus on the ignition delay, combustion, and emission characteristics of diesel surrogate species, representatives such as n-alkanes, aromatics, and olefins have been used. The specific species considered are N-heptane (nC_7H_{16}), Toluene (C_7H_8), and 1-Hexene (nC_6H_{12}). These species were recommended for their emphasis on diesel combustion properties (Wang and Chen, 2017). Furthermore, the representative species for WCO B100 substitute

are derived from other significant works (Elhalwagy and Zhang, 2019; Kuti, Sarathy and Nishida, 2020; Wang and Chen, 2017).

Biodiesel combustion can be reasonably modelled using two single-bonded (saturated) components: methyl stearate (MSTEA) $C_{19}H_{38}O_2$ and methyl palmitate (MPA) $C_{17}H_{34}O_2$ Additionally, three unsaturated components have been represented, including methyl oleate (MEOLE) $C_{19}H_{36}O_2$ with one double bond, methyl linoleate (MLINO) $C_{19}H_{34}O_2$ with two double bonds, and methyl linolenate (MLIN1) $C_{19}H_{32}O_2$ with three double bonds. This modelling approach is based on findings from several studies (An *et al.*, 2013; Brakora and Reitz, 2013; Brakora, 2012; Elhalwagy and Zhang, 2019; Ismail *et al.*, 2012; Kuti *et al.*, 2013a; Kuti, Sarathy and Nishida, 2020; Mohan *et al.*, 2015; Tootoonchi and Micklow, 2016).

Table 10 demonstrates the species mass fraction used in the simulation.

Table 10 - Mass fraction of species used to represent WCO B100 and Diesel surrogate fuel model.

Specie	Diesel[a]	WCO B100[b]
N-heptane (nC_7H_{16})	0.72	0
1-Hexene (nC_6H_{12})	0.05	0
Toluene (C_7H_8)	0.23	0
(MEOLE) $C_{19}H_{36}O_2$	0	0.428
(MLIN1) $C_{19}H_{32}O_2$	0	0.103
(MLINO) $C_{19}H_{34}O_2$	0	0.355
(MPA) $C_{17}H_{34}O_2$	0	0.085
(MSTEA) $C_{19}H_{38}O_2$	0	0.029

[a]Corresponds to data detailed in the study (Wang and Chen, 2017)

[b]Is derived from (Kuti, Sarathy and Nishida, 2020).

4.3.1.1 Fuel Liquid Properties

The characteristics of fuel liquids vary with temperature changes. Based on literature reviews, the properties of n-dodecane and n-decane are commonly utilised for Diesel fuel. The ANSYS fuel library already contains diesel fuel properties, which have been selected to showcase the properties of diesel liquid.

For WCO B100, a range of liquid properties are available, both experimentally and numerically. These properties are influenced by the various feedstocks used in its production, as outlined in Chapter 2. Argent Energy Biodiesel, the provider of WCO B100, indicated that WCO B100 fuel consists of over 90% unsaturated fatty acid properties, with Methyl Soyate being the primary feedstock. Therefore, as a reference, the liquid properties available in the ANSYS fuel library for the five main species representing WCO B100 surrogate fuel have been chosen. In addition, research by various scholars that resulted in the identification of SME WCO biodiesel liquid properties has been integrated (Cheng, 2016; Cheng, Gan and Ng, 2020; Kuti, Sarathy and Nishida, 2020; Ng *et al.*, 2013; Raza *et al.*, 2020; Tootoonchi and Micklow, 2016).

Table 11 - Properties of Diesel and WCO B100 fuel

Droplet Properties	Diesel[a]	WCO B100[a]
Density ($\mathrm{kg/m^3}$)	837.7	885
Thermal conductivity($\mathrm{W/m.K}$)	0.149	0.158
Latent heat ($\mathrm{J/kg}$)	277000	229327
Surface tension (N/m)	0.02521	0.02715
Boiling point (K)	447.1	615.5[b]
Cetane number	45[c]	51[c]
Heating value ($\mathrm{kJ/g}$)	43.1[c]	39.03[c]

[a]Adapted from Ng *et al.* (2013).

[b]Corresponds to data detailed in the study (Cheng, Gan and Ng, 2020).

[c]Is derived from (Kuti, Sarathy and Nishida, 2020).

Details pertaining to the temperature-dependent liquid properties of the fuel are located in Appendix G.

4.3.2 Direct Injection Engine Batch Reactor Setup

For DI engine main reactor setup Table 6, Table 8, and Figure 19 are used for the engine specification needed. For vaporisation model droplet surface T equals to core T is selected. The assumption that the liquid temperature inside the droplet is consistent over its entirety is made by the Droplet Surface T = Core T option, which is then solved using the droplet energy conservation equation(ANSYS, 2020a; ANSYS, 2020b). The evaporation rate of a liquid component is synonymous with the mass transfer velocity of the vapour species across the interface delineating the droplet from its surrounding gaseous environment, as further detailed below:

$$\dot{m}_{vap,k} = 2\pi r_{drp}\bar{\rho}_f \bar{D}_{k,f}\left[Sh_k^* \ln(1 + \mathrm{B_{M,k}})\right] \tag{4.7}$$

The variables $\bar{\rho}_f$ and $\bar{D}_{k,f}$ represent the gas density and the mass diffusivity of the vapour species associated with the k-th liquid component within the thin film layer around the droplet, respectively.

The Spalding mass transfer number, $\mathrm{B_{M,k}}$, and the diffusional film correction factor, $F(\mathrm{B_{M,k}})$, are described as follows:

$$\mathrm{B_{M,k}} = \frac{y_{s,k} - y_{\infty,k}}{1 - y_{s,k}} \tag{4.8}$$

$$F(\mathrm{B_{M,k}}) = (1 + \mathrm{B_{M,k}})^{0.7} \frac{\ln(1 + \mathrm{B_{M,k}})}{\mathrm{B_{M,k}}} \tag{4.9}$$

The Sherwood number, Sh_k^*, for the vapour species corresponding to the k-th liquid component, is calculated as:

$$Sh_k^* = 2 + (Sh_{k,0} - 2)/F(\mathrm{B_{M,k}}) \tag{4.10}$$

$$Sh_{k,0} = 1 + \left(1 + Re_\infty Sc_{k,f}\right)^{1/3} f(Re_\infty) \qquad Re_\infty < 100 \tag{4.11}$$

$$Sh_{k,0} = 2 + 0.552 {Re_\infty}^{1/2} {Sc_{k,f}}^{1/3} \qquad Re_\infty \geq 100 \tag{4.12}$$

Table 12 - Definitions and Units of Variables Used in Equations 4.7 to 4.12

Name	Variable
Vaporisation rate of the vapour species associated with the k-th liquid component within the thin film layer enveloping the droplet (kg/s).	$\dot{m}_{vap,k}$
Radius of the droplet (m)	r_{drp}
Mass fraction of the vapour species corresponding to the k-th liquid component at the droplet surface.	$y_{s,k}$
Mass fraction of the vapour species corresponding to the k-th liquid component in the bulk gas.	$y_{\infty,k}$
Reynolds number of the bulk gas	Re_{∞}
Schmidt number for the vapour species associated with the k-th liquid component within the thin film layer enveloping the droplet.	$Sc_{k,f}$

Note that f(Re) at Re 1 and f(Re)=$Re^{0.077}$ at Re<100.

The central temperature of the droplet, T_d, is determined by employing the energy conservation equation as outlined below:

$$\left(\sum_k m_{L,k}\right)\bar{C}_{p_L}(T_d)\frac{dT_d}{dt} = \left(\sum_k \dot{m}_{vap,k}\right)\left(\bar{C}_{p_L}(T_d)T_d - \bar{C}_{p_L}(T_s)T_s\right) + \left(\dot{Q}_0 - \sum_k \dot{m}_{vap,k}\,\Delta H_{vap,k}\right) \quad (4.13)$$

Under the assumption that the droplets are adiabatic (with wall heat loss affecting only the air zone and not the droplets) and given that the droplet surface temperature is the same as its core temperature, $\dot{Q}_0$(representing heat transfer into the droplet) should be zero. With these conditions, Equation 4.13 simplifies as follows:

$$\left(\sum_k m_{L,k}\right)\bar{C}_{p_L}(T_d)\frac{dT_d}{dt} = -\sum_k \dot{m}_{vap,k}\,\Delta H_{vap,k} \quad (4.14)$$

Where $m_{L,k}$ represents the mass of the k-th liquid component in kg, and $\bar{C}_{p_L}(T_d)$ is the specific heat capacity of the liquid phase at the droplet core temperature T_d with a unit of J/kg·K. Furthermore, $\bar{C}_{p_L}(T_s)$ denotes the specific heat capacity of the liquid phase at the droplet surface temperature T_s. Lastly, $\Delta H_{vap,k}$ is referred to as the latent heat of vaporisation for the k-th component.

For heat transfer model the dimensional heat transfer correlation is used as defined below:

$$Q_{\text{wall}} = hA(T - T_{\text{wall}}) \tag{4.15}$$

$$h = a\mathrm{P}^{b}w^{b}D_{B}^{b-1}T^{c} \tag{4.16}$$

The heat transfer area, denoted as A, encompasses both the cylinder walls, which vary with time, and the end surfaces, approximated as $\pi D_B^2/4$. The cylinder pressure,P, is measured in kPa, while the characteristic gas velocity, w, and the bore diameter, D_B, are given in m/sec and m respectively. The unit for the heat transfer coefficient, h, stands at W/m^2 K. The cylinder wall temperature, denoted as T_{wall}, along with constants a, b, and c, are user specified values. The recommended constants for a, b, and c in direct injection diesel engine condition are 25, 0.8, and 1, respectively (ANSYS, 2020a; ANSYS, 2020b).

Before any spray parcel contacts the cylinder wall or undergoes auto-ignition, the wall heat transfer effect is applied exclusively to the air zone (ANSYS, 2020a; ANSYS, 2020b). Upon a spray parcel's collision with the cylinder wall, heat interaction ensues between the two. Notably, the wall heat transfer coefficient remains consistent across all spray parcels and the air zone (ANSYS, 2020a; ANSYS, 2020b). This model presupposes a proportional relationship between the parcel's volume and its heat transfer surface area. Importantly, in the Ansys Chemkin-Pro DI engine model, spray parcels cannot have zero volume, as they are conceptualised as reactors or zones (ANSYS, 2020a). One can modify the parcel volume using the 'Initial Gas Volume of Spray Parcels' parameter in the DI engine simulation. This parameter aligns the parcel volume proportionally to both the initial cylinder volume and the number of spray parcels. By default, this initial zone or parcel volume is set at $0.1\ \mathrm{cm}^3$ (ANSYS, 2020a). The objective here is to adjust the initial parcel volume to achieve the desired equivalence ratio evolution within the spray parcel. As for the reactant species, oxygen and nitrogen are introduced as oxidisers with molar fractions of 0.21 and 0.79, respectively.

Boundary conditions, as detailed in Table 13, were set to align with experimental data, specifically to achieve similar maximum pressure and ignition start points.

Table 13 - Boundary condition used for numerical modelling.

Properties	Value and Unit
Initial temperature	300 K
Initial pressure	1 bar
Piston crown temperature	600 K
Cylinder wall temperature	500 K
Cylinder head temperature	600 K
Initial gas volume of spray parcels	0.5 cm^3
Minimum air zone mass	20 g

4.4 Numerical Setup 3D-CFD

A sector IC engine model, as detailed in section 3.2.1, is selected for this study. The simulation duration spans from -126 CA to +126 CA, primarily based on the engine specifications outlined in Figure 15 and Table 6. Relevant details regarding the fuel mass flow rate, experimental initial conditions, air mass flow rate, boundary conditions, and liquid droplet properties can be found in Figure 19, Table 5, Table 8, Table 13, and Table 11, respectively, with additional information provided in Appendix G.

4.4.1 Geometry CAD

To facilitate the ANSYS Fluent sector combustion analysis, an accurate representation of the engine piston profile is essential. Therefore, a detailed replica is crafted using SOLIDWORKS. The injector's placement in actual engine conditions is juxtaposed with the CAD model assembly showcased in Figure 31.

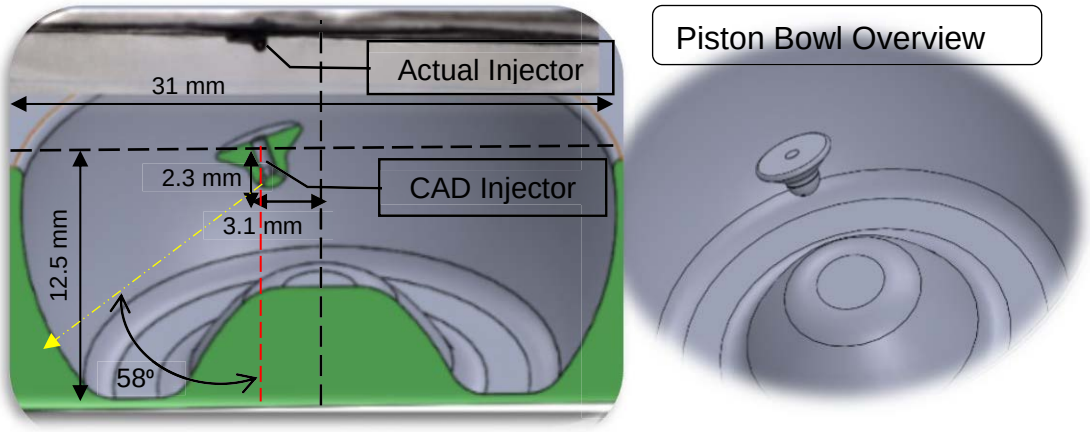

Figure 31 - Injector Placement: Robin DY23-2D vs. CAD Design

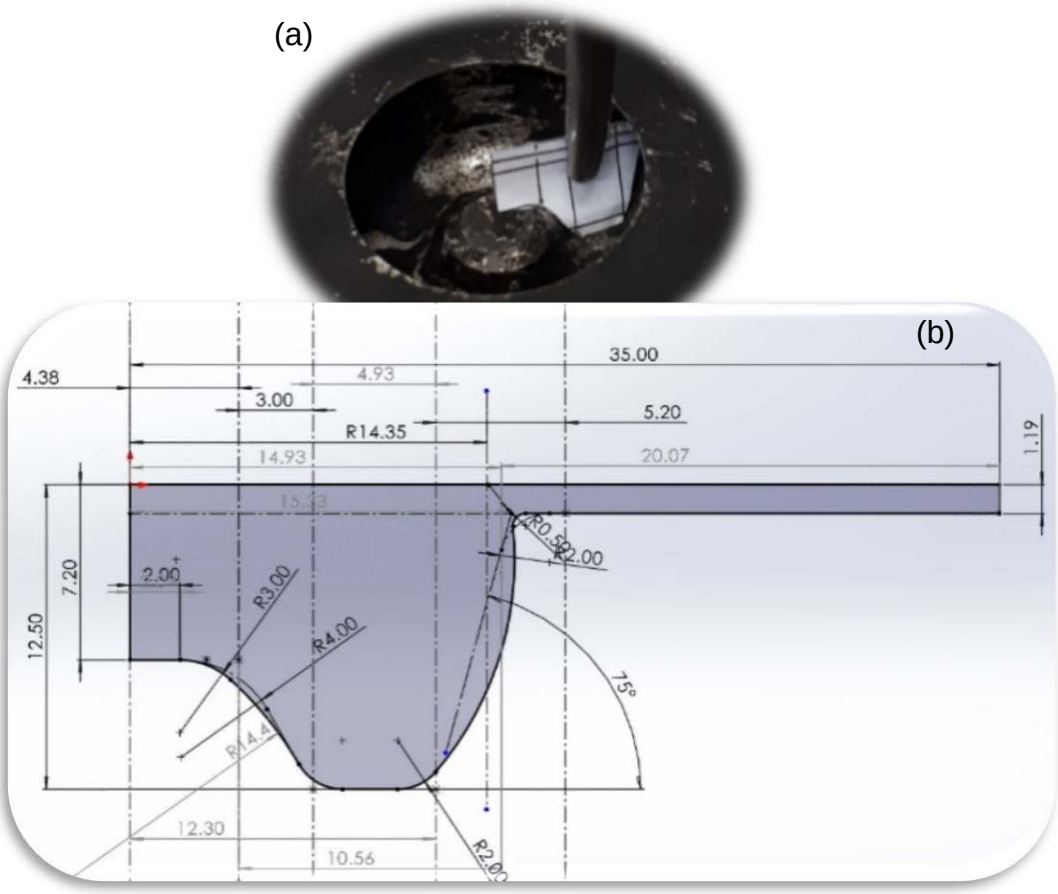

Figure 32 - a) Profile Fit in Robin DY23-2D Piston and b) Dimensional Schematic (in mm and degrees).

Figure 32 showcases the latest and most accurate CAD representation of the piston profile geometry. Due to its precision, it is employed in ANSYS Fluent as a dynamic moving profile.

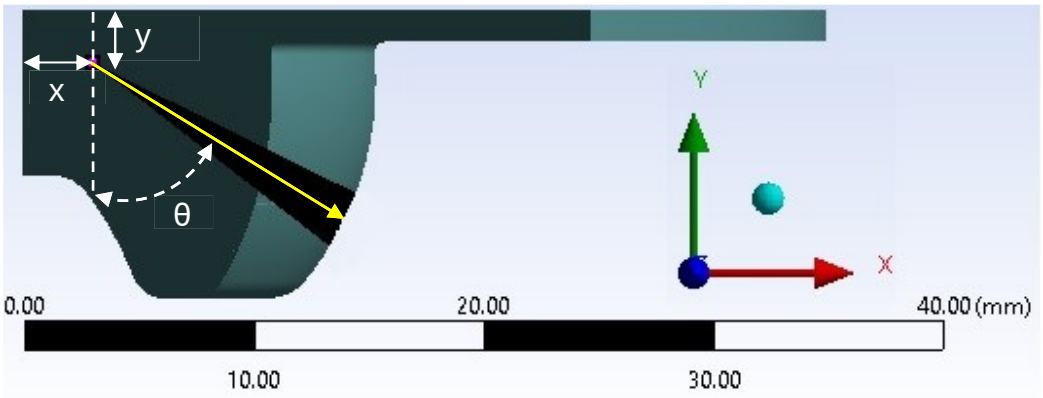

Figure 33 – In the ANSYS Fluent representation, the location of the spray point is denoted by specific coordinates. Here, 'x' symbolises the spray radius, 'y' represents the spray height, and Θ indicates the spray angle.

Table 14 provides the coordinates of the injector as illustrated in Figure 33, further elaborated upon in Figure 31, based on the actual engine configuration.

Table 14 - Coordinates of Spray Position in ANSYS Fluent

Spray	
Spray location height	$2.3\ mm$
Spray location radius	$3.1\ mm$
Spray angle	$58°$

4.4.2 Mesh

In ANSYS Fluent, the mesh quality is determined by two vital parameters, which are elaborated upon below:

1) Skewness. According to guidelines from ANSYS, the maximum acceptable skewness value is 0.96, with zero being the ideal (ANSYS, 2020d). Achieving a lower average skewness value is preferable. There are various strategies to meet this goal. For instance, one can attempt to refine the mesh. However, sometimes the model's geometry itself presents challenges that obstruct the attainment of an ideal skewness value. In such cases, it may be more effective to modify the CAD model directly. Given the potential issues with skewness and dynamic meshing, a hexahedral mesh is often the most reliable choice. Hexahedral meshes offer greater accuracy, computational efficiency, and are less prone to errors like negative volumes, particularly in dynamic mesh scenarios (ANSYS, 2020d).
2) Orthogonal quality: This parameter measures how closely the shape of the mesh elements approximates a perfect tetrahedron. The scale ranges from zero to one, with one being the ideal. Striving for a value close to one is recommended (ANSYS, 2020d).

In an in-depth study aimed at determining the optimal number of fine mesh elements while considering both computational time and result accuracy, a light-duty diesel engine with an extra 31 cc chamber volume, as compared to the Robin DY23-D model, was analysed. Various spatial resolutions were assessed for grid independence. The selected mesh for the Cheng (2016) study had a grid size of 1.5 mm and achieved an over-prediction of just 1.5%, while requiring a computational time of 60 hours. By comparison, a fine mesh with a grid size of 1 mm closely captured the experimental in-cylinder pressure profile but necessitated

a 70-hour computational run-time. Meanwhile, a coarse mesh with a 2.5 mm grid size resulted in an over-prediction of 7.2% (Cheng, 2016). Consequently, this study ultimately chose a mesh comprised of 674,000 elements and a very fine mesh with 1.6 million elements for further analysis. The respective quality reports and mesh density images at the inlet valve opening are presented in Table 15 and Figure 34.

Table 15 - Mesh quality report for two main mesh representatives

Properties	674k element mesh	1.6M element mesh
Max Skewness	0.66	0.69
Average Orthogonal quality	0.98	0.9751
Average Skewness	0.0386	0.0767

Figure 34 - Presentation of two distinct mesh strategies: a) comprising 674 thousand elements, and b) featuring a significantly greater quantity of elements, totalling 1.6 million.

Figure 35 presents a comparative analysis of pressure versus crank angle based on two different mesh resolutions in a combustion study simulation. Specifically, the mesh with 1.6 million elements necessitated a computational time of 60 hours using 95 logical CPU processors, whereas the 674,000-element mesh required approximately 18 hours.

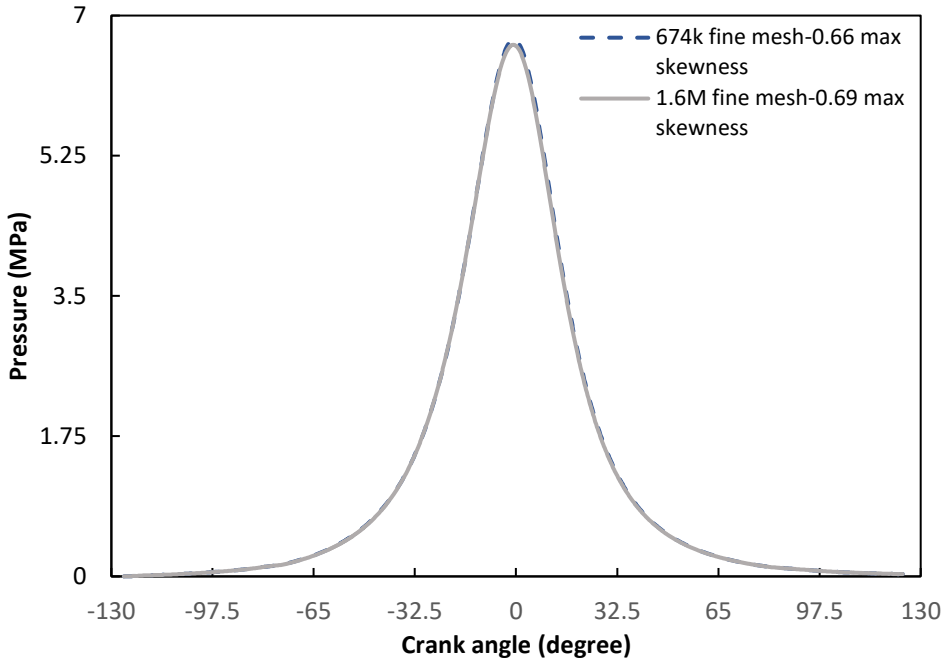

Figure 35 - Pressure vs. Crank Angle for Two Fine Mesh Elements

Figure 35 shows that the outcomes of both mesh approaches are nearly identical, with a marginal overprediction of 0.91% observed in the 674k element mesh. Moreover, simulations with the 674k element mesh require approximately 30% of the computational time needed for a mesh containing 1.6M elements. Consequently, the 674k element mesh is the preferred choice for this study.

4.4.3 Discrete Phase Model (DPM)

In the computational fluid dynamics (CFD) model study, the ERC-MultiChem plus Bio mechanism, consisting of 69 species and 204 reactions, is employed to simulate surrogate species for Diesel and WCO B100 fuels, as elaborated in Section 2.7.1. For diesel fuel, N-heptane (C_7H_{16}) serves as the surrogate, while bio-diesel combustion is represented through a combination of Methyl Decanoate (MD), Methyl-9-Decenoate (MD9D), and N-heptane. The ratios of saturated to unsaturated methyl esters in the simulated biodiesel are specified by the concentrations of MD and MD9D, as detailed in Table 16. Subsequently, the properties of the N-heptane surrogate are calibrated to closely match the molecular mass, heating value, and fuel-bound oxygen concentration of the real experimental diesel fuel.

Table 16 - Mass fraction of surrogate Diesel and WCO B100 fuel representative species in CFD study,(Kuti, Sarathy and Nishida, 2020).

Species	Diesel	WCO B100
N-heptane	1	0.51
MD9D	0	0.43
MD	0	0.06

4.4.3.1 Spray Cone Angle

The study involved injecting fluid into a system and employing a Computer-Aided Design (CAD) model to simulate the injector's behaviour. The objective was to observe the area covered by the fluid and to determine the necessary spray cone angle for the initial conditions of the discrete phase model's injection settings.

The geometry that was produced is the result of combining the location of the piston during injection with the position of the injector in accordance with the specifications for the Robin DY23-2D engine. The operating study condition is based on a model called the Volume of Fluid (VOF), which describes the interaction of air and diesel fuel as a two-phase flow. The initial boundary conditions that were imposed are detailed in Table 17.

Table 17 - VOF study boundary conditions input

Conditions	
Injection pressure	$19.1\ \mathrm{MPa}$
Injection mass flow rate	$0.00569\ \mathrm{kg/s}$
In-cylinder condition	$2.12\ \mathrm{MPa}$

Figure 36 presents the results of the Volume of Fluid (VOF) study, revealing that for the designated nozzle, the expected spray cone angle is 23 degrees, extending from the injector tip to a point near the piston wall. Accordingly, the effective radius of the spray cone angle is calculated to be half of the initial value, at 11.5 degrees.

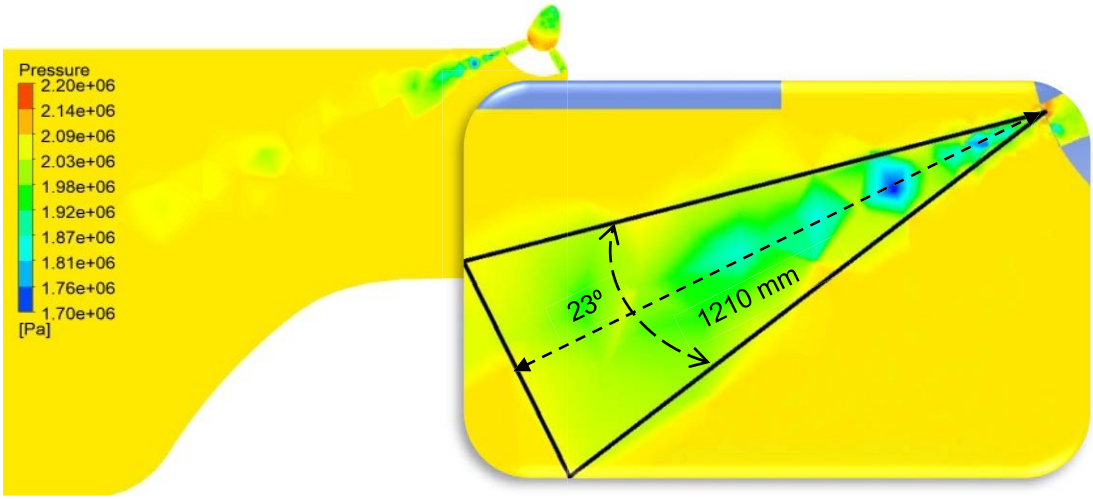

Figure 36 - Study on spray cone angle for initial condition inputs in ANSYS Fluent's Discrete Phase Model (DPM) injector.

4.4.3.2 KH-RT Breakup Model

As outlined in Section 3.2.9.1, the coefficients k_c, B_1, s, k_ε, and C_{bl} essential for the Kelvin-Helmholtz Rayleigh-Taylor (KHRT) model to yield accurate results are 0.61, 18, 0.5, 2.5, and 30, respectively. Key parameters integral to the spray model include the discharge coefficient C_d, the velocity coefficient C_v, and the contraction coefficient C_a. The discharge coefficient C_d is calculated using Equation 4.17, as detailed by Som *et al.* (2010).

$$C_d = \frac{{M_{actual}}^*}{\dot{M_{th}}} = \frac{{M_{actual}}^*}{A_{th}\sqrt{2\rho_{\mathrm{fluid}}\Delta P_b}} \tag{4.17}$$

In the Equation 4.17, ${M_{actual}}^*$ represents the mass flow rate injected from the nozzle, while ΔP_b denotes the pressure differential between the back pressure and the nozzle pressure within the injector. A_{th} is the surface area of the nozzle hole. Upon determining the required C_d for WCO B100, the ANSYS Fluent software dynamically utilises this value based on the mass flow rate and velocity at that specific time to calculate the velocity coefficient C_v (ANSYS, 2020c; ANSYS, 2020d). To predict the contraction coefficient C_a, Equation 4.18 is employed.

$$C_a = \frac{C_d}{C_v} \tag{4.18}$$

This provides a comprehensive framework for modelling the injector dynamics within the simulation. Hence, for the specific WCO B100 a discharge coefficient is calculated as below:

$$\frac{M_{actual}{}^{*}}{A_{th}\sqrt{2\rho_{fluid}\Delta P_b}} = \frac{0.006\,3\ {}^{Kg}/_{s}}{\left(\pi * 0.00022^{2}/_{4}\right) * \sqrt{2 * 885 * 10^{6} * 19.1}} = 0.901 \approx 0.9$$

The Sauter mean diameter (SMD) for the specific WCO B100 is calculated to be 93.75μm, as proposed in previous research (Kuti, Nishida and Zhu, 2013). The SMD is defined as the diameter of a hypothetical sphere that has the same volume-to-surface-area ratio as the particle in question (Som *et al.*, 2010).

To model fluid parcel injection, a set of assumptions is employed. For primary breakup, a 'blob' parcel close to the cone centre is considered. This implies that the first parcel ejected from the nozzle has a diameter identical to that of the orifice hole. For secondary breakup, the study utilises the Rosin-Rammler distribution concept. Within the liquid core, only aerodynamic forces are accounted for in terms of breakup mechanisms. Outside the liquid core, both Kelvin-Helmholtz (KH) and Rayleigh-Taylor (RT) instabilities are taken into account. This is particularly relevant for sprays with high Weber numbers, where RT instability rises at a faster rate due to high droplet acceleration. In any scenario, a new parcel is not generated until the mass of the cumulatively shed parcels exceeds 5% of the mass of the originating parcel.

The Rosin-Rammler distribution leverages a cumulative probability function that incorporates a gamma function (Γ), which is essential for determining the radius of subsequently injected droplets. The key parameter in this function is q_rr, an empirical constant that influences the shape of the distribution curve to align with the observed physical processes. This parameter can take on a range of values; for example, a value of 1 results in an exponential decay, while higher values such as 2, 3, or 4 produce distributions with varying degrees of skewness. The Rosin-Rammler distribution also introduces the Equation 4.19, which employs the Sauter mean radius as an internal parameter. For additional details, readers are referred to the ANSYS Fluent 20.2 manual (ANSYS, 2020c; ANSYS, 2020d) .

$$R(r) = 1 - exp\left[-\left(\frac{r}{\Gamma(1 - {q_{rr}}^{-1})r_{SMD}}\right)^{q\_rr}\right] \tag{4.19}$$

4.4.4 CFD Models Implementation

In conclusion, Figure 37 illustrates the models introduced in Chapter 3 and elaborates on the information discussed in Section 4.4. These models and information are utilised to initiate the ANSYS Fluent Sector IC Engine CFD simulation, and to demonstrate the implementation of the pressure-based solver.

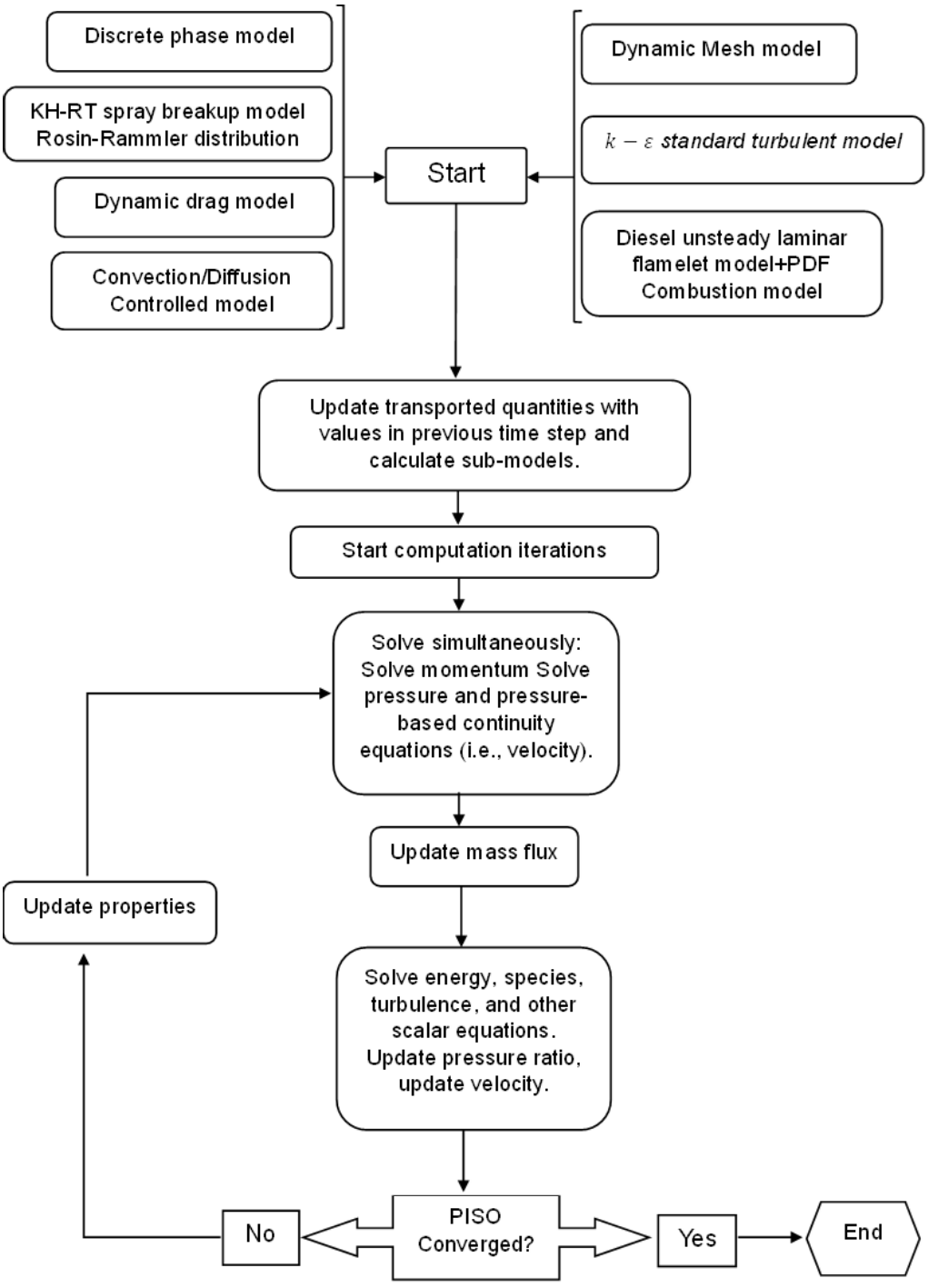

Figure 37 - An overview of the core concepts behind a CFD simulation run.

Chapter 5 – Combustion Characteristics

5.1 Introduction

This chapter begins with a validation of numerical studies focused on pressure changes related to crank angle variations. Following the validation, an in-depth examination is undertaken on the combustion characteristics and ignition delays of various fuels, specifically Diesel, Waste Cooking Oil (WCO) Biodiesel (B100), and four unique fuel blends.

The scope of the analysis is expanded to include the efficiency with which these fuels combust, as well as their thermal efficiency. Additionally, the chapter offers a comparative study aimed at linking the observed behaviours in combustion to the inherent physical and chemical properties of the fuels. This involves an investigation into how the molecular structures of these fuels influence their combustion characteristics.

The overarching aim of this chapter is to provide a comprehensive understanding of how different fuels perform in an engine, from ignition to efficient energy conversion, whilst also exploring the underlying factors that contribute to these behaviours.

5.2 Formulaic Approaches to Combustion Metrics

5.2.1 Heat Release Rate

Equation 5.1 is utilised to calculate the apparent heat release rate from data collected in the pressure-versus-crank-angle experiment (Heywood, 2018).

$$HRR = \frac{\gamma - 1}{\gamma} \mathrm{P} \frac{d\mathrm{V}}{d\theta} + \frac{1}{\gamma - 1} \mathrm{V} \frac{d\mathrm{P}}{d\theta} \tag{5.1}$$

Where θ is the crank angle and is γ the specific heat ratio assumed to be constant 1.33, V is the cylinder volume, P is the in-cylinder pressure.

5.2.2 Ignition Delay

In this study, the approach to representing ignition delay is defined based on Section 2.4 and Figure 5. Specifically, ignition delay is measured as the time interval from the start of injection (SOI) to a notable increase in the pressure gradient, denoted as $dP/d\theta$ at its maximum value. This corresponds to an

inflection point on a pressure-crank angle graph. For the purposes of this study, the SOI occurs at -23 crank angle degrees before top dead centre.

5.2.3 Combustion Efficiency

It is suggested that the efficiency of the combustion process improves with the addition of more surplus air, up to a certain threshold (Vallero, 2019). Beyond this threshold, if the excess air surpasses the level at which heat loss becomes significant, the net efficiency begins to decline. This relationship is illustrated in Figure 38.

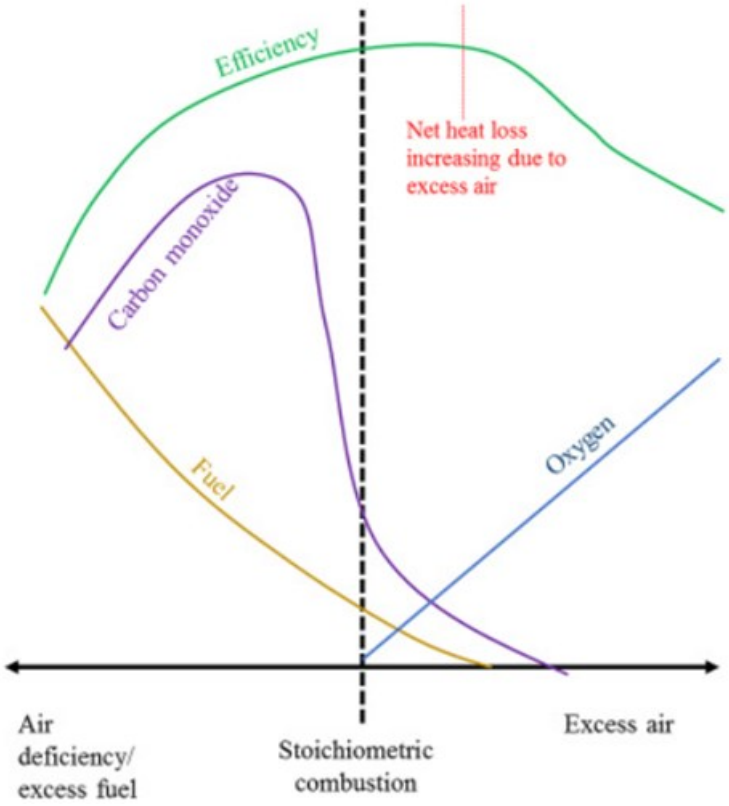

Figure 38 - Effect of air-fuel ratio on combustion efficiency and carbon monoxide production, (Vallero, 2019).

$$\text{Combustion efficiency} = \frac{\text{mass or ppm } CO_2}{\text{mass or ppm } CO_2 + \text{mass or ppm} CO} \times 100 \quad (5.2)$$

5.2.4 Thermal Efficiency

According to the literature, in the diesel cycle, the in-cylinder pressure before injection and after combustion is assumed to be equal, as this is the period during which the fuel is absorbing heat (Heywood, 2018). Consequently, the thermal efficiency of the diesel cycle is calculated using empirical Equation 5.3.

$$1+\frac{1}{\gamma}\left\{\frac{1}{\left(\frac{{r_c}^{\gamma}}{r_e}\right)-{r_c}^{\gamma-1}}-\frac{1}{{r_e}^{\gamma-1}-\left(\frac{{r_e}^{\gamma}}{r_c}\right)}\right\} \quad (5.3)$$

Here, γ represents the specific heat ratio, which is assumed to be 1.33, as suggested for the majority of fuels during the combustion period (Heywood, 2018). Additionally, r_c stands for the compression ratio, and r_e denotes the expansion ratio.

5.3 Validation and Results discussion

The approach to validation relies on in-cylinder pressure versus crank angle graphs. Key parameters such as peak pressure, the gradient of pressure relative to the crank angle, and the timing of injection are considered. An analysis of the heat transfer rate between CFD simulation and experimental data is conducted using Equation 5.1. Graphs depicting pressure validation under no load, half load, and full load conditions are shown in Figure 39, Figure 41, and Figure 43, respectively. Maintaining a consistent pressure gradient pattern across all fuels and load conditions, in accordance with experimental data, enables the study of spray penetration length. This is based on validation from the Start of Injection (SOI), which is at -23 crank angle degrees before top dead centre, up to the end of injection.

Figure 40, Figure 42, and Figure 44 present comparisons of Heat Release Rate (HRR) between experimental data derived from pressure graphs and CFD simulations. It is observed that the timing of maximum HRR in the experimental data is close to Top Dead Centre (TDC), which causes the maximum pressure point to shift past TDC, as shown in Figure 39, Figure 41, and Figure 43. Based on Figure 40, Figure 42, and Figure 44, the ignition starting points for the six different fuels are in the following order: WCO B100> WCO B80> WCO B60> WCO B40> WCO B20> Diesel. This indicates that WCO B100 experiences an earlier start of combustion.

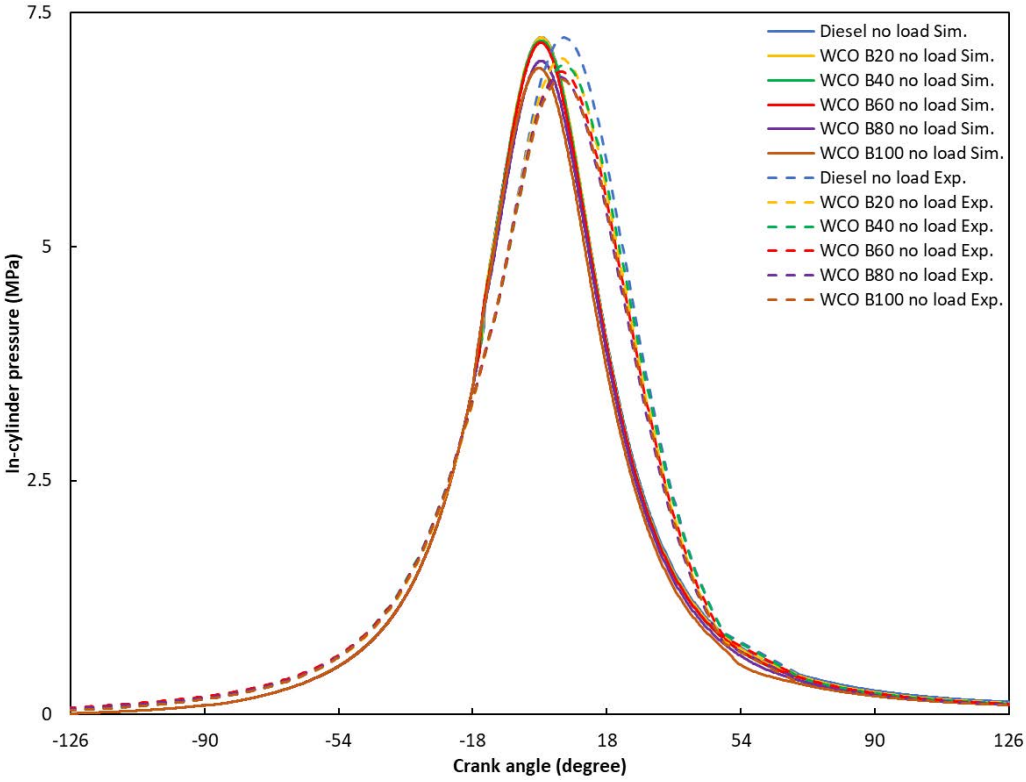

Figure 39 – CFD and experimental validation of in-cylinder pressure against crank angle at no load condition.

In Figure 39, overprediction of max pressure is quantified as percentage errors of 0.05%, 3.18%, 3.77%, 4.54%, 2.46%, and 1.69% for Diesel, WCO B20, WCO B40, WCO B60, WCO B80, and WCO B100, respectively.

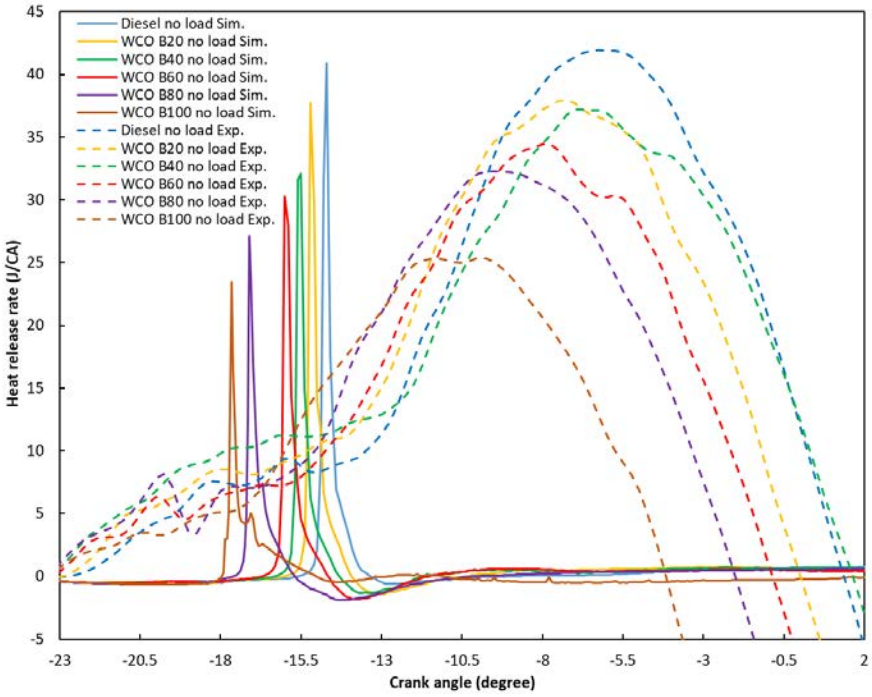

Figure 40 - CFD and experimental analysis of Heat Release Rate (HRR) against crank angle at no load condition (experiment data are extracted based on Equation 5.1).

In Figure 40, underprediction of max HRR is quantified as percentage errors of 2.42%, 0.63%, 13.7%, 12.1%, 16%, and 7.5% for Diesel, WCO B20, WCO B40, WCO B60, WCO B80, and WCO B100, respectively.

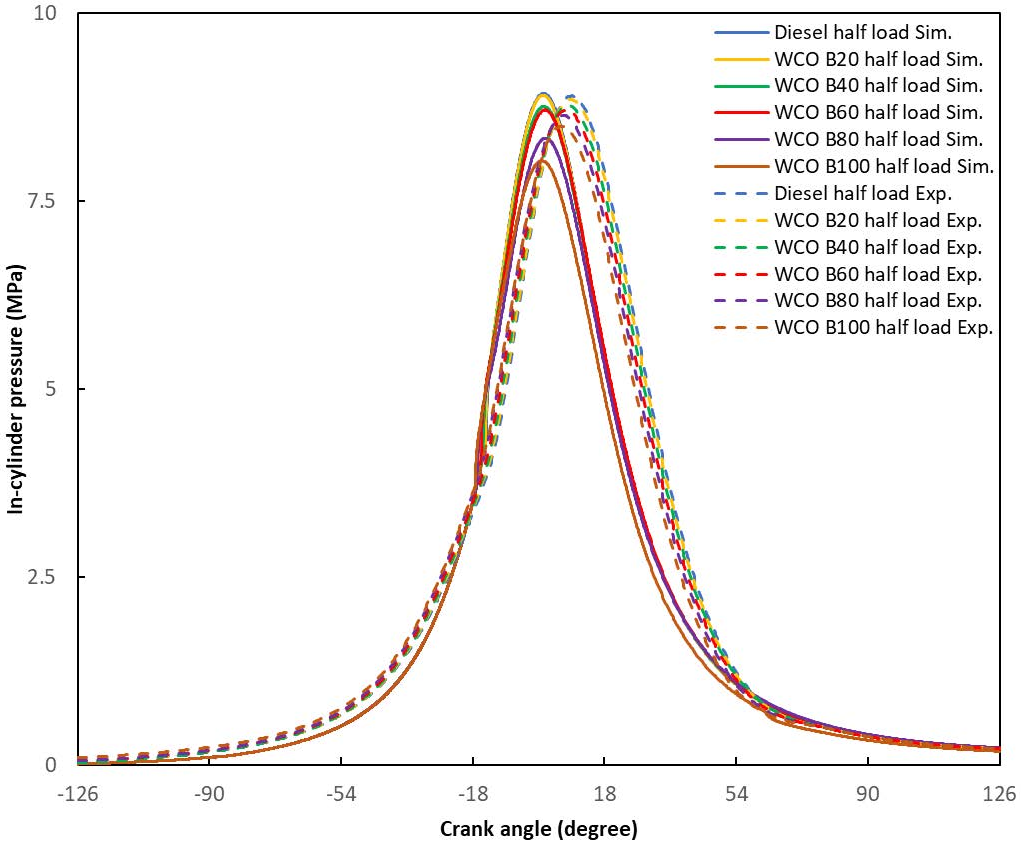

Figure 41 – CFD and experimental validation of in-cylinder pressure against crank angle at half load condition.

In Figure 41, overprediction of max pressure is quantified as percentage errors of 0.38% for Diesel and 0.7% for WCO B20. Conversely, underprediction of max pressure is represented as percentage errors of 0.15% for WCO B40, 0.02% for WCO B60, 3.47% for WCO B80, and 5.36% for WCO B100.

Overprediction of max HRR is quantified as percentage errors of 19.2%, 7.7%, 1.8%, 2.15%, 3.37%, and 3.6% for Diesel, WCO B20, WCO B40, WCO B60, WCO B80, and WCO B100, respectively as achieved in Figure 42.

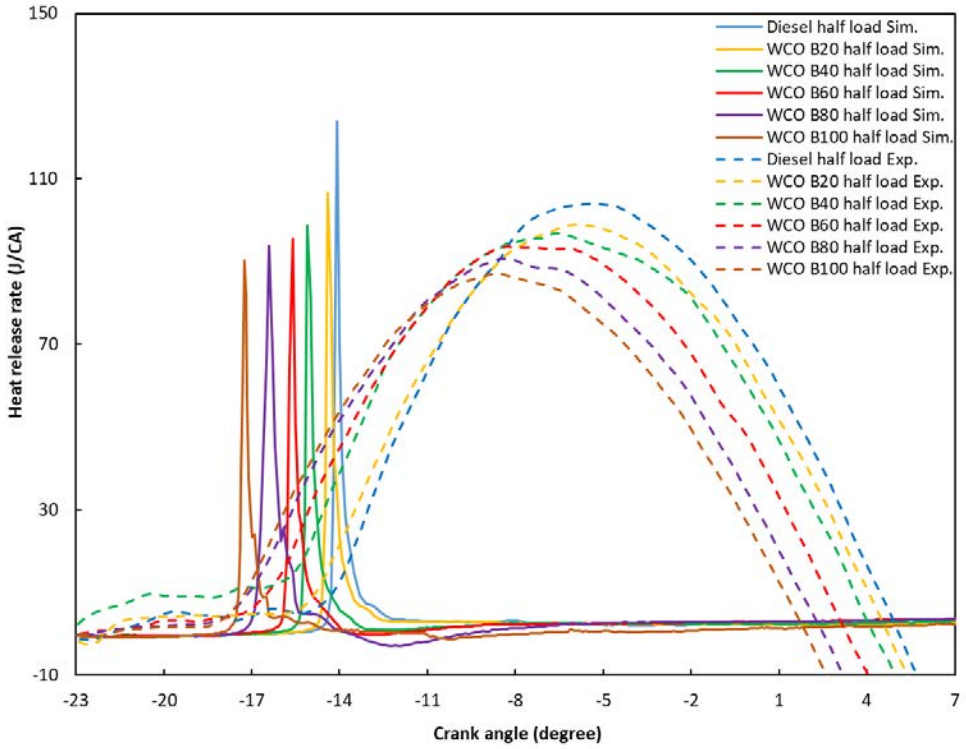

Figure 42 - CFD and experimental analysis of Heat Release Rate (HRR) against crank angle at half load condition (experiment data are extracted based on Equation 5.1).

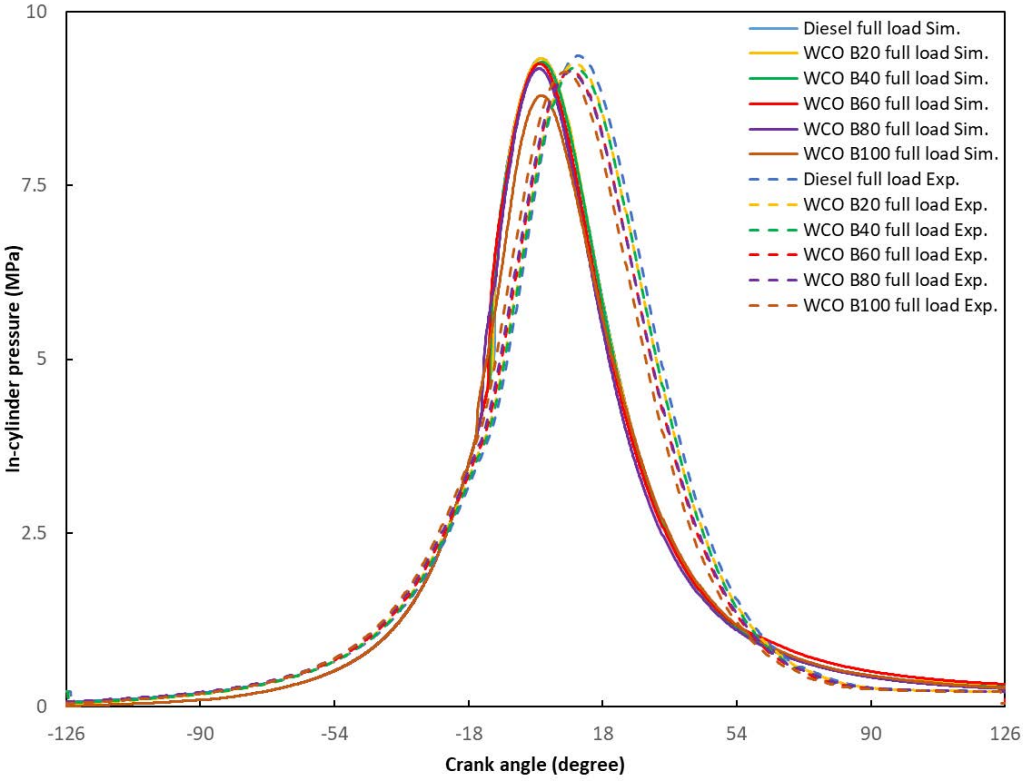

Figure 43 - CFD and experimental validation of in-cylinder pressure against crank angle at full load condition.

Figure 43 indicates that the underprediction of maximum pressure is characterised by percentage errors of 0.4% for Diesel and 3.72% for WCO B100. On the other

hand, the overprediction of maximum pressure is delineated by percentage errors of 0.8% for WCO B20, 0.84% for WCO B40, 1.17% for WCO B60, and 0.48% for WCO B80.

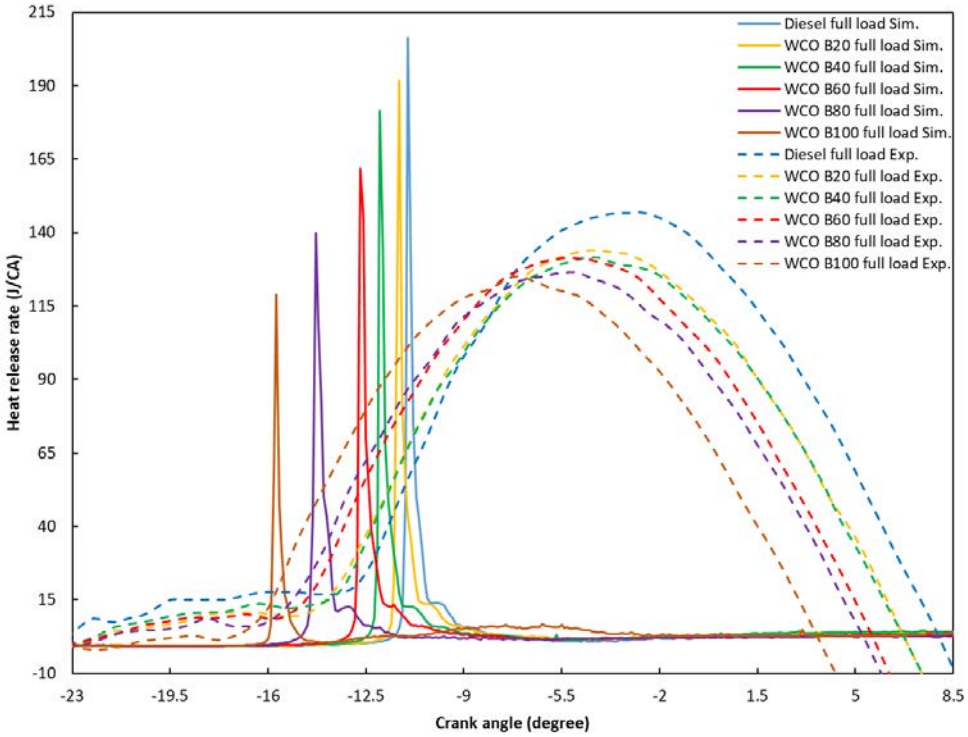

Figure 44 - CFD and experimental analysis of Heat Release Rate (HRR) against crank angle at full load condition (experiment data are extracted based on Equation 5.1).

Based on Figure 44, it can be concluded that the maximum Heat Release Rate (HRR) shows percentage errors of 40.5%, 42.9%, 37.72%, 23.1%, 10.4%, and 5.07% for Diesel, WCO B20, WCO B40, WCO B60, WCO B80, and WCO B100, respectively. The discrepancies observed between the experimental results and the CFD Heat Release Rate (HRR) depicted in Figures 40, 42, and 44 can be attributed to a specific limitation in the empirical approach outlined in Equation 5.1. Unlike the CFD models, which effectively incorporate the 'mass of fuel burnt' term represented as Y_i in Equations 3.38 and 3.39, and as m_p in Equation 3.74, the empirical equation neglects this critical variable. This oversight is significant, as the CFD models leverage both the unsteady laminar flamelet and the convection/diffusion models, which include this term, thus potentially offering a more accurate representation of the phenomena under study.

As demonstrated in the graph representing in-cylinder pressure, diesel fuel exhibits the highest peak pressure. This empirical finding is corroborated by data

on heat release rates, as delineated in a series of figures namely, Figure 39 through Figure 44. As evidenced by Figure 40, Figure 42, and Figure 44, the highest peak in Heat Release Rate (HRR) is observed for diesel fuel. It is noteworthy that with each incremental addition of WCO B100 to the fuel mixture, there is a corresponding decrease in the HRR peak. This trend holds true across varying load conditions and is consistent with observations regarding maximum in-cylinder pressure. Figure 45, Figure 46, and Figure 47 delineate the ignition delay values in accordance with Section 5.2.2, for no load, half load, and full load conditions, respectively. A consistent trend is observed: as the load increases, the ignition delay for all fuels lengthens, subsequently reducing the duration of the diffusion combustion phase.

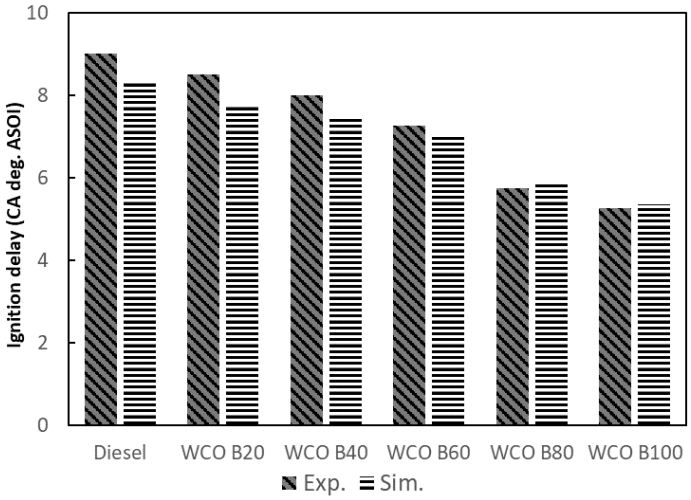

Figure 45 – Comparison of ignition delay between CFD simulation and experiment at no load condition, as detailed in Section 5.2.2.

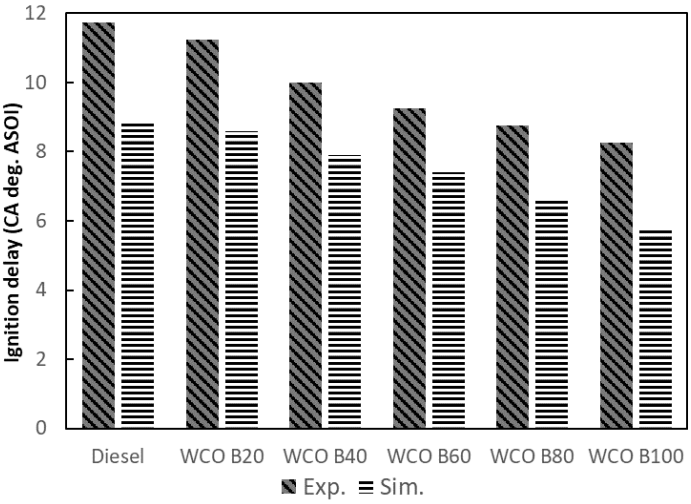

Figure 46 - Comparison of ignition delay between CFD simulation and experiment at half load condition, as detailed in Section 5.2.2.

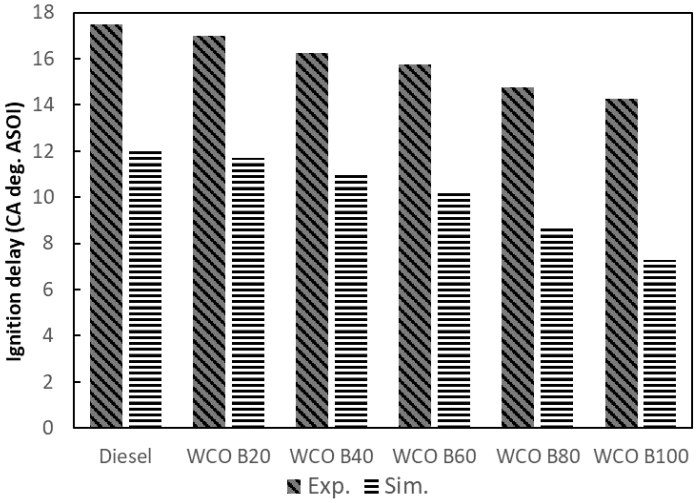

Figure 47 - Comparison of ignition delay between CFD simulation and experiment at full load condition, as detailed in Section 5.2.2.

As indicated in Table 6, injection pressure is held constant at 191.23 bar. To maintain a steady engine speed of 1300 rpm as the load increases, a greater volume of fuel is required. This, in turn, results in an extended injection duration. As can be discerned from Figure 45, Figure 46, and Figure 47, both CFD simulation and experimental results exhibit a consistent trend: an increase in the biodiesel component leads to a reduction in ignition delay. This suggests that biodiesel contributes to a faster reactivity of the fuel mixture. This observed reduction in ignition delays is attributed to the higher cetane number of WCO B100, as supported by Kuti, Sarathy, and Nishida (2020).

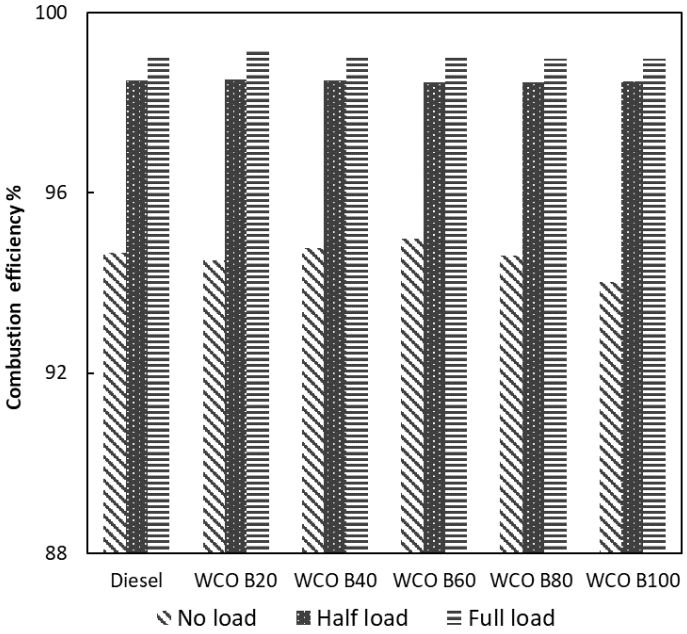

Figure 48 – Combustion efficiency of Diesel, WCO B100, and biodiesel blends as calculated by Equation 5.2.

Figure 48, drawing insights from the Heat Release Rate (HRR) and pressure data presented in Figure 39 through Figure 44 illustrates that an increase in load necessitating the injection of a greater fuel volume over an extended period results in a 1% improvement in combustion efficiency for Diesel as compared to WCO B100. Notably, blends with higher proportions of WCO B100 exhibit shorter durations of premixed combustion, consequently extending the diffusion combustion phase.

Furthermore, an examination of the experimental pressure data, encapsulated in Figure 39 to Figure 44, reveals that earlier ignition timing shifts the pressure peak closer to Top Dead Centre (TDC). This shift is likely to reduce the formation of emissions such as CO_2 and hydrocarbons (HC).

As elaborated in Section 2.7.1, the current mechanism slightly overestimates the percentage of NOx produced. Nonetheless, both experimental and simulated data indicate that due to the earlier onset of combustion and subsequently lower apparent heat release rates, despite the higher fuel volume injected, the in-cylinder peak temperature from the end of combustion to Exhaust Valve Opening (EVO) is diminished. This phenomenon suggests a potential for reduced NOx formation in scenarios involving WCO B100 and its blends, as supported by Brakora (2012).

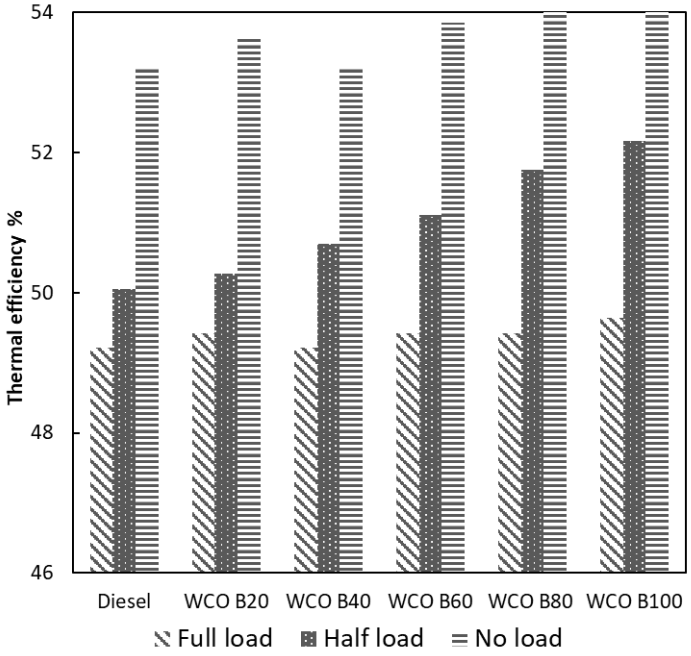

Figure 49 – Thermal efficiency of variant fuels at different loads, based on Equation 5.3.

Figure 49 delineates that the thermal efficiency follows an order: WCO B100 > WCO B80 > WCO B60 > WCO B40 > WCO B20 > Diesel, increasing as the biofuel percentage ascends. This trend suggests an effective utilisation of the heat supplied for fuel evaporation, thereby minimizing heat loss through additional heating of the cylinder walls and subsequent conduction to the ambient air.

Three key observations elucidate this phenomenon:

1. The heat imparted by compressed air to the fuel, particularly for blends with higher thermal efficiency, is used more effectively, reducing heat loss.
2. The characteristics of WCO B100 including high viscosity, density, and boiling point, as well as poor atomisation, lead to incomplete combustion when compared to Diesel.
3. The occurrence of 'cool flame' is more impactful on WCO B100 due to the significant influence of chemical delays and low-temperature reactions on combustion and ignition delay for unsaturated biodiesel fuels (Elhalwagy and Zhang, 2019).

Particularly noteworthy is that the combustion efficiency of WCO B100 is considerably lower than that of Diesel at no load conditions, primarily due to poor atomisation. The rate of vaporisation is initially most affected by surface tension and subsequently by liquid dynamic viscosity and vapour heat capacity for WCO B100 (Ismail *et al.*, 2012). This aspect will be further explored in Chapter 6.

Combustion efficiency is intrinsically linked to the production of CO and CO_2. The dominant chemical reactions involved in the production and consumption of CO_2 are detailed as follows:

$$CO+OH \rightarrow CO_2+H \qquad (5.4)$$
$$CO_2+OH \leftrightarrow CO+HO_2$$

A higher combustion efficiency is generally associated with a decrease in CO levels and an increase in CO_2 production. This observation indicates that near the Exhaust Valve Opening (EVO), conditions of higher combustion efficiency are characterised by a lower concentration of CO and a higher concentration of CO_2 when compared to one another. This aspect will be further explored in Chapter 7.

5.4 Conclusion

A comprehensive literature review encompassing a significant number of researchers' observations has indicated a shortened igniting delay for WCO B100 biofuel (Gharehghani, Mirsalim and Hosseini, 2017; Hosamani and Katti, 2018; Ismail *et al.*, 2012; Kannan *et al.*, 2011; Kuti, Sarathy and Nishida, 2020; Li *et al.*, 2018; Vijayaraj and Sathiyagnanam, 2016; Yu, Bari and Ameen, 2002). Kannan et al. (2011) reported a decreased heat release rate and an extended combustion time, a finding that aligns with data gathered by this study, particularly in the context of increased diffusion combustion prompted by increments of WCO B100.

Contrarily, Gharehghani et al. (2017) noted a higher heat release for WCO B100, which also resulted in a more considerable peak pressure near TDC, primarily because WCO B100 combustion initiated closer to TDC, hastening the ignition delay compared to diesel. Liu et al. (2019) highlighted that the primary rate of CH_2O consumption occurs at the peak heat release rate, facilitated by exothermic chemical reactions, primarily yielding CO and H. This observation is critical, given the advanced ignition of WCO B100 and its further distance from TDC, aspects not reflected in the dataset (refer to Figure 39 through Figure 44). Consequently, WCO B100 produces less CO, thereby reducing CO_2 emissions.

Vijayaraj and Sathiyagnanam (2016) emphasized that methyl ester blends had a reduced ignition delay and shorter combustion period compared to diesel. An increased engine compression ratio lowered the peak pressure and heat release rate for WCO B100, shifting the onset of heat release before TDC, which signifies a reduced ignition delay and a prolonged diffusion combustion period (Hosamani and Katti, 2018).

Furthermore, under full load conditions, with additional diesel fuel, the HRR for fuels like WCO B60, WCO B40, WCO B20, and diesel converged closer to each other. Importantly, before the end of the injection period, a significant portion of the fuel evaporated, facilitating earlier ignition, at around 4 CA for Diesel and 9 CA for WCO B100, confirming the observations of Hosamani and Katti (2018).

The current study recognizes a discrepancy with the data presented by Li et al. (2018). While attempting to stabilize the engine at 1300 rpm with a higher quantity of WCO B100 fuel, the recorded peak pressures for no load, half load, and full load were lesser by 2.14%, 6.4%, and 21.7%, respectively, than those reported by Li

et al. (2018). Contrastingly, the heat release rates were higher by 58% and 47.5% for half and full loads, but lower by 24.8% for no load. These discrepancies underscore the influence of the increased degree of unsaturation level, leading to a range of effects including a shorter ignition delay, earlier HRR, and shorter premixed combustion, alongside higher local temperatures, increased oxygen content, and a prolonged reaction residence time, thereby significantly affecting combustion characteristics (Li *et al.*, 2018).

A notable trend observed is the rise in the Cetane number with an increase in WCO B100 percentage in the blends, enhancing ignitability and generally reducing ignition delay, as corroborated by earlier studies (Cowart, Luning Prak and Hamilton, 2015).

The data presented in Table 11 and Appendix G show that WCO B100's lower heat capacity compared to diesel necessitates less heat for fuel evaporation, resulting in a shorter ignition delay. As detailed in Section 2.4 and Figure 7, the WCO B100 contains natural double bonds and features a cis orientation, yielding a curved molecular shape in its unsaturated fatty acid methyl esters. This structure leads to a decreased energy deficit in the frontier molecular orbital, thereby reducing the amount of heat energy necessary to break the Fatty Acid Methyl Ester (FAME) bonding energy, as explained by Ibadurrohman, Hamidi, and Yuliati (2022).

In conclusion, WCO B100 manifests a longer ignition delay, lower peak cylinder pressure, and reduced heat release rate than diesel, yet it emits fewer pollutants like carbon monoxide, unburned hydrocarbons, and particulate matter (Zhong *et al.*, 2018). Despite this, it is demonstrated that WCO B100 has the shortest ignition delay in all load conditions, coupled with a higher thermal efficiency, as calculated through Equation 5.3. This research posits that the liquid properties delineated in Table 11 and Appendix G enable WCO B100 and its increments in the blend to ignite earlier than diesel.

Nonetheless, further studies focusing on spray and emission formation are warranted to address the incomplete combustion resulting in CO emissions due to lower oxidation temperatures and extended residence time required for CO_2 conversion (Sharma, Hossain and Duraisamy, 2021).

Chapter 6 - Spray Formation Results

6.1 Introduction

In this chapter, the effects of different conditions on the liquid and vapour penetration lengths of Diesel and WCO B100 are examined, aiming to delineate the underlying dynamics and variations. This inquiry is grounded in a review of literature pertaining to the Leidenfrost phenomenon, droplet evaporation modelling, and the dynamic behaviour of the piston bowl. Existing research typically relies on constant volume vessel ignition quality testers or hot surface plates for investigating vapour and liquid penetrations, thereby operating within an unchanging volume or surface area throughout the examination. In contrast, this chapter utilises Computational Fluid Dynamics (CFD) studies for analysing individual fuel and load conditions. Given that spray formation is not covered in the experiment, validation is undertaken through a comparative analysis involving pressure and Heat Release Rate (HRR) versus crank angle graphs, as elaborated in Section 5.3. The chapter concludes with a discussion of the findings, synthesising the insights drawn from all the studies mentioned.

6.2 Results and discussion

As delineated in the literature, the simulated liquid length is determined by identifying the axial position that encompasses 95% of the mass of the injected fuel at a specific moment post-injection (Senecal *et al.*, 2003). A parallel methodology applies to vapour penetration, wherein the focal point is the axial location where 99% of the fuel mass is concentrated.

The term 'axial' refers to the trajectory spanning from the nozzle tip to the point where the liquid spray makes contact with the interior surface of the piston bowl, effectively drawing a diagonal line if viewed laterally, as illustrated Figure 33. It is able to provide an accurate perspective of whether or not WCO B100 has longer liquid penetration length when utilised in an ignition control volume quality tester, the volume of which does not change over the course of the testing period. This measurement, visually depicted in Figure 31, offers a precise understanding of the potential for extended liquid penetration length of WCO B100, especially when tested using an ignition quality tester characterized by a constant control volume, maintaining an unchanged volume throughout the testing period.

The data depicted in Figures 50 to 52 are derived from the CFD study outlined in Section 4.4, utilising the Discrete Phase Model (DPM) discussed in Section 3.2.9.2. This analysis was facilitated by the ANSYS Fluent software, which houses a specialized DPM model allowing for the meticulous study of various parameters. A notable feature of this model is its ability to enable users to extract critical data on vapour and liquid penetration by specifying a particular reference number pertaining to the fuel mass percentage. In this case, 95% and 99% were selected as the reference points for evaluating liquid and vapour penetration lengths, respectively. According to the engine configurations detailed in Table 6 and mass flow rate calculations in Appendix B, injection durations of 5 CA, 10 CA, and 15 CA are employed for no load, half load, and full load conditions, starting from -23 crank angle degrees at the onset of injection, respectively.

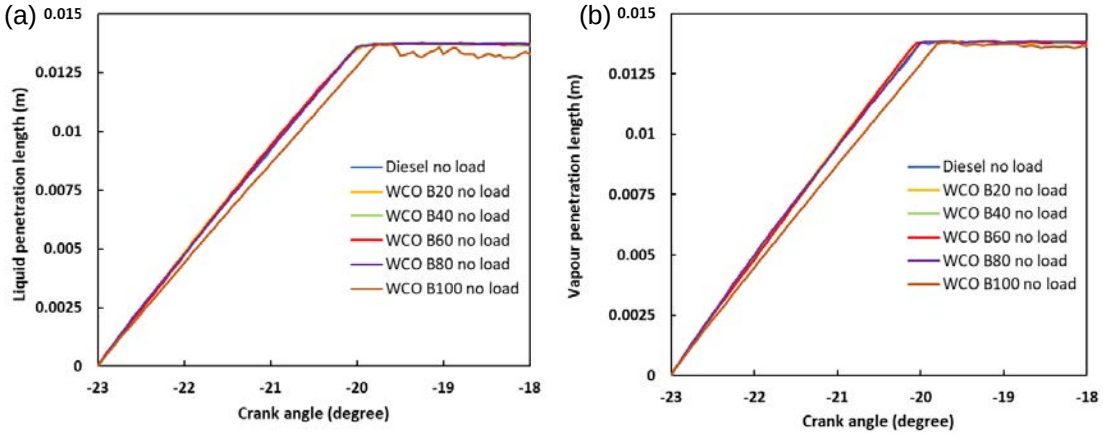

Figure 50 – a) Liquid penetration length and b) Vapour penetration length at no load condition for Diesel, WCO B20, WCO B40, WCO B60, WCO B80, and WCO B100 (CFD simulation).

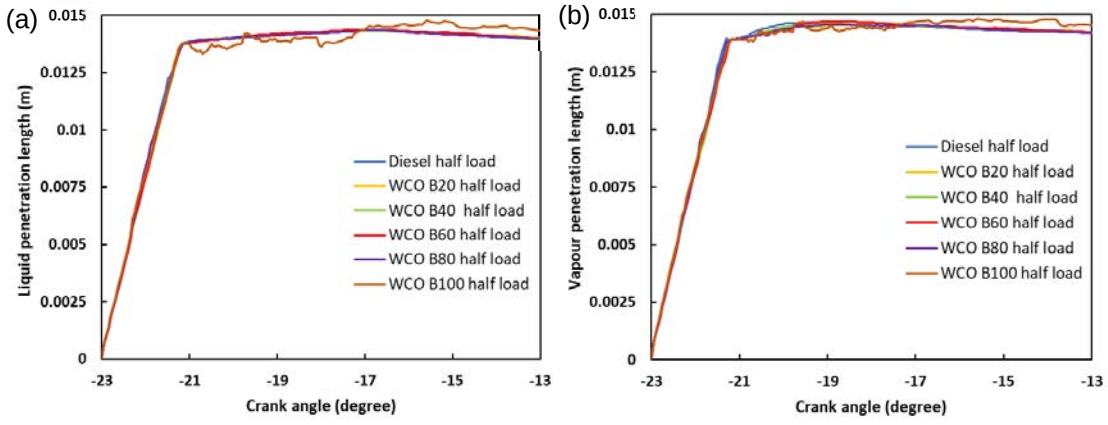

Figure 51 – a) Liquid penetration length and b) Vapour penetration length at half load condition for Diesel, WCO B20, WCO B40, WCO B60, WCO B80, and WCO B100 (CFD simulation).

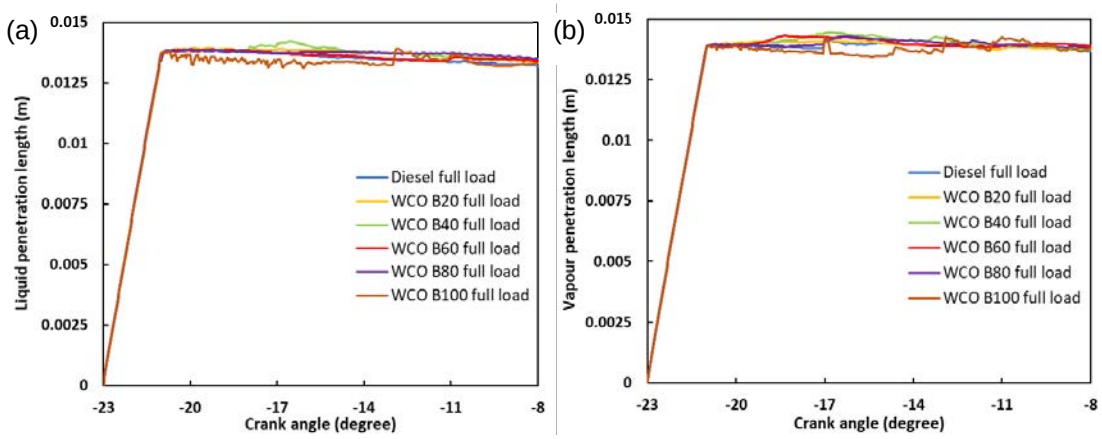

Figure 52 – a) Liquid penetration length and b) Vapour penetration length at full load condition for Diesel, WCO B20, WCO B40, WCO B60, WCO B80, and WCO B100 (CFD simulation).

According to Figures 50 to 52 , in the early stages of injection (from 1 CA after the start of injection to 2 CA ASOI for no load and full load, respectively), WCO B100 exhibits a greater liquid penetration length compared to diesel. As the piston ascends and the CA varies at the conclusion of the injection, there is a sharp decrease in the liquid penetration length of WCO B100. Conversely, with increasing quantities of Diesel, the vapour penetration duration extends. This phenomenon is due to the constant injector pressure maintained across different loads, as outlined in Table 6. Moreover, under varying injection pressures in a constant volume chamber study, WCO B100 tends to demonstrate longer liquid and shorter vapour penetration lengths than Diesel, as depicted in Figure 53 (Kuti, Sarathy and Nishida, 2020).

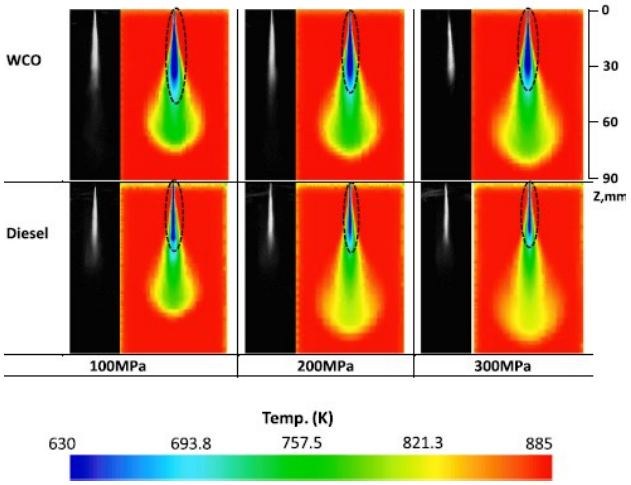

Figure 53 - At 1.5 ms ASOI, a variation in evaporating sprays is observed with changes in injection pressure. A contrast is drawn between the experimental evaporating spray (depicted on the left) and the simulated evaporating spray (shown on the right), both illustrated through contour pictures. Within the simulated images, broken black lines delineate the liquid length (highlighted in blue) of the evaporating spray, as referenced in the study by Kuti, Sarathy, and Nishida (2020).

This observation correlates with WCO B100 having a shorter ignition delay, faster reaction rate, and reduced flame lift-length, coupled with less air entrainment (Kuti, Sarathy and Nishida, 2020).

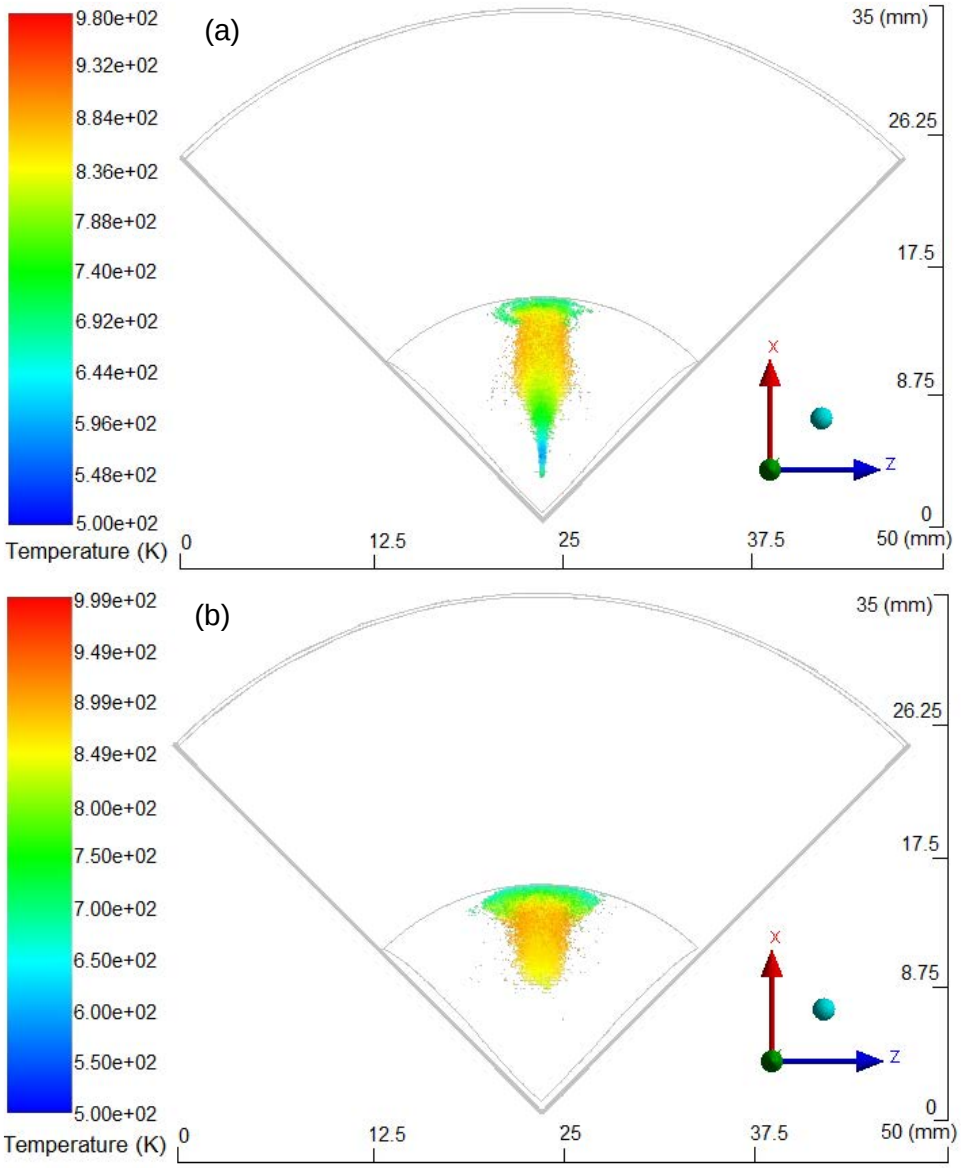

Figure 54 – A DPM (Discrete Particle Method) tracking model illustrating the diesel spray under a no load condition is presented; it showcases a) the spray characteristics at an injection timing of -18 CA (crank angle) degrees, and b) the continuation of the injection process at -16 CA degrees.

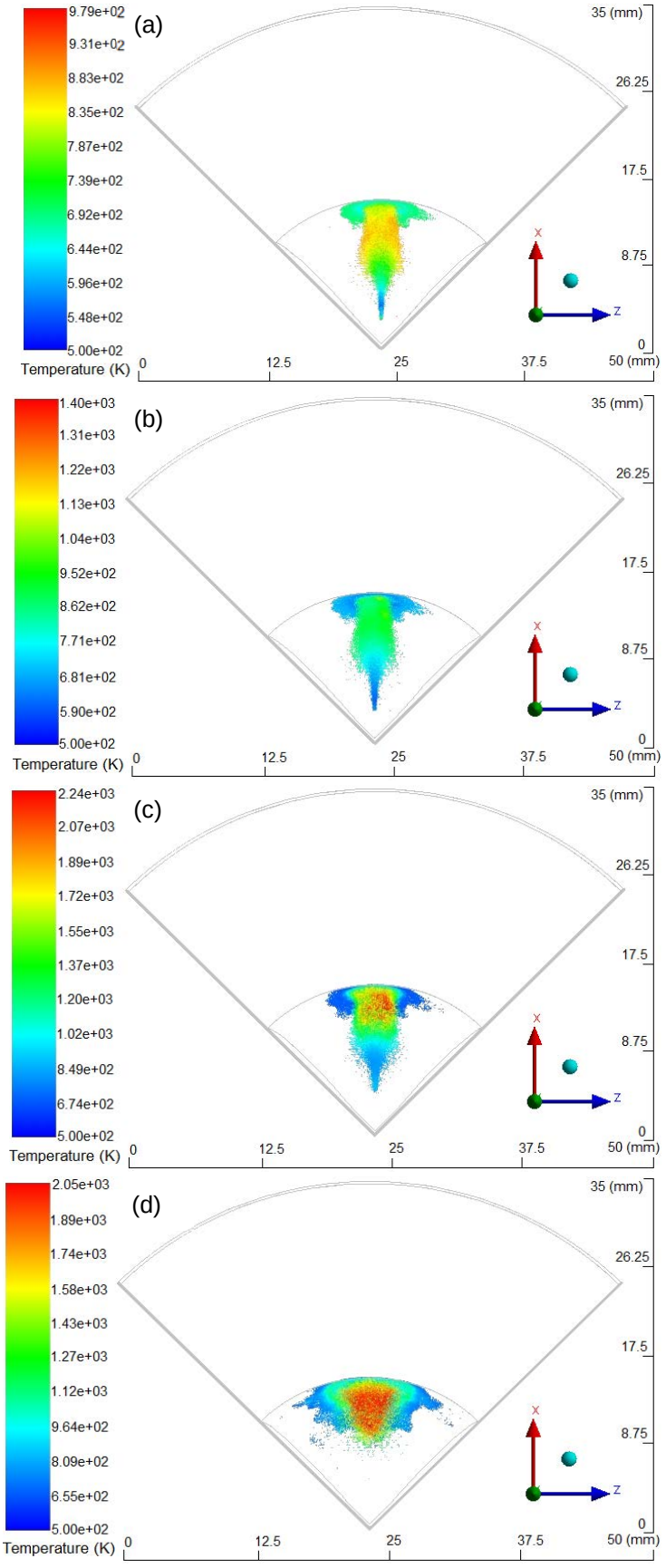

Figure 55 – At no load, a detailed representation of the in-cylinder spray production of WCO B100 is exhibited. Figure a) depicts the end of injection (EOI) occurring at -18 CA (crank angle) degrees, while figure b) represents the state at -17.9 CA degrees. Subsequent figures, namely c) and d), illustrate the evaporation times of WCO B100 at -17.6 CA and -16 CA degrees, respectively.

Figure 54 and Figure 55 showcase the injection temperature contours for two distinct types of fuel: Diesel and WCO B100, respectively. As observed in Figure 55c, a sudden temperature spike occurs at a crank angle of -17.6 degrees, marking the onset of the ignition process. This phase is characterized by a significant amount of fuel splashing onto the heat film on the wall of the piston bowl surface.

The phenomenon of splashing occurs when the impingement energy exceeds a critical energy threshold. It is worth noting that the majority of impacts in standard diesel sprays significantly surpass this upper boundary. Consequently, such splashing events typically result in the ejection of around seventy-five percent of the mass of the impinging droplet, as documented by O'Rourke (1981).

This process is facilitated because the temperature of the piston wall exceeds the necessary vaporisation temperature of the fluid coming into contact with the surface. Consequently, seventy-five percent of the primary droplet undergoes secondary breakup, generating a multitude of smaller 'child' droplets. The remaining fraction is deposited on the surface of the piston bowl at the point of contact. This phenomenon results in wall impingement heat transfer, described briefly below:

- When a liquid particle collides with a wall, it may deform, maintaining direct contact with the wall for a brief period before rebounding. During this interval, heat is exchanged between the particle and the wall.
- To facilitate droplet-to-wall heat transfer calculations, the ANSYS Fluent discrete phase model operates under the assumption that the droplet morphs into a cylinder upon colliding with the wall.

However, boiling events in liquid films are significantly more complicated, and the rate at which heat is transferred from a hot wall to a liquid film does not follow a linear dependency as the temperature gap between the wall and the liquid film increases. This divergence is a result of vapour pockets forming between the hot wall surface and the boiling film. These vapour pockets substantially influence not only the heat transmission but also the hydrodynamic characteristics of the film boiling process. A situation known as the Leidenfrost point is a limiting condition where the insulating vapour layer entirely covers the heated wall. The typical static temperatures in supersonic flow and piston wall temperatures in combustors are

in the range of approximately 450 to 600 K (Zhao *et al.*, 2022). This temperature range corresponds to the Leidenfrost region of liquid hydrocarbons. Therefore, in conclusion, a shorter evaporation period suggests a more efficient heat transmission between the droplet and the heated surface.

Taking into consideration the potential occurrence of the Leidenfrost effect, which is initiated when fuel is injected at a temperature of 368 K onto a wall surface, is corroborated by data from Table 13. This data illustrates that the in-cylinder wall temperature fluctuates between 500 and 600 K. Further evidence can be seen in the contours depicted in Figure 56a, Figure 56d, Figure 57a, and Figure 57d, signalling the substantial number of fuel droplets experiencing splashing and wall impingement, resulting in a deposit in the central region of the piston bowl.

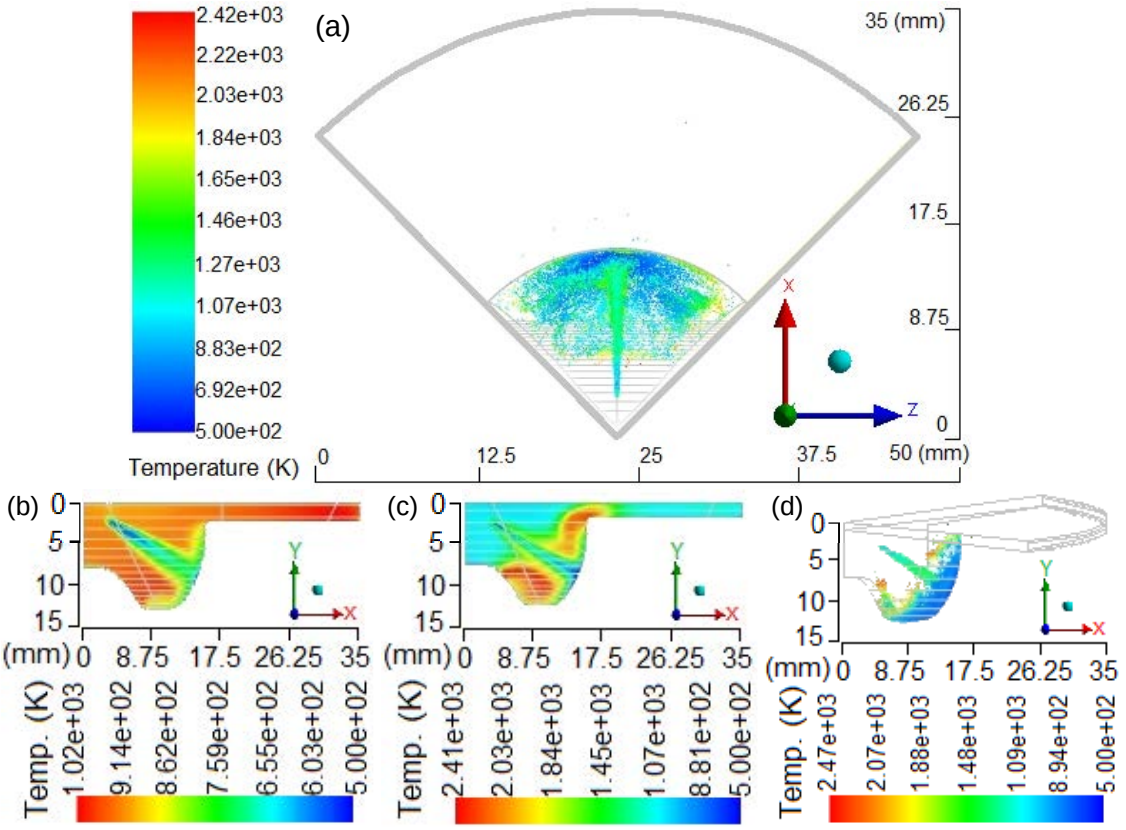

Figure 56 – The DPM tracking of diesel spray formation and species at full load condition is showcased. In the illustration, top contour a) captures the scenario at a crank angle of -10 degrees, vividly displaying the droplet scattering. Contours b) and c) offer a glimpse of the static temperature landscape on the X-Y plane within the cylinder during the diesel liquid fuel injection at -14 CA and -10 CA degrees, respectively, highlighting the interactions as the fuel encounters the hot surface of the piston bowl. Lastly, contour d) depicts the in-cylinder diesel injection occurring at a crank angle of 0.3 degrees after the end of injection.

This suggests one of the advantages of reduced liquid penetration length could be attributed to WCO B100's faster evaporation rate.

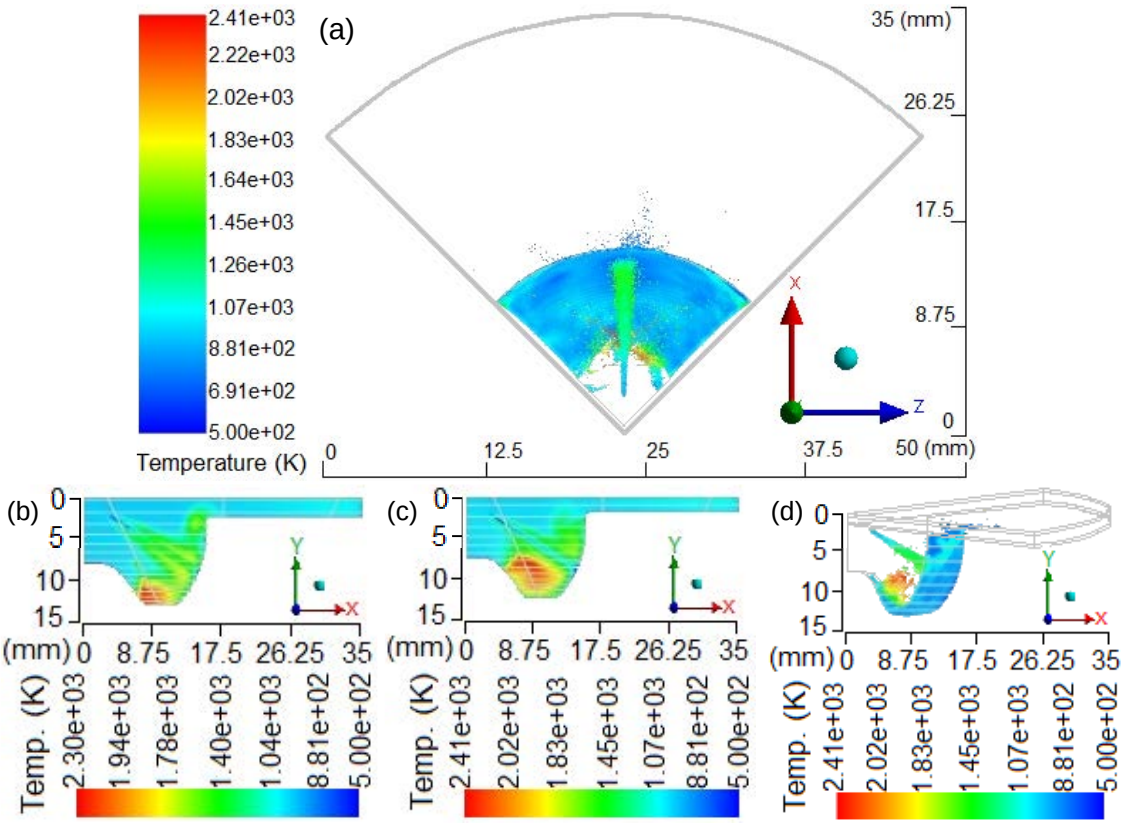

Figure 57 – The provided contours illustrate various stages of WCO B100 ignition. Contours a), c), and d) are associated with distinct events occurring at -10 CA (crank angle) degrees. Specifically, contour b) represents a stage 9 CA degrees after the start of injection (ASOI), where a hot deposit of fuel-air mixture is formed due to the interaction between WCO B100 droplets and the piston wall, creating a hot surface induced by droplet splashing.

According to Equation 3.70, the rate of vaporisation can be anticipated to be higher for WCO B100 compared to Diesel, given its higher surface tension, greater density, and increased mass injected during injection, as substantiated by data from Table 11, Appendix G, and Figure 19.

The Spalding transfer number, defined in Equation 3.71, reflects the balance between the driving force promoting vaporisation, derived from the heat of combustion, and the opposing force resisting vaporisation, stemming from the heat of vaporisation. WCO B100 exhibits a lower vapour mass fraction in the bulk gas as deduced from its vapour penetration length, implying a reduced requirement for combustion heat owing to its lower specific heat and latent heat values, outlined in Appendix G and Table 11 respectively. Moreover, its higher cetane number facilitates faster burning, and the substantial sensible heat alteration due to the prevalent vapour bulk gas in the environment enables it to absorb more heat, thereby encouraging vaporisation through combustion heat as described in Equation 3.74.

As Zhao et al. (2022) indicated, a truncated evaporation period denotes a more efficient heat exchange between the droplet and the hot surface. This necessitates a fuel with superior thermal conductivity, a characteristic evidenced for WCO B100 in Appendix G. Particularly at elevated temperatures above 550 K, WCO B100 maintains a higher thermal conductivity throughout its lifecycle, adapting to the temperature-dependent alterations in the utility of the liquid droplet.

As the piston bowl ascends, the WCO B100 droplets, propelled by a heightened density number from the injector toward the advancing piston bowl surface, demonstrate greater momentum compared to Diesel. This attribute of WCO B100, coupled with the characteristics mentioned above, results in initially extending the liquid penetration length, which is subsequently followed by a rapid diminution. This sequence effectively underscores the nuanced behaviour of WCO B100 during the vaporisation process.

6.3 Conclusion

- **Fuel Behaviour During Injection**: In the initial stages of injection, WCO B100 showcases greater liquid penetration length compared to diesel, as evidenced in Figures 50 to 52. However, as the crank angle (CA) varies at the end of the injection cycle, there is a notable decrease in the liquid penetration length for WCO B100. Diesel, on the other hand, sees an extension in vapour penetration duration. This behaviour is influenced by the constant injector pressure maintained throughout different loads (Table 6).

- **Ignition Process**: The ignition process starts visibly with a temperature spike at -17.6 degrees of the crank angle, as noted in Figure 55c. This marks the beginning of the fuel splashing significantly onto the heat film present on the piston bowl's wall surface.

- **Splashing and Secondary Breakup of Droplets**: During the injection process, a considerable amount of fuel experiences splashing, a phenomenon triggered when impingement energy surpasses a specific threshold, leading to the creation of smaller 'child' droplets, a process supported by the high temperatures of the piston wall which exceeds the fluid's vaporisation temperature. However, smaller droplets can be carried by the in-cylinder airflow and might impinge on the walls more readily.

- **Heat Transfer and Wall Impingement**: Heat transfer takes place when liquid particles hit a wall, transforming temporarily into a cylindrical shape (as modelled in ANSYS Fluent) before reverting. This process is influenced significantly by the temperature differences between the hot wall and the liquid film, with the Leidenfrost effect playing a pivotal role when the temperature range is between 450 and 600 K, a range typical for combustor piston wall temperatures.
- **Advantages of WCO B100**: WCO B100 demonstrates faster evaporation rates, facilitated by its higher surface tension, greater density, and more substantial injected mass, as explained through Equations 3.70 and 3.71 and supported by data from Table 11, Appendix G, and Figures 19, 56a, 56d, 57a, and 57d. This attribute allows for a higher rate of vaporisation compared to diesel, resulting in a reduced need for combustion heat (due to lower specific heat and latent heat), benefitting from its higher cetane number and more significant sensible heat changes.
- **Thermal Conductivity and Evaporation**: At elevated temperatures (above 550 K), WCO B100 maintains superior thermal conductivity, adapting well to temperature-dependent changes, thus necessitating a fuel with higher thermal conductivity for a more efficient heat exchange between the droplet and the hot surface, as highlighted in the study by Zhao et al. (2022).
- **Vaporisation Process of WCO B100**: As the piston bowl moves upwards, WCO B100 droplets, propelled with greater momentum compared to diesel, exhibit a significant initial extension in liquid penetration length, followed by a swift reduction, marking the complex behaviour of WCO B100 during the vaporisation process.

Figure 55 and 57 clearly illustrate that the shorter liquid and vapour penetration lengths of WCO B100 might foster a more localized and potentially richer combustion zone, as noted by Elhalwagy and Zhang (2019). This phenomenon possibly leads to higher thermal efficiency due to localized high-temperature regions but also results in lower combustion efficiency because of incomplete combustion stemming from non-optimal air-fuel mixtures.

It has been noted that for unsaturated biodiesel components, the spray vaporisation largely completes in the core region, and notably, the ignition process occurs near the wall, where temperatures are higher than in the core (Elhalwagy and Zhang, 2019). This phenomenon is documented in Figure 55c and 55d.

An interesting perspective on the shorter ignition delay and consequently reduced liquid penetration length during the dynamic movement of the piston bowl is provided by Yu, Bari, and Ameen (2002). They observed that the breakdown of linoleic (C18:2) and linolenic (C18:3) both unsaturated fatty acids results in a highly concentrated core of higher molecular weight liquids. This leads to rapid gasification at the fringe of the spray, encouraging the spray to spread out. Consequently, high combustible volatile compounds ignite sooner, reducing the ignition delay period (Yu, Bari and Ameen, 2002).

This dynamic can be interpreted as a manifestation of the faster vaporisation process influenced by the specific properties of WCO B100 and the engine conditions, coupled with in-cylinder air motion. This contributes to a shorter vapour penetration length for WCO B100 compared to diesel. Moreover, the lower heating value of WCO B100 implies that less energy is available to propel the vapour cloud further into the chamber, also influencing the vapour penetration length negatively.

Supporting this, Ismail et al. (2012) highlighted that biodiesel experiences a greater rate of temperature increase in fuel droplets than diesel under the same heat input, enhancing the vaporisation rate of biodiesel, including WCO B100.

Furthermore, the latent heat of vaporisation, representing the energy necessary to transition from liquid to gas, is lower for WCO B100 at its boiling point, as presented in Table 11. This translates to a reduced energy requirement for phase transition, facilitated by the molecular structure of unsaturated fatty acid methyl esters present in WCO B100. Notably, the ignition temperature of unsaturated hydrocarbons can be reduced by accelerating the removal rate of hydrogen atoms, a finding corroborated by studies from Gopinath et al. (2015) and Singh et al. (2019).

Chapter 7 - Emission Measurements and Sensitivity Analyses Results

7.1 Introduction

In this segment of the chapter, a comprehensive analysis of the creation of emission species including carbon monoxide (CO), carbon dioxide (CO_2), nitrogen oxides (NOx), and unburned hydrocarbons (HC) is undertaken across various fuel and load conditions. The analysis involves a detailed comparison of experimental results with the findings obtained through numerical methods.

Pursuant to the chosen approach, sensitivity route analysis has been carried out employing 0-D numerical modelling, thereby enabling a deep exploration of complex chemical processes. A discussion grounded on existing literature is formulated, presenting an extensive insight into the results garnered thus far.

As this chapter concludes, attention will turn to an exhaustive analysis of the fundamental chemical reactions governing the production and consumption of primary emission species, to be delineated in Section 7.4, which focuses on sensitivity analyses. This discussion embraces a wide array of substances such as CO, CO_2, NOx, formaldehyde (CH_2O), hydrogen peroxide (H_2O_2), hydroxyl radical (OH), ethane (C_2H_6), acetylene (C_2H_2), and other representative fuel surrogate species, delineating their roles and interconnected dynamics. These species are documented in Table 10.

7.2 Validation and Results discussion

The emission data central to this study were collected utilising the Horiba MEXA-584L kit, a tool detailed extensively in Section 4.2.10. To enhance the resolution and reliability of the data, an averaging method was employed; it encompasses the outcomes of 10 individual runs, each lasting one minute at a constant speed of 1300 RPM. The data collection occurred at the end of the cycle (EVO), a constraint dictated by the kit's capabilities, which allows for a fastest sampling rate of one second.

It is important to note the uncertainties associated with the measurements: NOx (± 1.3%), HC (± 1.3%), CO (± 0.1%), and CO_2 (± 3%). The refined results of this meticulous process are presented in Figures 58 to 60.

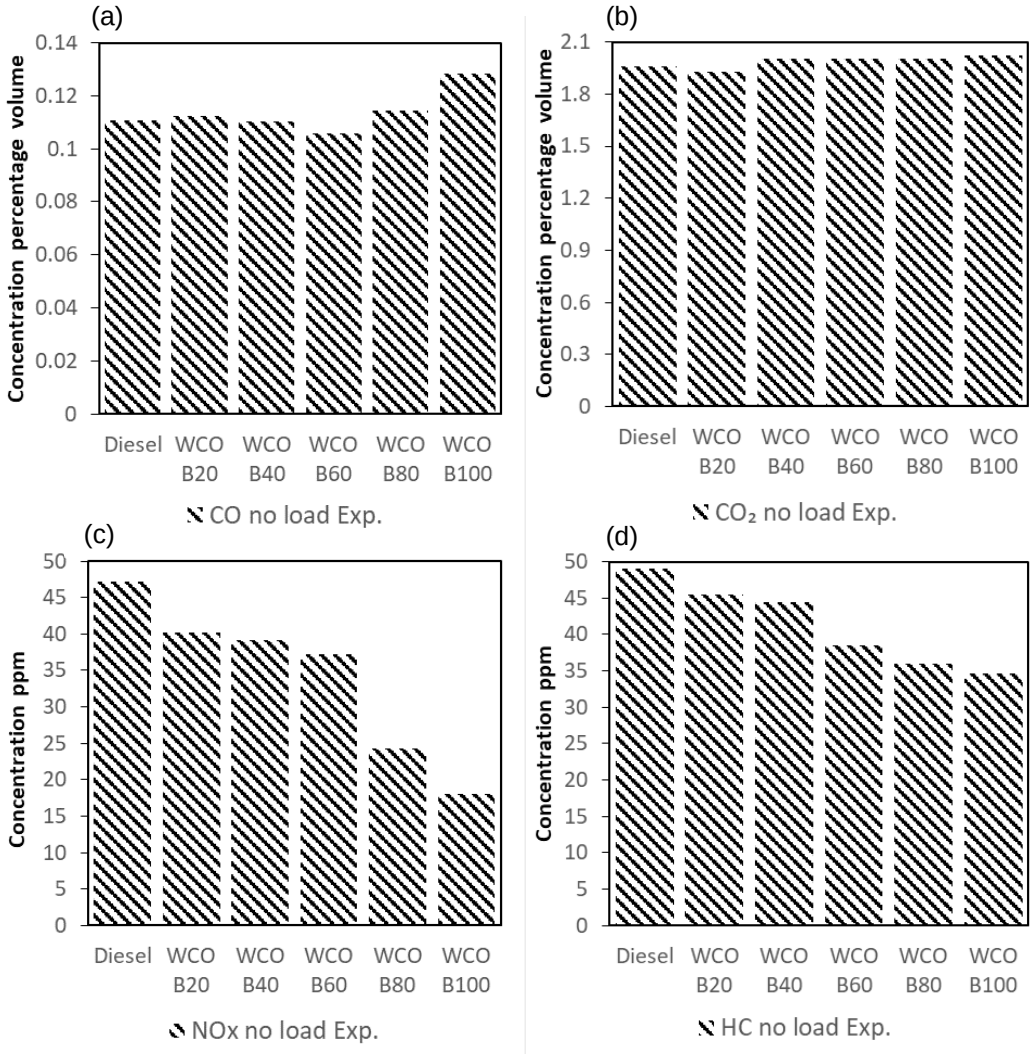

Figure 58 – Experimental data for a) CO concentration in %vol, b) CO_2 concentration in %vol, c) NOx concentration in ppm, and d) HC concentration in ppm was gathered from the exhaust at the end of a cycle that operated at 1300 rpm under a no load condition.

As can be observed from the emission Figures 58 to 60 obtained during the experiment, there was a substantial percentage reduction in HC particulate when transitioning from Diesel to WCO B100. Specifically, the reductions were 29.5%, 30%, and 23.5% under no load, half load, and full load conditions, respectively.

Similarly, NOx emissions decreased under all load conditions; reductions were recorded at 61.8% (no load), 36.3% (half load), and 27.9% (full load). This decrease can be attributed to the lower peak heat release rates observed in Figures 40, 42, and 44, a topic extensively discussed in Chapter 5. Essentially, WCO B100, and blends with a higher biofuel percentage, tend to exhibit reduced NOx emissions.

The decrease in HC particulate levels can be linked to the fact that the FAME structure of WCO B100 contains higher oxygen levels, a phenomenon

documented by Yaqoob et al. (2021).The reduced ignition delay witnessed with WCO B100 serves to lower the occurrences of mixture over-leaning as elaborated in Section 5.3. This, in turn, fosters quicker premixed combustion periods, which yields a reduction in HC emissions as the concentration of WCO B100 in the blends is increased (Sogbesan, Garner and Davy, 2021).

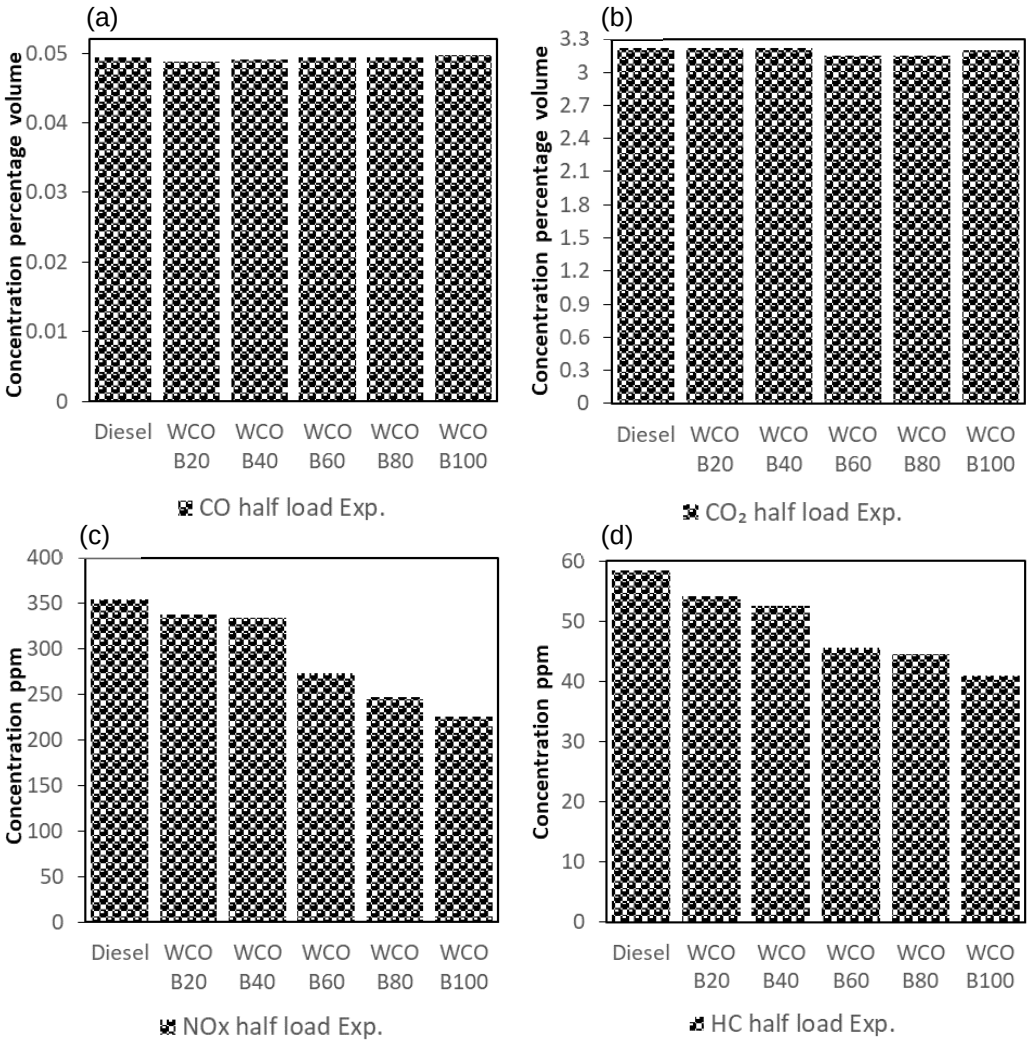

Figure 59 - Experimental data for a) CO concentration in %vol, b) CO_2 concentration in %vol, c) NOx concentration in ppm, and d) HC concentration in ppm was gathered from the exhaust at the end of a cycle that operated at 1300 rpm under a half load condition.

However, the data from Figure 60 indicates that as the load increases due to dilution, there is a corresponding increase in certain emissions including CO_2, NOx, and HC. For instance, transitioning from no load to full load conditions results in a 68.8% reduction in CO emissions but a notable increase in other emissions for WCO B100: CO_2 by 92.2%, NOx by 2550%, and HC by 27.4%.

Referencing experimental data from Figure 58, there is a documented increase in emissions with a higher biofuel concentration in the mixture under no load

conditions: a 16% increase for CO and a 3% increase for CO_2. It should be noted that the variations are less pronounced under half load conditions; a comparison between diesel and WCO B100 reveals a minor increase in CO by 0.77% and a slight reduction in CO_2 by 0.71%, offering a nuanced view of the emissions landscape as illustrated in Figure 59. Under full load conditions, depicted in Figure 60, there was a modest increase in CO by 1.33% and a 4.4% reduction in CO_2 emissions as the proportion of WCO B100 in the fuel mixture was augmented.

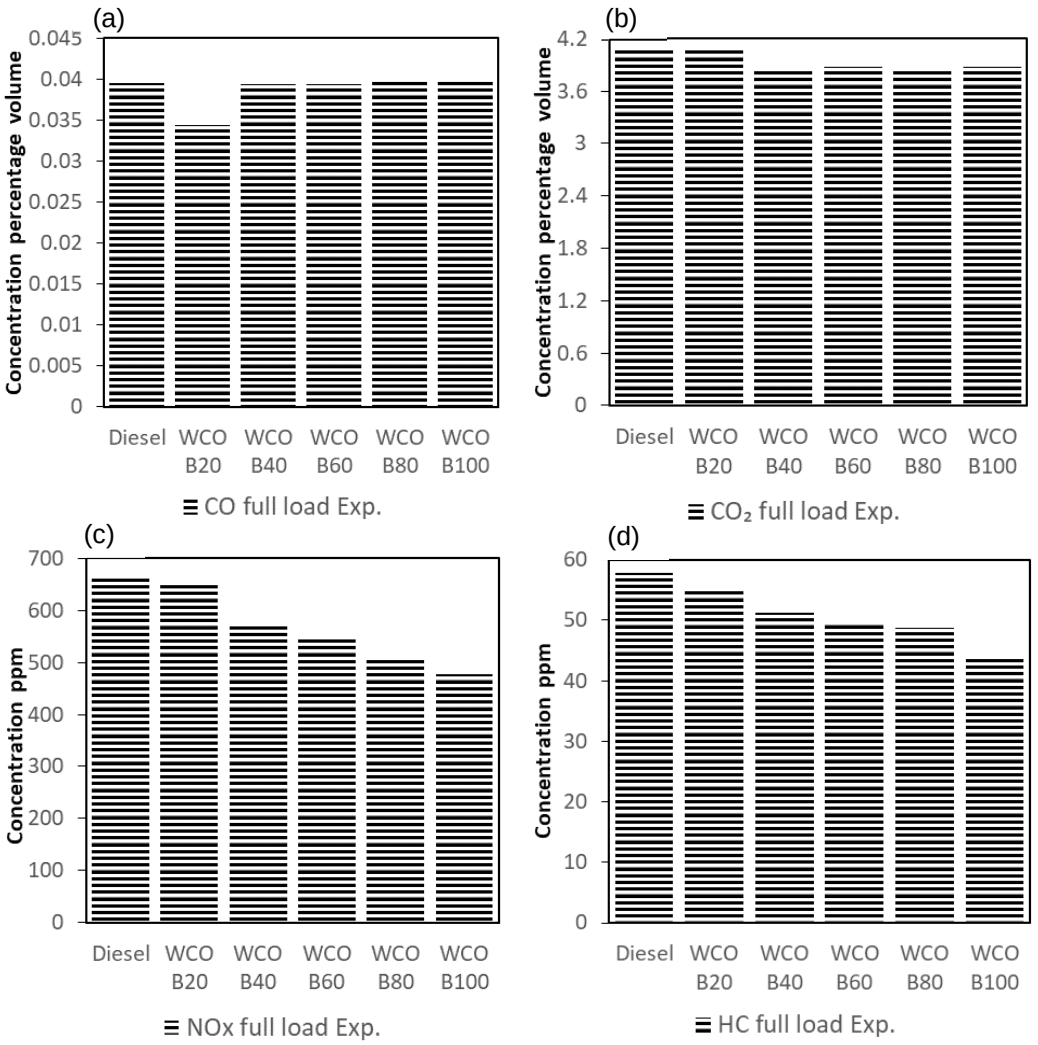

Figure 60 - Experimental data for a) CO concentration in %vol, b) CO_2 concentration in %vol, c) NOx concentration in ppm, and d) HC concentration in ppm was gathered from the exhaust at the end of a cycle that operated at 1300 rpm under a full load condition.

In the CFD simulation, acetylene (C_2H_2) serves as a representation of soot, while the role of a precursor for HC emissions is assigned to ethane (C_2H_6). This approach is grounded in the ERC-MultiChem plus Bio mechanism outlined by Brakora and Reitz (2013).

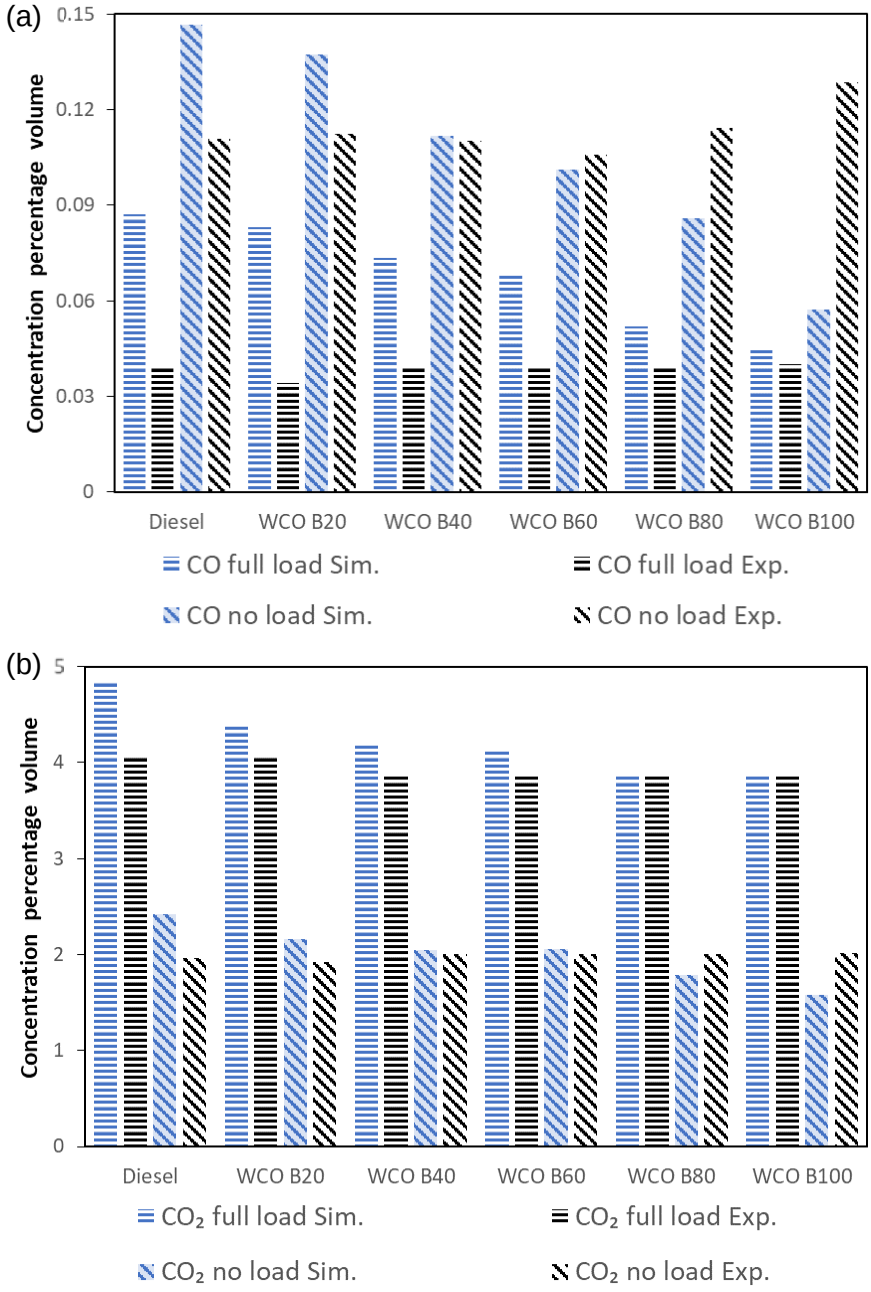

Figure 61 – a) CO and b) CO_2 validation for CFD simulation at EVO under no load and full load conditions in comparison with experimental results.

The validation of the CFD emission results leverages data on pressure and HRR versus the crank angle, a topic expanded upon in Section 5.3. This data complements experimental emission data points for CO, CO_2, NOx, and HC at EVO, acquired under full load and no load conditions for each blend, as illustrated in Figures 61 and 62. It should be noted that the validation robustness is somewhat restricted due to the limitations posed by the temporal specificity of the emission data points. The HORIBA emission kit was instrumental in obtaining this data, with results expressed in units of parts per million by volume (ppm) and percentage

volume. To align these units with the mass fractions derived from CFD simulations, the following conversion formula is employed:

$$\text{ppm(v)} = \text{mass fraction of specie} \times \frac{\text{total density of in} - \text{cylinder mixture}}{\text{density of specie}} \times 1000000 \qquad (7.1)$$

The conversion from ppm to percentage volume is then achieved by dividing the value by 10000. Data pertinent to emissions versus crank angle in CFD simulations were extracted from the species result section of ANSYS Fluent software. In order to facilitate a meaningful comparison with the experimental results at EVO, the total density of the in-cylinder mixture along with the density of the individual emission species were derived from the Report Definitions section within ANSYS Fluent.

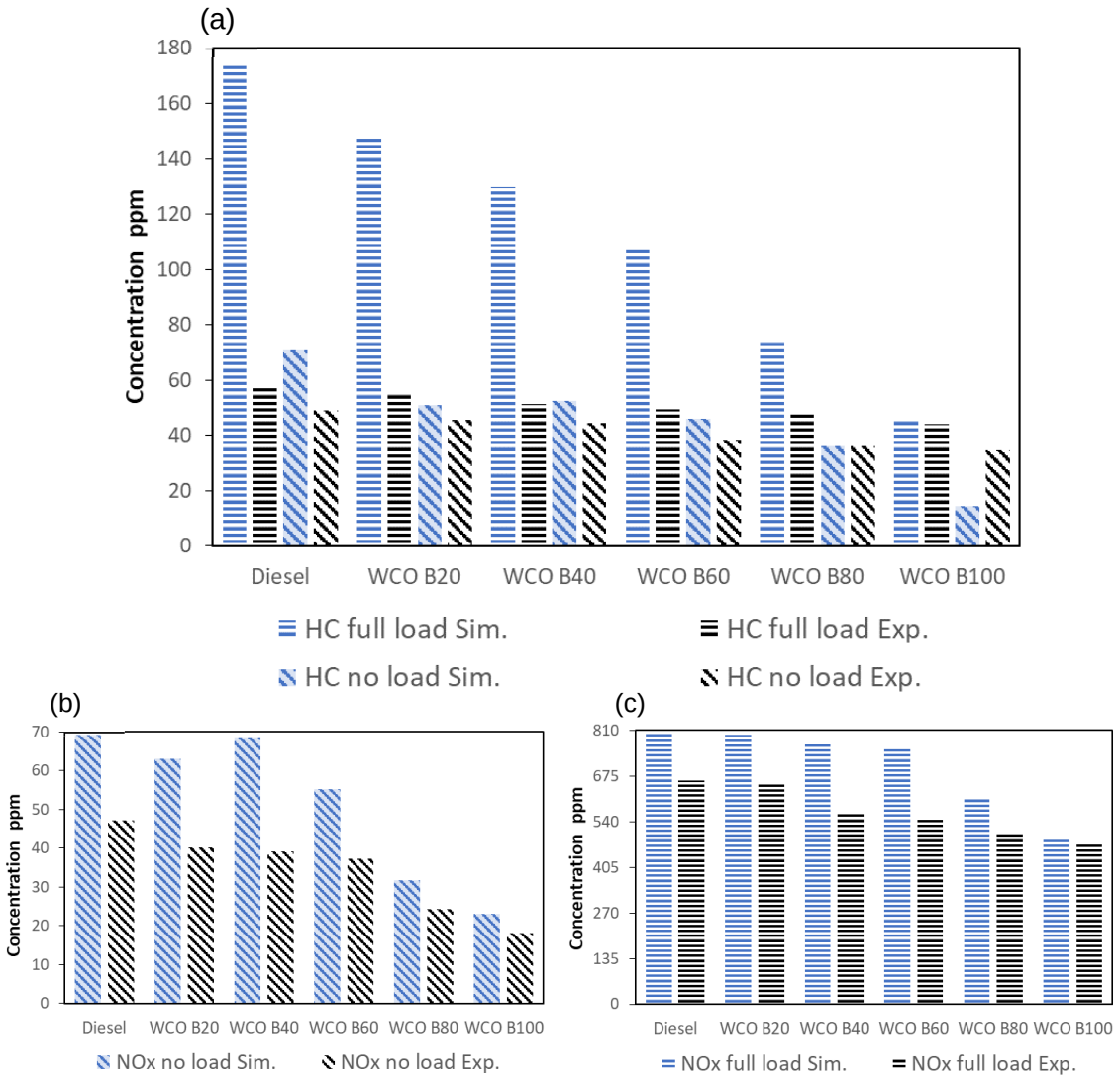

Figure 62 – Validation of CFD simulations for HC and NOx concentrations at EVO across no load and full load conditions in comparison with experimental results: a) HC validation, b) NOx validation at no load, c) NOx validation at full load.

Figure 61 illustrates the variances in the simulation data for both CO and CO_2 emissions at different load conditions, using various biodiesel blends as well as diesel.

At no load, the CO emission simulation overestimates the outcomes by 32.3% for Diesel, 22.4% for WCO B20, and 1.42% for WCO B40, while underestimating by 4.19% for WCO B60, 25% for WCO B80, and 55.5% for WCO B100. Concurrently, the simulation overpredicts CO_2 emissions by 23.2% for Diesel, 12% for WCO B20, 2.34% for WCO B40, and 2.43% for WCO B60, whereas it falls short by 11% and 21% for WCO B80 and WCO B100, respectively.

Shifting focus to full load conditions, a similar trend persists with CO emission predictions surpassing the actuals by 121% for Diesel, 141% for WCO B20, 86% for WCO B40, 72.2% for WCO B60, 31% for WCO B80, and 12% for WCO B100. CO_2 simulations at full load show an excess of 19.6% for Diesel, 8% for WCO B20, 8.2% for WCO B40, and 7% for WCO B60, with a slight overestimation of 0.2% for WCO B80, and a minor underprediction of 0.6% for WCO B100.

One specific detail to note is the behaviour of WCO B100 in the simulations compared to the experiments. While the experimental data shows an increase in CO generation by 16% at no load compared to diesel, the simulation projects a decrease of 55% for the same conditions.

Figure 62 presents a detailed validation comparison of the experimental data and CFD simulation results gathered at EVO, concerning HC and NOx emissions under no load and full load conditions.

Examining the no load conditions first, the CFD simulation tends to overpredict HC emissions, doing so by 44% for Diesel, and following with 11.8% for WCO B20, 18% for WCO B40, 19% for WCO B60, and 0.7% for WCO B80. Contrary to this, the WCO B100 results are underestimated by a margin of 58.3%. In the case of NOx emissions at no load, the overprediction is evident across all fuel types: 46.8% for Diesel, 57% for WCO B20, 75% for WCO B40, 48% for WCO B60, 30.4% for WCO B80, and 27.5% for WCO B100.

Focusing on the full load conditions, the NOx emissions continue to be overestimated, albeit to a reduced extent than at no load, with overpredictions of 21.6% for Diesel, 21.3% for WCO B20, 35.2% for WCO B40, 38.4% for WCO B60,

21% for WCO B80, and a minor overestimate of 1.8% for WCO B100. A similar pattern is noted for HC emissions at full load, with substantial overpredictions recorded at 202% for Diesel, 166.6% for WCO B20, 153% for WCO B40, 117% for WCO B60, and 52% for WCO B80. The overprediction is much smaller for WCO B100, standing at 4%. While the no load comparison aligns well with the experimental data, evidenced by the percentages previously noted for all emission species excluding the CO emission trend, the full load condition manifests significant variances in the predictions for HC and CO emissions derived from CFD analyses.

This discrepancy might arise due to variations in the fuel quantity administered to the engine. Additionally, it could be attributed to the overestimation inherent in the non-premixed unsteady laminar flamelet model and the convection/diffusion evaporation model, particularly concerning the heat release rate (Zhou *et al.*, 2019; Zhou *et al.*, 2021). It is elaborated that one might infer that the overpredictions manifested in the convection/diffusion model are partially due to the uncertainties inherent in the chemical kinetics (Gong *et al.*, 2014).

It is noted that mixture fraction-based models, including the unsteady laminar flamelet approach, generally tend to underestimate fuel consumption in the equilibrium region (Sakib, Farokhi and Birouk, 2023).

Despite the tendency to consistently overestimate CO emissions, this discrepancy could potentially stem from the fact that emission assessments were carried out at the exhaust pipe exit, a factor that might facilitate additional CO oxidation.

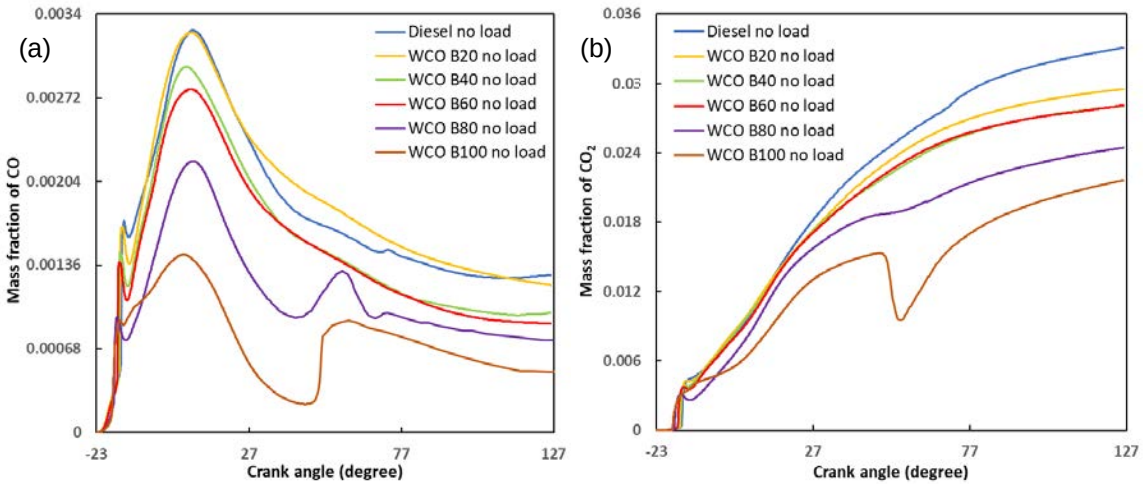

Figure 63 – Mass Fraction of a) CO and b) CO_2 versus Crank angle during CFD simulation at no load condition.

Figures 63 to 66 demonstrate that upon fuel introduction, WCO B100 markedly reduces peak emissions relative to diesel across a range of metrics: CO is reduced by 55.7% and 52.2%, CO_2 by 34.6% and 20.5%, HC (C_2H_6) by 77.7% and 73.7%, soot (C_2H_2) by 67.3% and 60.6%, and NO_x by 25% and 20%, under no load and full load conditions, respectively. Despite these initial reductions, a pronounced increase in emissions is observed in the post-combustion phase. This surge is attributed to the remnants of non-evaporated WCO B100, a consequence of wall impingement, which ignites upon contact with the hot surface of the piston bowl, as elucidated in Chapter 6. This process eventually leads to a decline in emissions, corroborating the discussions in Chapters 5 and 6 regarding the suboptimal combustion efficiency of WCO B100. Building on this, it is vital to heed Vallero's (2019) insights, referenced in Equation 5.2, which advocate for lower oxidation temperatures and extended residence times to facilitate effective CO_2 conversion. The existing scenario, characterized by incomplete combustion, inherently fosters higher CO levels compared to CO_2, highlighting the pivotal role of refining combustion processes to balance these emissions more effectively.

Figures 64 and 65 illustrate that emissions including soot (C_2H_2) and unburned hydrocarbons (C_2H_6) are significantly reduced in the case of WCO B100 compared to diesel fuel. This beneficial outcome is attributed to the ability of biodiesel to incorporate oxygen in its spray molecules during combustion, thereby aiding in the reduction of soot, a phenomenon documented by McCormick et al. (2001). Further supporting this observation, Liu et al. (2014) found that, under diesel engine conditions, Soybean Methyl Ester (SME) biodiesel generated nearly half the total soot mass produced when using diesel. Correspondingly, the current study, as detailed in Figures 63 through 66, demonstrates a notable decrease by 60% in soot mass under no load conditions with the utilisation of WCO B100 compared to diesel. The underpinning reason for this reduction is the presence of extra oxygen atoms within the methyl functional groups of biodiesel, as elucidated by Feng et al. (2012).

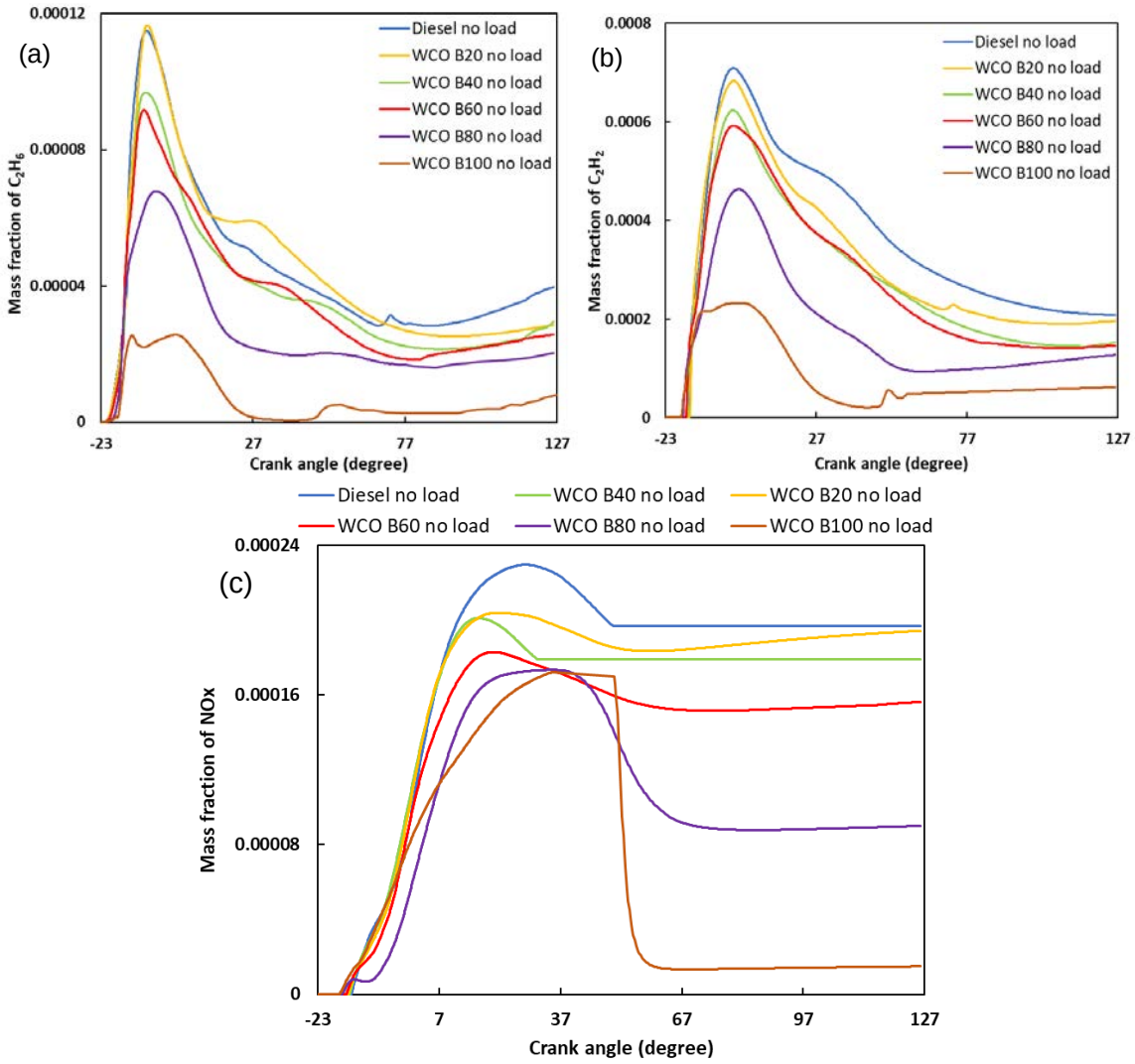

Figure 64 - Mass fraction of a) C_2H_6, b) C_2H_2, and c) NO_X versus Crank angle during CFD simulation at no load condition.

The early evaporation characteristic of WCO B100 prolongs the duration of diffusion combustion, subsequently affecting the adiabatic flame temperature. As detailed in Chapter 5 through the analysis of Heat Release Rate (HRR) depicted in Figures 40, 42, and 44, this results in a lower flame temperature. This progression in flame dynamics, therefore, culminates in a reduced NOx production rate, as substantiated by the data presented in Figures 64 and 65. Subsequently, the diminished levels of NOx may be attributed to the reduced energy content (Table 11) found in WCO B100 (Wang *et al.*, 2006). Additionally, research highlighted in Hellier et al. (2018) noted a direct correlation between extended ignition delays and a rise in NOx production volumes. Hence, as the concentration of WCO B100 escalates, culminating in shortened ignition delays (Figures 45 to 47), a concurrent decline in NOx levels is observed (Hellier *et al.*, 2018).

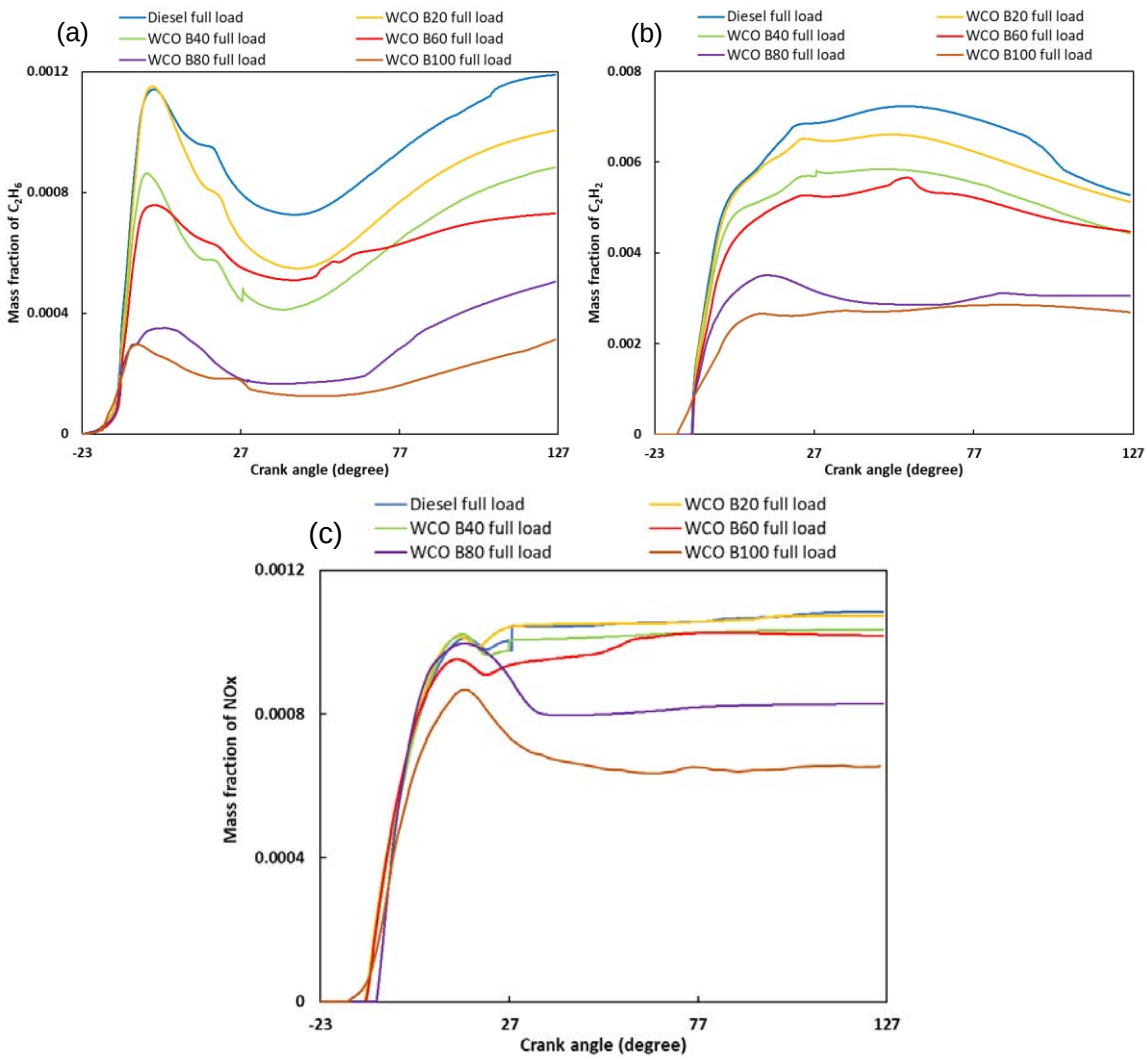

Figure 65 - Mass fraction of a) C_2H_6, b) C_2H_2, and c) NOx versus Crank angle during CFD simulation at full load condition.

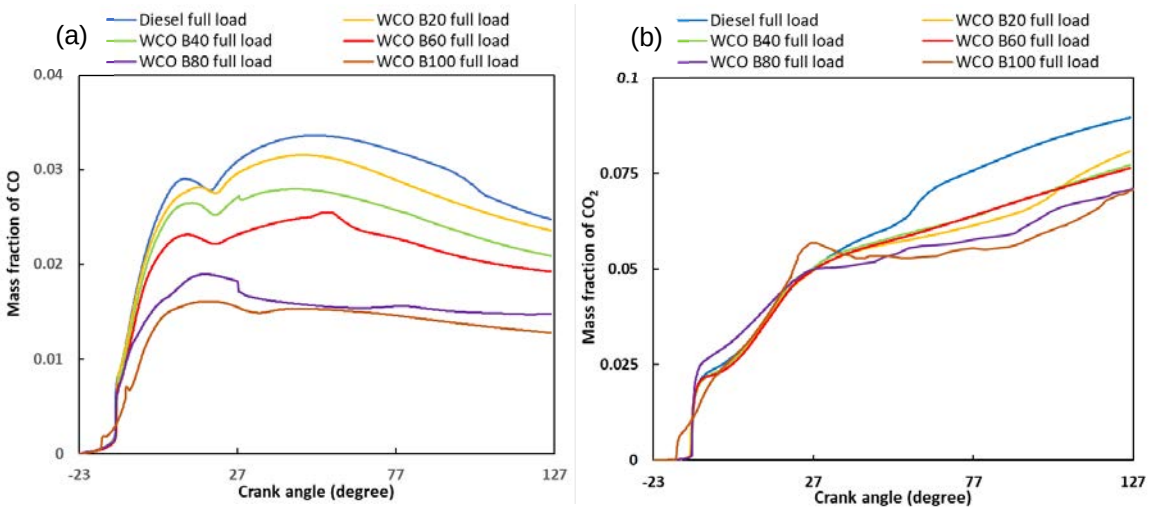

Figure 66 - Mass Fraction of a) CO and b) CO_2 versus Crank angle during CFD simulation at full load condition.

As deduced from the analyses presented in this study, WCO B100 undergoes incomplete combustion, a phenomenon grounded in a set of intertwined factors delineated through various data and graphical representations; a detailed scrutiny of which brings to a converging point of understanding. The pivotal Equation 5.2 becomes instrumental when considering the ratio of deposited CO to CO_2, a parameter that resonates significantly with the data extrapolated from the CFD analyses illustrated in Figure 61 and corroborated by the combustion efficiency insights garnered from Figure 48. The physical properties of the fuel, notably its higher viscosity and surface tension as documented in Table 11 and Appendix G, play a cardinal role. It is these inherent properties that govern the non-optimal air-fuel mixtures, leading to the formation of smaller droplets that are more prone to being carried by the in-cylinder airflow, eventually impinging more readily on the walls, a process vividly illustrated in Chapter 6, Figures 55d, and 57a.

Furthermore, as elucidated by Elhalwagy and Zhang (2019), this scenario sets a stage for a more localized and potentially richer combustion zone. While this entails a surge in thermal efficiency attributed to high-temperature regions localized strategically, it inversely affects the combustion efficiency. The rich combustion zone nurtures a ground for incomplete combustion, a direct consequence of non-optimal air-fuel mixtures.

Adding a layer to this, it is pivotal to note the nuanced performance of WCO B100 in combustion dynamics. According to a study by Hosamani and Katti (2018), WCO B100 yields a lesser burned mass fraction in comparison to diesel, delineating a distinct differential in combustion efficiency. However, they noted a redeeming feature where an increase in the compression ratio facilitated a more substantial fuel burn, hinting at a potential pathway for optimizing the combustion process of WCO B100.

In essence, while WCO B100 exhibits potentials for enhanced thermal efficiency, it grapples with the drawback of incomplete combustion, a phenomenon rooted in its non-optimal air-fuel mixtures, showcasing a pressing need for meticulous optimization in its application.

7.3 Conclusion

- **Emission Changes:**
    - Transitioning from Diesel to WCO B100, HC particulate was reduced by 29.5% (no load), 30% (half load), and 23.5% (full load) (Figures 58-60).
    - NOx emissions were down by 61.8% (no load), 36.3% (half load), and 27.9% (full load). This decline correlates with lower peak heat release rates (Figures 40, 42, 44; Chapter 5).
    - However, increasing load led to emission escalation for CO_2, NOx, and HC. Notably, there was a CO emissions reduction of 68.8% from no load to full load for WCO B100, but CO_2, NOx, and HC increased by 92.2%, 2550%, and 27.4% respectively (Figure 60).
    - A mixture with a higher biofuel concentration increased CO emissions by 16% and CO_2 emissions by 3% under no load conditions (Figure 58). Under half load, there was a 0.77% CO increase and 0.71% CO_2 decrease. Under full load conditions, CO and CO_2 shifted by 1.33% and -4.4% respectively (Figure 59, 60).
- **CFD Simulation Observations:**
    - Acetylene (C_2H_2) represented soot, while ethane (C_2H_6) indicated HC emissions, based on the ERC-MultiChem plus Bio mechanism (Brakora and Reitz, 2013).
    - The validation of CFD results employed pressure and HRR vs. the crank angle (Section 5.3). These comparisons took into account experimental emission data points for CO, CO_2, NOx, and HC at EVO (Figures 61, 62).
    - Simulation discrepancies existed, especially for CO and CO_2 emissions at different load conditions with different fuel types. For instance, under no load, CO emission simulation for WCO B100 underestimated the outcomes by 55.5% while CO_2 simulation underestimated by 21% (Figure 61).

- The discrepancies between simulation and experimental data could be attributed to a variety of interconnected factors: inherent overestimations in the non-premixed unsteady laminar flamelet and the convection/diffusion evaporation models particularly concerning the heat release rate (Zhou et al., 2019; Zhou et al., 2021); potential overpredictions due to uncertainties associated with the chemical kinetics within the convection/diffusion model (Gong et al., 2014); the general trend of mixture fraction-based models, including the unsteady laminar flamelet approach, to underestimate fuel consumption in equilibrium scenarios (Sakib, Farokhi and Birouk, 2023); and the methodology of conducting emission assessments at the exhaust pipe exit which could foster additional CO oxidation, potentially influencing the overestimated CO emissions.

- **Emission Characteristics of WCO B100:**
  - WCO B100, in comparison to diesel, prominently reduces peak emissions, especially during fuel introduction (Figures 63 to 66).
  - Wall impingement of unevaporated WCO B100 ignited upon the hot piston bowl surface, contributing to a spike in post-combustion emissions (Chapter 6). This underlines the suboptimal combustion efficiency of WCO B100.
  - WCO B100 combustion led to higher CO levels as compared to CO_2, emphasizing the need to improve combustion processes for effective emission balance.
  - Emissions of soot and unburned hydrocarbons were notably reduced with WCO B100, a result of biodiesel's oxygen incorporation during combustion (McCormick et al., 2001; Liu et al., 2014; Figures 63 to 66).
  - The WCO B100's early evaporation characteristic, combined with the extra oxygen atoms in its structure, led to a reduced NOx production rate (Figures 40, 42, 44, 64, 65; Feng et al., 2012).

- **Insights on WCO B100 Combustion:**
    - Equation 5.2 significance:
        - Serves as a linchpin in understanding the CO to CO_2 ratio, substantially corroborated by the insights derived from CFD analyses in Figure 61 and combustion efficiency parameters in Figure 48.
    - Physical properties and their Impact:
        - Viscosity and surface tension: recognized as cardinal factors affecting combustion; documented extensively in Table 11 and Appendix G.
        - Air-fuel mixture: non-optimal ratios lead to smaller droplets prone to being carried away easily, facilitating frequent collisions with the chamber walls, a phenomenon illustrated vividly in Chapter 6, Figures 55d, and 57a.
    - Literature Support and Previous Studies:
        - Elhalwagy and Zhang (2019): elaborated on the creation of localized and richer combustion zones, thereby increasing thermal efficiency but also fostering grounds for incomplete combustion.
        - Hosamani and Katti (2018): highlighted a lesser burned mass fraction for WCO B100 when compared to diesel, pointing towards a substantial differential in combustion efficiency.

A salient theme emanating from the literature, particularly underscored by Demirbas (2009), is the inherent ability of biodiesel, owing to its complex unsaturated composition, to influence emission attributes positively. This phenomenon has been affirmed in the recent experimentation wherein substantial reductions in HC particulate emissions were observed across various load levels when utilising WCO B100.

Furthermore, the findings resonate with Liu et al. (2014) and Feng et al. (2012) who identified a pronounced reduction in soot formation facilitated by the oxygen atoms present in the biodiesel's methyl functional groups. The current research robustly supports this trend, documenting a substantial decrease in unburned hydrocarbons and soot during WCO B100 combustion.

When analysing NOx emissions, a nuanced picture emerges. While Xue et al. (2011) reported an escalation in NOx levels with biodiesel utilisation, the present study delineated a contrary trend, showcasing a decline in NOx emissions with WCO B100 usage across all load spectrums. This aligns with assertions posited by Feng et al. (2012) attributing the reduced NOx production rate to early evaporation characteristics and additional oxygen atoms in biodiesel.

One of the critical revelations of the current investigation pertains to the influence of ignition delay on emission characteristics. Ermen et al. (2020) established a correlation between increased ignition delay and the formation of an over-diluted or excessively lean mixture, which invariably culminated in a surge in carbon monoxide generation. This theoretical postulation found empirical resonance in the present dataset, highlighting a modest increase in CO emissions, attributed to mixture quenching at the cylinder walls instigated by extended ignition delays.

Notwithstanding, it is prudent to underscore that the present study introduces a divergence from several scholarly perspectives, potentially instigated by the distinct combustion behaviour manifested by WCO B100 compared to traditionally studied biodiesel classifications.

The discourse surrounding CO and CO_2 emissions unveils congruencies with the insights presented by Yaqoob et al. (2021), delineating a correlated trend in emission variations at disparate engine loads. Additionally, Bergthorson and Thomson (2015) highlighted the necessity to optimise the combustion process to harmonise emission levels, a focal point underscored in the present research which elucidated a rise in CO_2, NOx, and HC emissions with increasing engine loads.

The discrepancies observed in the simulation outcomes within this study echo the apprehensions voiced in the research conducted by Zhou et al. (2019; 2021) and Gong et al. (2014), pinpointing the limitations inherent in the prevailing modelling strategies, including the non-premixed unsteady laminar flamelet and the convection/diffusion model. This observation accentuates the pressing need for the development of more sophisticated simulation frameworks to foster a nuanced understanding of biodiesel combustion dynamics.

7.4 Sensitivity analyses

7.4.1 Introduction

In this section, the 0-D ANSYS Chemkin-Pro DI Engine simulations, elaborated in Section 4.3, are leveraged to analyse the major reactions that significantly influence the consumption and production of pivotal emission species such as CO (carbon monoxide), CO_2 (carbon dioxide), NO_x (nitrogen oxides), C_2H_2 (acetylene) as a soot precursor, and C_2H_6 (ethane) as a hydrocarbon precursor. This analysis is extended to encompass key ignition species, namely OH (hydroxyl radicals), CH_2O (formaldehyde), and H_2O_2 (hydrogen peroxide).

Adding to this, the "cool flame" phenomenon, delineated by a two-stage ignition process and a prominent role in low-temperature chemistry, engages species such as H_2O_2 in its initial phase (Liu *et al.*, 2019). Notably, the presence of H_2O_2 and CH_2O can facilitate a transition to higher temperature zones, potentially decomposing to form OH radicals, which are vital in the combustion process (Liu *et al.*, 2019). Concluding this section, the major reactions involving the fuel representative species outlined in Table 10 are thoroughly examined.

Key reactions were selected based on their significant contributions to the production rates of specific species across various fuels, including Diesel (B7), WCO B20, WCO B40, WCO B60, WCO B80, and WCO B100. These pivotal reactions, identified through sensitivity analyses in ANSYS Chemkin-Pro, consistently manifested prominent contributions under both no-load and full-load conditions. Organized meticulously by their absolute rate of production (ARP), these reactions remained dominant and common denominators for each species across varying load scenarios.

The validation of the simulation is based on in-cylinder pressure versus crank angle as presented in Figures 67 and 68.

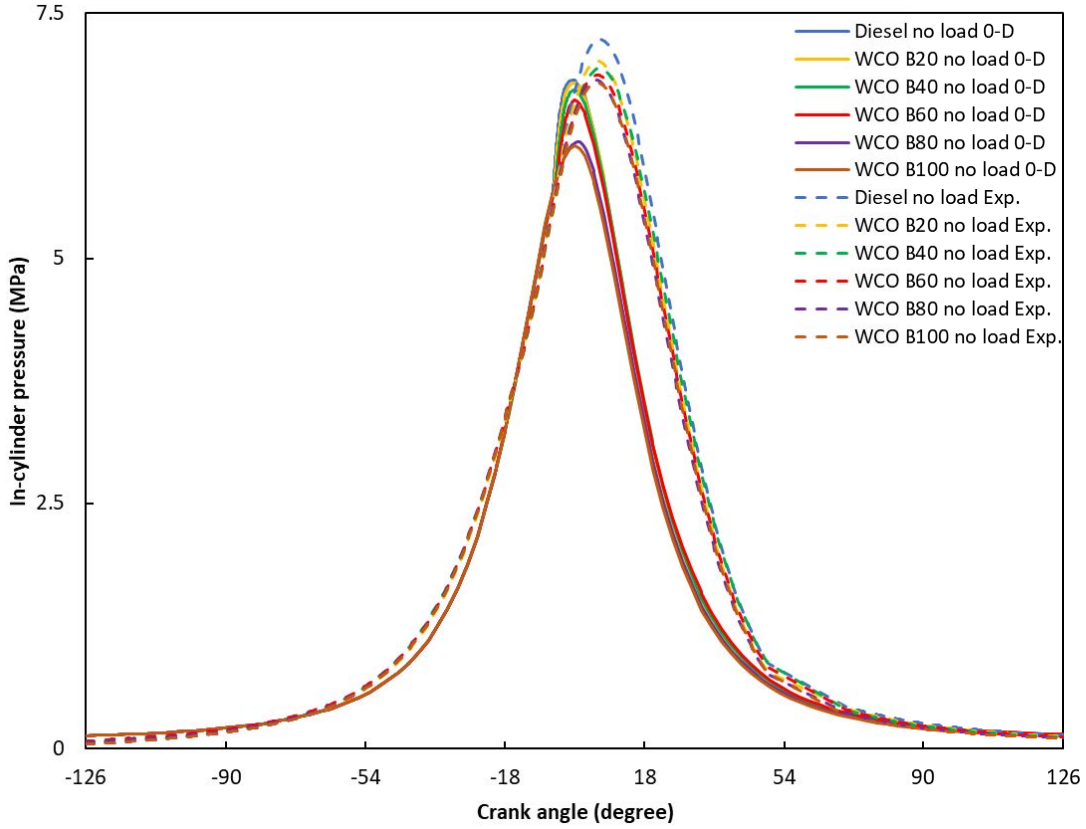

Figure 67 – 0-D and experimental validation of in-cylinder pressure against crank angle at no load condition.

In Figures 67 and 68, the discrepancies in the prediction of maximum pressure are scrutinised, with distinctive focus on underprediction and overprediction across various fuel types, which include Diesel, WCO B20, WCO B40, WCO B60, WCO B80, and WCO B100. Specifically, Figure 67 delineates the underprediction of the maximum pressure, establishing it through percentage errors that amount to 5.7% for Diesel, followed by 3.17% for WCO B20, 3.19% for WCO B40, 3.75% for WCO B60, 9.2% for WCO B80, and culminating at 9.5% for WCO B100. In juxtaposition, Figure 68 engages with the overprediction of the maximum pressure, identifying percentage errors; accordingly, Diesel at 5%, WCO B20 at 5.7%, WCO B40 at 5.9%, WCO B60 at 5.8%, WCO B80 at 5.2%, and WCO B100 at 4.25%. This analysis unfolds a critical assessment of the predictive accuracy, thereby shedding light on the specific margins of error that characterize the pressure predictions for each fuel type.

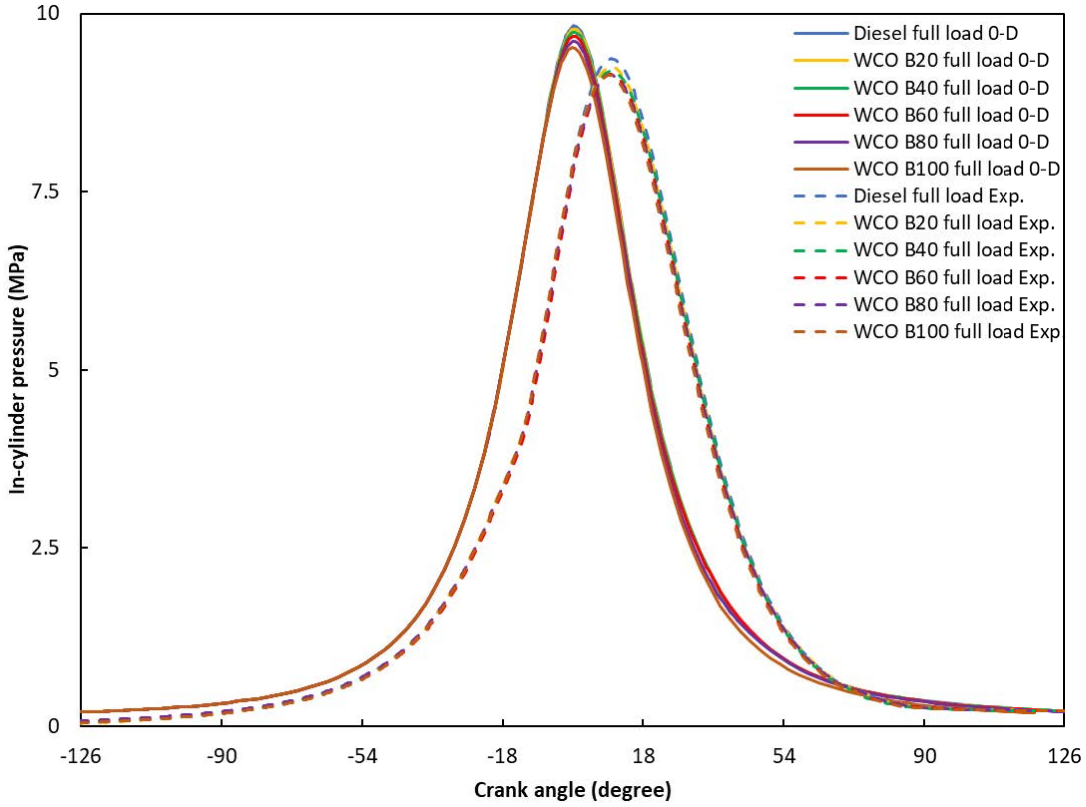

Figure 68 - 0-D and experimental validation of in-cylinder pressure against crank angle at full load condition.

7.4.2 Results and discussion

7.4.2.1 Ignition species

Formaldehyde (CH_2O)

$OH+CH_2CO \rightarrow HCO+CH_2O$	ARP: 1.68E-2	(7.2)
$O+CH_2O \leftarrow OH+HCO$	ARP: 1.51E-2	(7.3)
$NC_7\text{-}QOOH \rightarrow OH+CH_2O+NC_4H_8+C_2H_4$	ARP: 4.39E-4	(7.4)
$OH+CH_2O \rightarrow H_2O+HCO$	ARP: 4.14E-4	(7.5)
$CH_3O(+M) \leftrightarrow CH_2O+H(+M)$	ARP: 3.06E-4	(7.6)
$HO_2+CH_2O \rightarrow H_2O_2+HCO$	ARP: 1.38E-4	(7.7)
$O_2+CH_2CHO \rightarrow CH_2O+OH+CO$	ARP: 6.62E-5	(7.8)
$O_2+CH_3O \rightarrow HO_2+CH_2O$	ARP: 3.97E-5	(7.9)
$O+CH_2O \rightarrow 2H+CO_2$	ARP: 9.38E-6	(7.10)
$OH+CH_2O \rightarrow H+H_2+CO_2$	ARP: 4.69E-6	(7.11)
$C_2H_5OO+CO \rightarrow CO_2+CH_3+CH_2O$	ARP: 2.74E-6	(7.12)
$CH_2+CO_2 \leftrightarrow CO+CH_2O$	ARP: 5.2E-16	(7.13)

In the intricate chemical ballet of combustion, formaldehyde (CH_2O) stands out as a pivotal intermediary, involved in a diverse array of reactions. A closer look at the

ARP values gives a clear indication of the significance and dominance of certain pathways over others. Reactions 7.2 and 7.3, with ARP values of 1.68E-2 and 1.51E-2 respectively, emerge as the predominant routes, indicating that the interactions involving OH, ketene (CH_2CO), and O play a major role in the generation or consumption of CH_2O. Specifically, the conversion of OH with ketene (CH_2CO) and O's interaction with CH_2O highlight the dynamic balance of formaldehyde in combustion systems. Moving down the scale of prominence, reactions like 7.4 to 7.7 with ARP values in the range of E-4, indicating moderate significance in the overall CH_2O dynamics are found. It's interesting to note the transformation led by nC_7 hydroperoxy alkyl radicals (NC_7-QOOH) in reaction 7.4, which, although having a comparatively lower ARP, provides insight into the multifaceted interactions leading to CH_2O generation alongside other products. Reactions 7.8 to 7.12 shed light on the lesser, but still important, pathways involving CH_2O. Whether it's the addition of O_2 in the context of acetaldehyde (CH_2CHO) or methoxy radical (CH_3O), or the more intricate pathways leading to the production or consumption of CO_2, these reactions underscore the versatility and ubiquity of formaldehyde in combustion reactions.

Lastly, reaction 7.13, with its significantly lower ARP value of 5.2E-16, points towards a negligible role in the CH_2O-centric processes.

Hydrogen peroxide (H_2O_2)

$2OH(+M)\leftrightarrow H_2O_2(+M)$	ARP: 2.57E-3	(7.14)
$2HO_2\leftrightarrow H_2O_2+O_2$	ARP: 2.3E-3	(7.15)
$HO_2+NC_7H_{16}\rightarrow H_2O_2+NC_7H_{15}$	ARP: 2.81E-4	(7.16)
$HO_2+CH_2O\rightarrow H_2O_2+HCO$	ARP: 1.38E-4	(7.17)
$HO_2+C_7H_8\rightarrow H_2O_2+C_7H_7$	ARP: 7.1E-5	(7.18)
$CH_3O+HO_2\rightarrow H_2O_2+CH_2O$	ARP: 1.82E-6	(7.19)
$HO_2+MEOLE\rightarrow H_2O_2+RMEOLES$	ARP: 3.06E-8	(7.20)

The dynamics of hydrogen peroxide in combustion processes are intricate, playing a pivotal role in the oxidative environment. For H_2O_2, the two reactions with the highest ARP involve the combination of OH radicals (2.57E-3) reaction 7.14 and the reaction 7.15 between hydroperoxyl radical (HO_2) species (2.3E-3). These dominant reactions suggest a strong influence of hydroxyl radicals and HO_2 in the production of H_2O_2.

Hydroxyl radicals (OH)

$OH+NC_7H_{16}\leftarrow H_2O+NC_7H_{15}$	ARP: 6.16E-3	(7.21)
$CH_3+H_2O\rightarrow CH_4+OH$	ARP: 3.7E-3	(7.22)
$2OH(+M)\leftrightarrow H_2O_2(+M)$	ARP: 2.57E-3	(7.23)
$NC_7\text{-}QOOH\rightarrow NC_7H_{14}O+OH$	ARP: 9.04E-4	(7.24)
$O_2+CH_2CHO\rightarrow CH_2O+OH+CO$	ARP: 7.58E-4	(7.25)
$OH+CH_2O\leftarrow H_2O+HCO$	ARP: 4.14E-4	(7.26)
$O+NC_7H_{16}\rightarrow OH+NC_7H_{15}$	ARP: 2.37E-4	(7.27)
$OH+HO_2\leftrightarrow H_2O+O_2$	ARP: 1.86E-4	(7.28)
$O+H_2\leftrightarrow OH+H$	ARP: 5.63E-6	(7.29)
$OH+CH_3\leftrightarrow CH_2O+H_2$	ARP: 4.46E-6	(7.30)

In the realm of combustion chemistry, hydroxyl radicals (OH) emerge as central players, intricately woven into various pathways. Firstly, the prominent ARP of 6.16E-3 for the reaction $OH+NC_7H_{16}$ (reaction 7.21) showcases the hydrocarbon oxidation's efficiency, where hydrocarbons are adeptly converted into OH radicals, thereby bolstering the combustion cascade. Equally notable is water's multifaceted role, which goes beyond being a mere combustion end-product. The CH_3+H_2O pathway (reaction 7.22, ARP: 3.7E-3) underscores water's active participation in radical generation, emphasizing its indispensable role in the oxidative landscape. Further shedding light on the tightly interwoven dynamics, reaction 7.23 (ARP: 2.57E-3) reinforces the intricate connection between H_2O_2 and OH, illustrating a complex interplay pivotal for the balance of reactive species. Delving deeper into the maze of radical interactions, reactions such as O_2+CH_2CHO leading to OH (reaction 7.25, ARP: 7.58E-4) and the transformation steered by (NC_7-QOOH) nC_7 hydroperoxy alkyl radicals (reaction 7.24, ARP: 9.04E-4) spotlight the myriad avenues contributing to OH radical genesis. Combined with OH's role in reactions 7.26 to 7.30, these processes show the complexity of combustion, highlighting how molecules and radicals work closely together in this system.

7.4.2.2 Emission species

Carbon monoxide (CO)

$O_2+HCO\leftrightarrow HO_2+CO$	ARP: 7.21E-3	(7.31)
$HCO+M\leftrightarrow CO+H+M$	ARP: 2.67E-3	(7.32)
$HCCO+O_2\leftrightarrow 2CO+OH$	ARP: 1.76E-3	(7.33)

$CH_3CO+M \leftrightarrow CH_3+CO+M$	ARP: 1.6E-3	(7.34)
$CH_3OCO \leftrightarrow CO+CH_3O$	ARP: 1.5E-3	(7.35)
$CO+OH \leftrightarrow CO_2+H$	ARP: 1.1E-3	(7.36)
$CO+HO_2 \leftrightarrow CO_2+OH$	ARP: 8.8E-4	(7.37)
$CH_3OO+CO \rightarrow CO_2+CH_3O$	ARP: 4.62E-6	(7.38)
$C_2H_5OO+CO \rightarrow CO_2+CH_3+CH_2O$	ARP: 2.74E-6	(7.39)
$C_7H_7+CO \leftrightarrow BZFUR+H$	ARP: 1.26E-9	(7.40)
$CO+H_2O \leftrightarrow CO_2+H_2$	ARP: 1.1E-10	(7.41)
$CH_2+CO_2 \leftrightarrow CO+CH_2O$	ARP: 5.2E-16	(7.42)

Carbon monoxide (CO) is a pivotal species within combustion processes, serving as both a reactant and a product in various reactions. Analysing the ARP values offers insights into the hierarchy of these chemical pathways, emphasizing the predominant reactions influencing CO's dynamics in the combustion system. Reactions 7.31 to 7.35, with ARP values in the range of E-3, stand out as significant pathways determining CO's presence in the system. Specifically, the interaction of O_2 with HCO in reaction 7.31, holding an ARP of 7.21E-3, is highlighted as a central pathway for CO production. Concurrently, reactions such as 7.32 and 7.33 showcase the decomposition of hydrogen carbonate (HCO) and ketenyl radical (HCCO), elucidating the multifaceted evolution of CO within this complex chemical environment.

Further into the processes, reactions 7.36 and 7.37, characterized by ARP values nearing 1E-3, underscore the consumption of CO in the presence of OH and HO_2 radicals. These reactions point to CO's transition to CO_2, emphasizing the pivotal role radicals play in ensuring an efficient CO conversion — a factor essential for mitigating emissions in practical scenarios. Although reactions 7.38 to 7.40 possess lower ARP values ranging from E-6 to E-9, they nonetheless merit consideration. These reactions depict diverse interactions, from the transformation of CO_2 in the company of organic peroxides to more specialized pathways involving larger hydrocarbons such as benzyl (C_7H_7).

Lastly, reactions 7.41 and 7.42, having ARP values of 1.1E-10 and 5.2E-16, respectively, might play minor roles in the immediate dynamics of CO. However, their inclusion offers a comprehensive perspective on the potential pathways CO might undertake, irrespective of their immediate significance.

Carbon dioxide (CO_2)

$CO+OH \leftrightarrow CO_2+H$	ARP: 1.1E-3	(7.43)
$CO+HO_2 \leftrightarrow CO_2+OH$	ARP: 8.8E-4	(7.44)
$CH_3OCO \leftrightarrow CO_2+CH_3$	ARP: 9.03E-5	(7.45)
$OH+CH_2CO \rightarrow CH_3+CO_2$	ARP: 8.88E-5	(7.46)
$HCCO+O_2 \leftrightarrow CO_2+HCO$	ARP: 1.9E-5	(7.47)
$O_2+CH_2CO \rightarrow CH_2O+CO_2$	ARP: 1.42E-5	(7.48)
$OH+C_2H_3CHO \rightarrow CO_2+C_2H_4+H$	ARP: 1.18E-5	(7.49)
$O+CH_2O \rightarrow 2H+CO_2$	ARP: 9.38E-6	(7.50)
$OH+CH_2O \rightarrow H+H_2+CO_2$	ARP: 4.69E-6	(7.51)
$CO+H_2O \leftrightarrow CO_2+H_2$	ARP: 1.1E-10	(7.52)
$HCO+CH_2O \leftrightarrow CO_2+CH_3$	ARP: 7E-12	(7.53)
$CH_2+CO_2 \leftrightarrow CO+CH_2O$	ARP: 5.2E-16	(7.54)

Carbon dioxide (CO_2) production and consumption are pivotal to the dynamics of combustion chemistry, as illustrated by the following reactions. The reaction between carbon monoxide (CO) and the hydroxyl radical (OH) is a significant source of CO_2, as shown in reaction 7.43 with an ARP value of 1.1E-3. This is further validated by reaction 7.44, where CO reacts with hydroperoxyl radical (HO_2) to produce CO_2, though with a slightly lesser ARP value of 8.8E-4. These reactions highlight the role of radicals in CO_2 formation. Other contributors to CO_2 production are reactions involving methyl radicals and acetyl radicals. Reaction 7.45 presents the decomposition of the methyl formate radical (CH_3OCO) leading to CO_2 and CH_3, while in reaction 7.46, the hydroxyl radical reacts with ketene (CH_2CO) to form CO_2 and CH_3.

Several reactions with lower ARP values, such as reactions 7.47 through 7.49, further emphasize the myriad pathways contributing to CO_2 generation. Notably, reactions 7.50 and 7.51 underline the significance of formaldehyde (CH_2O) in CO_2 production, even if their ARP values are smaller in comparison to the top reactions. On the consumption side, CO_2's role seems to be relatively minor based on the given reactions. Reaction 7.52 showcases a potential CO_2 consumption route, where CO reacts with water (H_2O) to produce CO_2, but the ARP value is extremely low at 1.1E-10. Similarly, reactions 7.53 and 7.54 also present potential pathways

for CO_2 consumption, but the extremely low ARP values suggest these are not dominant pathways.

In summary, CO_2 production is facilitated majorly through reactions involving radicals like OH and HO_2, and its consumption appears to be less significant based on the given ARP values. The presented reactions serve as a testament to the complexity of combustion chemistry and the multitude of pathways governing CO_2 dynamics.

Nitrogen oxides (NOx)

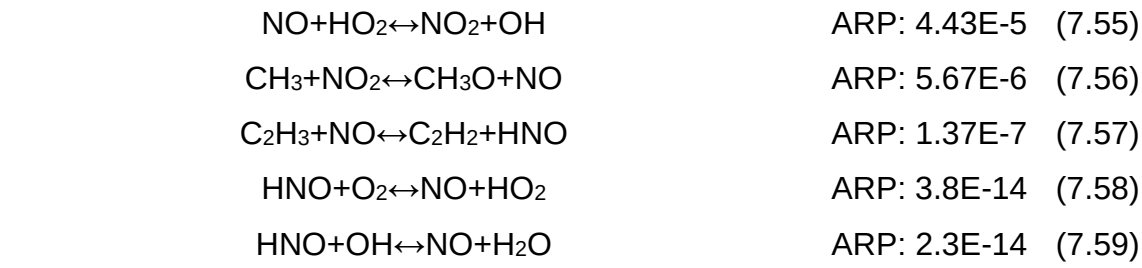

$NO+HO_2 \leftrightarrow NO_2+OH$	ARP: 4.43E-5	(7.55)
$CH_3+NO_2 \leftrightarrow CH_3O+NO$	ARP: 5.67E-6	(7.56)
$C_2H_3+NO \leftrightarrow C_2H_2+HNO$	ARP: 1.37E-7	(7.57)
$HNO+O_2 \leftrightarrow NO+HO_2$	ARP: 3.8E-14	(7.58)
$HNO+OH \leftrightarrow NO+H_2O$	ARP: 2.3E-14	(7.59)

The most significant reaction in this category is NO interacting with HO_2, producing NO_2 and OH, with an ARP value of 4.43E-5 (reaction 7.55). This reaction showcases the transformation of primary nitrogen oxide (NO) into secondary nitrogen oxide (NO_2) under the influence of the hydroperoxy radical. Given the high ARP value, this pathway can be a predominant route in combustion processes, especially under high-temperature conditions. Other reactions exhibit a notable decrease in ARP values, suggesting that they play a secondary role in the dynamics of NOx formation and consumption. The low ARP values for reactions involving HNO (reactions 7.58 and 7.59) indicate their minimal significance under typical combustion environments.

Acetylene (C_2H_2)

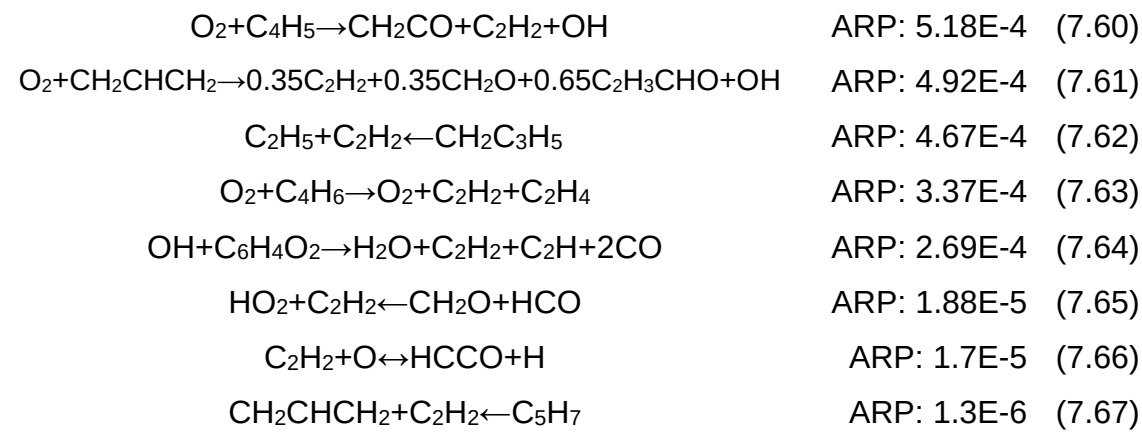

$O_2+C_4H_5 \rightarrow CH_2CO+C_2H_2+OH$	ARP: 5.18E-4	(7.60)
$O_2+CH_2CHCH_2 \rightarrow 0.35C_2H_2+0.35CH_2O+0.65C_2H_3CHO+OH$	ARP: 4.92E-4	(7.61)
$C_2H_5+C_2H_2 \leftarrow CH_2C_3H_5$	ARP: 4.67E-4	(7.62)
$O_2+C_4H_6 \rightarrow O_2+C_2H_2+C_2H_4$	ARP: 3.37E-4	(7.63)
$OH+C_6H_4O_2 \rightarrow H_2O+C_2H_2+C_2H+2CO$	ARP: 2.69E-4	(7.64)
$HO_2+C_2H_2 \leftarrow CH_2O+HCO$	ARP: 1.88E-5	(7.65)
$C_2H_2+O \leftrightarrow HCCO+H$	ARP: 1.7E-5	(7.66)
$CH_2CHCH_2+C_2H_2 \leftarrow C_5H_7$	ARP: 1.3E-6	(7.67)

$$OH+C_2H_2 \leftarrow CH_3+CO \quad \text{ARP: 1.1E-6} \quad (7.68)$$

The pivotal role of acetylene (C_2H_2) in combustion processes is illuminated by the provided reactions. Acetylene often emerges as a key intermediate during the early stages of hydrocarbon decomposition, especially under fuel-rich conditions. It then either engages in pathways that lead to larger molecules or gets consumed in oxidative sequences. The prominence of specific reactions can be gauged using Absolute Rate Parameter (ARP) values. Notably, the elevated ARP values for reactions (7.60, 7.61, and 7.62) suggest that these acetylene-involved pathways are particularly significant under the given conditions. Furthermore, acetylene's propensity to interact with other radicals or hydrocarbons, as evidenced by its reaction (7.62) with the ethyl radical (C_2H_5) to spawn the 1 buten-3-yl radical ($CH_2C_3H_5$), underlines the intricate nature of combustion chemistry.

Ethane (C_2H_6)

$$2CH_3(+M) \leftrightarrow C_2H_6(+M) \quad \text{ARP: 5.25E-6} \quad (7.69)$$

$$OH+C_2H_6 \leftarrow H_2O+C_2H_5 \quad \text{ARP: 3.41E-6} \quad (7.70)$$

$$C_2H_5+NC_7H_{16} \rightarrow C_2H_6+NC_7H_{15} \quad \text{ARP: 9.47E-7} \quad (7.71)$$

The predominant route for ethane formation appears to be via the combination of two methyl radicals, as indicated by the ARP value of 5.25E-6 (reaction 7.69). This reaction underscores the importance of radical recombination in producing more significant hydrocarbons during combustion. The consumption of ethane, as suggested by the reaction with the hydroxyl radical (reaction 7.70), points towards the typical oxidative pathways that alkanes undergo in combustion environments. The interaction of ethane with larger hydrocarbons, as seen in the last reaction 7.71, highlights the complexity and interconnectedness of hydrocarbon reactions, even in seemingly simple combustion systems.

7.4.2.3 Fuel representative species

7.4.2.3.1 Diesel

Toluene (C_7H_8)

$$OH+C_7H_8 \rightarrow C_7H_7+H_2O \quad \text{ARP: 2.73E-4} \quad (7.72)$$

$$OH+C_7H_8 \rightarrow C_6H_4CH_3+H_2O \quad \text{ARP: 1.09E-4} \quad (7.73)$$

$$O+C_7H_8 \leftrightarrow RCRESOLO+H \quad \text{ARP: 8.44E-5} \quad (7.74)$$

$$HO_2+C_7H_8 \rightarrow H_2O_2+C_7H_7 \quad \text{ARP: 7.1E-5} \quad (7.75)$$

$$CH_3+C_7H_8 \leftrightarrow CH_4+C_7H_7 \quad \text{ARP: 9.02E-7} \quad (7.76)$$

1-Hexene (NC_6H_{12})

$$OH+NC_6H_{12}\rightarrow H_2O+C_4H_6+C_2H_5 \quad \text{ARP: 3.3E-4} \quad (7.77)$$

N-heptane (NC_7H_{16})

$$OH+NC_7H_{16}\rightarrow H_2O+NC_7H_{15} \quad \text{ARP: 3.01E-3} \quad (7.78)$$

$$HO_2+NC_7H_{16}\rightarrow H_2O_2+NC_7H_{15} \quad \text{ARP: 2.81E-4} \quad (7.79)$$

$$O+NC_7H_{16}\rightarrow OH+NC_7H_{15} \quad \text{ARP: 2.37E-4} \quad (7.80)$$

$$CH_2CHCH_2+NC_7H_{16}\rightarrow C_3H_6+NC_7H_{15} \quad \text{ARP: 4.6E-6} \quad (7.81)$$

$$C_2H_5+NC_7H_{16}\rightarrow C_2H_6+NC_7H_{15} \quad \text{ARP: 9.47E-7} \quad (7.82)$$

Within the domain of diesel major species, Toluene (C_7H_8), 1-Hexene (NC_6H_{12}), and N-heptane (NC_7H_{16}) are central players. The provided reactions shed light on their consumption and production mechanisms, illustrating how these species contribute to and emerge from the combustion processes.

For Toluene, the most significant pathway of consumption is through its reaction with OH radicals, producing benzyl (C_7H_7) and water, as given by reaction 7.72 with an ARP of 2.73E-4. Another pathway of Toluene's consumption involves its decomposition into methylphenyl ($C_6H_4CH_3$) and water, represented by reaction 7.73 with an ARP value of 1.09E-4. Lesser pathways include its interaction with O radicals leading to RCRESOLO (cresol radical, fenoxy like) and H in reaction 7.74 and its conversion with HO_2 radicals to produce H_2O_2 and C_7H_7, denoted by reaction 7.75. CH_3's addition to Toluene, although having a negligible ARP of 9.02E-7 (reaction 7.76), further enriches the intricate web of Toluene's interaction dynamics.

Turning to 1-Hexene, its primary consumption pathway involves a reaction with OH radicals, leading to the formation of water, C_4H_6 (butadienes plus butyne), and ethyl (C_2H_5), as highlighted in reaction 7.77 with an ARP value of 3.3E-4. This reaction elucidates how 1-Hexene contributes to the formation of multiple products during combustion.

In the case of N-heptane, a significant consumption pathway is evident through its reaction with OH radicals, producing NC_7H_{15} (nC_7 alkyl radicals) and water (7.78, ARP: 3.01E-3). Other notable reactions include its interaction with HO_2 radicals, resulting in H_2O_2 and NC_7H_{15} in reaction 7.79 with an ARP value of 2.81E-4, and its interaction with O radicals, leading to OH and NC_7H_{15} as denoted in reaction 7.80. Although less significant, interactions like those in reactions 7.81 and 7.82

further emphasize the diverse pathways through which N-heptane is consumed during combustion processes.

7.4.2.3.2 Waste Cooking Oil Biodiesel (WCO B100)

Methyl oleate (MEOLE)

$$H+MEOLE \rightarrow RSTEAX \quad \text{ARP: 2.82E-5} \quad (7.83)$$

$$OH+MEOLE \rightarrow H_2O+RMEOLES \quad \text{ARP: 1.93E-6} \quad (7.84)$$

$$HO_2+MEOLE \rightarrow H_2O_2+RMEOLES \quad \text{ARP: 3.06E-8} \quad (7.85)$$

Methyl stearate (MSTEA)

$$OH+MSTEA \rightarrow H_2O+RSTEAX \quad \text{ARP: 1.75E-6} \quad (7.86)$$

Methyl palmitate (MPA)

$$OH+MPA \rightarrow H_2O+RMPAX \quad \text{ARP: 9.64E-6} \quad (7.87)$$

Methyl linolenate (MLIN1)

$$OH+MLIN1 \rightarrow ALDEST+H_2+C_{12}H_{18}+CH_3 \quad \text{ARP: 1.36E-5} \quad (7.88)$$

$$OH+MLIN1 \rightarrow H_2O+RMLIN1A \quad \text{ARP: 5.47E-6} \quad (7.89)$$

$$OH+MLIN1 \rightarrow H_2O+RMLIN1X \quad \text{ARP: 3.64E-6} \quad (7.90)$$

Methyl linoleate (MLINO)

$$OH+MLINO \rightarrow H_2O+RMLINA \quad \text{ARP: 1.6E-5} \quad (7.91)$$

$$OH+MLINO \rightarrow H_2O+RMLINX \quad \text{ARP: 1.2E-5} \quad (7.92)$$

The reactions associated with waste cooking oil biodiesel (WCO B100) offer insights into the combustion dynamics of its primary constituents: Methyl oleate (MEOLE), Methyl stearate (MSTEA), Methyl palmitate (MPA), Methyl linolenate (MLIN1), and Methyl linoleate (MLINO). For Methyl oleate (MEOLE), the transformation into methyl stearate radicals (RSTEAX) with the assistance of a hydrogen radical is evident in reaction 7.83 with an ARP value of 2.82E-5. Furthermore, the reaction with OH, as observed in 7.84, leads to the formation of water and secondary radical methyl oleate (RMEOLES). An additional pathway involving hydroperoxyl radical (HO_2) presents itself in 7.85, resulting in H_2O_2 and RMEOLES, although with a lesser ARP value of 3.06E-8, indicating its reduced likelihood.

Methyl stearate (MSTEA) primarily interacts with the OH radical to form water and RSTEAX, as depicted in reaction 7.86 with an ARP value of 1.75E-6, denoting

moderate significance in the combustion environment. In the context of Methyl palmitate (MPA), the major route is through its reaction with OH, which yields water and methyl palmitate radicals (RMPAX), as described in reaction 7.87 with an ARP value of 9.64E-6.

A wider range of reactions is observed for Methyl linolenate (MLIN1). Its interactions with OH manifest in multiple pathways that lead to the production of compounds such as 5-oxohexanoic acid (ALDEST), hydrogen (H_2), dodecaquatriene ($C_{12}H_{18}$), methyl (CH_3), RMLIN1A (all radical melinolenate), and RMLIN1X (radical melinolenate), as detailed from reactions 7.88 to 7.90. Among these, the production of ALDEST and $C_{12}H_{18}$ in reaction 7.88 appears more predominant with an ARP value of 1.36E-5. Methyl linoleate (MLINO) predominantly undergoes reactions with OH, resulting in the formation of water and either radical methyl linoleate (RMLINA) or RMLINX (all radical methyl linoleate). These pathways, shown in reactions 7.91 and 7.92, have ARP values of 1.6E-5 and 1.2E-5 respectively, suggesting comparable importance in the combustion process of the waste cooking oil biodiesel.

7.4.3 Summary of findings

Formaldehyde (CH_2O) is predominantly produced through reactions 7.2 and 7.3, which involve OH and O radicals, but its multifaceted presence in combustion systems is also influenced by reactions such as 7.4 and 7.5. Hydrogen Peroxide (H_2O_2) has its primary production pathway due to the reaction of OH radicals (7.14) and the interaction between hydroperoxyl radical (HO_2) species, as demonstrated by 7.15. Central to combustion chemistry, Hydroxyl Radicals (OH) largely participate in reactions 7.21 and 7.22, emphasizing its role in hydrocarbon oxidation and radical generation with water and hydrogen peroxide.

Carbon Monoxide (CO) showcases a complex evolution in combustion. Reactions like 7.32 with HCO and 7.31 with O_2 highlight its production, while its conversion to CO_2 is heavily reliant on reactions like 7.36 with OH and 7.37 with HO_2. The primary production of Carbon Dioxide (CO_2) is steered by reactions 7.43 and 7.44 with OH and HO_2 radicals, even though its consumption appears to be minor based on the given ARPs. In the realm of NOx formation, the conversion of NO to NO_2 is significantly noted through reaction 7.55 under high-temperature conditions. Acetylene (C_2H_2) acts as a pivotal intermediate, with reactions like 7.60 and 7.62

signifying its pathways leading to larger molecules or its consumption in oxidative sequences. For Ethane, radical recombination is majorly represented by 7.69, but its typical oxidative pathways in combustion also include reactions like 7.70 and 7.71.

For major species in diesel, Toluene prominently reacts with OH radicals as seen in 7.72, while 1-Hexene and N-heptane display significant consumption pathways through reactions 7.77 and 7.78 with radicals like OH and HO_2. In the context of Waste Cooking Oil Biodiesel (WCO B100) constituents, Methyl oleate undergoes crucial transformations as indicated by 7.83 and 7.84; Methyl stearate and Methyl palmitate predominantly interact with OH as depicted in 7.86 and 7.87; Methyl linolenate and Methyl linoleate are predominantly involved in reactions such as 7.88 and 7.91, primarily interacting with OH.

Chapter 8 - Conclusion and Recommendations

8.1 Conclusion summary

In Chapter 5, a meticulous analysis was conducted on the autoignition and combustion characteristics of Waste Cooking Oil (WCO) Biodiesel (B100). The research concluded that increasing the WCO proportion in the biofuel mixture leads to a reduction in heat release rate (HRR) and ignition delay. This shift was also accompanied by alterations in the before top dead centre (BTDC) metrics. A notable decrease in peak cylinder pressure was observed, indicating an extension in the diffusion burning period for WCO B100. This extended burning period, however, resulted in diminished combustion efficiency for WCO B100, in contrast to its heightened thermal efficiency when compared to diesel and other blends.

The subsequent segment of the research investigated spray penetration dynamics of WCO B100 and diesel, underscoring the pivotal role of piston velocity in influencing liquid penetration length. The findings pointed to a superior evaporation rate for WCO B100, attributed to several factors including its higher density, lower latent heat, higher cetane number, and enhanced thermal conductivity, amongst others. Additionally, the unique molecular structure of unsaturated fatty acid methyl ester in WCO B100 propels faster vaporisation through heightened heat of combustion. A noteworthy revelation was that the ignition predominantly occurs near the wall, a region with a higher temperature compared to the core. This phenomenon delineates the nuanced interplay of varying physical and chemical properties governing the vapour and liquid penetration lengths of WCO B100 in comparison to diesel, offering a rich ground for understanding combustion dynamics.

Lastly, a comparative analysis entailing experimental and computational modelling laid the groundwork for evaluating emission generation. This endeavour manifested in a decline in HC and NOx levels. The investigative route also paved the way for the delineation of primary chemical reactions involving species pivotal in emission formation, with key reactions such as 7.36, 7.37, 7.41, 7.43, 7.44, and 7.52 playing a critical role in the consumption or production of CO and CO_2.

Synthesising these insights offers a multi-faceted understanding of WCO B100's potential in engine applications. While it showcases promising prospects with

shorter ignition delays and higher thermal efficiencies, it brings to fore challenges such as wall impingement and reduced combustion efficiency. These findings forge a path for incisive future research, steering toward optimal engine adaptations leveraging WCO B100 as a viable fuel alternative.

8.2 Recommendation and future works

- For efficiency and simplicity, it is recommended to use a single species as a representative in the surrogate fuel model.
- Perform double phase and multiple-phase injection schedules to reduce the emissions and to increase the thermal efficiency.
- Enhance the combustion efficiency by substituting the liquid fuel with alternative gaseous fuel like hydrogen in dual-fuel combustion technology.
- Increase the homogeneity between the liquid fuel and premixed charge by implementing the low-temperature combustion concept like Reactivity Controlled Compression Ignition (RCCI) and Homogeneous Charge Compression Ignition (HCCI).
- Optimise the performance and engine-out emissions characteristics by performing a parametric study in terms of advancing the liquid fuel injections.
- Mitigate the emissions by using alternative green diesel fuel like HVO instead of diesel.
- In order to integrate the LES turbulence model in the CFD research owing to the fact that when developing a better LES turbulence model, one of the most crucial considerations to keep in mind is how to account for non-linear interactions in a way that does not compromise numerical stability.
- To gain advantage of more accurate and resulting mesh model, such employing CONVERGE CFD software or open-source software such as OpenFOAM to be able to change and modify different types of essential computational models.
- To utilise the most modern commercial internal combustion engines, integrating new injectors can expose a variety of injection profile models.
- To conduct a study on a VCR engine with a glass through cylinder head to examine the spray and flame propagation in real time relative to piston movement.

- To create a more defined and robust experimental laboratory engine setup, it is suggested to incorporate an amplifier specifically designed for use with piezoelectric sensors.
- To gain the advantage of ECU by controlling the data and engine runs electronically.
- High thermal conductivity is crucial for devising effective heat transfer strategies in biodiesel fuels. To enhance this characteristic, the utilisation of metallic nanoparticles is recommended. Additionally, further research into this type of fuel is imperative to thoroughly assess its combustion and thermal efficiency.

Appendices

A Amplifier and pressure transducer calculation

For instance, upon recording a voltage of 4.67V by the amplifier and considering the pressure transducer's sensitivity of 15.64 pC/Bar, adjustments are made to the nodes sequentially from left to right as follows: 1, 5, 6. The sensitivity lever is calibrated within a range of 1 to 11. Given the amplifier's maximum capacity at 11 pC, this configuration illustrates a tenfold differential in sensitivity.

$$1.56 \times 10 = 15.6\ \mathrm{pC/Bar}$$

By using Equation 4.2 the result is given as below:

$$\frac{4.67}{(10(\text{times } 10 \text{ senstivity}) \times ((10^{3} \times 10^{-3})\text{mvunit/ouput})/1 \text{ unit out}} = 0.467\ \mathrm{V}$$

$$0.467 \times 100\ \mathrm{Bar} = 46.7\ \mathrm{Bar} = 4.67\ \mathrm{MPa}$$

Afterwards assigning the lowest and highest number of results in Equation 4.3 the final pressure is as below :

$$\frac{(10 \text{ voltage reference} \times (4.67 + 0.335 \text{ lowest number read}))}{(5.1 \text{ Highest pressure number read} + 0.335)} = 9.24\ \mathrm{MPa}$$

B Fuel mass flow rate

It can be observed from Table 5 at full load condition $10\ \mathrm{ml}$ is used at 61 seconds.

At 1300 rpm a full 720 crank angle degree is equal to 0.0923 seconds.

$$\frac{0.0923\ \mathrm{s} \times 10\ \mathrm{ml}}{61\ \mathrm{s}} = 0.0151 \times 10^{-6}\ \mathrm{m^3}$$

Density of WCO B100 is equivalent to $885\ {}^{\mathrm{kg}}/_{\mathrm{m^3}}$, thus mass of fuel is equal to as below:

$$1.513 \times 10^{-8}\ \mathrm{m^3} \times 885\ {}^{\mathrm{kg}}/_{\mathrm{m^3}} = 1.339 \times 10^{-5}\ \mathrm{kg}$$

Based on Table 6 injection pressure is $1.91 \times 10^{7}\ \mathrm{Pa}$ and diameter of nozzle hole is $0.22\ \mathrm{ml}$. In order to calculate the injection duration formula below is used:

$$t\,(s) = \sqrt{\frac{mass^2}{2 \times \rho \times P \times A^2}}$$

$$t\,(s) = \sqrt{\frac{(1.339 \times 10^{-5}\ kg)^2}{2 \times 885\ {}^{kg}/_{m^3} \times 1.91 \times 10^{7}\ Pa \times (1.445 \times 10^{-15}\ m^2)^2}}$$

$$= 0.00191\ s \times 6 \times 1300 \sim 15\ CA$$

Hence, fuel mass flow rate for WCO B100 at full load condition is equal to $0.00696\ {}^{kg}/_{s}$ as demonstrated below:

$$\frac{1.339 \times 10^{-5}\ kg}{0.00191\ s} = 0.00696\ {}^{kg}/_{s}$$

C Air mass flow rate

For Full load condition an air velocity of $3.4\ {}^{m}/_{s}$ is read on anemometer. Based on Table 5 density of air is $1.2\ {}^{kg}/_{m^3}$, therefore, using equation 4.4 will provide air mass flow rate from intake port to engine in-cylinder.

$$3.4 \times \frac{\pi \times (25 \times 10^{-3})^2}{4} \times 1.2 = 2 \times 10^{-3}\ {}^{kg}/_{s} = 2\ {}^{g}/_{s}$$

D Negative torque load

For illustrative purposes, consider a half load condition where the hydraulic dynamometer applies a force of 0.5 kg to the shaft of the Robin DY23-2D engine. The calculations that follow determine the equivalent torque, as derived from Equation 4.5.

$$0.5\ kg \times 9.81\ \frac{m}{s^2} \times 0.38\ m = 1.86\ N.m$$

E LabVIEW block diagram

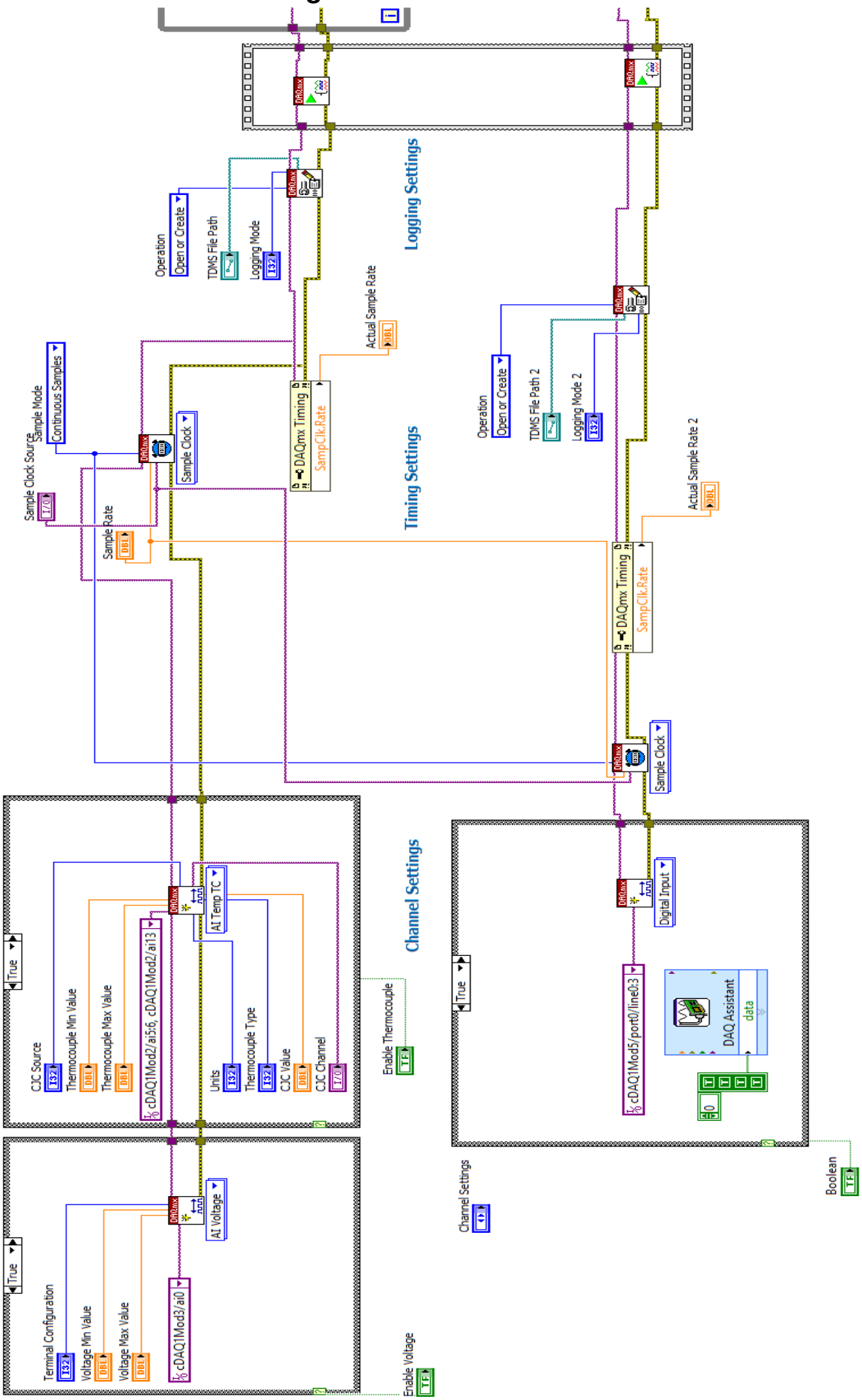

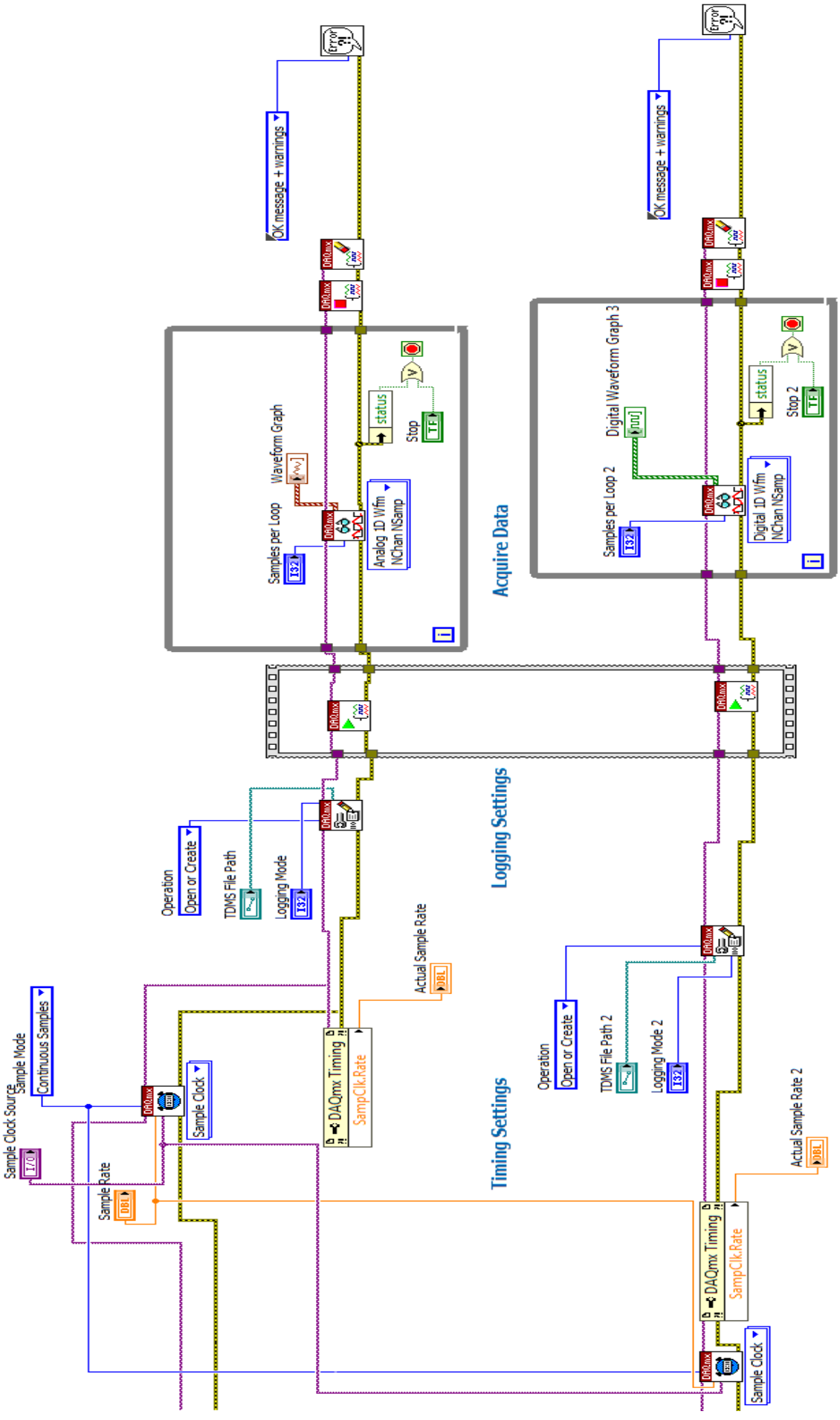
OK message + warnings
Acquire Data
Waveform Graph
Samples per Loop
Analog 1D Wfm NChan NSamp
status
Stop
Digital Waveform Graph 3
Digital 1D Wfm NChan NSamp
Logging Settings
Operation
Open or Create
TDMS File Path
Logging Mode
Actual Sample Rate
Timing Settings
Sample Clock Source
Sample Mode
Continuous Samples
Sample Clock
Sample Rate
DAQmx Timing
SampClk.Rate
Actual Sample Rate 2

F Engine setup schematic

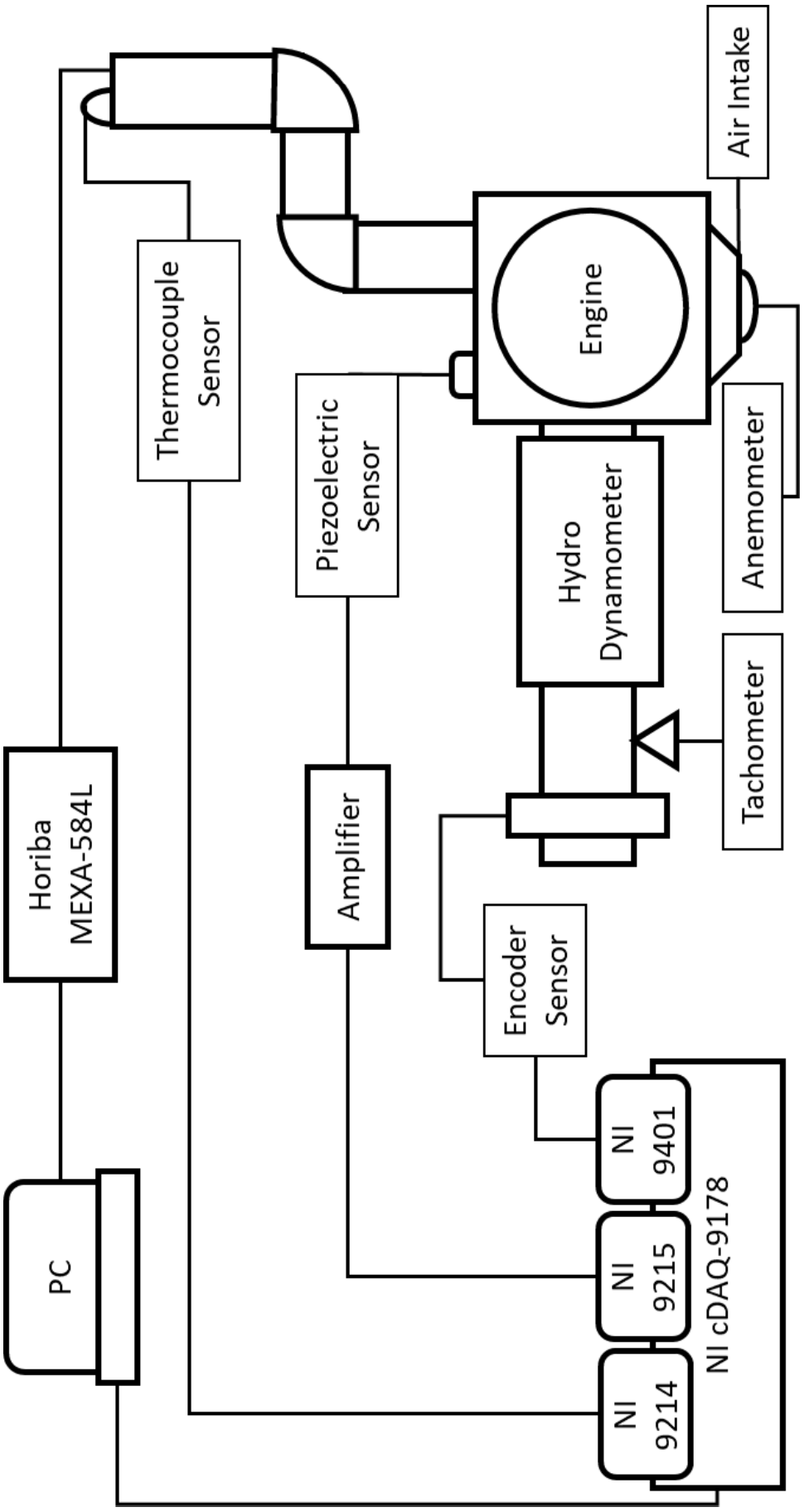

G Liquid droplet properties versus temperature

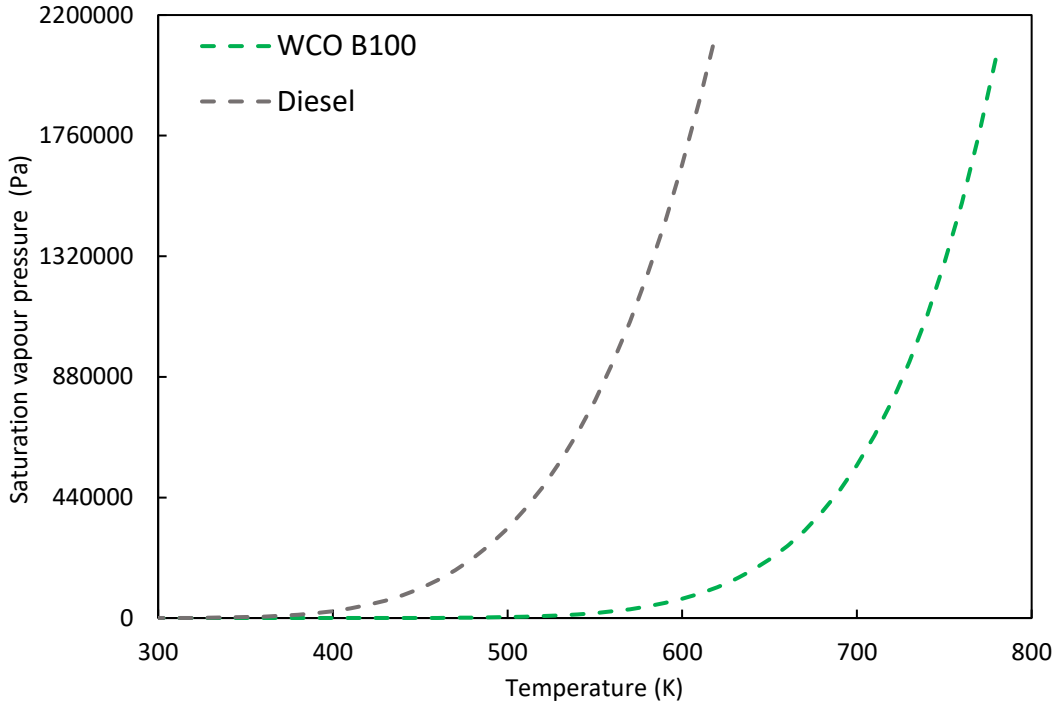

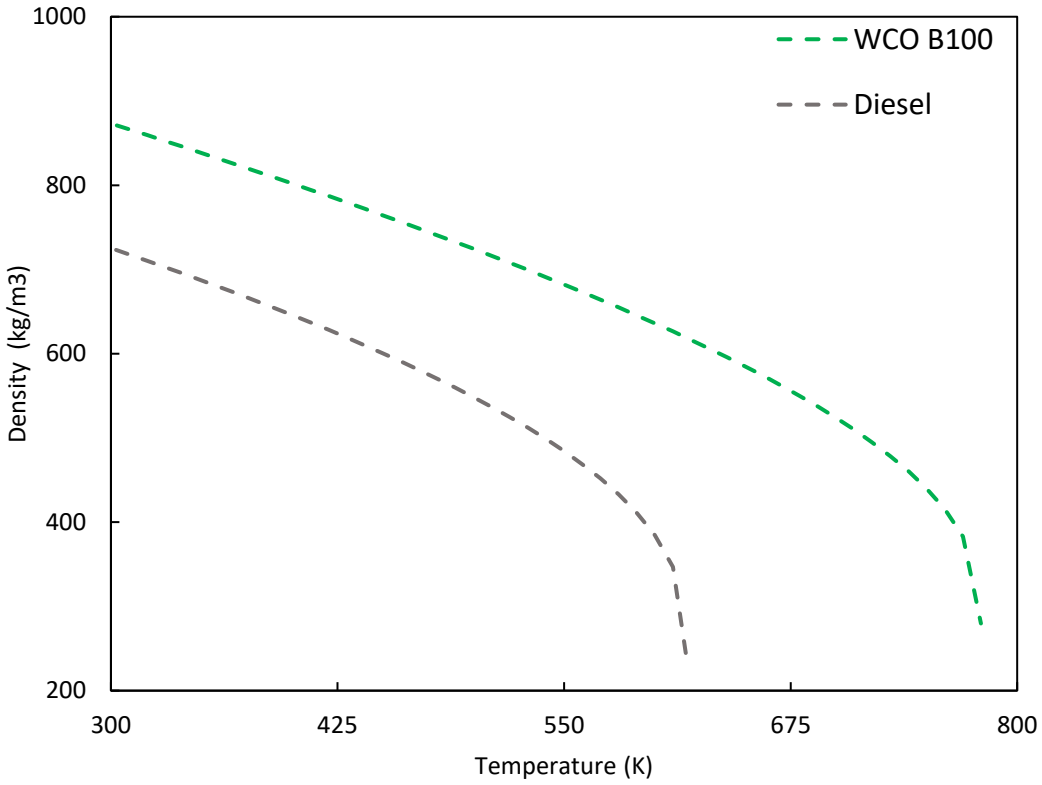

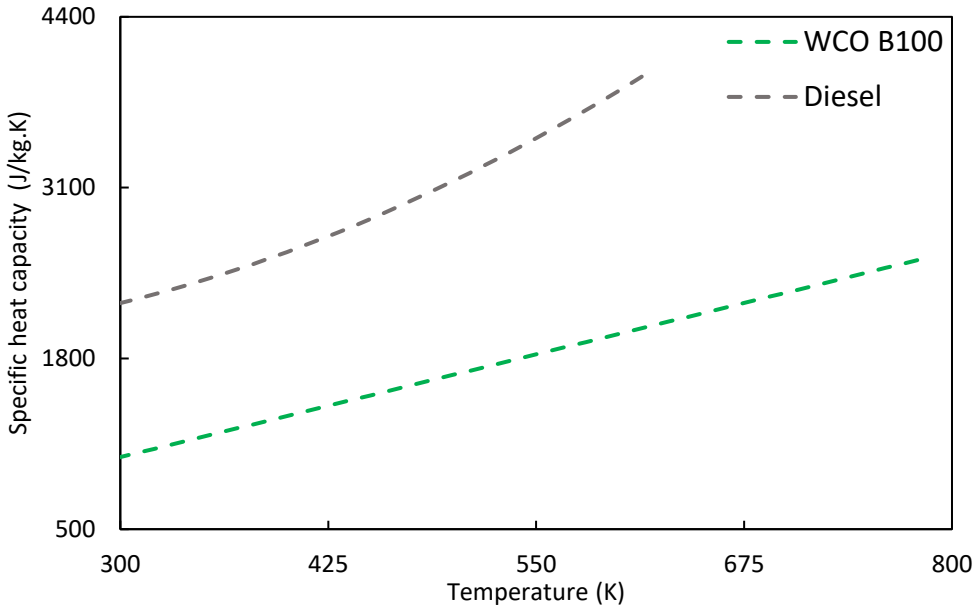
4400
3100
1800
500
Specific heat capacity (J/kg.K)
300
425
550
675
800
Temperature (K)
WCO B100
Diesel

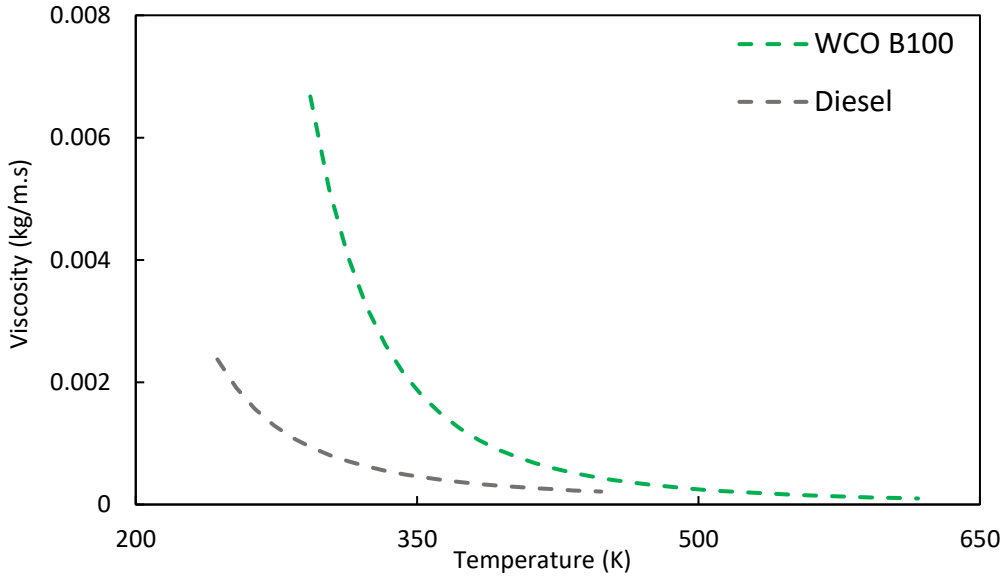
0.008
0.006
0.004
0.002
0
Viscosity (kg/m.s)
200
350
500
650
Temperature (K)
WCO B100
Diesel

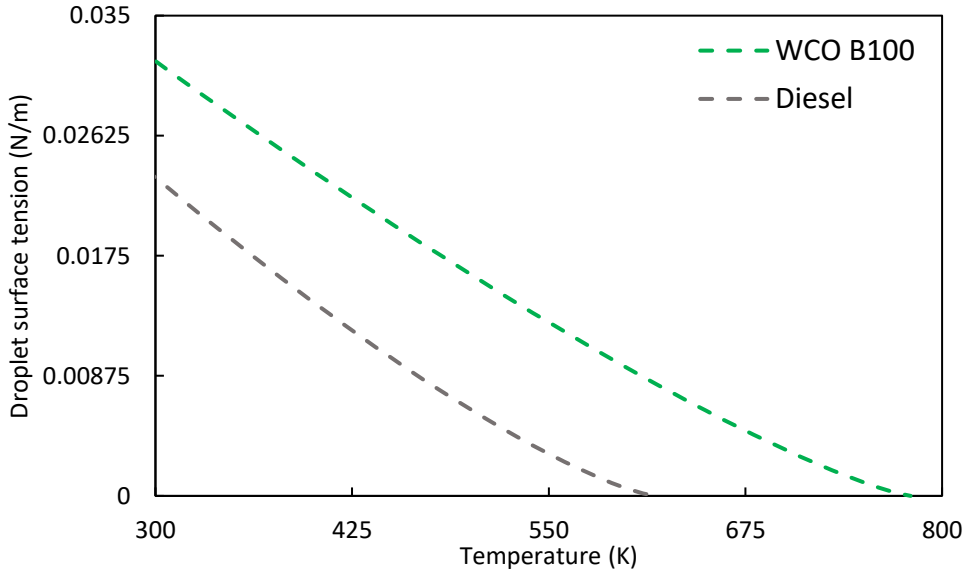
0.035
0.02625
0.0175
0.00875
0
Droplet surface tension (N/m)
300
425
550
675
800
Temperature (K)
WCO B100
Diesel

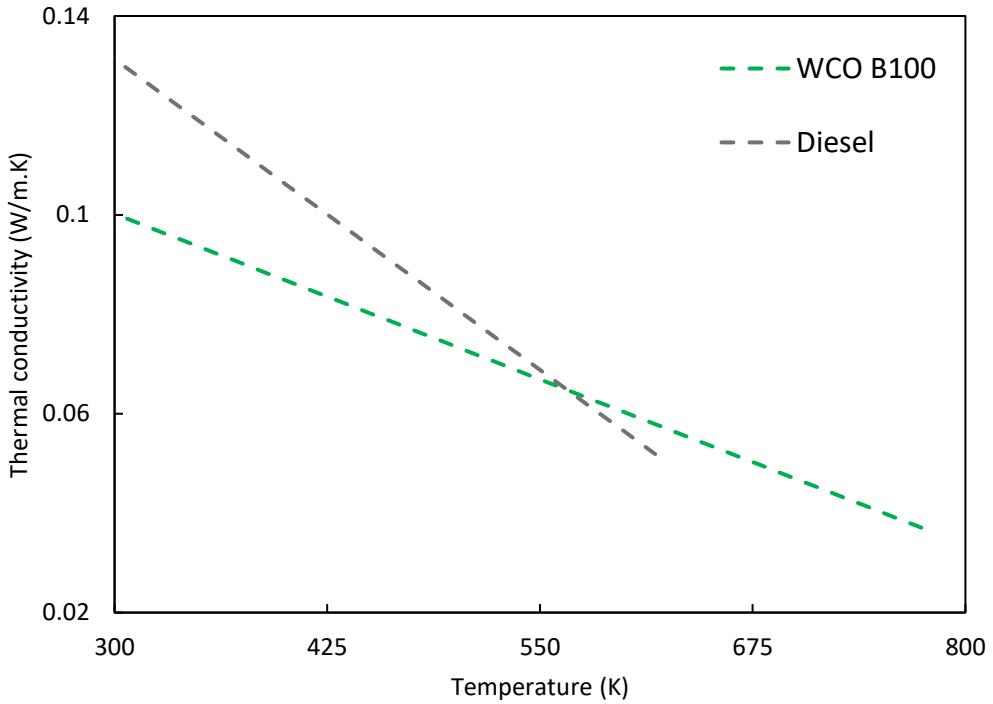
0.14
0.1
0.06
0.02
Thermal conductivity (W/m.K)
300
425
550
675
800
Temperature (K)
WCO B100
Diesel

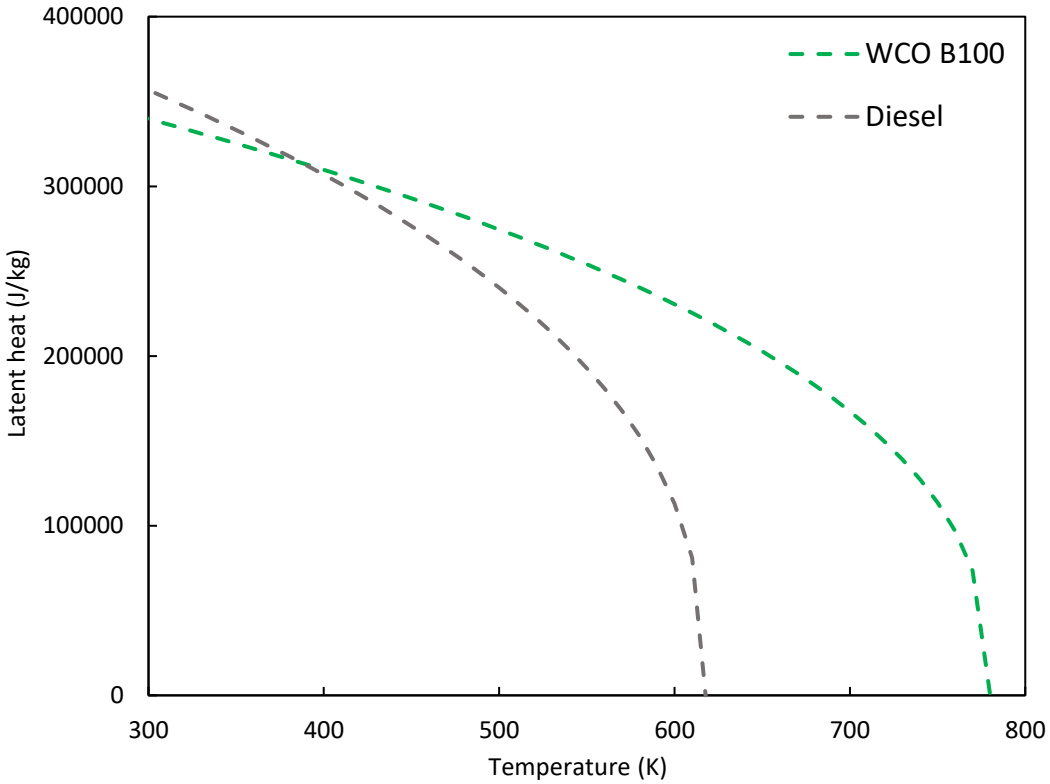
400000
300000
200000
100000
0
Latent heat (J/kg)
300
400
500
600
700
800
Temperature (K)
WCO B100
Diesel

References

Abbaszaadeh, A., Ghobadian, B., Omidkhah, M. R. and Najafi, G. (2012) 'Current biodiesel production technologies: A comparative review', *Energy Conversion and Management,* 63, pp. 138-148.

Abraham, J., Bracco, F. and Reitz, R. (1985) 'Comparisons of computed and measured premixed charge engine combustion', *Combustion and flame,* 60(3), pp. 309-322.

Adewale, P., Dumont, M.-J. and Ngadi, M. (2015) 'Recent trends of biodiesel production from animal fat wastes and associated production techniques', *Renewable and Sustainable Energy Reviews,* 45, pp. 574-588.

Alfazazi, A., Kuti, O. A., Naser, N., Chung, S. H. and Sarathy, S. M. (2016) 'Two-stage Lagrangian modeling of ignition processes in ignition quality tester and constant volume combustion chambers', *Fuel,* 185, pp. 589-598.

An, H., Yang, W., Maghbouli, A., Chou, S. and Chua, K. (2013) 'Detailed physical properties prediction of pure methyl esters for biodiesel combustion modeling', *Applied energy,* 102, pp. 647-656.

An, H., Yang, W., Maghbouli, A., Li, J., Chou, S., Chua, K., Wang, J. and Li, L. (2014) 'Numerical investigation on the combustion and emission characteristics of a hydrogen assisted biodiesel combustion in a diesel engine', *Fuel,* 120, pp. 186-194.

Anderson, J. D. and Wendt, J. (1995) *Computational fluid dynamics.* Springer.

ANSYS, I. (2020a) *Ansys Chemkin-Pro 2020 R2 Tutorials* Cannonsburg, PA: ANSYS, Inc.

ANSYS, I. (2020b) *Ansys Chemkin 2020 R2 Theory Manual* Cannonsburg, PA: ANSYS, Inc.

ANSYS, I. (2020c) *Ansys Fluent 2020 R2 Theory Guide* Cannonsburg, PA: ANSYS, Inc. .

ANSYS, I. (2020d) *Ansys Fluent 2020 R2 User Guide* Cannonsburg, PA: ANSYS, Inc.

Aransiola, E. F., Ojumu, T. V., Oyekola, O., Madzimbamuto, T. and Ikhu-Omoregbe, D. (2014) 'A review of current technology for biodiesel production: State of the art', *Biomass and bioenergy,* 61, pp. 276-297.

ASTM, A. (2010) 'Standard test method for determination of ignition delay and derived cetane number (DCN) of diesel fuel oils by combustion in a constant volume chamber', *D6890-10a*.

Atabani, A. E., Silitonga, A. S., Badruddin, I. A., Mahlia, T., Masjuki, H. and Mekhilef, S. (2012) 'A comprehensive review on biodiesel as an alternative energy resource and its characteristics', *Renewable and sustainable energy reviews,* 16(4), pp. 2070-2093.

Banerjee, S., Liang, T., Rutland, C. and Hu, B. (2010) *Validation of an LES multi mode combustion model for diesel combustion*: SAE Technical Paper (0148-7191.

Barnwal, B. and Sharma, M. (2005) 'Prospects of biodiesel production from vegetable oils in India', *Renewable and sustainable energy reviews,* 9(4), pp. 363-378.

Bergthorson, J. M. and Thomson, M. J. (2015) 'A review of the combustion and emissions properties of advanced transportation biofuels and their impact on existing and future engines', *Renewable and sustainable energy reviews,* 42, pp. 1393-1417.

Bharathiraja, B., Chakravarthy, M., Kumar, R. R., Yuvaraj, D., Jayamuthunagai, J., Kumar, R. P. and Palani, S. (2014) 'Biodiesel production using chemical and biological methods–A review of process, catalyst, acyl acceptor, source and process variables', *Renewable and Sustainable Energy Reviews,* 38, pp. 368-382.

Bogin Jr, G. E., DeFilippo, A., Chen, J., Chin, G., Luecke, J., Ratcliff, M. A., Zigler, B. T. and Dean, A. M. (2011) 'Numerical and experimental investigation of n-heptane autoignition in the ignition quality tester (IQT)', *Energy & Fuels,* 25(12), pp. 5562-5572.

Borugadda, V. B. and Goud, V. V. (2012) 'Biodiesel production from renewable feedstocks: Status and opportunities', *Renewable and Sustainable Energy Reviews,* 16(7), pp. 4763-4784.
Brakora, J. and Reitz, R. D. (2013) *A comprehensive combustion model for biodiesel-fueled engine simulations*: SAE Technical Paper (0148-7191.

Brakora, J. L. (2012) *A comprehensive combustion model for biodiesel-fueled engine simulations.* Doctoral dissertation, University of Wisconsin-Madison.

Brakora, J. L., Ra, Y., Reitz, R. D., McFarlane, J. and Daw, C. S. (2009) 'Development and validation of a reduced reaction mechanism for biodiesel-fueled engine simulations', *SAE International Journal of Fuels and Lubricants,* 1(1), pp. 675-702.

Chang, Y., Jia, M., Li, Y., Zhang, Y., Xie, M., Wang, H. and Reitz, R. D. (2015) 'Development of a skeletal oxidation mechanism for biodiesel surrogate', *Proceedings of the Combustion Institute,* 35(3), pp. 3037-3044.

Chen, M., Herrmann, M. and Peters, N. (2000) 'Flamelet modeling of lifted turbulent methane/air and propane/air jet diffusion flames', *Proceedings of the Combustion Institute,* 28(1), pp. 167-174.

Cheng, X. (2016) *Development of reduced reaction kinetics and fuel physical properties models for in-cylinder simulation of biodiesel combustion.* Doctoral dissertation, University of Nottingham.

Cheng, X. W., Gan, S. Y. and Ng, H. K. (2020) 'A numerical study on the quasi-steady spray and soot characteristics for soybean methyl ester and its blends with ethanol using CFD-reduced chemical kinetics approach', *Energy,* 200, pp. 117540.

Cowart, J., Luning Prak, D. and Hamilton, L. (2015) 'The effects of fuel injection pressure and fuel type on the combustion characteristics of a diesel engine', *Journal of Engineering for Gas Turbines and Power,* 137(10).

Crowe, C. T., Schwarzkopf, J. D., Sommerfeld, M. and Tsuji, Y. (2011) *Multiphase flows with droplets and particles.* CRC press.

Cuoci, A., Frassoldati, A., Faravelli, T. and Ranzi, E. (2009) 'Formation of soot and nitrogen oxides in unsteady counterflow diffusion flames', *Combustion and Flame,* 156(10), pp. 2010-2022.

Daud, N. M., Abdullah, S. R. S., Hasan, H. A. and Yaakob, Z. (2015) 'Production of biodiesel and its wastewater treatment technologies: a review', *Process Safety and Environmental Protection,* 94, pp. 487-508.

Demirbas, A. (2009a) 'Biodiesel from waste cooking oil via base-catalytic and supercritical methanol transesterification', *Energy Conversion and Management,* 50(4), pp. 923-927.

Demirbas, A. (2009b) 'Progress and recent trends in biodiesel fuels', *Energy Conversion and Management,* 50(1), pp. 14-34.

Ejim, C., Fleck, B. and Amirfazli, A. (2007) 'Analytical study for atomization of biodiesels and their blends in a typical injector: surface tension and viscosity effects', *Fuel,* 86(10-11), pp. 1534-1544.

Elhalwagy, M. and Zhang, C. (2019) 'A Proposed Biodiesel Combustion Kinetics Based on the Computational Fluid Dynamics Results in an Ignition Quality Tester', *Journal of Energy Resources Technology,* 141(8).

Engines, R. I. (2000) *Service manual models DY23-2, DY27-2*.

Erman, A. G., Hellier, P. and Ladommatos, N. (2020) 'The impact of ignition delay and further fuel properties on combustion and emissions in a compression ignition engine', *Fuel,* 262, pp. 116155.

Fangfang, F., Alagumalai, A. and Mahian, O. (2021) 'Sustainable biodiesel production from waste cooking oil: ANN modeling and environmental factor assessment', *Sustainable Energy Technologies and Assessments,* 46, pp. 101265.

Feng, Q., Jalali, A., Fincham, A. M., Wang, Y. L., Tsotsis, T. T. and Egolfopoulos, F. N. (2012) 'Soot formation in flames of model biodiesel fuels', *Combustion and Flame,* 159(5), pp. 1876-1893.

Fontaras, G., Kousoulidou, M., Karavalakis, G., Tzamkiozis, T., Pistikopoulos, P., Ntziachristos, L., Bakeas, E., Stournas, S. and Samaras, Z. (2010) 'Effects of low concentration biodiesel blend application on modern passenger cars. Part 1: Feedstock impact on regulated pollutants, fuel consumption and particle emissions', *Environmental Pollution,* 158(5), pp. 1451-1460.

Frassoldati, A., Faravelli, T. and Ranzi, E. (2003) 'Kinetic modeling of the interactions between NO and hydrocarbons at high temperature', *Combustion and Flame,* 135(1-2), pp. 97-112.

Gaïl, S., Sarathy, S., Thomson, M., Diévart, P. and Dagaut, P. (2008) 'Experimental and chemical kinetic modeling study of small methyl esters oxidation: Methyl (E)-2-butenoate and methyl butanoate', *Combustion and Flame,* 155(4), pp. 635-650.

Garner, S., Sivaramakrishnan, R. and Brezinsky, K. (2009) 'The high-pressure pyrolysis of saturated and unsaturated C7 hydrocarbons', *Proceedings of the Combustion Institute,* 32(1), pp. 461-467.

Garzón, N. A. N., Oliveira, A. A. and Bazzo, E. (2019) 'An ignition delay correlation for compression ignition engines fueled with straight soybean oil and diesel oil blends', *Fuel,* 257, pp. 116050.

Gerveni, M., Hubbs, T. and Irwin, S. (2023) 'Biodiesel and Renewable Diesel: What's the Difference?', *farmdoc daily,* 13(22).

Gharehghani, A., Mirsalim, M. and Hosseini, R. (2017) 'Effects of waste fish oil biodiesel on diesel engine combustion characteristics and emission', *Renewable Energy,* 101, pp. 930-936.

Gong, C., Jangi, M., Lucchini, T., D'Errico, G. and Bai, X.-S. (2014) 'Large eddy simulation of air entrainment and mixing in reacting and non-reacting diesel sprays', *Flow, turbulence and combustion,* 93, pp. 385-404.

Gopinath, A., Sairam, K., Velraj, R. and Kumaresan, G. (2015) 'Effects of the properties and the structural configurations of fatty acid methyl esters on the properties of biodiesel fuel: a review', *Proceedings of the Institution of Mechanical Engineers Part D-Journal of Automobile Engineering,* 229(3), pp. 357-390.

Hellier, P., Talibi, M., Eveleigh, A. and Ladommatos, N. (2018) 'An overview of the effects of fuel molecular structure on the combustion and emissions characteristics of compression ignition engines', *Proceedings of the Institution of Mechanical Engineers, Part D: Journal of Automobile Engineering,* 232(1), pp. 90-105.

Hergart, C., Barths, H. and Peters, N. (1999) *Modeling the combustion in a small-bore diesel engine using a method based on representative interactive flamelets*: SAE Technical Paper (0148-7191.

Heywood, J. B. (2018) *Internal combustion engine fundamentals.* McGraw-Hill Education.

Hoekman, S. K., Broch, A., Robbins, C., Ceniceros, E. and Natarajan, M. (2012) 'Review of biodiesel composition, properties, and specifications', *Renewable and sustainable energy reviews,* 16(1), pp. 143-169.

Hosamani, B. and Katti, V. (2018) 'Experimental analysis of combustion characteristics of CI DI VCR engine using mixture of two biodiesel blend with diesel', *Engineering science and technology, an international journal,* 21(4), pp. 769-777.

Ibadurrohman, I. A., Hamidi, N. and Yuliati, L. (2022) 'The role of the unsaturation degree on the droplet combustion characteristics of fatty acid methyl ester', *Alexandria Engineering Journal,* 61(3), pp. 2046-2060.

Isidro, M. 1992. Termodinámica Básica y Aplicada. Dossat. Madrid.

Islamova, A., Tkachenko, P., Shlegel, N. and Kuznetsov, G. (2023) 'Secondary Atomization of Fuel Oil and Fuel Oil/Water Emulsion through Droplet-Droplet Collisions and Impingement on a Solid Wall', *Energies,* 16(2), pp. 1008.

Ismail, H. M., Ng, H. K., Cheng, X., Gan, S., Lucchini, T. and D'Errico, G. (2012) 'Development of thermophysical and transport properties for the CFD simulations of in-cylinder biodiesel spray combustion', *Energy & Fuels,* 26(8), pp. 4857-4870.

Kannan, G., Balasubramanian, K., Sivapirakasam, S. and Anand, R. (2011) 'Studies on biodiesel production and its effect on DI diesel engine performance, emission and combustion characteristics', *International Journal of Ambient Energy,* 32(4), pp. 179-193.

Karmee, S. K. and Chadha, A. (2005) 'Preparation of biodiesel from crude oil of Pongamia pinnata', *Bioresource technology,* 96(13), pp. 1425-1429.

Kathrotia, T. (2011) *Reaction kinetics modeling of OH*, CH*, and C2* chemiluminescence.*

Knothe, G. (2005) 'Dependence of biodiesel fuel properties on the structure of fatty acid alkyl esters', *Fuel Processing Technology,* 86(10), pp. 1059-1070.

Knothe, G. (2014) 'A comprehensive evaluation of the cetane numbers of fatty acid methyl esters', *Fuel,* 119, pp. 6-13.

Kulkarni, M. G. and Dalai, A. K. (2006) 'Waste cooking oil-an economical source for biodiesel: A review', *Industrial & Engineering Chemistry Research,* 45(9), pp. 2901-2913.

Kuti, O., Nishida, K., Sarathy, M. and Zhu, J. (2013a) 'Fuel spray combustion of waste cooking oil and palm oil biodiesel: direct photography and detailed chemical kinetics', *SAE Technical Paper,* (1).

Kuti, O. A., Bahmanisangesari, S., Gilmour, R., Albarbar, A., Qian, L. and Nishida, K. 'Characterization of Waste Cooking Oil Biodiesel as a Low Carbon Fuel for Direct Injection Diesel Engine', *THIESEL 2022 Conference on Thermo- and Fluid Dynamics of Clean Propulsion Powerplants*, Valencia Spain.

Kuti, O. A., Nishida, K. and Zhu, J. Y. (2013) 'Experimental studies on spray and gas entrainment characteristics of biodiesel fuel: Implications of gas entrained and fuel oxygen content on soot formation', *Energy,* 57, pp. 434-442.

Kuti, O. A., Sarathy, S. M. and Nishida, K. (2020) 'Spray combustion simulation study of waste cooking oil biodiesel and diesel under direct injection diesel engine conditions', *Fuel,* 267, pp. 117240.

Kuti, O. A., Xiangang, W. G., Zhang, W., Nishida, K. and Huang, Z. H. (2010) 'Characteristics of the ignition and combustion of biodiesel fuel spray injected by a common-rail injection system for a direct-injection diesel engine', *Proceedings of the Institution of Mechanical Engineers Part D-Journal of Automobile Engineering,* 224(D12), pp. 1581-1596.

Kuti, O. A., Zhu, J. Y., Nishida, K., Wang, X. G. and Huang, Z. H. (2013b) 'Characterization of spray and combustion processes of biodiesel fuel injected by diesel engine common rail system', *Fuel,* 104, pp. 838-846.

Labecki, L., Cairns, A., Xia, J., Megaritis, A., Zhao, H. and Ganippa, L. (2012) 'Combustion and emission of rapeseed oil blends in diesel engine', *Applied Energy,* 95, pp. 139-146.

Labecki, L. and Ganippa, L. (2012) 'Effects of injection parameters and EGR on combustion and emission characteristics of rapeseed oil and its blends in diesel engines', *Fuel,* 98, pp. 15-28.

Lahane, S. and Subramanian, K. (2014) 'Impact of nozzle holes configuration on fuel spray, wall impingement and NOx emission of a diesel engine for biodiesel–diesel blend (B20)', *Applied Thermal Engineering,* 64(1-2), pp. 307-314.

Lapuerta, M., Herreros, J. M., Lyons, L. L., García-Contreras, R. and Briceño, Y. (2008) 'Effect of the alcohol type used in the production of waste cooking oil biodiesel on diesel performance and emissions', *Fuel,* 87(15-16), pp. 3161-3169.

Launder, B. E. and Spalding, D. B. (1972) 'Lectures in mathematical models of turbulence'.

Lee, S. Y., Kim, H. M. and Cheon, S. (2015) 'Metabolic engineering for the production of hydrocarbon fuels', *Current opinion in biotechnology,* 33, pp. 15-22.

Li, H., Yang, W. M., Zhou, D. Z. and Yu, W. B. (2018) 'Numerical study of the effects of biodiesel unsaturation on combustion and emission characteristics in diesel engine', *Applied Thermal Engineering,* 137, pp. 310-318.

Liu, H., Huo, M., Liu, Y., Wang, X., Wang, H., Yao, M. F. and Lee, C. F. F. (2014) 'Time-resolved spray, flame, soot quantitative measurement fueling n-butanol and soybean biodiesel in a constant volume chamber under various ambient temperatures', *Fuel,* 133, pp. 317-325.

Liu, X., Wang, H., Zhang, Y. and Yao, M. F. (2019) 'A Numerical Investigation on the Chemical Kinetics Process of a Reacting n-Dodecane Spray Flame under Compression Ignition Combustion Condition', *Energy & Fuels,* 33(11), pp. 11899-11912.

Luo, Z., Plomer, M., Lu, T., Som, S., Longman, D. E., Sarathy, S. M. and Pitz, W. J. (2012) 'A reduced mechanism for biodiesel surrogates for compression ignition engine applications', *Fuel,* 99, pp. 143-153.

Maceiras, R., Míguez, J. L. and González, M. V. (2019) 'The role of the restaurant sector in the transition towards a circular economy: a Spanish case study', *Journal of Cleaner Production,* 230, pp. 1128-1137.

McCormick, R. L., Graboski, M. S., Alleman, T. L., Herring, A. M. and Tyson, K. S. (2001) 'Impact of biodiesel source material and chemical structure on emissions of criteria pollutants from a heavy-duty engine', *Environmental science & technology,* 35(9), pp. 1742-1747.

Menon, S. (2000) 'Subgrid combustion modelling for large-eddy simulations', *International Journal of Engine Research,* 1(2), pp. 209-227.

Miller, R., Harstad, K. and Bellan, J. (1998) 'Evaluation of equilibrium and non-equilibrium evaporation models for many-droplet gas-liquid flow simulations', *International Journal of Multiphase Flow,* 24(6), pp. 1025-1055.

Mohan, B., Tay, K. L., Yang, W. and Chua, K. J. (2015) 'Development of a skeletal multi-component fuel reaction mechanism based on decoupling methodology', *Energy Conversion and Management,* 105, pp. 1223-1238.

Naik, C. V., Puduppakkam, K., Meeks, E. and Liang, L. (2012) *Ignition quality tester guided improvements to reaction mechanisms for n-alkanes: n-heptane to n-hexadecane*: SAE Technical Paper (0148-7191.

Nayak, P. K., Dash, U., Rayaguru, K. and Krishnan, K. R. (2016) 'Physio-chemical changes during repeated frying of cooked oil: A Review', *Journal of Food Biochemistry,* 40(3), pp. 371-390.

Ng, H. K., Gan, S., Ng, J.-H. and Pang, K. M. (2013) 'Simulation of biodiesel combustion in a light-duty diesel engine using integrated compact biodiesel–diesel reaction mechanism', *Applied energy,* 102, pp. 1275-1287.

O'Rourke, P. J. (1981) *Collective drop effects on vapourizing liquid sprays.* Princeton University.

Pagotto, C., Richard, Y., Veillette, M. and Proulx, D. (2007) 'Occurrence of Cryptosporidium and Giardia in raw and finished drinking water in a rural setting: Implication for system management', *Canadian Journal of Microbiology,* 53(10), pp. 1188-1192.

Pitsch, H. (2005) *Large eddy simulation of turbulent combustion*: LELAND STANFORD JUNIOR UNIV STANFORD CA.

Pitsch, H., Barths, H. and Peters, N. (1996) 'Three-dimensional modeling of NO x and soot formation in DI-diesel engines using detailed chemistry based on the interactive flamelet approach', *SAE transactions*, pp. 2010-2024.

Proctor, C. L. and Armstrong, L. V. H. (2023) *diesel engine*: Encyclopædia Britannica. Available at: https://www.britannica.com/technology/diesel-engine (Accessed: 10 August 2023.

Ranzi, E., Cavallotti, C., Cuoci, A., Frassoldati, A., Pelucchi, M. and Faravelli, T. (2015) 'New reaction classes in the kinetic modeling of low temperature oxidation of n-alkanes', *Combustion and flame,* 162(5), pp. 1679-1691.

Raza, A., Mehboob, H., Miran, S., Arif, W. and Rizvi, S. F. J. (2020) 'Investigation on the Characteristics of Biodiesel Droplets in the Engine Cylinder', *Energies,* 13(14), pp. 3637.

Richards, K., Senecal, P. and Pomraning, E. 2017. CONVERGE 2.4 Manual. Madison, WI: Convergent Science. Inc.

Rodríguez, R. P., Sierens, R. and Verhelst, S. (2011) 'Ignition delay in a palm oil and rapeseed oil biodiesel fuelled engine and predictive correlations for the ignition delay period', *Fuel,* 90(2), pp. 766-772.

Rosenberg, A. A., McCully, S. B. and Allen, T. F. (2019) 'Causes of nutrient enrichment and oxygen depletion in lakes', *Freshwater Biology,* 65(5), pp. 879-896.

Rutland, C. (2011) 'Large-eddy simulations for internal combustion engines–a review', *International Journal of Engine Research,* 12(5), pp. 421-451.

Saggese, C., Frassoldati, A., Cuoci, A., Faravelli, T. and Ranzi, E. (2013) 'A lumped approach to the kinetic modeling of pyrolysis and combustion of biodiesel fuels', *Proceedings of the combustion institute,* 34(1), pp. 427-434.

Sakib, A. N., Farokhi, M. and Birouk, M. (2023) 'Evaluation of flamelet-based partially premixed combustion models for simulating the gas phase combustion of a grate firing biomass furnace', *Fuel,* 333, pp. 126343.

Sazhin, S. S. (2006) 'Advanced models of fuel droplet heating and evaporation', *Progress in Energy and Combustion Science,* 32(2), pp. 162-214.

Schirmer, A., Rude, M. A., Li, X., Popova, E. and Del Cardayre, S. B. (2010) 'Microbial biosynthesis of alkanes', *Science,* 329(5991), pp. 559-562.

Schönborn, A., Ladommatos, N., Williams, J., Allan, R. and Rogerson, J. (2009) 'The influence of molecular structure of fatty acid monoalkyl esters on diesel combustion', *Combustion and flame,* 156(7), pp. 1396-1412.

Schumacher, L., Wetherell, W. and Fischer, J. 'Cold flow properties of biodiesel and its blends with diesel fuel'. *ASAE/CSAE-SCGR Annual International Meeting, Toronto, Ontario, Canada, 18-21 July, 1999.*: American Society of Agricultural Engineers (ASAE).

Senecal, P., Pomraning, E., Richards, K., Briggs, T., Choi, C., McDavid, R. and Patterson, M. (2003) 'Multi-dimensional modeling of direct-injection diesel spray liquid length and flame lift-off length using CFD and parallel detailed chemistry', *SAE transactions*, pp. 1331-1351.

Sharma, V., Hossain, A. K. and Duraisamy, G. (2021) 'Experimental Investigation of Neat Biodiesels' Saturation Level on Combustion and Emission Characteristics in a CI Engine', *Energies,* 14(16), pp. 5203.

Singh, D., Sharma, D., Soni, S. L., Sharma, S. and Kumari, D. (2019) 'Chemical compositions, properties, and standards for different generation biodiesels: A review', *Fuel,* 253, pp. 60-71.

Smith, K. R., Chafe, Z., Woodward, A., Campbell-Lendrum, D., Chadee, D., Honda, Y., Liu, Q., Olwoch, J., Revich, B. and Sauerborn, R. (2015) 'Human health: impacts, adaptation, and co-benefits', *Climate Change 2014 Impacts, Adaptation and Vulnerability: Part A: Global and Sectoral Aspects*, pp. 709-754.

Sogbesan, O., Garner, C. P. and Davy, M. H. (2021) 'The effects of increasing FAME biodiesel content on combustion characteristics and HC emissions in high-EGR low temperature combustion', *Fuel,* 302, pp. 121055.

Som, S., Aggarwal, S. K., El-Hannouny, E. and Longman, D. (2010) 'Investigation of nozzle flow and cavitation characteristics in a diesel injector', *Journal of Engineering for Gas Turbines and Power,* 132(4).

Steen, E. J., Kang, Y., Bokinsky, G., Hu, Z., Schirmer, A., McClure, A., Del Cardayre, S. B. and Keasling, J. D. (2010) 'Microbial production of fatty-acid-derived fuels and chemicals from plant biomass', *Nature,* 463(7280), pp. 559-562.

Stone, R. (1999) *Introduction to internal combustion engines.* Springer.

Taylor, C. F. (1985) *Internal Combustion Engine in Theory and Practice, revised, Volume 2: Combustion, Fuels, Materials, Design.* MIT press.

Tootoonchi, E. and Micklow, G. J. (2016) 'Thermophysical properties validation for soy methyl ester biodiesel through experimental spray data', *Biofuels-Uk,* 7(6), pp. 677-688.

Tripathi, S. and Subramanian, K. A. (2018) 'Control of fuel spray wall impingement on piston bowl in palm acid oil biodiesel fueled direct injection automotive engine using retarded injection timing, EGR and increased compression ratio', *Applied Thermal Engineering,* 142, pp. 241-254.

Tsang, C.-W. and Rutland, C. J. 'Effects of fuel physical properties and breakup model constants on large-eddy simulation of diesel sprays'. *Internal Combustion Engine Division Fall Technical Conference*: American Society of Mechanical Engineers, V002T06A018.

Vallero, D. (2019) *Air pollution calculations: Quantifying pollutant formation, transport, transformation, fate and risks.* Elsevier.

Vasudevan, V., Davidson, D. F., Hanson, R. K., Bowman, C. T. and Golden, D. M. (2007) 'High-temperature measurements of the rates of the reactions CH2O+ Ar→ Products and CH2O+ O2→ Products', *Proceedings of the Combustion Institute,* 31(1), pp. 175-183.

Versteeg, H. K. and Malalasekera, W. (2007) *An introduction to computational fluid dynamics: the finite volume method.* Pearson education.

Vidigal, I. G., Siqueira, A. F., Melo, M. P., Giordani, D. S., da Silva, M. L., Cavalcanti, E. H. and Ferreira, A. L. (2021) 'Applications of an electronic nose in the prediction of oxidative stability of stored biodiesel derived from soybean and waste cooking oil', *Fuel,* 284, pp. 119024.

Vijayaraj, K. and Sathiyagnanam, A. (2016) 'Combustion characteristics of a DI diesel engine fuelled with blends of methyl ester of cotton seed oil', *International Journal of Ambient Energy,* 37(6), pp. 633-638.

Wang, Q. and Chen, C. (2017) 'Simulated kinetics and chemical and physical properties of a four-component diesel surrogate fuel', *Energy & Fuels,* 31(12), pp. 13190-13197.

Wang, W. J., Gowdagiri, S. and Oehlschlaeger, M. A. (2013) 'Comparative Study of the Autoignition of Methyl Decenoates, Unsaturated Biodiesel Fuel Surrogates', *Energy & Fuels,* 27(9), pp. 5527-5532.

Wang, Y., Al-Shemmeri, T., Eames, P., McMullan, J., Hewitt, N., Huang, Y. and Rezvani, S. (2006) 'An experimental investigation of the performance and gaseous exhaust emissions of a diesel engine using blends of a vegetable oil', *Applied thermal engineering,* 26(14-15), pp. 1684-1691.

Westbrook, C. K., Naik, C. V., Herbinet, O., Pitz, W. J., Mehl, M., Sarathy, S. M. and Curran, H. J. (2011) 'Detailed chemical kinetic reaction mechanisms for soy and rapeseed biodiesel fuels', *Combustion and Flame,* 158(4), pp. 742-755.

Xue, J., Grift, T. E. and Hansen, A. C. (2011) 'Effect of biodiesel on engine performances and emissions', *Renewable and Sustainable energy reviews,* 15(2), pp. 1098-1116.

Yang, J. (2012) *Biodiesel spray combustion modeling based on a detailed chemistry approach.* Chalmers University of Technology.

Yanowitz, J., Ratcliff, M. A., McCormick, R. L., Taylor, J. D. and Murphy, M. J. (2017) *Compendium of experimental cetane numbers*: National Renewable Energy Lab.(NREL), Golden, CO (United States).

Yaqoob, H., Teoh, Y. H., Sher, F., Farooq, M. U., Jamil, M. A., Kausar, Z., Sabah, N. U., Shah, M. F., Rehman, H. Z. U. and Rehman, A. U. (2021) 'Potential of waste cooking oil biodiesel as renewable fuel in combustion engines: A review', *Energies,* 14(9), pp. 2565.

Yu, C., Bari, S. and Ameen, A. (2002) 'A comparison of combustion characteristics of waste cooking oil with diesel as fuel in a direct injection diesel engine', *Proceedings of the Institution of Mechanical Engineers, Part D: Journal of Automobile Engineering,* 216(3), pp. 237-243.

Yuan, W., Hansen, A. and Zhang, Q. (2005) 'Vapour pressure and normal boiling point predictions for pure methyl esters and biodiesel fuels', *Fuel,* 84(7-8), pp. 943-950.

Zhao, Z., Huang, X., Sheng, H., Chen, Z. and Liu, H. (2022) 'Enhanced low-temperature stable combustion of hydrocarbon with suppressing the Leidenfrost effect', *International Journal of Heat and Mass Transfer,* 185, pp. 122413.

Zhong, W., Tamilselvan, P., Wang, Q., He, Z., Feng, H. and Yu, X. (2018) 'Experimental study of spray characteristics of diesel/hydrogenated catalytic biodiesel blended fuels under inert and reacting conditions', *Energy,* 153, pp. 349-358.

Zhou, Q., Lucchini, T., D'Errico, G. and Hardy, G. (2019) *Validation of Diesel combustion models with turbulence chemistry interaction and detailed kinetics*: SAE Technical Paper (0148-7191.

Zhou, Q., Lucchini, T., D'Errico, G., Hardy, G. and Lu, X. (2021) 'Modeling heavy-duty diesel engines using tabulated kinetics in a wide range of operating conditions', *International Journal of Engine Research,* 22(4), pp. 1116-1132.